

Surface brightness fluctuation measurements of dwarf
elliptical galaxies in nearby galaxy clusters

Dissertation

zur Erlangung des Doktorgrades (Dr. rer. nat.)

der

Mathematisch-Naturwissenschaftlichen Fakultät

der

Rheinischen Friedrich-Wilhelms-Universität Bonn

vorgelegt von

Steffen Mieske

aus

Neuwied

Bonn, März 2005

Angefertigt mit Genehmigung der Mathematisch-Naturwissenschaftlichen Fakultät
der Rheinischen Friedrich-Wilhelms-Universität Bonn

1. Referent: Prof. Dr. Leopoldo Infante
2. Referent: Prof. Dr. Klaas S. de Boer

Tag der Promotion: 31.3.2005

Abstract

This thesis deals with the application of the surface brightness fluctuations (SBF) method to estimate distances to dwarf elliptical galaxies (dEs) in nearby galaxy clusters. We start with simulations quantifying the potential of the SBF method to determine the membership of candidate dEs in nearby clusters. These simulations show that with large telescopes and under good atmospheric conditions, unambiguous cluster memberships out to $\simeq 20$ Mpc can be derived down to very faint absolute magnitudes $M_V \simeq -11$ mag. In a first application, we present the cluster membership confirmation of 10 candidate dEs in the Fornax cluster using SBF-distances. Combining this with morphological cluster membership selection, the faint end slope α of the early-type galaxy luminosity function in Fornax is found to be $\alpha = -1.1 \pm 0.1$. This confirms the strong discrepancy between the number of low mass dark matter halos expected in a Λ CDM universe and the number of low luminosity galaxies. Based on the SBF measurements for the Fornax cluster dEs, the SBF calibration at blue colours is discussed. In a second application, we derive SBF-distances to a set of 31 early-type galaxies in the Hydra and Centaurus clusters, among them 26 dwarf galaxies. We obtain a mean distance of 41.2 ± 1.4 Mpc for Hydra and 45.3 ± 2.0 for Centaurus. From the scatter of the SBF distances around their mean we derive an upper limit of ± 3 Mpc radial extension for Hydra and ± 6 Mpc for Centaurus, corresponding to about three times their tangential extension. Based on our cluster distances we estimate a peculiar velocity of 1225 ± 235 km s $^{-1}$ for Hydra and 210 ± 295 km s $^{-1}$ for Centaurus, different at the 98% confidence level. This finding is consistent with the presence of a massive “Great Attractor” of $\simeq 10^{16} M_*$ in close projection to and slightly behind the Hydra cluster. We rule out the hypothesis that the Centaurus cluster is identical to the Great Attractor at 94% confidence. For all three galaxy clusters investigated, the limiting absolute dE magnitude for application of the SBF method is in very good agreement with the limits predicted from the simulations.

Contents

1	Introduction	1
1.1	The cosmic distance ladder	2
1.1.1	Distances within the Milky Way	2
1.1.2	Extragalactic distances	3
1.2	The surface brightness fluctuations method	5
1.2.1	Measuring SBF	7
1.2.2	Empirical calibration of SBF	8
1.3	Aim of this thesis	12
2	Potential of the SBF method to measure distances to dwarf elliptical galaxies in nearby clusters	13
2.1	Abstract	13
2.2	Introduction	14
2.2.1	The faint end of the galaxy luminosity function	14
2.2.2	Distances to galaxies with the SBF Method	15
2.3	Deriving \bar{M}_I from $(V - I)_0$	17
2.4	Simulating and measuring surface brightness fluctuations for dEs	18
2.4.1	Simulation of surface brightness fluctuations	19
2.4.2	Measurement of SBF	20
2.5	Results of the simulations and their discussion	23
2.5.1	Limiting absolute magnitudes	28
2.5.2	Comparing real SBF data with simulations	30
2.6	Summary	31
3	SBF distances to candidate dEs in the Fornax cluster	33
3.1	Abstract	33
3.2	Introduction: search for dE candidates in Fornax	34
3.2.1	Observations and data analysis	34
3.2.2	The faint end of the luminosity function from morphology	38
3.3	“Fornax Deep Field”	38
3.3.1	The data	40

3.3.2	Discussion I: Improved constraints on the Fornax galaxy luminosity function	46
3.3.3	Discussion II: Distance to the Fornax cluster and SBF calibration at blue colours	68
3.4	Summary	76
4	SBF distances to dEs and Es in the Centaurus and Hydra clusters	79
4.1	Abstract	79
4.2	Introduction	80
4.2.1	Peculiar velocities for galaxies	80
4.2.2	Peculiar velocities towards Hydra-Centaurus	81
4.2.3	Aim of this chapter	82
4.3	The data	83
4.3.1	Centaurus	83
4.3.2	Hydra	86
4.3.3	Data reduction before SBF measurement	86
4.3.4	SBF measurement for the dwarfs	89
4.3.5	SBF measurements for the giants	91
4.4	Results	97
4.4.1	Relative distance between Hydra and Centaurus from SBF	97
4.4.2	Peculiar velocities of Hydra and Centaurus	100
4.4.3	Depth of the Hydra and Centaurus clusters	100
4.5	Discussion	103
4.5.1	The Great Attractor acting upon Hydra and Centaurus	103
4.5.2	Some other ideas	106
4.5.3	Comparison with literature distances	111
4.5.4	Systematic effects in our data?	117
4.5.5	Consequence of a higher Hydra and lower Centaurus distance for the GA model	122
4.5.6	Cen30 and Cen45	122
4.6	Summary	124
5	Conclusions and Outlook	127
6	Zusammenfassung	131
A	Appendix	XI
A.1	Danksagung	XI
A.2	Versicherung	XIII
A.3	Curriculum vitae	XIV

Chapter 1

Introduction

A frequent first question in oral astronomy exams, but also a question that has surely been asked by many other people over many millennia, is:

When we look up to the sky in a moonlit night, how far away from us are the small brilliant dots that we see?

The desire to construct a 3D model of the universe out of the 2D imagery that we see from the Earth certainly has existed since before delivered history.

For people from outside astronomy, it might come as a small surprise that there only is one method that gives us direct distances to stars outside the Solar System. This method is called trigonometric parallax. It is based on the same principle that allows humans and animals to see their own world in 3D: if we combine two images of an object taken from two different positions along a given baseline, we can estimate its distance by the amount that this object apparently moves with respect to a distant reference mark. For humans, these two baseline positions are the two eyes. When we stretch our arm and put up one finger, then blink between both eyes, the finger will shift its position with respect to a more distant reference object. From combining the two images, the human brain allows us to perceive the world in 3D.

Exactly the same principle, only on a much larger scale, holds for the trigonometric parallax method. Here, the orbit of the Earth around the Sun is used as baseline: every half a year, the Earth is at opposite sides of the Sun, separated by about 3×10^8 km. Although this is a very large distance compared to the diameter of the Earth, it is small compared to cosmic distances: the nearest star outside the Solar System is Proxima Centauri at a distance of 1.3 parsec (abbreviated as pc, 1 parsec = 3.086×10^{13} km, or 3.26 light years), about 260000 times more distant than the Sun. The angle by which its position on the sky apparently changes in the course of half a year (its parallax) is only 0.763 arcseconds (").

Due to the unavoidable atmospheric blurring that degrades the achievable spatial resolution, parallaxes from ground-based imaging can be obtained with an accuracy not better than 0.05 to 0.1". Only with satellite missions has it been possible to obtain

parallaxes to stars more than about 25 pc away. One very important mission was that of the Hipparcos satellite in 1997 (ESA, [1997]) which obtained accurate parallaxes and hence distances of many thousand stars out to 100 pc and beyond.

Distances in astronomy are often expressed in logarithmic form in the so called distance modulus, defined as the difference between apparent magnitude m and absolute magnitude M of an astronomical source. It is $(m - M) = 5 \times \log(d) - 5$, with d in pc. The absolute magnitude M is defined as the apparent magnitude m of an object at 10 pc distance. It holds $m = -2.5 \times \log(L) + ZP$, where L the apparent luminosity in physical units and ZP the appropriate zero point of the photometric system. As an absolute calibration one uses the Sun, which has $M = 4.82$ mag in the visual V -band.

All distance determination methods in astronomy except the trigonometric parallax are indirect, they all rely on the trigonometric parallaxes of stars in the solar neighbourhood.

1.1 The cosmic distance ladder

In this section, a short description of the “cosmic distance ladder” is given: distance determination methods start out with the trigonometric parallax in the solar neighbourhood and successively continue to larger distances, every distance method being calibrated by the previous step in the distance ladder. For a distance determination method one requires “standard candles”, i.e. astronomical objects that have a constant absolute brightness or one that can be easily derived from distance independent observables. Clearly, the absolute distance uncertainties increase the more steps one climbs up the distance ladder.

1.1.1 Distances within the Milky Way

The main method to derive distances within the Milky Way beyond the reach of trigonometric parallax is the so-called photometric parallax (for recent applications see for example Siegel et al. [2002], Costa & Mendez [2003]). Here, one deduces the absolute magnitude M of a star from a distance independent observable, for example its spectral type. This method has been calibrated in the solar neighbourhood for low-mass stars. For higher mass stars, that are scarce in the solar neighbourhood, one uses star clusters and shifts their main sequence such that it matches that of locally calibrated low-mass stars. The part of the main sequence that extends beyond the locally calibrated range is then used as an extension of the calibration. This procedure is repeated for younger clusters whose main sequence is populated more at higher masses until an absolute calibration of the entire main sequence is achieved. A related method is the main sequence fitting, which is applied to star clusters (for which all stars can be assumed to be at the same distance). The locus of the main sequence in apparent magnitude is shifted until it matches the reference sequence. The amount of the shift yields the distance modulus $(m - M)$.

1.1.2 Extragalactic distances

A very important distance determination method out to about 20 Mpc is the use of variable stars as standard candles. There are two prominent types of variable stars: Cepheids have a quite well defined relation between their pulsation period and absolute brightness (P-L relation), which has been calibrated using Cepheids in the Large Magellanic Cloud (LMC) (e.g. Madore & Freedman [1991]). They have a typical absolute brightness of $M_V \simeq -7$ mag and can therefore readily be detected with the HST out to about the Fornax/Virgo cluster ($\simeq 20$ Mpc distance). As Cepheids occur in young stellar populations, they are mainly found in late-type galaxies.

The most prominent variables in the older populations of early-type galaxies are the RR Lyrae stars (for recent applications see for example Catelan et al. [2004], Benedict et al. [2002], Sandage & Saha [2002]). They have lower absolute brightnesses of $M_V \simeq 1$ mag and are found in the instability strip of the horizontal branch. They do not exhibit a notable P-L relation in optical bands, their absolute brightness depends mainly on their metallicity.

Fig. 1.1 shows a colour-absolute magnitude diagram (CMD) of a typical early-type stellar population with different detection limits in dependence on the distance indicated. Cepheids are located several magnitudes beyond the upper y-limit of that plot, indicating the large distance range over which they can be used as standard candles. RR Lyrae lie on the horizontal branch (at about $M_V = 0.7$ mag in the CMD), and can consequently not be used as standard candles much beyond the distance of about 0.7 Mpc to the Andromeda galaxy (M31).

Another distance estimator that requires resolving a galaxy into its stars is the location of the tip of the red giant branch (TOTRGB, e.g. Rejkuba [2004]), which is at about $M_V = -2.5$ mag in Fig. 1.1. This method is of intermediate range between that of Cepheids and RR Lyrae. From ground based imaging it is possible to apply this method to the closest elliptical galaxy Cen A (NGC 5128) at about 3.6 Mpc distance. One refers to the above distance determination methods as primary distance indicators, as they can be calibrated within the Milky Way. Secondary indicators are those methods that still use single astronomical objects as standard candles, but which need to be calibrated outside the Milky Way. Examples are the luminosity function of planetary nebulae (PNLF, e.g. Arnaboldi et al. [2002]), with a similar applicable range as the Cepheid method, and the luminosity function of globular clusters (GCLF, e.g. Kundu & Whitmore [2001]), which can be applied out to about 40 Mpc from ground based imaging. A further very important secondary standard candle is the peak brightness of Type Ia supernovae (SN) (e.g. Gibson et al. [2000], Riess et al. [2004]). Due to their enormous brightness of $M_V \simeq -19$ mag, SN Ia can be used as standard candles over cosmological distances. A disadvantage of that method is that supernovae are very seldom events, occurring about once every forty years in the Milky Way and much less frequent in more evolved early-type galaxies. One can in practice get SN Ia distances for only a very small fraction of all observable galaxies. Fortunately for us, the scarceness of

supernovae will probably prevent the Earth from suffering hazardous supernovae winds for many Myrs to come.

Going away from single astronomical objects as standard candles, one enters the regime of tertiary distance indicators which use integrated properties of galaxies as a distance estimator. One very often applied method is the Tully-Fisher relation (Tully & Fisher [1977]). This exploits the observational fact that for spiral galaxies there is a good correlation between the global neutral hydrogen (H I) line profile width, a distance-independent observable, and its absolute magnitude M . A similar approach applicable to early-type elliptical galaxies is the so-called $D_n - \sigma$ relation (Dressler et al. [1987a] and Dressler [1987b]). Here, σ is the central velocity dispersion of an elliptical galaxy or the bulge of a spiral galaxy, and D_n is the diameter of the aperture that encloses a determined integrated surface brightness μ . This method replaced the Faber-Jackson relation (Faber & Jackson [1976]), which used the correlation between M and σ as a distance indicator. Indeed, the Faber-Jackson relation is a special projection of the so-called Fundamental Plane (FP, Dressler et al. [1987c]): early-type galaxies populate a well defined plane in the M - σ - μ_e space, with μ_e being the effective surface brightness. All the mentioned distance estimators have rms uncertainties between 0.3 and 0.5 mag for the measurement of a single galaxy. They are purely empirical, and therefore require several previous calibration steps. Furthermore, one needs both imaging and spectroscopy for their application. An advantage is that only short integration times are needed to measure central velocity dispersions and effective radii for giant galaxies and that these measurements are observationally straightforward.

We mention two further tertiary indicators that require only imaging, have larger ranges, but also are more uncertain: first, the colour-magnitude relation of early-type galaxies. There is a well defined relation between the colour and total absolute brightness of elliptical galaxies (e.g. Barrientos et al. [2003]), probably driven by a mass-metallicity relation. The scatter in $(V - I)$ around this relation is such that the absolute brightness of a single galaxy can only be derived with about 2 mag uncertainty. This uncertainty drops significantly when investigating entire clusters, where dozens of galaxies together form this so-called “red sequence”. This method can be applied to quite large distances ≥ 1000 Mpc. Somewhat related is the method of the brightest cluster galaxy (BCG, e.g. Gonzales et al. [2002]). The brightness of the brightest cluster member in rich clusters has a rather small rms dispersion of about 0.4 mag, once a correction for cluster “richness” is applied (Sandage [1988], Aragon-Salamanca et al. [1993]). An important requirement for this method is the proper identification of the BCG, for which multicolour photometry and possibly spectroscopy is required to assess whether a galaxy really belongs to the cluster or is a background object.

Finally we refer to another indirect but very fundamental distance estimator: due to the expansion of the universe, the radial velocity of astronomical objects scales linearly with their radial distance, a relation first proposed by Hubble ([1929]). In the nearby universe it holds $d = \frac{v_{\text{rad}}}{H_0}$, with d normally expressed in Mpc, v_{rad} in km s^{-1} and H_0 in $\text{km s}^{-1} \text{Mpc}^{-1}$. Determination of H_0 and hence the expansion velocity of the universe

is one of the key issues of modern cosmology. Most of the recent estimates derived from large scale surveys are consistent with $H_0 \simeq 72 \text{ km s}^{-1} \text{ Mpc}^{-1}$ (Riess et al. [2004], Spergel et al. [2003]). A change of H_0 in the very early universe may have been detected (Riess et al. [2004]), suggesting an early acceleration of the universe and giving rise to the hypothesis that the energy density of the universe is dominated by the so-called Λ term. In the nearby universe ($d \leq 100 \text{ Mpc}$), peculiar velocities caused by clumpy matter distribution can constitute a large fraction of the observed radial velocities of galaxies. This is why deviations from an ideal Hubble flow are used to map the matter distribution in the local universe. Sect. 4 presents an application of this concept.

1.2 The surface brightness fluctuations method

The measurement of surface brightness fluctuations (SBF) in a galaxy image was first suggested by Tonry & Schneider ([1988]) as a useful tool to measure distances to galaxies whose structural features are large compared to the image resolution (see also Jacoby et al. [1992] for a review). The SBF method is based on two very fundamental facts: A) the number of stars contained in each resolution element of a galaxy image is *finite*. B) the number of stars contained in each resolution element is on average *constant* along one isophote (per definition of an isophote).

From these two facts, a third fact is deduced: the number of stars per resolution element along one isophote has a statistical fluctuation equal to the square root of the average star number.

How can one use these fluctuations as a distance indicator?

Assume a galaxy at a determined distance $d=d_0$ and do not consider seeing (see Fig. 1.2). Then assume that in the CCD image of a certain region of that galaxy, there are on average 100 stars imaged in each pixel. Therefore, there will be a 10% pixel-to-pixel fluctuation of that number and correspondingly a 10% pixel-to-pixel fluctuation of the measured flux. Now assume the same galaxy at a distance $d=4*d_0$. In the same region as before, there will be 1600 stars per pixel, since the metric area sampled by one pixel increases by a factor of $4^2=16$. The corresponding pixel-to-pixel fluctuations decrease to 2.5% of the mean flux. That is, the amplitude of these *surface brightness fluctuations* is inversely proportional to distance and can therefore be used as a distance indicator. In the following, we give a more mathematical definition of the SBF variances and observables, based on the pioneering paper by Tonry & Schneider ([1988]):

Assume that the stellar population one is looking at consists of stars with apparent luminosities L and corresponding expectation number of stars $n(L)$. The expectation value of the total apparent luminosity then is

$$\langle L \rangle = \int n(L)LdL \quad (1.1)$$

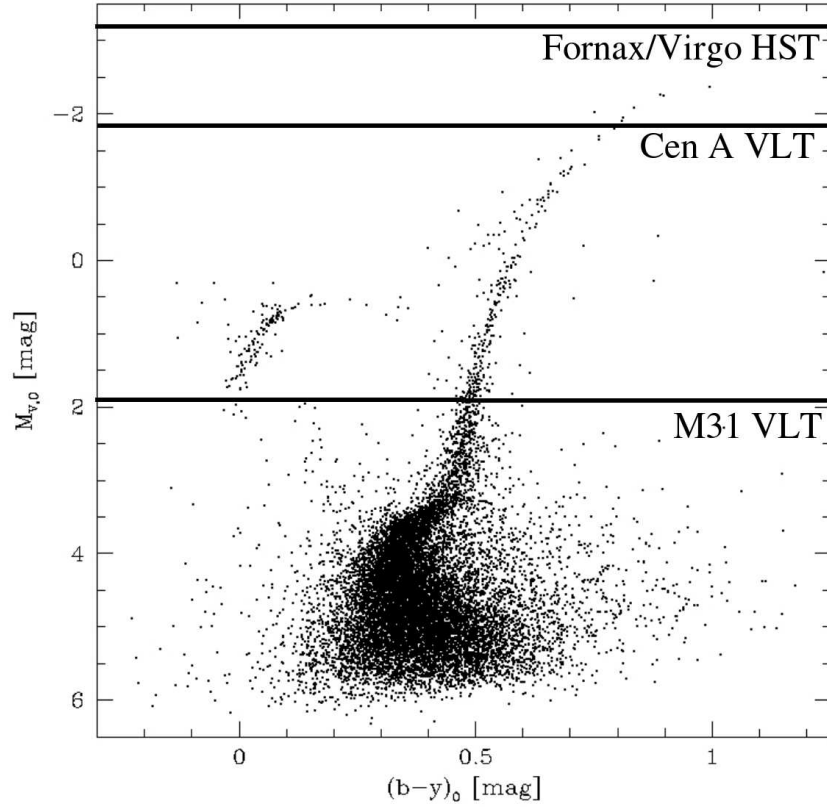


Figure 1.1: Absolute colour magnitude diagram of the Milky Way globular cluster M55, courtesy of M. Hilker (private communications). This diagram is shown as a representative for an early-type galaxy population, indicating as horizontal lines the detection limits at the distance of M31 ($(m - M) \simeq 24.2$ mag), Cen A ($(m - M) \simeq 27.8$ mag) and the Virgo/Fornax cluster ($(m - M) \simeq 31.2$ mag). For the two lower distances, a limiting magnitude for point source detection of $V = 26$ mag is assumed, typical for deep VLT exposures. For the Fornax/Virgo distance, a limiting magnitude of $V = 28$ mag is assumed, typical for moderately deep HST exposures.

In a real galaxy image, this corresponds to the mean flux in ADU per pixel of the galaxy along one isophote. The pixel-to-pixel flux variance σ_L is then given as

$$\sigma_L^2 := \langle (L - \langle L \rangle)^2 \rangle = \int n(L)L^2 dL \quad (1.2)$$

Looking at the definition of the mean luminosity weighted luminosity of the stellar population \bar{L}

$$\bar{L} = \frac{\int n(L)L^2 dL}{\int n(L)L dL} \quad (1.3)$$

it becomes clear that

$$\bar{L} = \sigma_L^2 / \langle L \rangle \quad (1.4)$$

\bar{L} is the observable derived from the observations, as both σ_L (the pixel-to-pixel variance normalised to the galaxy flux) and $\langle L \rangle$ (the mean galaxy flux) are readily measurable. The entity \bar{m} is called apparent fluctuation magnitude and defined as $\bar{m} = -2.5 \times \log(\bar{L}) + ZP$. The relative distance modulus between two galaxies 1 and 2 with identical stellar populations then is $\bar{m}_1 - \bar{m}_2$.

The SBF method becomes useful at distances where the brightest red giants cannot be detected anymore, i.e. for $d \geq 10$ Mpc (see Fig. 1.1). The conceptual advantage of this method is that one requires only imaging and no spectroscopy. Furthermore, the relative accuracy of the SBF method can be between 5 and 10% in distance for the brightest giant ellipticals, as will be shown in this thesis. In addition, it can be applied readily also to dwarf galaxies, hence increasing the number of independent distance estimates when observing a galaxy cluster.

There are also some caveats when using this method, of both technical and theoretical nature: For the derivation of the distance modulus ($m - M$) with the SBF method, one does not only require to measure the apparent fluctuation magnitude \bar{m} but also one must derive the absolute fluctuation magnitude \bar{M} from some distance independent observable. Both aspects will be dealt with in some detail in the course of this thesis, thus we present here a short overview of the main issues:

1.2.1 Measuring SBF

For measuring \bar{m} , or the corresponding apparent fluctuation luminosity \bar{L} , the principle steps are, see also Fig. 1.2:

1. Subtract a smooth model of the galaxy light distribution from the original galaxy image, such that only the fluctuations remain.
2. Divide the resulting fluctuation image by the square root of this model. This normalises the amplitude of the fluctuations to the same level across the image.
3. Calculate the power spectrum (PS) of this normalised fluctuation image. The power spectrum (PS) is defined as the Fourier transform (FT) of the Autocorrelation Function (AF):

$$AF(r) = \int_{-\infty}^{+\infty} f(x)f(x+r)dx \quad (1.5)$$

$$PS(k) = \int_{-\infty}^{+\infty} AF(r)e^{-jkr} dr \quad (1.6)$$

Here, $f(x)$ simply is the normalised fluctuation image, which can be expressed as $F(x)/\sqrt{\langle L(x) \rangle}$, where $F(x)$ is the non-normalised fluctuation image. From these definitions and equations (1.2) to (1.4) it is clear that $\overline{PS}(f(x)) = \overline{L}$, where $\overline{PS}(f(x))$ is the average of $PS(f(x))$ over the fluctuation image. In simple terms: the mean of the normalised fluctuation image's power spectrum is \overline{L} , the desired observable.

This holds as long as one does not take into account that the real fluctuations are smeared out by the atmospheric blurring (see the two right columns of Fig. 1.2), characterised by the point spread function (PSF). That is, in reality we do not calculate $PS(f(x))$, but rather

$$PS(PSF(x) \otimes f(x)) = PSF(k) \times \overline{L} \quad (1.7)$$

That is, the final result of the SBF measurement procedure is the power spectrum of the point spread function $PSF(k)$ – normalised to unity at $k=0$ – scaled by the fluctuation amplitude \overline{L} . One uses in practice the azimuthal average of that power spectrum to fit for \overline{L} , see the two right columns of Fig. 1.2.

Approaching reality ever more, three more things have to be taken into account: first, there always is significant photon shot noise from the detector. The power spectrum of this white noise is flat, and hence adds as a constant to the power spectrum of the PSF convolved SBF. Second, there are sources fainter than the detection limit which also contribute to the measured fluctuations and carry the signature of the PSF, such as background sources or globular clusters associated with the galaxy. In Sects. 3.3 and 4, the amount of these unwanted contributions will be thoroughly investigated. Third, the measurements have to be corrected for foreground absorption.

Assuming that the contributions from undetected sources are subtracted from the total fluctuations before the azimuthal averaging, a realistic representation of the azimuthally averaged power spectrum is then given as

$$P(k) = PSF(k) \times P_0 + P_1 \quad (1.8)$$

Here, P_1 is the wavenumber independent white noise component, while P_0 is the amplitude of the surface brightness fluctuations in the limit $k=0$. it holds

$$\overline{m}_I = -2.5 * \log(P_0) + ZP - A - \Delta k \quad (1.9)$$

A is the foreground absorption, Δk the k -correction for SBF.

1.2.2 Empirical calibration of SBF

Having measured \overline{m} , the next step is to derive the absolute fluctuation magnitude \overline{M} from a distance independent observable. From the definition of \overline{m} as the *luminosity weighted* mean luminosity it is clear that the fluctuations of early-type stellar populations are dominated by stars on the red giant branch. \overline{M} can therefore be considered

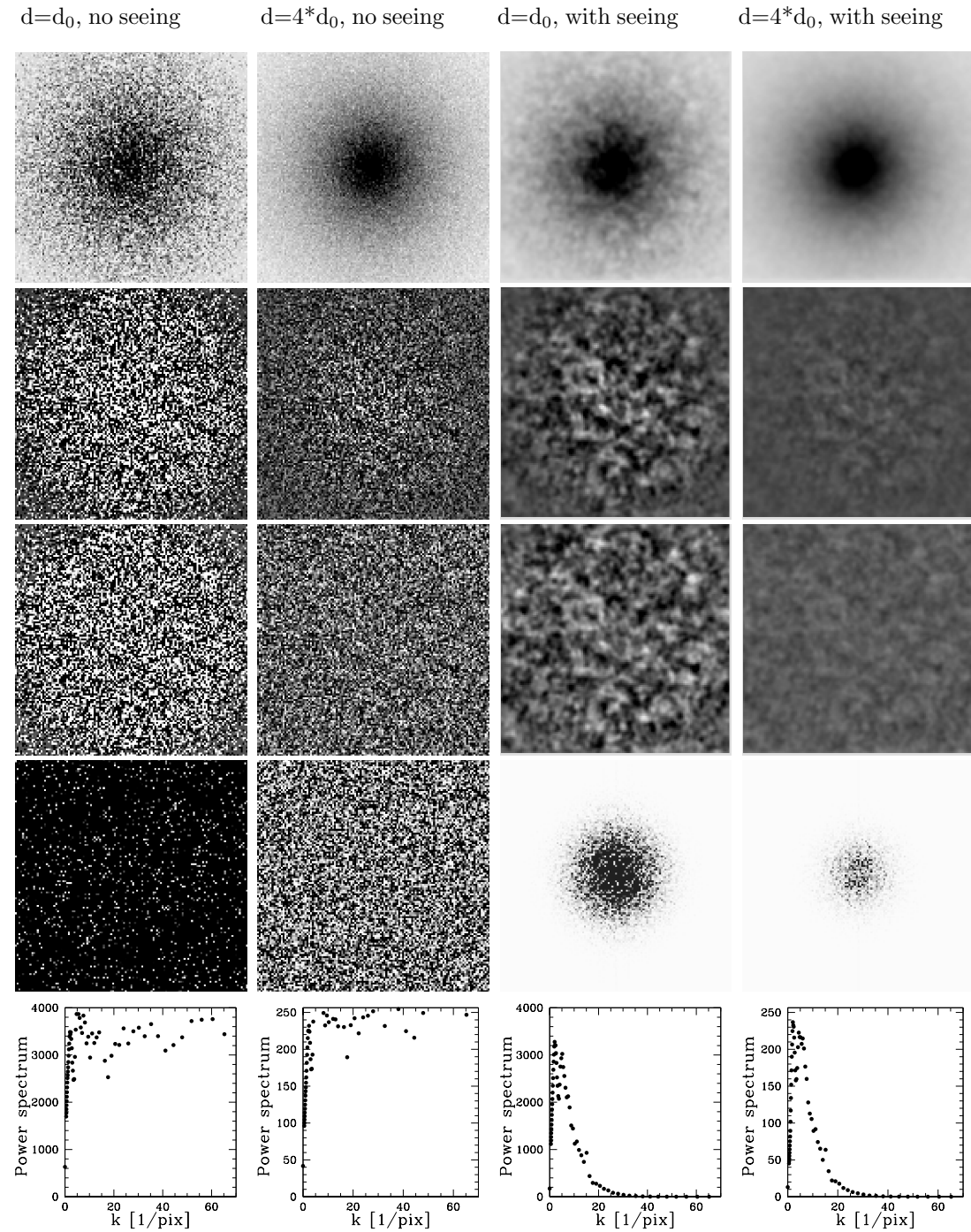


Figure 1.2: Idealised SBF measurement procedure. The 4 columns correspond to (from left to right): galaxy at arbitrary distance $d=d_0$ with no seeing; the same galaxy at $d=4*d_0$; the same galaxy at $d=d_0$ with seeing; the same galaxy at $d=4*d_0$. From top to bottom: 1. galaxy image; 2. smooth galaxy light model subtracted from galaxy image; 3. former image divided by square root of smooth galaxy light model, yielding a normalised fluctuation image; 4. power spectrum of former image. 5. Azimuthal average of the former image. The intensity cuts in the upper 4 rows are the same within each row. No instrumental noise was implemented, i.e. all luminosity fluctuations are pure SBF.

a “typical” red giant absolute brightness of the stellar population. The brighter the brightest red giants are, the brighter \overline{M} . This is illustrated in Fig. 1.3, where isochrones of different metallicities and old to intermediate ages are plotted over the response curves of the V and I -filter bands. Two things are striking: first, the average stellar brightness in the I -band is much higher than in the V -band, which is why SBF in the I -band are much stronger than in the V -band. Second, the average I -band brightness increases with decreasing metallicity. This means that for old to intermediate age stellar populations, \overline{M}_I becomes brighter with decreasing metallicities. \overline{M}_I also becomes brighter with bluer colour, since a decrease in metallicity causes a colour shift to the blue.

Tonry et al. ([1997], [2000], [2001]) have carried out an extensive survey to measure SBF for bright ellipticals and bulges of spiral galaxies in 22 nearby galaxy groups and clusters within 40 Mpc. Using distances derived from Cepheids or SN Ia in the respective galaxies or the clusters they are associated with, they obtained a relation between the absolute fluctuation magnitude \overline{M}_I and the dereddened colour $(V - I)_0$, determined in the range $1.0 < (V - I)_0 < 1.3$:

$$\overline{M}_I = -1.74 + 4.5 \times ((V - I)_0 - 1.15) \text{ mag} \quad (1.10)$$

Note that the correlation between \overline{M}_I and $(V - I)_0$ is in the direction mentioned above, namely brighter \overline{M}_I for bluer $(V - I)_0$. In Sect. 2.3, a comparison of that calibration with theoretical stellar population model predictions will be presented. In Sect. 3.3.3, the behaviour of \overline{M}_I for $(V - I)_0 < 1.0$ mag, i.e. bluer than the colour range investigated by Tonry et al., will be discussed.

The luminosity weighted mean luminosity tends to be higher in redder pass-bands (see Fig. 1.3), i.e. the average number of stars per unit surface brightness decreases for redder colours. SBF measurements have therefore mainly been performed in red (e.g. Johnson I or Sloan r) optical pass-bands (e.g. Tonry et al. [1990], Tonry [1991], Tonry et al. [1997], Lauer et al. [1998], Bothun et al. [1991], Mei et al. [2000], [2001], [2003] and [2005], Neilsen et al. [1997], Neilsen & Tsetanov [2000], Morris & Shanks [1998], Pahre et al. [1999], Sodemann & Thomsen [1995] and [1996], Thomsen et al. [1997]) and in the infrared (e.g. Liu & Graham [2001], Jensen et al. [1996], Jensen et al. [2001] and [2003], Liu et al. [2002], Luppino & Tonry [1993], Pahre & Mould [1994]), both from the ground and with HST. Also V -band (Simard & Pritchett [1994]) and R -band fluctuation measurements exist (e.g. Jerjen et al. [1998], [2000], [2001], [2004]). Depending on the purpose of the study, the SBF measurements have either been used to calibrate the method by targeting galaxies of known distance or to derive a distance estimate by applying the calibration.

A counter-effect of the much stronger fluctuations in redder bands is that the sky brightness also is much higher. This becomes a serious problem as soon as the surface brightness of the investigated galaxy is too low for detection. In that case, even a very low number of stars per unit surface brightness does not compensate the fact that the galaxy light itself cannot be detected. For low surface brightness galaxies one therefore uses

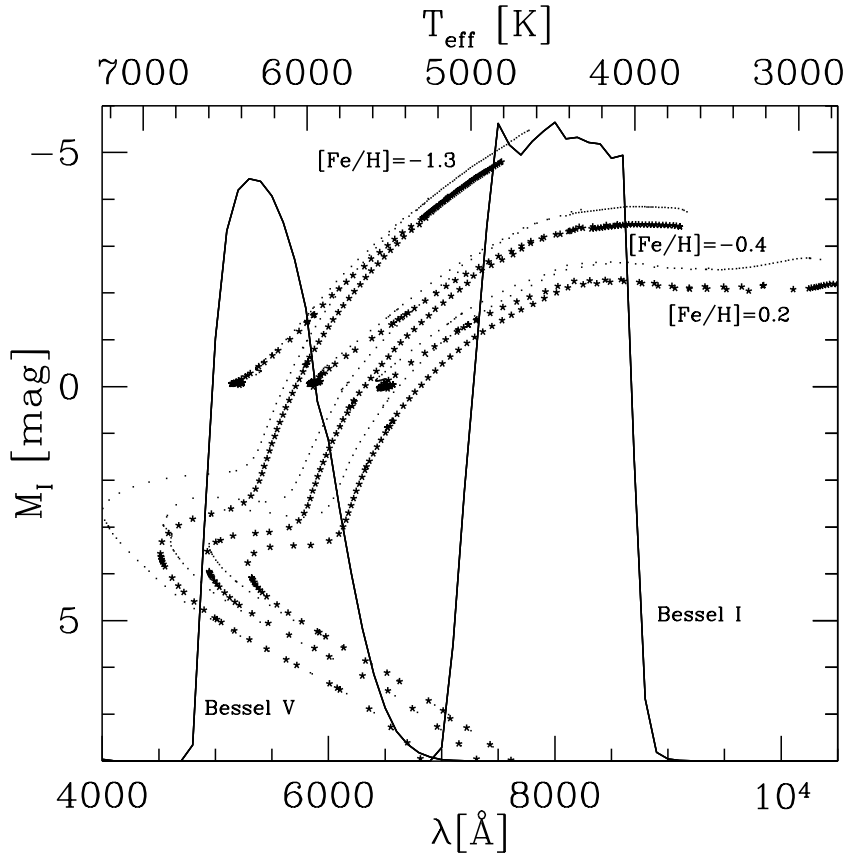


Figure 1.3: Theoretical Padova isochrones from Girardi et al. ([2002]), combining the basic sets from Girardi et al. ([2000]) for low and intermediate mass stars with those of Bertelli et al. ([1994]) and Girardi et al. ([1996]) for high mass stars. Metallicities as indicated. Isochrones with bold asterisks refer to an age of 12 Gyrs, while dotted isochrones are 5 Gyrs. Overplotted as solid lines are the arbitrarily scaled response curves of the Bessel-*I* and *V* filters as a function of wavelength, taken from <http://www.eso.org/instruments/fors/inst/Filters/curves.html>. Effective temperature T_{eff} was converted to λ using Wien's law.

optical imaging in red pass-bands instead of IR pass-bands.

The SBF method has been found to agree well with other tertiary or secondary distance measurement methods such as FP or SN Ia (e.g. Blakeslee et al. [2001] and [2002], Ajhar et al. [2001], Blakeslee et al. [1999], Ciardullo et al. [1993]). It has also been used for some other applications: Bartelmann & White ([2002]) use the SBF technique to detect clusters in SDSS data. Blakeslee & Tonry ([1995]) use it to measure specific frequencies of globular cluster systems in galaxies of the Coma cluster. Ajhar & Tonry ([1994]) apply the SBF method to galactic globular clusters in an attempt to improve the empirical SBF calibration.

1.3 Aim of this thesis

This thesis deals with SBF measurements of dwarf elliptical galaxies (dEs) in nearby clusters. It starts with simulated SBF measurements, followed by two applications to real data. Each of the corresponding chapters contains a separate introduction. The thesis is structured as follows:

In chapter 2 we investigate via simulations the potential of the SBF method to measure distances to dEs in nearby galaxy clusters. We derive limiting absolute galaxy magnitudes for application of the SBF method as a function of galaxy distance and observing conditions. Chapter 3 presents the first application: SBF measurements of Fornax cluster candidate dEs are used to establish their cluster membership and in combination with morphological selection criteria to improve constraints on the faint end of the galaxy luminosity function in Fornax. The SBF calibration at blue colours will be discussed. Chapter 4 presents the second application: SBF-distances to about 30 Hydra and Centaurus cluster galaxies (mainly dwarfs) are used to derive absolute distances to both clusters, upper limits for their depth, relative distances between them and peculiar velocities. Implications for the presence of significant mass overdensities in the nearby universe (“Great Attractor”) will be discussed. We finish this thesis in chapter 5 with the conclusions.

Throughout this thesis, we use the term “dwarf elliptical” (dE) to refer to early-type dwarf galaxies ($M_V \geq -18$ mag) in general. To the faint sub-samples we will refer to as “faint dEs” or equivalently as “dwarf spheroidals” (dSphs). This has historical reasons: the fainter ($M_V \geq -14$ mag) early-type Local Group dwarfs are commonly referred to as “dwarf spheroidals” (e.g. Grebel et al. [2001]). This is only a semantic, not a physical distinction.

Chapter 2

Potential of the SBF method to measure distances to dwarf elliptical galaxies in nearby clusters

This chapter is based on the publication *Mieske, S., Hilker, M. & Infante, L. 2003, A&A, 403, 43.*

2.1 Abstract

The potential of the SBF method to determine the membership of dwarf elliptical galaxies (dEs) in nearby galaxy clusters is investigated. Extensive simulations for SBF measurements of dEs in the I -band for various combinations of distance modulus, seeing and integration time are presented, based on average VLT FORS1 and FORS2 zero points. The simulations show that for distances up to 20 Mpc (Fornax or Virgo cluster distance), reliable membership determination of dEs can be obtained down to very faint magnitudes $-10 > M_V > -12$ mag ($\mu_0(V) \simeq 25$ mag arcsec $^{-2}$) within integration times of the order of 1 hour and with good seeing. By comparing the limiting magnitudes of the method for the different simulated observing conditions we derive some simple rules to calculate the limiting dE magnitude for SBF application as a function of distance modulus and observing conditions. To check whether our simulations represent well the behaviour of real data, SBF measurements for a real and simulated sample of bright Centaurus Cluster dEs are presented. They show that our simulations are in good agreement with the achievable S/N of SBF measurements on real galaxies.

2.2 Introduction

2.2.1 The faint end of the galaxy luminosity function

Dwarf elliptical galaxies (dEs) are the most numerous type of galaxies in the nearby universe, especially in clusters. This statement has been well established since the advent of CCD detectors and the building of telescopes with 4-8m diameter that enabled observers to detect low surface brightness (LSB) objects substantially fainter than the night sky. With the improvement of observing facilities, the emphasis has over the last decade switched from detecting faint dwarf galaxies to quantifying well their properties and frequencies. Most of the times dEs are investigated in galaxy clusters, where the distance and therefore the approximate angular size of candidate dwarf galaxies is known.

One of the most important statistical tools in investigating galaxy populations is the galaxy luminosity function $\Phi(M)$, describing the frequency of galaxies per magnitude interval. The knowledge of its logarithmic faint end slope α is very useful for testing models of galaxy formation. There are two fundamental steps involved in determining the faint end of $\Phi(M)$ in galaxy clusters: first, finding the dwarf galaxy candidates; second, verifying that they are cluster members.

For the Local Group, $\Phi(M)$ has been determined down to $M_V \simeq -9$ mag (e.g. Mateo [1998], Pritchet [1999], Van den Bergh [2000]), suggesting $\alpha \simeq -1.1$. Local Group dwarf galaxies can nowadays readily be resolved into single stars with HST and/or active optics techniques. Thus, their distance can be determined; the second step in establishing $\Phi(M)$ is quite easy to perform. The first step, finding them, is more difficult due to their large angular extent and small contrast against the stars of the Milky Way. The latest discoveries of more and more faint dSphs (e.g. Armandroff et al. [1999], Whiting et al. [1999], Zucker et al. [2004]) raise the question of how complete the Local Group sample is.

The opposite is true for nearby galaxy clusters. Here, finding candidate dwarf spheroidals is quite straightforward when performing deep enough photometry, but it is extremely time consuming to resolve them into single stars (see Fig. 1.1). For example, the brightest red giants of an early-type galaxy at the Fornax cluster distance (19 Mpc, Ferrarese et al. [2000]) have $V \simeq 29.4$ mag (Bellazzini et al. [2001]). The confirmation of candidate dwarf spheroidals as cluster members must consequently be based on morphology and is therefore subject to possible confusion with background LSB galaxies. One depends on statistical subtraction of background number counts to estimate the faint end slope. Due to the generally low number counts, the Poisson error involved in this statistical subtraction constitutes a major source of uncertainty in determining α , especially in magnitude-surface brightness bins where the contribution of background galaxies is of the order of, or higher than, that from cluster galaxies.

The majority of studies that have determined $\Phi(M)$ in nearby galaxy clusters (e.g. Sandage et al. [1985], Ferguson & Sandage [1988], Trentham et al. [2001], [2002a],

[2002b]) suggest a logarithmic faint end slope of $-1.0 < \alpha < -1.5$, being in substantial disagreement with CDM theory (Press & Schechter [1974]), which predicts $\alpha \simeq -2.0$ for the mass function of low-mass dark matter halos (e.g. Kauffmann et al. [2000], Moore et al. [1999]). Other authors, such as Phillips et al. ([1998]) for the Virgo cluster and Kambas et al. ([2000]) for the Fornax cluster, suggest a significantly steeper faint end slope of $\alpha \simeq -2$. This large discrepancy shows that much care must be taken when assigning cluster membership to galaxies for which no direct distance measurement is available. The Poisson statistics involved, especially when subtracting background number counts, can lead to different authors obtaining very different results for the same cluster.

Various methods for distance determination that can be applied to brighter galaxies outside the Local Group are not suited for the faintest dEs: standard candles such as SN Ia or Cepheids are very rare; radial velocity measurements, if possible, are very time consuming due to the large fields that have to be covered and the low surface brightness of the dwarfs.

2.2.2 Distances to galaxies with the SBF Method

An intriguing possibility to unambiguously determine cluster membership of large samples of dEs in nearby clusters is deep wide field imaging and the application of the SBF method. Until recently, the SBF method had only been applied to small samples of nearby dEs (e.g. Bothun [1991], Jerjen et al. [1998], [2000], [2001], [2003], [2004]) as due to their low surface brightness one needs quite long integration times on large telescopes to achieve that the stellar SBF are clearly detected above the sky noise. The fact that wide field imagers on large telescopes have now become available (e.g. IMACS@Magellan, VIMOS@VLT, SUBARU) gives the possibility to pursue large scale SBF surveys of dEs.

In this chapter, we focus on the potential of the SBF method to determine cluster membership of dEs in nearby clusters. We measure SBF of simulated sets of dEs at three distance moduli between 7.5 and 48 Mpc for various combinations of observing times and seeing. This chapter is structured as follows: In Sect. 2.3, the impact of the age-metallicity degeneracy on SBF magnitudes is discussed. In Sect. 2.4, the technical details of simulating and measuring SBF are described and the properties of the different sets of simulated dEs are shown. In Sect. 2.5, the results of the SBF measurements for all simulated sets are presented and the limiting absolute magnitudes for cluster membership determination is discussed. A validity check of the simulations is presented by comparing real and simulated SBF data. We finish this chapter with the summary in Sect. 2.6.

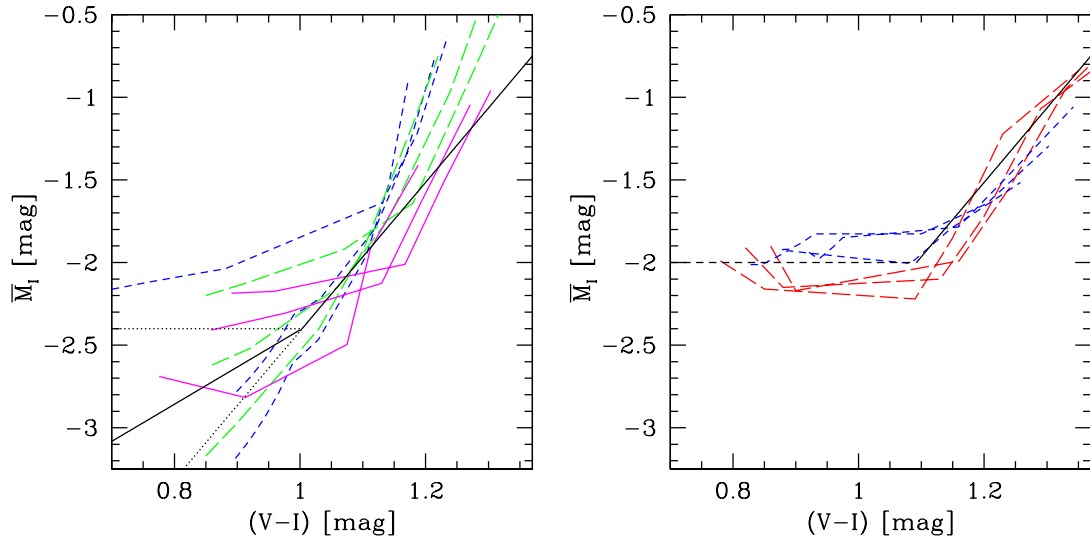


Figure 2.1: Theoretical “isochrones” in the \overline{M}_I - $(V - I)_0$ diagram from 5 different sources. For the sake of clarity, those were separated into two different plots. *Left*: Short dashed lines from Worthey ([1994]) using Padova isochrones from Bertelli et al. [1994] (http://astro.wsu.edu/worthey/dial/dial_a_pad.html). Plotted are (from top to bottom in the blue range): 17, 12 and 8 Gyrs. Metallicities range from -1.7 to 0 dex from blue to red colours. Long dashed lines from Blakeslee et al. ([2001]) for ages of 7.9, 12.6 and 17.8 Gyrs and metallicities from -1.7 to +0.2 dex. Solid lines from Cantiello et al. [2003] for ages of 5, 11 and 15 Gyrs and metallicities from -2.3 dex to 0.3 dex. The solid line for $(V - I)_0 \geq 1.0$ indicates the empirical calibration (1.10) by Tonry et al. [1997], the solid line for $(V - I)_0 \leq 1.0$ indicates equation (2.1), whose slope is half that of equation (1.10). The dashed lines indicate a constant $\overline{M}_I = -2.40$ mag and the continuation of equation (1.10) for $(V - I)_0 \leq 1.0$ (see this section, Sects. 3.3.3 and 4 for further details). *Right*: Short dashed lines from Worthey ([1994], http://astro.wsu.edu/worthey/dial/dial_a_model.html). Plotted are 17, 12 and 8 Gyrs. Metallicities range from -1.7 to 0 dex from blue to red colours. Long dashed lines from Liu et al. ([2000]) for ages 8, 12 and 17 Gyrs and metallicities between -2.3 and 0.4 dex. The solid line for $(V - I)_0 \geq 1.09$ indicates equation (1.10). The horizontal dashed line at $\overline{M}_I = -2.00$ indicates the approximate mean prediction of the Liu and Worthey models in the blue colour range.

2.3 Deriving \overline{M}_I from $(V - I)_0$

For I -band SBF measurements, the distance modulus of a galaxy is given by the difference between apparent and absolute fluctuation magnitude ($\overline{m}_I - \overline{M}_I$). To estimate the reliability of the method, one must know *both* the accuracy in measuring \overline{m}_I at the cluster distance and the uncertainty in deriving \overline{M}_I for a dE with a given $(V - I)_0$.

In Fig. 2.1, theoretical values for \overline{M}_I are plotted vs. $(V - I)_0$ for a set of old to intermediate age stellar populations with a wide range of metallicities, taken from different literature sources: Worthey ([1994]), who uses his own stellar population models based on Vandenberg ([1985]) and Yale (Green et al. [1987]) isochrones; Liu et al. ([2000]), who use the updated models by Bruzual & Charlot ([1993]) plus the Bertelli et al. [1994] Padova isochrones; Blakeslee et al. ([2001]) who use the stellar population models of Vazdekis et al. ([1996]) and the updated Girardi et al. ([2000]) Padova isochrones; and Cantiello et al. ([2003]), who use the stellar population synthesis code by Brocato et al. ([1999], [2000]) and the Teramo-Pisa-Rome isochrones (e.g. Castellani et al. [1991], Castellani et al. [1992] and Bono et al. [1997a], [1997a]). Equation (1.10) is also indicated in Fig. 2.1. The Worthey model predictions are split up into the original predictions from Worthey ([1994])¹ and those that use the alternate stellar evolutionary isochrone library from Bertelli et al. ([1994])².

For red colours, all models trace equation (1.10) reasonably well, with the original Worthey-models and those of Blakeslee et al. being more deviant from the empirical calibration than the other models. In the blue range, there is a huge discrepancy between the model predictions: the original Worthey ([1994]) models and those of Liu et al. ([2000]) predict a colour independent $\overline{M}_I \simeq -2.0$ mag for $(V - I)_0 < 1.10$ mag. In contrast, Worthey models using the Bertelli et al. ([1994]) Padova isochrones, those of Blakeslee et al. and Cantiello et al. show a large spread in \overline{M}_I caused by age differences, predicting a continuation of equation (1.10) for intermediate ages and a flattening of the relation for very old ages. At $(V - I)_0 \simeq 0.90$ this leads to an uncertainty of up to 0.5 mag in relating \overline{M}_I to $(V - I)_0$. Jerjen et al. ([1998], [2000], [2004]) have found an analogous spread of the order of 0.5 mag from R -band SBF measurements for blue dEs in the Sculptor and Centaurus A group and a few dEs in the Virgo cluster. Mei et al. ([2005]) find a significant flattening of the SBF-colour relation for blue colours from the investigation of about 80 early-type galaxies in the Virgo cluster, still with a large scatter. However, they do obtain a significant slope in that colour range (4.5σ), in contrast to the predictions by Liu et al. [2000]) and Worthey ([1994]). We will assume in the following that indeed there is a large spread in the \overline{M}_I - $(V - I)_0$ plane for blue colours, caused by degenerate age-metallicity combinations at constant colour. Anticipating Sect. 3.3.3, a colour independent \overline{M}_I mag for $(V - I)_0 < 1.10$ mag is also not favoured by the I -band SBF measurements of blue dwarf galaxies in our project ‘‘Fornax Deep Field’’.

¹http://astro.wsu.edu/worthey/dial/dial_a_model.html

²http://astro.wsu.edu/worthey/dial/dial_a_pad.html

While this age-metallicity degeneracy is an important source of uncertainty for distance measurements to blue *field* galaxies, it becomes useful as a relative age-metallicity indicator for blue *cluster* galaxies, as most of the time the cluster is separated from background/foreground galaxies by significantly more than 0.5 mag in distance modulus. Spectroscopic surveys of the Fornax cluster (Drinkwater et al. [2000], Hilker et al. [1999]) revealed a significant gap in radial velocity between Fornax members and background galaxies corresponding to $\simeq 3$ mag in $(m - M)$. Confusion of a blue and young background galaxy with a blue and old cluster galaxy is therefore very unlikely to happen. Arguing the other way around, SBF measurements of blue galaxies in a cluster with known distance can also be used to test calibration relations predicted from stellar population modelling (see Fig. 2.1), as will be shown in Sect. 3.3.3.

Note that dIrr candidate cluster members, to which the SBF method is difficult to apply due to their irregular shape, can be distinguished morphologically in a straightforward manner from blue young background galaxies like anaemic spirals. The galaxy population in the central Fornax cluster is dominated by early-types (Ferguson & Sandage [1988]) with only very few irregular Fornax members known, so this is not a serious issue for the Fornax cluster. For clusters with a significant fraction of dIrrs, this morphological cluster membership assignment can complement the assignment based on SBF-distances for the smoothly shaped dE candidates and allow derivation of $\Phi(M)$ for the entire dwarf galaxy population.

2.4 Simulating and measuring surface brightness fluctuations for dEs

We have simulated sets of dEs in the *I*-band with three distance moduli 29.4, 31.4 and 33.4 mag, corresponding to 7.6, 19 and 48 Mpc distance. This range was chosen to include distances to the more nearby groups like Leo I (10 Mpc) as well as to the more distant clusters like Centaurus and Hydra (33.1 to 33.3 mag, see Sect. 4). Note that 31.4 mag is the approximate distance modulus to Fornax and Virgo. The integration time was 3600 seconds, the gain was 1 and the zero point 27.0 mag. The latter value is a mean of the VLT FORS1 and FORS2 zeropoint for imaging in the *I*-band when including an averaged colour term and extinction coefficient. The pixel scale was $0.2''/\text{pixel}$, the image size 2048×2048 pixel. For each distance modulus, a set with $0.5''$ and $1.0''$ seeing was simulated. Additionally, for 31.4 mag distance modulus and $0.5''$ seeing, 4 different integration times were adopted, namely 900, 1800, 3600 and 7200 seconds. Note that varying the integration time from t_1 to t_2 is equivalent to keeping the integration time fixed and adding $2.5 \log \frac{t_2}{t_1}$ to the zero point.

The photometric properties of our simulated dEs are derived from the values found for Fornax cluster dEs in Sect. 3.2. For a given absolute magnitude M_V , the colour-magnitude- and surface brightness-magnitude relation from Sect. 3.2 is used to obtain $(V - I)_0$ and $\mu_0(V)$. An exponential intensity profile of the form $I(r) = I_0 \times \exp(-r/r_0)$

was adopted, with r_0 calculated from M_V , $\mu_0(V)$ and the adopted distance modulus. The ellipticity was chosen as zero. Globular Cluster (GC) systems are included, with a specific frequency of $S_N = 5$ (Miller et al. [1998]) for all galaxies, an absolute turnover magnitude $M_I = -8.5$ mag (Kundu et al. [2001]) and the projected spatial GC density following the galaxy light distribution.

\overline{M}_I was adopted as a function of $(V - I)_0$ according to Tonry's equation (1.10) for $(V - I)_0 > 1.0$. For $(V - I)_0 < 1.0$, it was decided to split the sample into two halves, acknowledging that there probably is a significant age-metallicity degeneracy for $(V - I)_0 < 1.0$ (see Fig. 2.1). For 50% of the simulated galaxies, \overline{M}_I was calculated according to equation (1.10). For the other 50%, \overline{M}_I was kept constant at $\overline{M}_I((V - I)_0 = 1.0) = -2.4$ mag. For the bluest galaxies simulated, with $(V - I)_0 \simeq 0.8$ ($M_V \simeq -8.5$ mag), this implies a range in \overline{M}_I of about 0.9 mag between the two simulated samples. The effect for the simulations is that, on average, the SBF signal is weaker than if all dEs with $(V - I)_0 < 1.0$ were simulated according to equation (1.10). One can express this splitting up of the simulated sample for $(V - I)_0 < 1.0$ also by defining a modified calibration equation of the following form:

$$\overline{M}_I = -2.415 + 2.25 \times ((V - I)_0 - 1.00) \text{ mag} \quad (2.1)$$

This equation is indicated as a solid line in the left panel of Fig. 2.1.

To allow for varying seeing and integration times, the background field had to be created artificially. In a real background field obtained with VLT FORS1 in the I -band at 3000 sec integration, we fitted a power law distribution of the form $n(m) = A \times 10^{\gamma(m_I - m_0)}$ to the magnitude distribution of the objects detected by SExtractor down to the completeness limit of $I \simeq 25$ mag. The fitted values were $A = 14900/\text{degree}^2$, $\gamma = 0.305$, $m_0 = 22$. According to this distribution, an artificial object field was created with the IRAF task mkobjects in the ARTDATA package, with $I=27$ mag as the faint limiting magnitude. Seeing and integration time were chosen as needed for the simulations. The sky brightness was adopted as 19.9 mag arcsec $^{-2}$ in I , which holds within three days before and after new moon. To simulate large-scale flat-field effects, the background fields were multiplied by the normalised sky-map obtained from applying SExtractor to a VLT FORS1 flat field image.

Into each 2048×2048 pixel field, 16 dEs were implemented. For each set with constant seeing, distance modulus and integration time, 6 fields were created, each with a different (random) spatial distribution of the background objects. This means that 96 dEs were simulated for each set. An excerpt of one of the simulated images for $0.5''$ seeing and 3600 seconds exposure time is shown in Fig. 2.2.

2.4.1 Simulation of surface brightness fluctuations

For each modelled pixel with a given distance r to the galaxy centre, first the number of stars corresponding to the surface brightness $\mu(r)$ of the exponential profile was

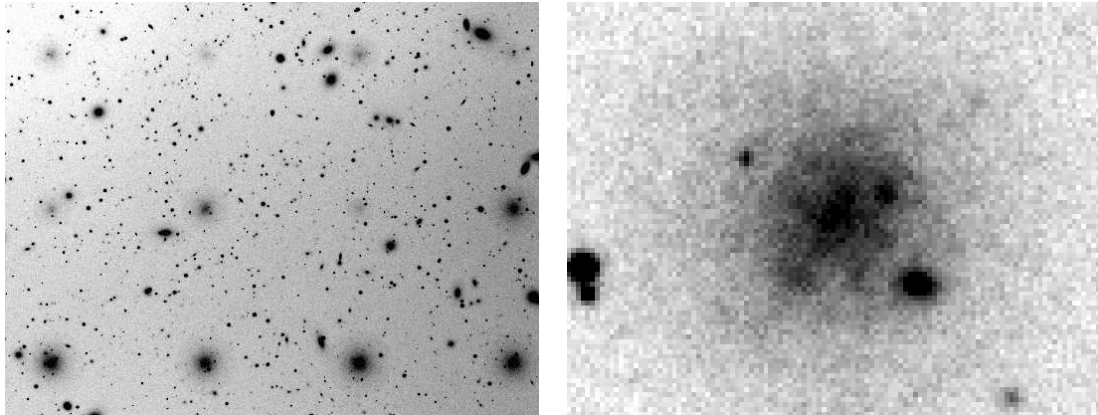


Figure 2.2: *Left*: Excerpt of one of the simulated background fields with dEs implemented at determined grid positions. Image width is $6'$. This example is for an integration time of 1 hour and $0.5''$ seeing. The SBF signal of the dEs is implemented according to the Fornax cluster distance of 31.4 mag. The large scale sky level gradient was implemented to include the effect of flat field imperfections in real images. *Right*: $20''$ wide thumbnail of one of the simulated dEs (second from left in the middle row).

calculated:

$$N_{\text{stars/pixel}}(r) = 10^{-0.4 \times (\overline{M}_I + (m-M) - \mu(r))} \times p^2 \quad (2.2)$$

with p being the pixel scale. Then, a random number N^* was chosen within a Poisson distribution centered on $N_{\text{stars/pixel}}(r)$. The intensity adopted at that pixel was then defined as

$$I(\text{pixel}, r) = 10^{-0.4 \times (\mu(r) - ZP)} \times p^2 \times \frac{N^*}{N_{\text{stars/pixel}}(r)} \quad (2.3)$$

with ZP being the zero point, 27 mag in our case. The implementation of the SBF is achieved by multiplying with $\frac{N^*}{N_{\text{stars/pixel}}(r)}$. This means that along an isophote with radius r , the intensity $I(r)$ has a pixel-to-pixel rms of $\frac{I(r)}{\sqrt{N_{\text{stars/pixel}}(r)}}$. The image with the implemented SBF was then convolved with a Moffat seeing profile, which was modelled out to 7 times the FWHM. Finally, Poisson noise with $\text{rms} = \sqrt{I}$ was implemented. Once modelled, the galaxies were added onto the artificial background fields (see Fig. 2.2).

2.4.2 Measurement of SBF

To measure the SBF of a simulated dE, the following steps were undertaken, see also Sect. 1.2:

1. Create object map of the entire image with SExtractor (Bertin & Arnouts [1996])
2. Mask the dEs on the object map, subtract this image from original image
3. Create and subtract SExtractor sky map

4. Determine and subtract local sky level by a curve of growth analysis with the IRAF-task ELLIPSE in the ISOPHOTE package
5. Model mean galaxy light with ELLIPSE using a sigma clipping algorithm to disregard contaminating sources hidden below the galaxy light, subtract the model
6. Divide resulting image by square root of the model, cut out portion where SBF are measured
7. Mask out contaminating sources like foreground stars, background galaxies and globular clusters
8. Calculate the power spectrum (PS) of the cleaned image
9. Obtain the azimuthal average of the PS
10. Fit function of the form (1.8) to the azimuthally averaged PS.

$PSF(k)$ is determined from a simulated star with no close neighbours by fitting a Moffat profile to its PS. P_1 is the white noise component, proportional to the ratio between sky and galaxy brightness in the range where SBF were measured. It is independent of seeing. P_0 is the amplitude of the pixel-to-pixel surface brightness fluctuations, being the zero wavenumber limit of the seeing convolved pixel-to-pixel star count fluctuations, and therefore seeing-independent, too.

Assuming that the contribution of undetected point sources to the fluctuation signal is negligible, i.e. $\bar{L} = P_0$ – which is a valid assumption for these simulations –, it holds

$$\bar{m}_I = -2.5 * \log(P_0/t_{\text{exposure}}) + ZP \quad (2.4)$$

Values at small k (long wavelength) are rejected for the fit, as they are often considerably influenced by large-scale residuals from imperfect galaxy subtraction and the finite width of the image portion used to measure SBF.

The (seeing independent) signal-to-noise ratio S/N of the measurement was defined as $S/N=P_0/P_1$, following Tonry & Schneider ([1988]). In the following it will be referred to as canonical S/N . Note however that the detectability of SBF decreases with increasing seeing: by convolving with the seeing the star count pixel-to-pixel fluctuations are smoothed out. Additionally, the larger the seeing is, the fewer the independent data points per unit angle. To take this dependence of the SBF detectability on the seeing into account, we define a modified signal-to-noise ratio S/N^* in the following way:

$$S/N^* = P_0/P_1 \times \sqrt{N_{\text{sd}}}/sf \quad (2.5)$$

with N_{sd} being the number of seeing discs – i.e. independent data points – contained in the image portion where SBF are measured, and sf being the smoothing factor by which the seeing convolution reduces the amplitude of the pixel-to-pixel fluctuations. sf was 5 for $0.5''$ seeing and 10 for $1.0''$ seeing, as determined from measuring the pixel-to-pixel fluctuations on a simulated seeing convolved fluctuation image.

Examples of simulated dEs

In Fig. 2.3, example images and power spectra of simulated dEs are shown. The innermost pixels which were neglected in the power spectrum fit are especially marked. Note

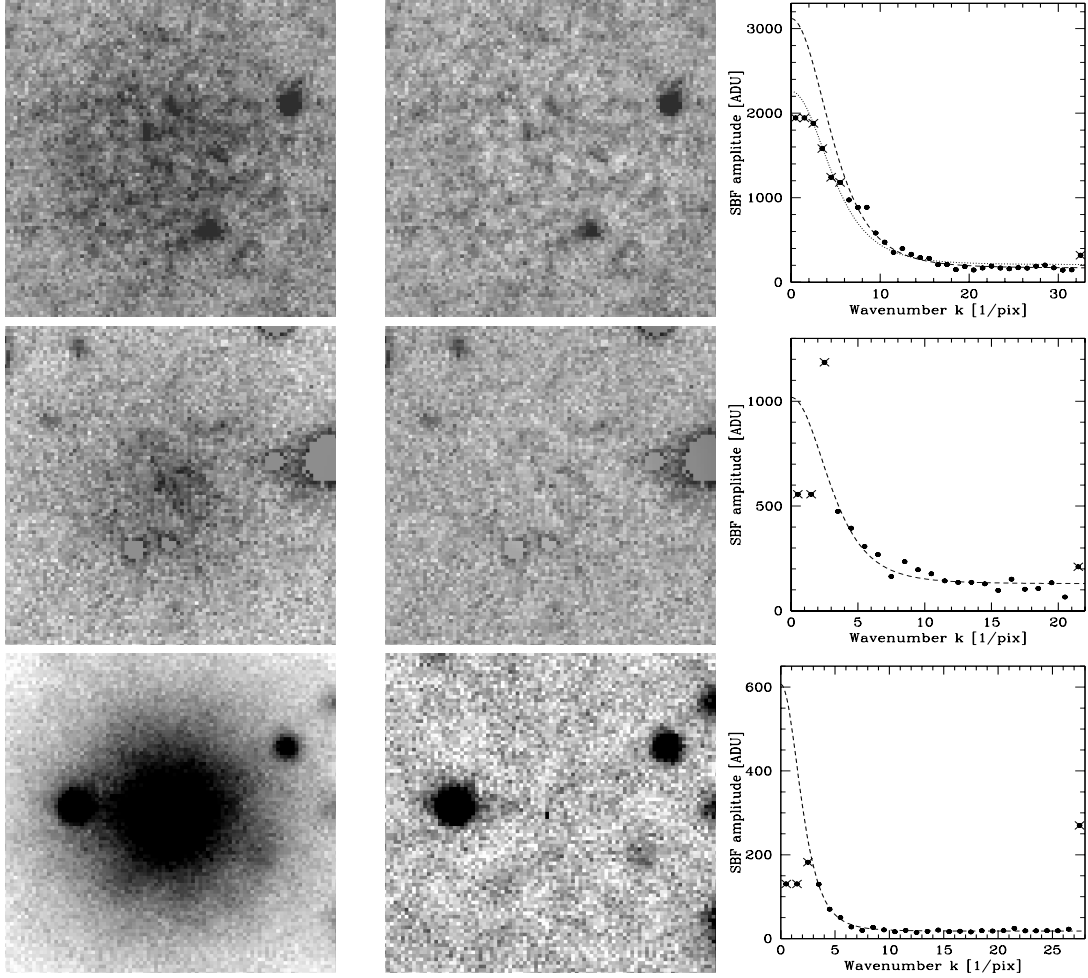


Figure 2.3: Examples of SBF measurements for simulated dEs in the I band (see Figs. 3.7 to 3.10 and Fig. 4.3 for examples of real galaxies). The image sequence is: Original image — Original image minus smooth galaxy light model — Power spectrum of the normalized and cleaned former image. For the power spectra, the dashed line is the best fit of $P(k) = PSF(k) \times P_0 + P_1$, when rejecting the points marked with crosses. For the first example from the top, the dotted line represents a fit to all datapoints except the outermost and innermost one. The simulated integration time was 1 hour for all examples. Parameters of the simulated dEs:

1st row from top: $M_V = -10.57$ mag, $(m - M) = 29.4$ mag, $\mu_V = 25.5$ mag arcsec $^{-2}$, $(V - I)_0 = 0.88$ mag, $\overline{M}_I = -2.4$ mag, $\delta\overline{m}_I = \overline{m}_{I,\text{simulated}} - \overline{m}_{I,\text{measured}} = -0.22$ mag. Seeing $0.5''$.

2nd row from top: $M_V = -11.13$ mag, $(m - M) = 31.4$ mag, $\mu_V = 25.1$ mag arcsec $^{-2}$, $(V - I)_0 = 0.90$ mag, $\overline{M}_I = -2.86$ mag, $\delta\overline{m}_I = 0.06$ mag. Seeing $0.5''$.

3rd row from top: $M_V = -13.72$ mag, $(m - M) = 31.4$ mag, $\mu_V = 23.42$ mag arcsec $^{-2}$, $(V - I)_0 = 0.99$ mag, $\overline{M}_I = -2.44$ mag, $\delta\overline{m}_I = -0.02$ mag. Seeing $1.0''$.

the effect of the twice as large seeing of $1.0''$ in the third example: the width of the seeing power spectrum is about half that of the other two examples, where the seeing was $0.5''$.

Rejecting the innermost pixels is crucial to determine the correct SBF amplitude, as low wavenumbers are affected by imperfect galaxy subtraction and large scale sky gradients in the investigated image. The limiting wavenumber beyond which one has to reject pixels has to be determined individually for each galaxy, as image dimensions and loci and number of contaminating sources change. We have adopted the following criterion for deciding which pixels to reject or not: if the χ^2 of the fit improves by more than a factor of 2 when rejecting the innermost pixel, it is rejected. Then, the same is tested for the second pixel, and so on until χ^2 improves by less than a factor of 2. For the examples given in Fig. 2.3, this criterion works fine for the lower two power spectra.

Unfortunately, as illustrated in the upper example, things can also be more complicated. If only rejecting the inner- and outermost data point, the obtained fit fits well to wavenumbers smaller than 6, but underestimates the signal for wavenumbers between 6 and 10 and overestimates slightly the white noise component P_0 . When rejecting wavenumbers smaller than 6, the outer part is fit much better. The difference in P_1 between the two possibilities is considerable, about 40%. In cases like that, the uncertainty in which pixels to reject or not is the major source of error. As is noted in Fig. 2.3's caption, the difference $\delta\overline{m}_I$ between simulated and measured \overline{m}_I obtained when rejecting the inner 5 pixels is much smaller than for only rejecting the innermost pixel. Therefore, whenever fits to the outer and inner part of the power spectrum differed considerably, more emphasis was put on fitting well the outer part.

However, this restriction the outer power spectrum part can also lead to significant uncertainties, because at higher wavenumbers the white noise component starts to dominate over the PS of the PSF. As our simulations were performed on artificial **dwarf** galaxies, the image portions chosen for the SBF measurements had relatively small dimensions of typically 30 to 60 pixel (6 to $12''$). Therefore the wavenumber range over which the amplitude of the PSF is determined is only of the order of 10 or fewer independent data points. This small number, together with the uncertainty in which wavenumbers to disregard or not, is the major source of uncertainty for the SBF measurements we performed. For the simulated galaxies at $1.0''$ seeing, the wavenumber range over which to perform the fit to the PS is only half of that for $0.5''$ seeing, which means the uncertainty at $1.0''$ seeing is significantly higher than for $0.5''$ seeing.

2.5 Results of the simulations and their discussion

In Figs. 2.4 to 2.7, the results of the simulations are shown. Figs. 2.4 to 2.6 show the results for the three different distance moduli with 3600 seconds integration time: S/N^* and $\delta\overline{m}_I$ are plotted vs. M_V for the two different seeing values. In Fig. 2.7, the same observables are plotted for 4 different integration times at a fixed 31.4 mag distance

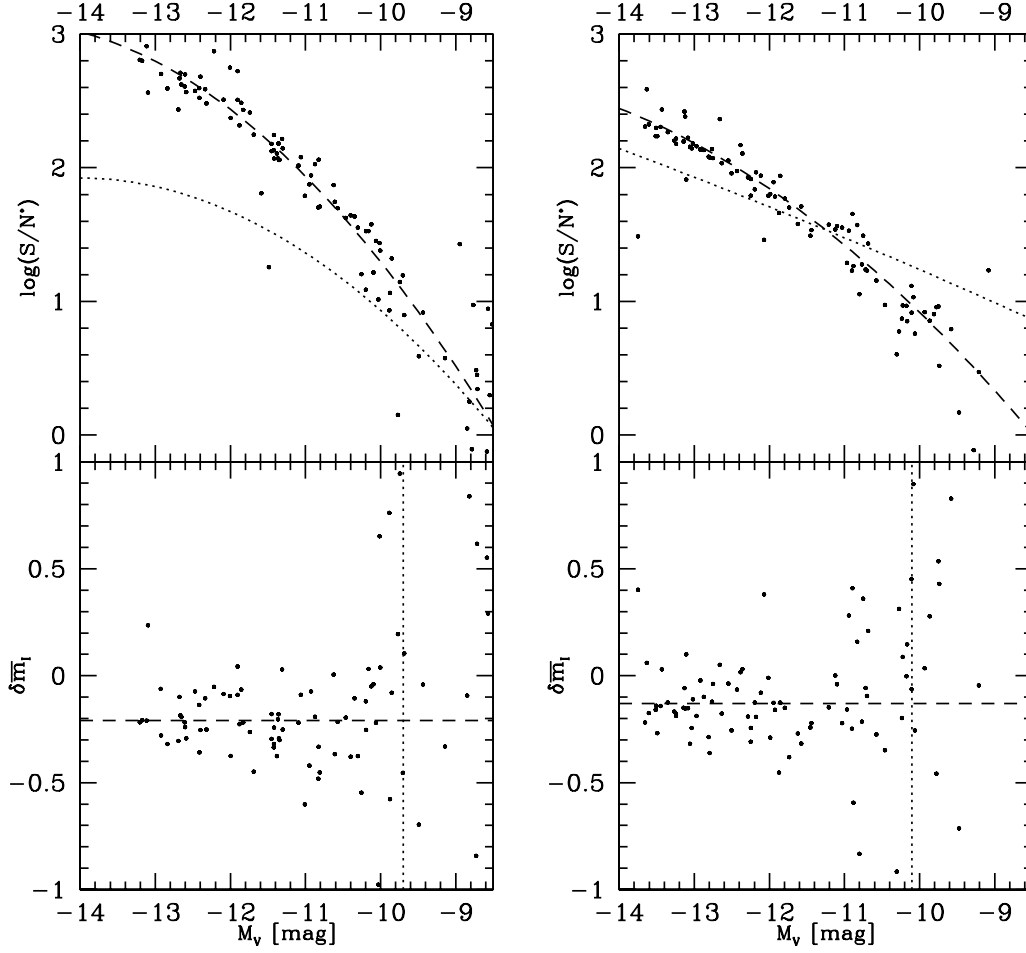


Figure 2.4: Results of the simulations for $(m - M) = 29.4$ mag and zero point $ZP = 27.0 + 2.5 * \log(3600)$ mag. **Left panel:** Seeing = $0.5''$. **Right panel:** Seeing = $1.0''$. **Top panel:** Logarithm of S/N^* (definition see text) plotted vs M_V . The dashed line is a 2nd order polynomial fit to the data points. The dotted line is the fit corresponding to the canonically defined S/N (see text). **Bottom panel:** $\delta \overline{m}_I = \overline{m}_{I,\text{simulated}} - \overline{m}_{I,\text{measured}}$ plotted vs. M_V . For magnitudes fainter than the limiting magnitude M_V^* indicated by the dotted vertical line, more than 50% of the measured galaxies have $S/N^* < 6$ or a deviation of more than 0.5 mag from the mean $\delta \overline{m}_I$ for the measured galaxies brighter than M_V^* . $\delta \overline{m}_I$ is indicated as a dashed line. $\delta \overline{m}_I$ and M_V^* were determined iteratively.

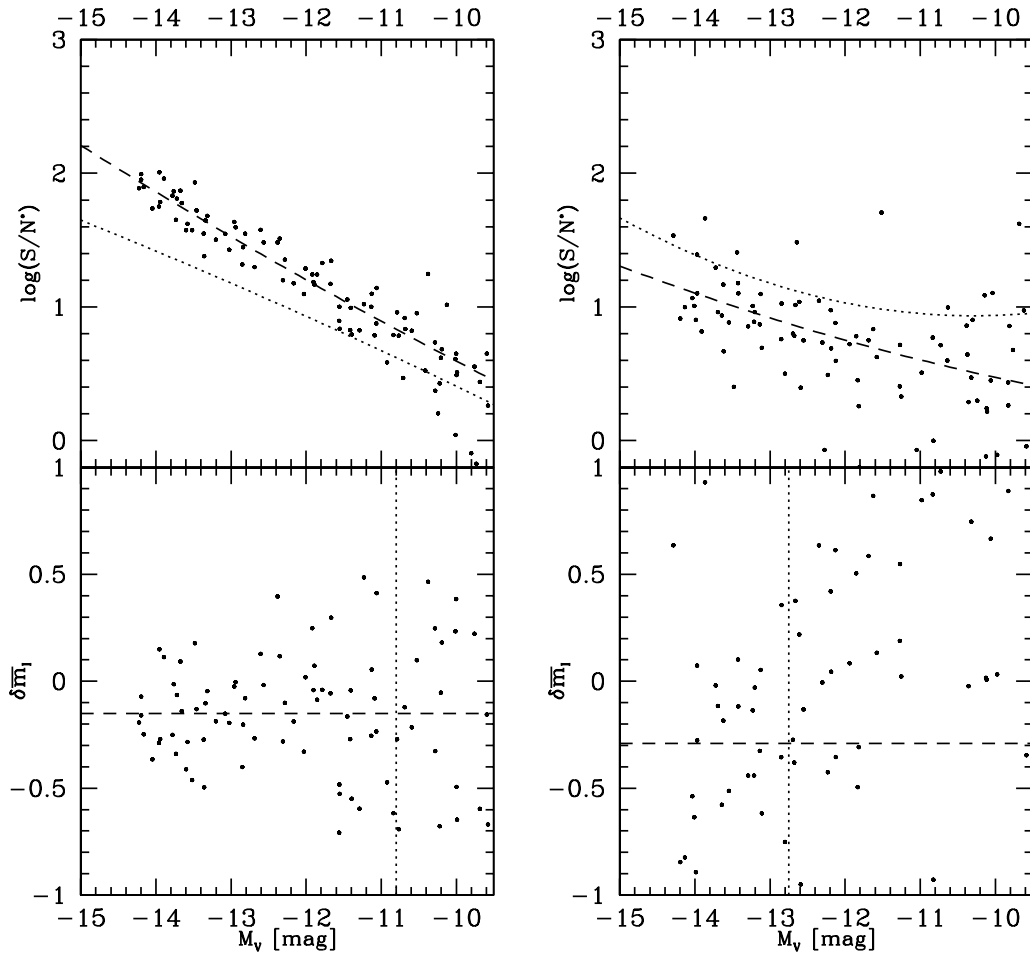


Figure 2.5: Results of the simulations for $(m - M)=31.4$ mag. Symbols/lines as in Fig. 2.4.

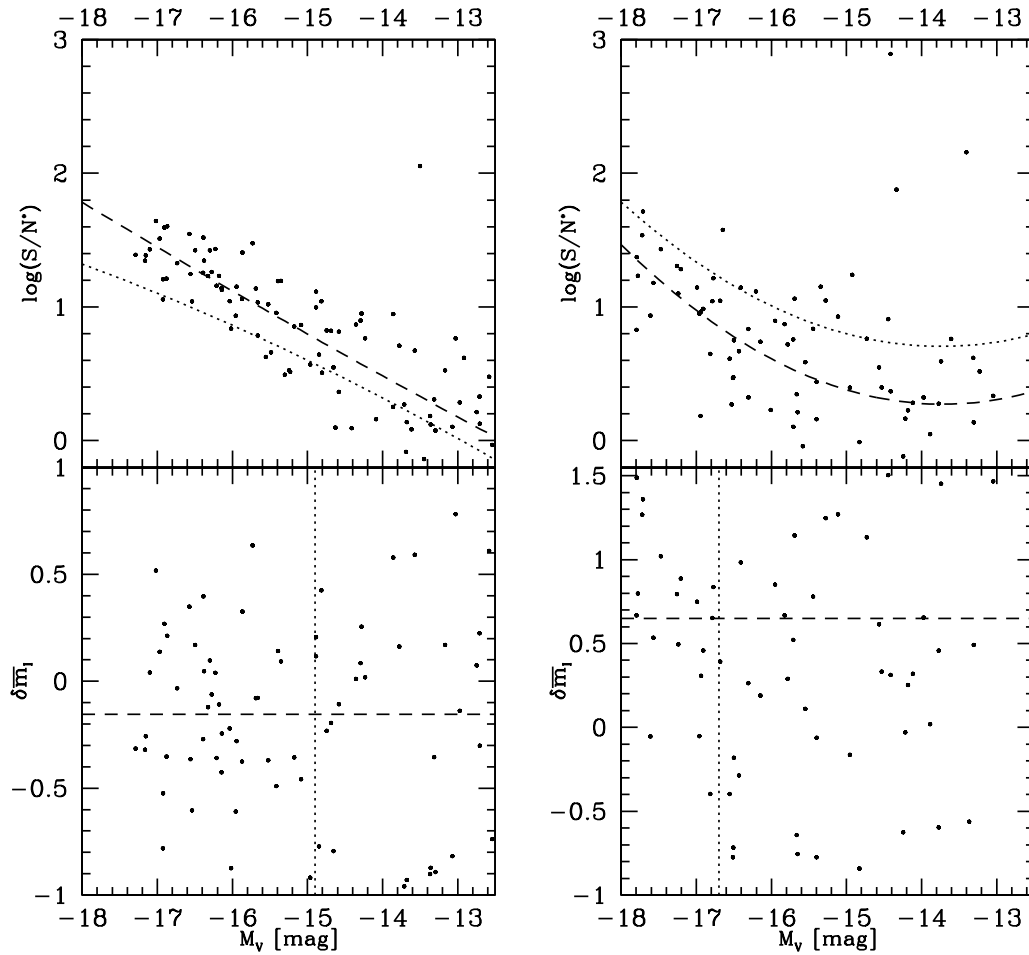


Figure 2.6: Results of the simulations for $(m - M) = 33.4$ mag. Symbols/lines as in Fig. 2.4.

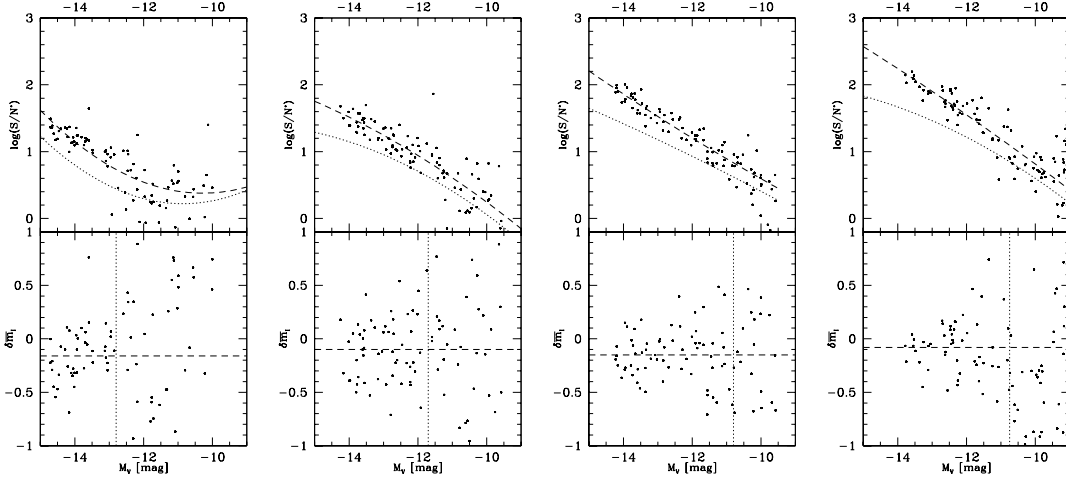


Figure 2.7: Results of the simulations for $(m - M)=31.4$ and seeing= $0.5''$ at varying integration time / zero point $ZP=27.0+2.5*\log(t)$. From left to right: $t= 900; 1800; 3600; 7200$ seconds.

modulus and $0.5''$ seeing. A 2nd order polynomial fit to S/N^* vs. M_V is plotted over the data points. The corresponding fit for the canonical S/N is given as well. It is interesting to note that for $0.5''$ seeing the modified S/N^* is consistently higher than the canonical S/N , while for $1.0''$ it is the opposite. This shows that for our simulations, $0.75''$ is about the limiting seeing below/above which S/N^* becomes higher/lower than the canonical S/N .

One can see that for the highest S/N^* data, the relative accuracy of the SBF method is of the order of 0.1-0.2 mag, i.e. 5-10% in distance. From the bottom panels of Figures 2.4 to 2.7, one immediately notices an average offset between simulated and measured SBF amplitude of the order of 0.15 mag in the sense of measuring too faint SBF. The mean offset, when disregarding the two most extreme values, is 0.14 mag. The reason for this offset is that in equation (1.8) we assume an undisturbed power spectrum $PSF(k)$. Doing so implicitly neglects the fact that the FT of the seeing convolved SBF is in frequency space convolved with the FT of the mask used to excise contaminating point sources and restrict the measurement area. This results in a damping of the SBF amplitude at low wavenumbers, as the “ideal” power spectrum of an infinitely large fluctuation image is convolved by a Bessel-like function, due to the finite sample area (see Fig. 3.6).

For our simulations – whose aim is to define limits down to which the SBF can be unambiguously measured for dEs – this effect is not important. Indeed, in making the idealised approach of assuming an undisturbed PSF power spectrum for the measurement of simulated SBF one can nicely illustrate the amount of fluctuation signal that is lost because of the wave-power damping at low wavenumbers.

For the SBF-measurements on real dEs in sections 3 and 4 the distortion of the PSF

	0.5''	1.0''
29.4	-9.7	-10.1
31.4	-12.8; -11.7; -10.8; -10.8	-12.75
33.4	-14.9	-16.75

Table 2.1: Limiting absolute magnitude $M_{V,\text{lim}}$ for the different combinations of distance modulus (denoted in the left column) and seeing (denoted in the top line). The integration time t was 3600 seconds except for the 4 different values at 0.5'' and 31.4 which correspond to 4 different integration times $t=900, 1800, 3600$ and 7200 seconds from left to right. The zero point including integration time t is given by $27 + 2.5 * \log(t)$.

power spectrum due to the “window function effect” is taken into account.

2.5.1 Limiting absolute magnitudes

For each of the 9 simulated sets of dEs a limiting absolute magnitude $M_{V,\text{lim}}$ was determined, below which the determination of cluster membership is not reliable anymore. These are the two conditions for reliable cluster membership determination we adopted: First, the difference between offset corrected measured and simulated \overline{m}_I must be smaller than 0.5 mag. The mean offset with regard to which the measurement difference is defined is denoted as $\overline{\delta m}_I$ and indicated in Figures 2.4 to 2.7. The value of 0.5 mag was chosen as it is about equal to the maximum uncertainty in deriving \overline{M}_I from $(V - I)_0$, see Sect. 2.3. To require a higher measurement accuracy than the systematic uncertainty of the method would be unnecessary.

Second, the modified S/N^* of the measurement must be higher than 6. This limit was adopted to avoid an SBF measurement of an object with $S/N^* < 4$ mimicking a S/N^* of the order of 5 or 6 because of a measured \overline{m}_I 0.5 mag brighter than simulated.

$M_{V,\text{lim}}$ is then defined as the absolute magnitude at which 50% of the measured galaxies fulfil the above criteria. It is indicated for each set in Figures 2.4 to 2.7. As $\overline{\delta m}_I$ and $M_{V,\text{lim}}$ depend on each other, they were determined iteratively.

In Table 2.1, $M_{V,\text{lim}}$ is tabulated. One can see that for the two smaller distance moduli 29.4 and 31.4, the SBF-Method can reach very faint magnitudes. For galaxies with $M_V \simeq -10$ to -11 mag within a distance of about 20 Mpc, reliable SBF measurements with accuracies better than 0.5 mag can be obtained at about 0.5'' seeing, the given zeropoint of 27 mag and an integration time of 1hr. The SBF-Method is therefore a very valuable tool for extragalactic distance measurements out to the Fornax/Virgo distance for even the faintest early-type galaxies.

What are in detail the effects of varying seeing, integration time and distance modulus on the limiting dE magnitude for SBF application?

Effects of varying seeing

Table 2.1 shows that for the distance moduli 31.4 and 33.4, increasing the seeing by a factor of 2 brightens $M_{V,\text{lim}}$ by about 2 mag. This corresponds to about 1.4 mag in central surface brightness $\mu_0(V)$, or a factor of 3.6 in central intensity. This increase by almost a factor of 4 in central intensity is plausible: the pixel-to-pixel fluctuations are smoothed by a factor of 2 at $1.0''$ seeing compared to $0.5''$ while the SBF amplitude is proportional to the square root of the intensity; therefore the intensity must be increased by a factor of 4 to compensate for the smoothing.

The “rule” extracted from that behaviour is: Increasing seeing by a factor x needs increase of intensity by a factor of x^2 to be compensated.

For the 29.4 mag distance modulus, there is no large difference between $0.5''$ and $1.0''$ seeing. This is because at the faint magnitudes around -10 mag, the central surface brightness is about $25 \text{ mag arcsec}^{-2}$ in I , which is only $2\text{-}3\sigma$ above the sky standard deviation, i.e. the mean surface brightness is close to the detection limit, and measuring its fluctuations is very difficult, even if the SBF amplitude is not much smaller than the mean surface brightness. That is why going from $1.0''$ to $0.5''$ seeing, no significant improvement of limiting absolute magnitude is reached for the 29.4 mag distance modulus.

Effects of varying integration time / zero point

What is the necessary scaling in integration time t to account for varying seeing? At 31.4 mag distance modulus, only $t=900$ seconds are needed for $0.5''$ seeing to reach the same $M_{V,\text{lim}}$ as for $1.0''$ seeing and $t=3600$ seconds.

Thus, increasing seeing by a factor x needs increase of integration time by a factor of x^2 to be compensated. This is equivalent to keeping integration time fixed and increasing the zero point by $2.5 \cdot \log(x^2)$.

Table 2.1 shows that increasing the integration time t by a factor of 2 results in a 1 magnitude fainter $M_{V,\text{lim}}$, or about a factor of 2 in central intensity. As S/N and SBF amplitude are proportional to \sqrt{t} and \sqrt{I} , respectively, this result should be expected. Thus, increasing integration time t by a factor x allows SBF measurement for objects with central intensity fainter by the same factor x . This is equivalent to keeping integration time fixed and increasing the zero point by $2.5 \cdot \log(x^2)$.

No notable change in limiting magnitude is seen when increasing t from 3600 to 7200 seconds. This might be partially due to statistical reasons, but the major reason is that the mean surface brightness is close to the detection limit (about 5 sigma above the sky noise) and the angular extent of the simulated dEs is only a few arcseconds. For galaxies with $M_V \simeq -11$ mag, the additionally detected region when going from 3600 to 7200 seconds carries no measurable SBF signal anymore.

Effects of varying distance modulus

The strength of the SBF relative to the underlying mean surface brightness decreases linearly with distance. As the SBF are proportional to the square root of the intensity, the intensity must increase by a factor of x^2 when distance increases by a factor of x to compensate for that. Table 2.1 shows that increasing distance modulus by 2 mag results in a 3-4 mag brighter limiting magnitude $M_{V,\text{lim}}$. This corresponds to about a factor of 10 in central intensity, which is slightly more than the expected value of $2.5^2=6.25$. The reason for this is that the angular area over which the SBF signal is sampled is smaller at 2.5 higher distance for the same object.

A simple rule

Summarising the scaling relations found, we give the following rule to calculate the limiting magnitude $M_{V,\text{new}}^*$ at new observing conditions different to the reference ones adopted in our simulations:

$$M_{V,\text{new}}^* = M_{V,\text{ref}}^* - 2.5 * 2.66 * \log\left(\frac{s_{\text{new}}}{s_{\text{ref}}}\right) - 1.33 * (ZP_{\text{ref}} - ZP_{\text{new}}) \quad (2.6)$$

$M_{V,\text{ref}}^*$ is the limiting magnitude calculated from our simulations at the given distance modulus. s_{ref} is the seeing FWHM in our simulations, s_{new} the new seeing FWHM. ZP_{ref} is the total zero point in the simulations, i.e. $ZP_{\text{ref}} = 27.0 + 2.5 * \log(t)$ with t being the total integration time. ZP_{new} is then the new total zero point. This all refers to a gain of 1, i.e. the zero point is expressed in terms of electrons and not ADU.

Note, however, that equation (2.6) is restricted to cases where the mean surface brightness of the galaxy is significantly higher than the sky noise. As when the surface brightness gets too close to the sky noise (less than about 5 sigma, see the former three subsections), changing integration time or seeing does not have strong effects on SBF detectability.

We note that unresolved background galaxies and globular clusters generally increase the measured SBF signal, which has to be corrected for in real data (see Sect. 3 and 4). For our simulations, we do not take these contributions into account, as they are small compared to the SBF signal of the galaxies: Using formula (13) of Jensen et al. ([1998]) for the I -band and inserting the values used for the magnitude distribution of background objects, we get for the relative contribution of background galaxies to the SBF signal at 33.4 distance modulus a value of the order of 2-4%, depending on seeing and the galaxy's magnitude. For the distance moduli 29.4 and 31.4, the contribution is below 1%.

2.5.2 Comparing real SBF data with simulations

The S/N achieved in SBF measurements for 6 bright Centaurus cluster dEs from VLT FORS1 images (see Sect. 4) is compared with the S/N obtained from simulations tuned

to reproduce the measured values. A colour-SBF relation, a colour-magnitude relation and surface brightness-magnitude relation were fit to the measured values of the Centaurus dEs, and 64 galaxies were simulated according to these relations. Their SBF amplitude was measured as described in Sect. 2.4. In Fig. 2.8, the $\log(S/N)$ values of the real measurements are plotted over the results for the simulations. A line is fit to both real and simulated data. One can see that the simulations do not overestimate the S/N of the real data. Both fits are consistent with each other.

This consistency between real and simulated data suggests that the simulations presented in the previous sections probably are a good approximation of reality. The applied generalisations like zero ellipticity and purely exponential profile apparently do not introduce a notable bias towards too high or too low S/N .

2.6 Summary

Extensive simulations of SBF measurements on dEs for three different distance moduli 29.4, 31.4 and 33.4 mag, two different seeing 0.5'' and 1.0'' and 4 different observing times 900, 1800, 3600 and 7200 seconds have been presented. For each of the simulated sets of dEs, the limiting magnitude $M_{V,\text{lim}}$ below which a distance measurement is not reliable anymore has been determined. The following results have been obtained:

1. For distances ≤ 20 Mpc, the SBF method can yield reliable cluster membership of dEs down to very faint limiting magnitudes, e.g. $M_{V,\text{lim}} \simeq -10$ mag for a distance of 7.5 Mpc, and $M_{V,\text{lim}} \simeq -11$ mag for 19 Mpc distance, at 1hr integration time, 0.5'' seeing and a zero point of 27 mag in the I -band.

2. A number of simple rules are derived in order to calculate limiting magnitudes, needed integration times or seeing for observing conditions different to the ones adopted for our simulations.

3. By comparing real SBF data of Centaurus Cluster dEs with simulations tuned to reproduce the real data, we find that our simulations do not overestimate the achievable S/N of the SBF method, but are consistent with real measurements. Therefore the statements about limiting magnitudes for the technique made in this chapter are reasonable and we would not expect a very different behaviour in real observations.

An ideal application of the SBF technique would be a deep *and* wide field survey of several nearby clusters such as Fornax, Virgo or Doradus. With the arrival of wide field cameras on large telescopes (Suprime cam on the Subaru telescope or IMACS on Magellan), this is a very promising possibility to determine well the very faint end of the galaxy luminosity function in nearby clusters.

In the next chapter, the first part of such a survey in the central Fornax cluster using IMACS@Magellan (LCO) is presented.

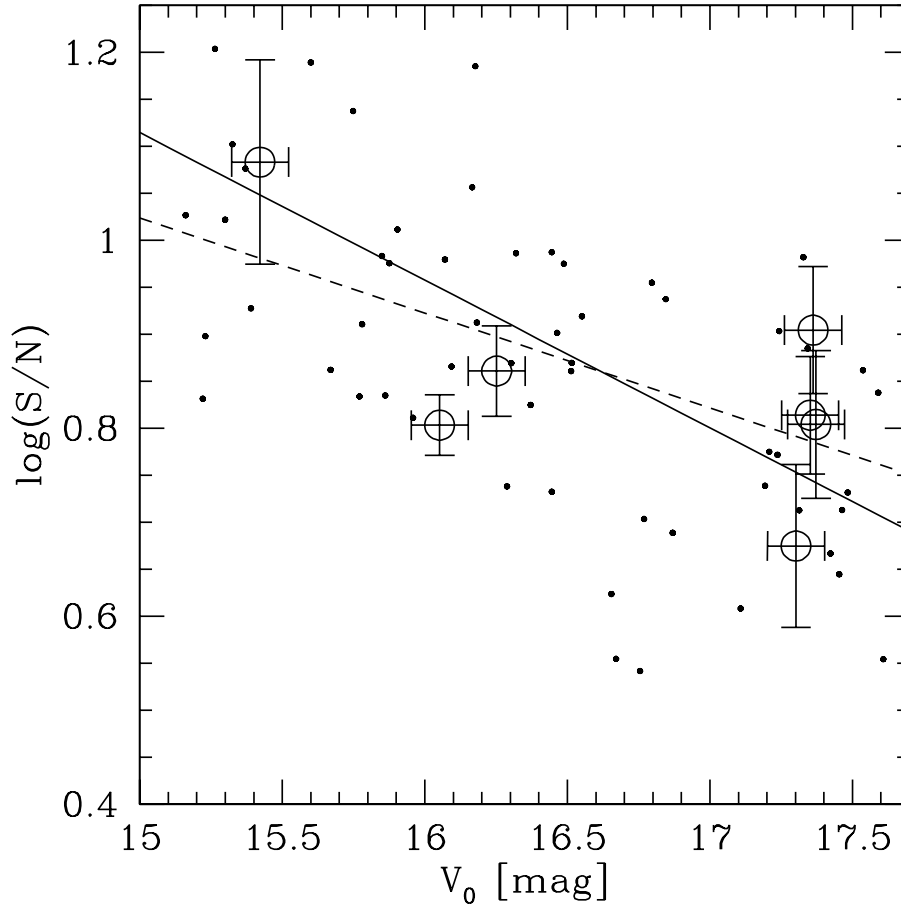


Figure 2.8: S/N of the SBF measurement vs. apparent V_0 . Large circles are the real Centaurus data (from Sect. 4). Dots represent galaxies simulated according to the Centaurus data's colour-SBF relation, colour-magnitude relation and surface brightness-magnitude relation. The dashed line represents a fit to the real data, the solid line is a fit to the simulated data. Both fits are consistent with each other within the error ranges.

Chapter 3

SBF distances to candidate dEs in the Fornax cluster

Section 3.2 of this chapter is based on the publication *Hilker, M., Mieske, S. & Infante, L., 2003, A&A letters, 397, 9.*

3.1 Abstract

In this chapter, the faint end slope of the early-type galaxy luminosity function in the Fornax cluster is investigated by means of SBF cluster membership confirmation and morphological selection of candidate dEs. We first describe the discovery of $\simeq 70$ very faint dE candidates in Fornax based on data obtained with the 2.5m du Pont telescope at Las Campanas Observatory (LCO), Chile. The joint sample of newly found and previously known candidate dEs has a luminosity function with a faint end slope $\alpha \simeq -1.1 \pm 0.1$, based on purely morphological cluster membership assignment. To improve the membership assignment, we have re-imaged the central Fornax cluster with substantially better spatial resolution using IMACS and Magellan at LCO. From the first part of our survey, we directly determine the cluster membership for 10 previously unconfirmed candidate dEs in the magnitude range $-14.2 < M_V < -11$ mag using the SBF method. Furthermore, we improve the morphological cluster membership assignments for fainter galaxies with $M_V < -10$ mag. For the vast majority of dE candidates we confirm the probable cluster membership, such that α changes by less than 0.02. We find two new dSph candidates from our IMACS imaging. Including them does not change α by more than 0.02, either. This confirms the strong discrepancy between the number of low mass dark matter halos expected in a Λ CDM universe and the number of low luminosity galaxies. We find that Fornax dEs are on average slightly larger than their Local Group counterparts. The SBF measurements indicate a weaker dependence of the absolute fluctuation magnitude \overline{M}_I on $(V - I)_0$ at blue colours compared to the empirical calibration at redder colours.

3.2 Introduction: search for dE candidates in Fornax

This section presents the detection of $\simeq 70$ previously undetected very faint dwarf elliptical galaxy candidates in the central Fornax Cluster, plus photometry of $\simeq 80$ brighter already known candidates, based on deep imaging in V and I with the 2.5m du Pont telescope at Las Campanas Observatory, Chile. The follow-up imaging survey ‘‘Fornax Deep Field’’ is described in the next section 3.3.

3.2.1 Observations and data analysis

The observations were performed in an observing run in December 1999 with the 100-inch du Pont telescope at Las Campanas Observatory (LCO), Chile, using the WFCCD camera which images a $25'$ diameter field onto the detector, with a scale of $0.774''/\text{pixel}$. 14 fields in the central region of the Fornax cluster and one additional background field were observed through the Johnson VI filters. All nights were photometric throughout, and the seeing was in the range $1.5\text{--}2.0''$.

The CCD frames were processed with standard IRAF routines, instrumental aperture magnitudes were derived using SExtractor (Bertin & Arnouts [1996]). Surface brightness profiles of all galaxies were measured with the ellipse fitting routines under the STSDAS package of IRAF.

In order to optimise the detection of faint resolved sources by the software routines, all CCD fields were first inspected carefully by eye, independently by the author of this thesis and Dr. M. Hilker, to search for low surface brightness objects with sizes of Local Group dSphs (effective diameter between 150pc and 1kpc, see Mateo [1998], corresponding to $2''$ to $12''$ at the Fornax distance of 31.4 mag (Ferrarese et al. [2000])). This search resulted in the detection of about 70 previously uncatalogued dSph candidates, see Figs. 3.4, 3.5 and Figs. 3.7 to 3.13 for example images of those candidates imaged also in the higher resolution follow-up in Sect. 3.3. The possible missing of objects close to the WFCCD resolution limit is dealt with in Sect. 3.3.

The detection-sensitive parameters of SExtractor were optimised such that most objects of the by-eye-catalog were detected by the program. Further visual inspection of the SExtractor detections within the same parameter space as the visual detections, added about 10% more dSph candidates to the by-eye-catalog. About 10% of the obvious by-eye detections could still not be found by the routine. These sources were kept in the catalog, but not considered for the determination of the LF.

For the study of the faint end of the LF, the number counts of dSph candidates were corrected for incompleteness in the photometric detection. We randomly distributed 2000 simulated dSphs (in 100 runs) in each of the 14 CCD fields. The magnitudes and central surface brightnesses were chosen such that they extended well beyond the observed parameter space at the faint limits. The optimised detection parameters were used to recover the artificial galaxies. The same selection criteria as for the discovered

dSphs were applied to derive the completeness values as a function of magnitude and central surface brightness (see Fig. 3.2). For the number counts of the LF the completeness in each CCD field was corrected individually to account for the differing number densities.

To decrease the contamination of the sample by fore- or background galaxies, the “allowed” range for probable dSph candidates was restricted to within $\pm 2\sigma$ of the colour-magnitude and magnitude-surface brightness relation (see Figs. 3.1 and 3.2).

The photometric parameters of the dwarf galaxies were derived from the analysis of their surface brightness profiles: the total magnitude by a curve of growth analysis, the colour within an aperture of $8''$ diameter, and the central surface brightness from an exponential fit to the outer part of the profile.

The colour-magnitude relation

In Fig. 3.1 the colour-magnitude diagram (CMD) of all objects is shown. The newly discovered dSphs are highlighted by large triangles. Except for some outliers, they follow a well defined colour-magnitude sequence in the sense that the fainter galaxies are bluer. A linear fit to the data yields: $(V - I)_0 = -0.035 \cdot V + 1.61$ with a rms of 0.14.

The colour-magnitude relation of early-type galaxies is well known from other clusters (e.g. Secker et al. [1997], Barrientos & Lilly [2003]). It might be explained by a strong metallicity-luminosity relation (see Poggianti et al. [2001]). Here we show that this relation extends all the way down to the regime of dSphs. For the Local Group dSphs, there do not exist homogeneous $(V - I)_0$ colours. However, assuming that they are single stellar populations and then transforming their average iron abundances $[\text{Fe}/\text{H}]$ (Grebel et al. [2003]) to $(V - I)_0$ colours using equation (4) given in Kissler-Patig et al. ([1998]), they follow surprisingly well the same colour-magnitude relation (Fig. 3.1).

The magnitude-surface brightness relation

Dwarf ellipticals are known to follow a distinct $r_{\text{eff}}-M_V$ relation (e.g. Bender et al. [1992]). Also, they follow a tight $M_V-\mu_V$ relation in the sense that central surface brightness increases with increasing luminosity (Ferguson & Sandage [1988], Graham & Guzman [2003]). The validity of this relation has been a subject of lively debate. A number of authors have in the past argued against the existence of a magnitude-surface brightness relation for dEs (i.e. Irwin et al. [1990]) and questioned the cluster membership assignment to dEs based on morphology. However, Drinkwater et al. ([2001b]) confirm the surface brightness-magnitude relation for Fornax dwarfs, based on their spectroscopic survey.

Our data shows that the magnitude-surface brightness relation continues to even fainter magnitudes. As one can see in Fig. 3.2, the sequence of Fornax cluster dSphs matches quite well the location of Local Group dSphs in this plot (data from Grebel et al. [2003]), although the Fornax dSphs are somewhat shifted towards larger sizes with respect to

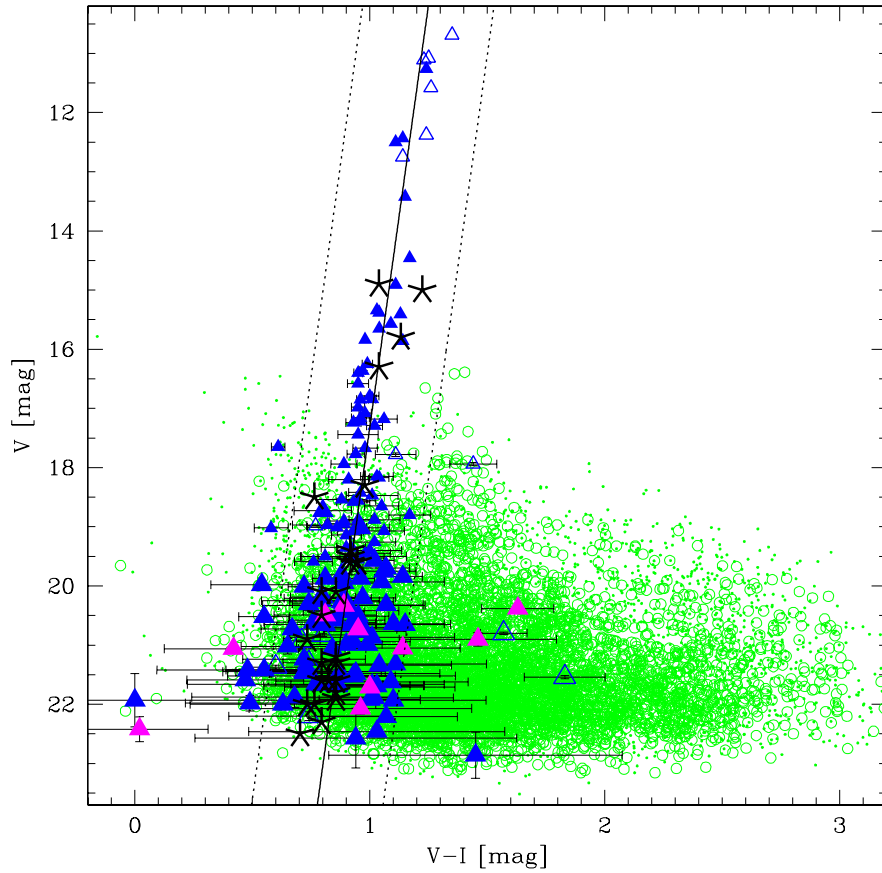


Figure 3.1: CMD of all extended (circles) and point sources (dots) in our Fornax WFCCD fields, also in comparison with Local Group dSphs. The formerly known candidate dEs from the Fornax Cluster Catalog (FCC, Ferguson & Sandage [1988]) – classified in that catalog as probable members – are shown as small triangles. The larger triangles are newly discovered dSphs. Light grey triangles are dwarfs that have been detected only by eye. Open symbols mark galaxies that lie outside 2σ of the magnitude-surface brightness relation. The solid line is a fit to the colour-magnitude relation of dEs between $0.3 < (V - I)_0 < 1.4$. Dotted lines are the 2σ deviations from the fit. Asterisks are the Local Group dSphs (data from Grebel et al. [2003]) projected to the Fornax distance.

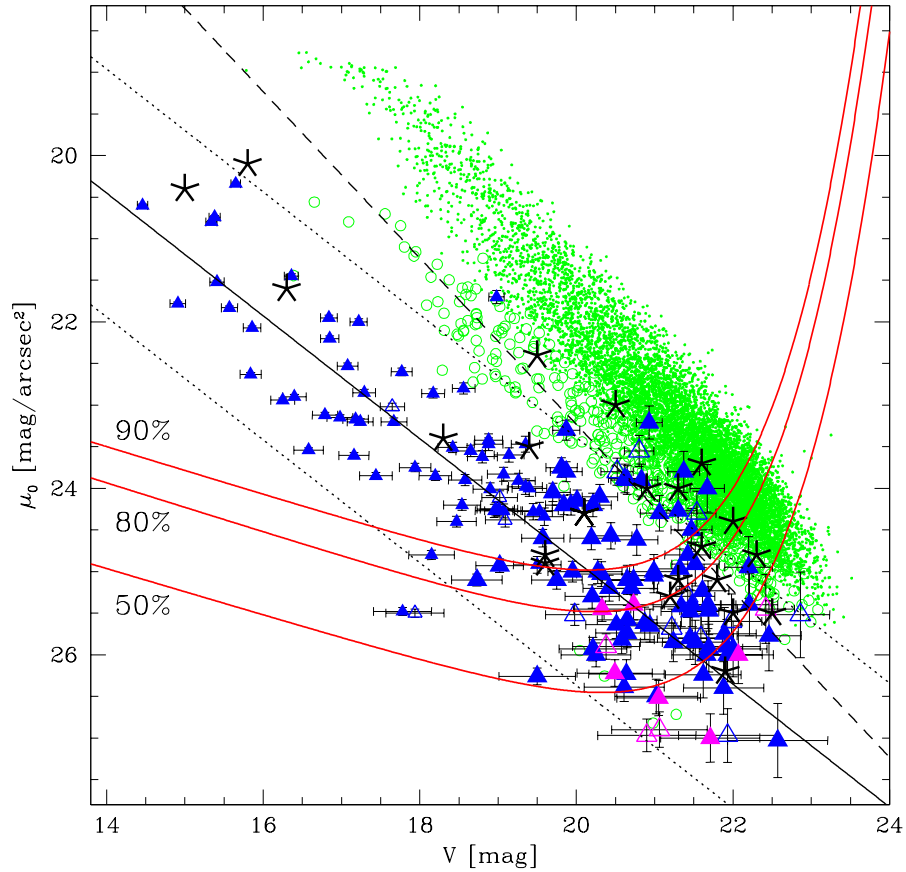


Figure 3.2: Magnitude-surface brightness diagram in our Fornax WFCCD field and the Local Group dSphs. The central surface brightness derived from an exponential fit is plotted. Symbols are as in Fig. 3.1, except that open triangles here mark galaxies that lie outside 2σ of the colour-magnitude relation. The dashed line indicates a scale length of $2.5''$ for an exponential profile. The solid and dotted lines are the fit to the magnitude-surface brightness relation and its 2σ deviations. The solid curves show the detection completeness limits of 90, 80 and 50%.

their Local Group counterparts. Some more compact dSphs might still be hidden in the barely resolved objects. This will be discussed in more detail in Sect. 3.3 based on the higher resolution follow-up imaging data presented there.

3.2.2 The faint end of the luminosity function from morphology

In Fig. 3.3, the luminosity distribution of the dEs and dSphs in Fornax is shown. When fitting a Schechter ([1976]) function to the counts with a completeness larger than 50% the faint-end slope is $\alpha = -1.11 \pm 0.10$. This agrees with the result by Ferguson & Sandage ([1988]), although their faintest dwarfs were 2.5 mag brighter than ours.

There seems to be a dip in the luminosity distribution at about $M_V = -14$ mag. Although this might be due to small number counts (the amplitude of the dip is about equal to the Poisson error of the number density at the corresponding magnitude), it is interesting to note that this is near the luminosity where the separation of dEs and dSphs is defined (e.g. Grebel [2001]). A sum of two Schechter functions better fits the data (see lower panel in Fig. 3.3) but does not change the faint end slope. If theory is right, this shallow slope might point to the destruction of a large number of dwarfs during the evolution of a cluster. One might suggest that the debris of these dwarfs have partly built up the huge cD halo around the central galaxy (e.g. Hilker et al. [1999b]).

One potentially important restriction of this survey is that we cannot apply reliable corrections for contamination by background galaxies as a function of apparent magnitude: in a comparison background field, 2 objects within a magnitude range of $-14 < M_V < -10$ mag match the selection criteria described above (see Fig. 3.14). The average number of objects in each Fornax field is 6.5 ± 0.7 . This indicates on the one hand that the majority of dE and dSph candidates detected by us should be cluster members, a conclusion which is supported by the location of the colour-magnitude and magnitude-surface brightness relation of our candidate dSphs and also by the fact that both background sources are somewhat offset from the magnitude surface-brightness relation towards smaller size. On the other hand, the mere fact that there *are* two background sources matching the colour and surface brightness selection criteria also indicates that higher resolution follow up images are clearly needed: both to confirm the cluster membership of dSph candidates by measuring their distance with the SBF method and to improve the morphological discrimination between cluster candidates and background sources (e.g. spirals) close to the resolution limit of the WFCCD data. The results of a survey aimed at these tasks are described in the next section 3.3.

3.3 “Fornax Deep Field”

The principle task of our project “Fornax Deep Field” (FDF) was to re-image the central Fornax cluster with a larger telescope and significantly better spatial resolution than in the WFCCD data from Sect. 3.2. While these latter data had the sufficient depth to

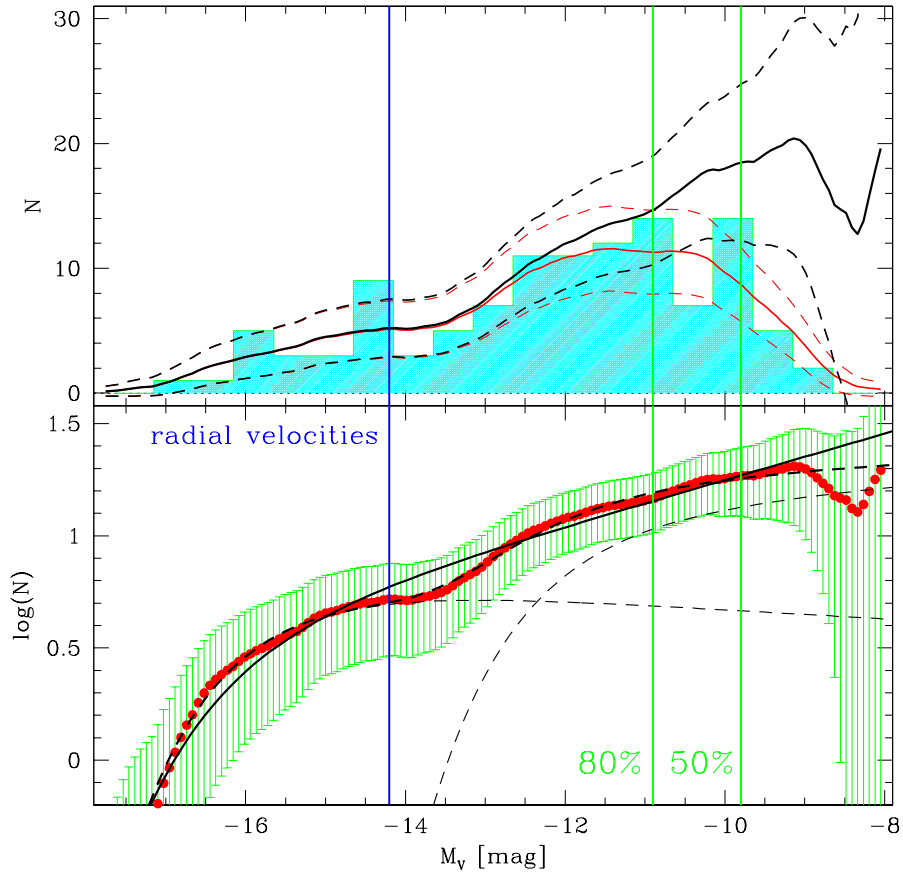


Figure 3.3: Luminosity function of dEs and dSphs in Fornax from the WFCCD data. The 80% and 50% detection completeness limits are indicated by vertical lines. The magnitude limit down to which dEs have been confirmed as cluster members via radial velocity measurement is indicated by a vertical line at $M_V \simeq -14$ mag. Upper panel: The shaded histogram gives the uncorrected number counts. The thin line gives a binning independent representation of the counts (Epanechnikov kernel of 0.5 mag width). The thick line shows the completeness corrected counts with the 1σ uncertainty limits (dashed). Lower panel: completeness corrected number counts in logarithmic representation. The best fitting single Schechter function (solid curve) and sum of two Schechter functions (dashed curves) are shown.

accurately derive structural parameters for the brighter dE candidates already known from the Fornax Cluster Catalog (FCC, see Ferguson & Sandage [1988]) and to detect very faint dSph candidates, they did not allow to directly measure distances to these objects.

There are two main aims of “Fornax Deep Field”:

1. **Measure SBF-distances to candidate dEs with $M_V \leq -11$ mag.** By that one pushes the magnitude limit of direct cluster membership about 3 mag fainter than the current limit (see Fig. 3.3) down to the regime where the detection incompleteness in the WFCCD data becomes important.
2. **Improve the morphological classification of fainter candidate dEs.** By that one further extends the magnitude limit for cluster membership determination, as the WFCCD data can be checked for morphological misclassifications like spiral galaxies or spurious detections, taking advantage of the much better spatial resolution. In addition, new cluster member candidates possibly overlooked close to the resolution limit of the WFCCD data can be searched for.

3.3.1 The data

The observations for “Fornax Deep Field” were taken in the nights 25th of October 2003 and 5-7 of December 2004 at Las Campanas Observatory (LCO), Chile. Here we present the results of the first night. The instrument used was the Inamori Magellan Areal Camera and Spectrograph “IMACS” in imaging mode with the “short” f/2 camera, mounted at the 6.5m Baade telescope. The double-asphere, glass-and-oil-lens f/2 camera produces an image of 27.4' field diameter at 0.20 arcsec per pixel. The field is vignetted in the corners (by the tertiary mirror and its mounting assembly), changing from 0% flux loss at $R = 12'$ to 10% at $R = 15'$. The IMACS detector is an 8192×8192 CCD mosaic camera which uses 8 thinned 2k×4k detectors. Gaps of about 50 pixels separate the chips (<http://www.lco.cl/lco/magellan/instruments/IMACS>). Going from WFCCD to IMACS gives an increase in light collecting area by a factor 6.7, an improvement in pixel scale by almost a factor of 4 with an corresponding improvement in seeing FWHM of about a factor of 3. As a comparison, Fig. 3.5 shows the same area on the sky imaged by the WFCCD camera and IMACS.

In the first night of the observations in 10/2003, two fields in the central Fornax cluster were observed in the two bands V and I , see Fig. 3.4. The dE candidates imaged in these two fields are especially marked in Fig. 3.14. Thumbnail comparison between the WFCCD and IMACS images for all these candidates are shown in Figs. 3.7 to Fig. 3.13. The total integration time in V was 1800 seconds, divided into three single exposures of 600 seconds each. The I -band integration time was chosen from formula (2.6) to achieve as a limiting absolute magnitude for SBF-measurement that of the faintest dE candidate brighter than $M_V = -11$ mag. We assumed the median LCO seeing of 0.6'' (see <http://www.lco.cl>) and scaled the VLT-zero point to the Magellan one according to

the ratio of their light collecting areas. The total *I*-band integration time then was 4200 seconds for Field 1 and 5160 seconds for Field 6, divided up into 12 single exposures for Field 1 and 16 single exposures for Field 6. As at the time of the observations the Atmospheric Dispersion Corrector (ADS) had not yet been installed at the instrument, the image quality decreased significantly towards the outer parts of the field of view (FOV). The seeing-FWHM was about $0.6''$ in the central 5-10 arcminutes of the image and became as bad as about $2''$ towards the image borders. Repeated adjustment of the instrument focus and appropriate shifts of the image pointing nevertheless allowed us to image the major part of the candidate dEs in our FOV with a seeing better than $0.8''$.

Standard star images of the three Landolt fields SA92, SA95 and SA98 were taken at different airmass values during the night in one short (2 seconds) and long exposure (10 seconds), resulting in about 100 data points for a total of 35 standard stars.

Image reduction before SBF measurement

The image reduction steps before the SBF measurement were the following: first, a masterbias was created for each chip which was then subtracted from the raw science frames and domeflat exposures. Then for each chip the bias corrected dome flats were combined. The dome flats of all 8 chips were then merged to a single $8k \times 8k$ flat image. The single chip domeflats were normalised with respect to the mean of this merged $8k \times 8k$ domeflat. The CCD sensitivities varied significantly, within a range of about $\pm 20\%$ between the single chips. The bias subtracted science frames were then divided by the normalised dome-flats. They were registered with integer pixel shifts, combined and merged into an $8k \times 8k$ image.

The same image reduction procedure was performed for the standard star images. Their instrumental magnitudes were measured with the IRAF package APPHOT in apertures equal to those used by Landolt ([1994]). Then, a single photometric solution was determined for the entire $8k \times 8k$ image. There were still sky-background variations of the order of $\pm 2-3\%$ between the single chips, resulting in similar photometric zeropoint variations. For the final galaxy photometry, these variations were corrected for by comparing the photometric zero-point on the particular chip where the galaxy was located with the overall zero-point. This was possible due to the large total number of standard star measurements. Table 3.1 shows the photometric calibration coefficients.

For each investigated galaxy, the local background level was determined in both passbands via a curve of growth analysis, yielding the total apparent magnitudes in *V* and *I*. To correct for galactic reddening and absorption, we used the values from Schlegel et al. ([1998]), who give $A_I = 0.025$ and $E(V - I) = 0.018$ for the coordinates of the Fornax cluster.

ZP_I	ZP_V	CT_I	CT_V	k_I	k_V
26.667 ($\sigma = 0.027$ mag)	27.070 ($\sigma = 0.037$ mag)	0.066	0.019	0.073	0.153

Table 3.1: Photometric calibration coefficients for the first night of Fornax Deep Field. Calibration equation is: $m = m_{instr} + ZP - CT * (V - I) - k * AIRMASS$. The σ values indicate the zero point scatter between the different chips.

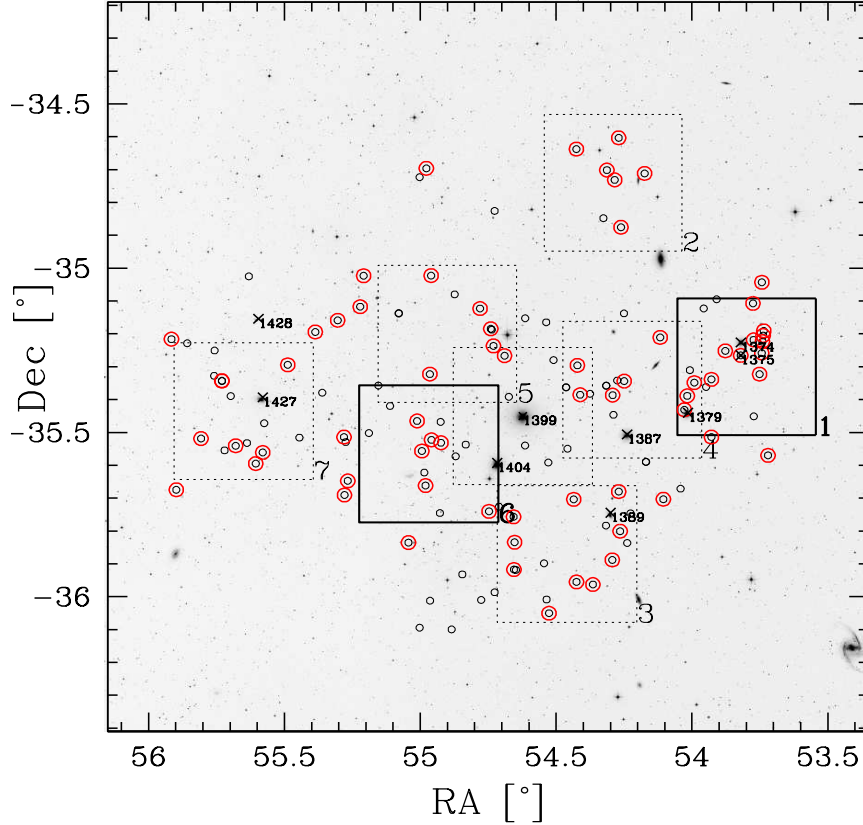


Figure 3.4: Map showing the location of the fields observed in our survey Fornax Deep Field. The two fields No. 1 and 6 indicated by solid lines were observed in October 2003, the rest of the fields in December 2004. The small circles mark all dE candidates with unconfirmed cluster membership observed with the WFCCD imaging from see Sect. 3.2. The ones marked by an additional larger circle are those bright enough ($M_V \leq -11$ mag) that a clear SBF signal should be detected if they were cluster members, see Sect. 2.5. The underlying image of the Fornax cluster comes from the DSS (<http://stdata.stsci.edu/dss/>). Note that due to their intrinsic low surface brightness, none of the dE candidates is visible in this image. Some of the dE candidates marked within the solid squares were finally not observed due to vignetting or the gaps between the different chips.

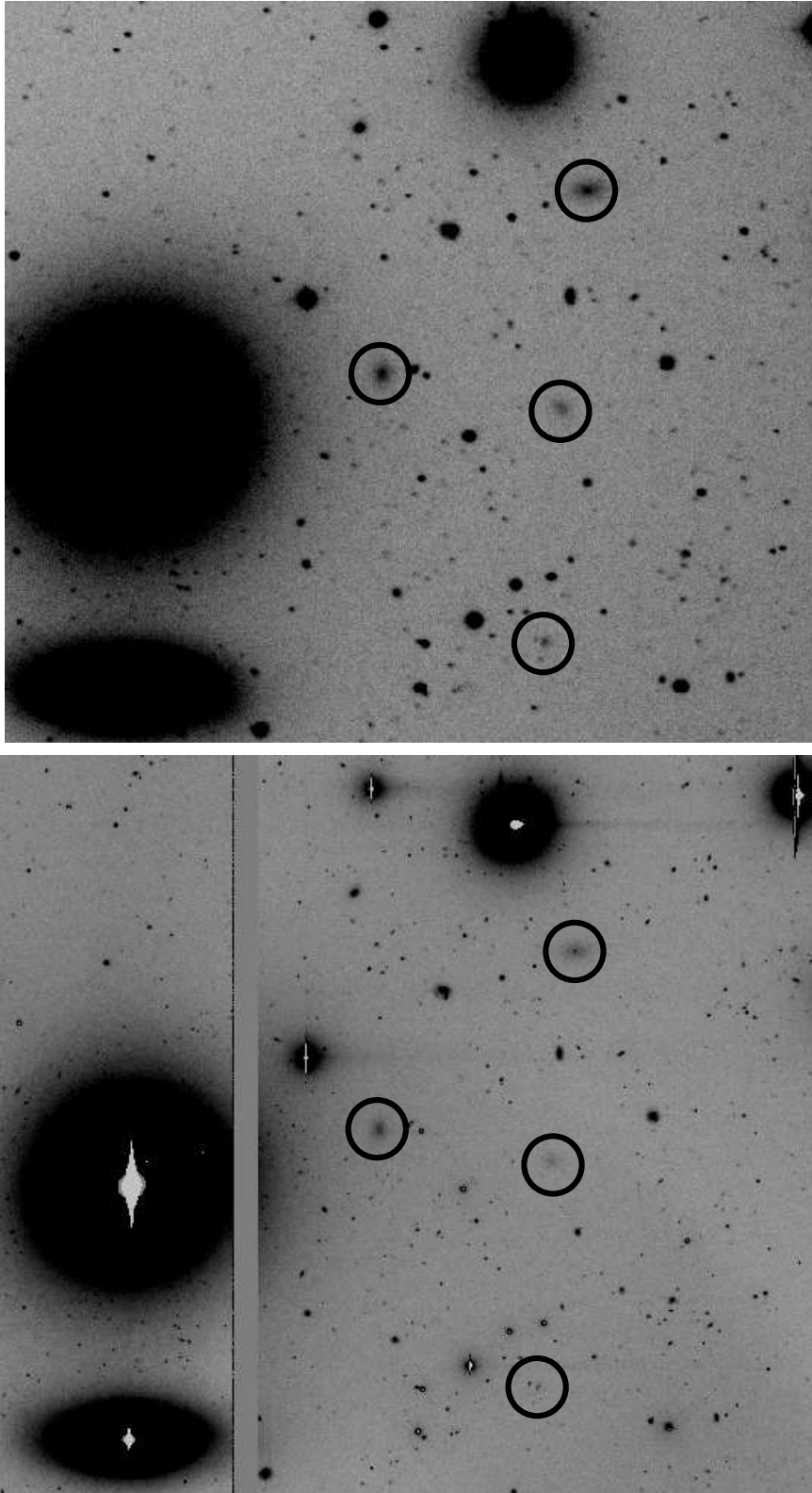


Figure 3.5: Comparison between a $6\times 6'$ image excerpt from the WFCCD data (top, see Sect. 3.2) and an excerpt from the IMACS data dealt with in Sect. 3.3. The circles indicate from left to right the 4 galaxies FCC 145, LSB 6-3, FCC 141 and FCC 140, see Sect. 3.3.2 and Figs. 3.7 to 3.12 for further details.

SBF measurement

The SBF measurement procedure was similar to that outlined in Sect. 2.4.2 for the simulated data. However, as we now deal with real data, several observational effects have to be taken into account.

The first one is that a not negligible fraction of fluctuation arises from the sky background, namely by undetected background sources and instrumental effects like fringing or large scale sky level gradients. This contribution is estimated by measuring the fluctuations in three different blank image sections close to the investigated galaxy. The second change with respect to the simulations is that now the distortion of the PSF power spectrum that is caused from multiplying the fluctuation image with a mask image is corrected for. Another additional fluctuation contribution comes from undetected globular clusters associated with the galaxy. However, this contribution is negligibly small because at the Fornax cluster distance the globular cluster luminosity function (GCLF) is mapped about 1.5 mag fainter than its turnover magnitude, given that the 50% completeness magnitude for point source detection is about $I = 24.5$ mag (as determined from artificial star experiments). Assuming equation (15) from Blakeslee & Tonry ([1995]), a turn-over magnitude (TOM) of $M_I = -8.46$ mag and Gaussian width $\sigma = 1.2$ mag for the GCLF (Kundu & Whitmore [2001]), a Fornax distance modulus of 31.4 mag, a galaxy colour $(V - I)_0 = 1.0$ and a specific frequency of its GC system $S_N := \frac{N_{GC}}{10^{-0.4*(M_V+15)}} = 5$ (Miller et al. [1998]), the relative fluctuation contribution of the undetected GCs to the SBF signal is 0.0035 mag.

These are the relevant measurement steps for determining the SBF magnitude, see also Sect. 2.4.2:

1. Model mean galaxy light with ELLIPSE using a sigma clipping algorithm to disregard contaminating sources, subtract the model.
2. Detect and subtract remaining contaminating objects from original image.
3. Model mean galaxy light on the cleaned image.
4. Subtract model of original image.
5. Divide resulting image by square root of the model, cut out circular portion with radius typically 20-25 pixel ($4 - 5''$), corresponding to about 8 seeing disk diameters.
6. Mask out contaminating sources like foreground stars and background galaxies.
7. Calculate the power spectrum (PS) of the cleaned image.
8. Calculate the PS of the sky background in three different blank image sections close to the investigated galaxy. Normalise these fluctuations by dividing these blank images by the mean galaxy intensity in the region where SBF are measured. Subtract this normalised background PS ΔBG from the PS of the SBF image.
9. Obtain the azimuthal average of the resulting PS.
10. Fit function of the form

$$P(k) = E(k) \times P_0 + P_1 \tag{3.1}$$

to the result. Here, $E(k) = PSF(k) \otimes W(k)$ with $W(k)$ the PS of the mask used to excise contaminating sources and restrict the measurement area. $PSF(k)$ is the undistorted power spectrum of the PSF. Using $E(k)$ instead of $PSF(k)$ implicitly corrects for the power spectrum damping at low wavenumbers that is caused by the convolution of the undistorted $PSF(k)$ with the power spectrum of the mask, see also Sect. 2.5 and Fig. 3.6.

11. Obtain the desired observable \overline{m}_I from

$$\overline{m}_I = -2.5 * \log(P_0) + ZP_I - A_I - \Delta k \quad (3.2)$$

A_I is the foreground absorption, $\Delta k = z \times 7$ the k-correction for SBF in the I -band (Tonry et al. [1997]).

The colour $(V - I)_0$ of each galaxy was determined in the region where SBF were measured. We compared the $(V - I)_0$ estimates from the IMACS data with the values derived in Sect. 3.2 from the WFCCD imaging to get a feeling for their absolute accuracy. When restricting to those 17 galaxies with $\mu_0(V) < 25 \text{ mag/arcsec}^2$, we find that the mean difference in $(V - I)_0$ between the IMACS and WFCCD data is $\Delta(V - I) = 0.062 \text{ mag}$ with a scatter of 0.10 mag. This difference is significant at the 2.4σ level and hints at the possible presence of small residual zero-point uncertainties in the photometric calibrations of both data sets. Another reason could be systematic biases in the sky background determination for both data sets. However, we re-did the curve of growth analysis for several galaxies in the WFCCD and IMACS data and found no significant indications for an systematically offset background adjustment in one of the filters. A possible reason for a bias in the zeropoint calibration could be the significant distortion of the PSF in the outer regions of both the WFCCD and IMACS data. However, for both data sets we measured the instrumental magnitudes within very large apertures, and even if distortion effects play some role, they should be only of minor importance for colour determinations. During the first night of observation with IMACS, the $(V - I)$ zero-point varied by less than 0.03 mag during the night, given an upper limit on the effect of possible non-photometric conditions as a reason for the colour offset.

To take this colour shift into account, we adopt the $(V - I)$ colour derived in IMACS minus a global correction of 0.031 mag, half of the difference between the IMACS and WFCCD colours. This global absolute colour uncertainty translates into a lower limit of 7 % (0.14 mag) absolute distance accuracy, assuming the empirically calibrated slope 4.5 of the $(V - I)_0 - \overline{M}_I$ relation.

With the galaxy colour $(V - I)_0$ at hand and keeping its systematic absolute accuracy limit of 0.03 mag in mind, \overline{M}_I was then derived using equation (1.10), yielding the distance modulus $(m - M)_{SBF}$. The distance error had two major, equally important, contributions: uncertainty in $(V - I)_0$ and P_0 . The measurement uncertainty in $(V - I)_0$ was estimated from the uncertainty in the sky-background determination. It was about 0.07 mag, which is relatively large due to the low surface brightness of the galaxies investigated, and translates into a 0.30 mag distance uncertainty. The error of P_0 was estimated in two ways: based on the Monte Carlo simulations presented in Sect. 2.5,

yielding an error of about 0.30 mag, and from the scatter of the fitted values for P_0 when subtracting the three different sky background power spectra. The maximum of both error estimates was adopted as error in P_0 .

3.3.2 Discussion I: Improved constraints on the Fornax galaxy luminosity function

Thumbnails of all 24 candidate Fornax dEs imaged in FDF are shown in Figs. 3.7 to 3.13. This sample consists of all dE candidates listed as probable cluster members from the Fornax Cluster Catalog (FCC, Ferguson & Sandage [1988]) plus the newly found, fainter, low surface brightness (LSB) candidate dEs from Sect. 3.2. Their photometric properties are summarized in Table 3.2. Fig. 3.14 illustrates their location in the magnitude-surface brightness plane.

The galaxies for which SBF could be detected are shown in Figs. 3.7 to 3.10. In these plots, also the SBF-measurement steps are illustrated. The results of the SBF measurements are listed in Table 3.3. Also indicated are the PS contribution from the background ΔBG and the amount of power spectrum damping $\Delta_{mask} = 2.5 \times \log(\frac{E(k=0)}{PSF(k=0)})$ (see Fig. 3.6). In Table 3.3, both the canonical S/N as well as the modified S/N^* as defined in Sect. 2.4.2 is given. For most galaxies, $S/N^* > S/N$, because the seeing was better than about $0.75''$ for these galaxies. Due to the significant distortion at the image borders, some galaxies with rather bad seeing have $S/N^* < S/N$.

As can be seen from Table 3.3 and also Fig. 3.22, all the galaxies with an SBF signal detected have SBF-distances roughly corresponding to the Fornax cluster. Due to the significant redshift gap behind Fornax (Drinkwater et al. [2001a], Hilker et al. [1999]) and its high galaxy density (Ferguson & Sandage [1988]), we classify all these galaxies as cluster members. In Fig. 3.10 we also show galaxy LSB 1-3 whose SBF signal was classified as too weak to be considered a confidential detection. For that galaxy, the S/N of the SBF measurement is around unity and the amount of background fluctuation is about two times as high as the fluctuations in the galaxy. Apart from this galaxy, which was excluded from the SBF-sample, there are two galaxies that we include in the SBF-sample but which have rather low S/N and S/N^* : FCC 154 and LSB 5-6 (see Table 3.3). Furthermore, galaxy FCC 160 has a quite high S/N of about 9, but a rather low modified S/N^* (see Sect. 2), due to bad seeing. The effect of ex- or including these objects into the distance sample is discussed in Sect. 3.3.3. As they morphologically clearly classify as cluster members, ex- or inclusion in the SBF-sample has no effect on the shape of the LF but only on the distance estimate to Fornax. Note that no galaxy that was bright enough to detect a strong SBF signal at the Fornax distance turned out to have a non-measurable signal. This rules out a significant contamination of our sample by giant LSB background galaxies.

The limiting galaxy magnitude for reliably detecting an SBF signal in our data is about $V \simeq 20$ ($M_V \simeq -11.5$) mag (see Fig. 3.14). This is marginally brighter than the limit of $M_V = -11$ mag based upon which the integration time for the imaging was chosen.

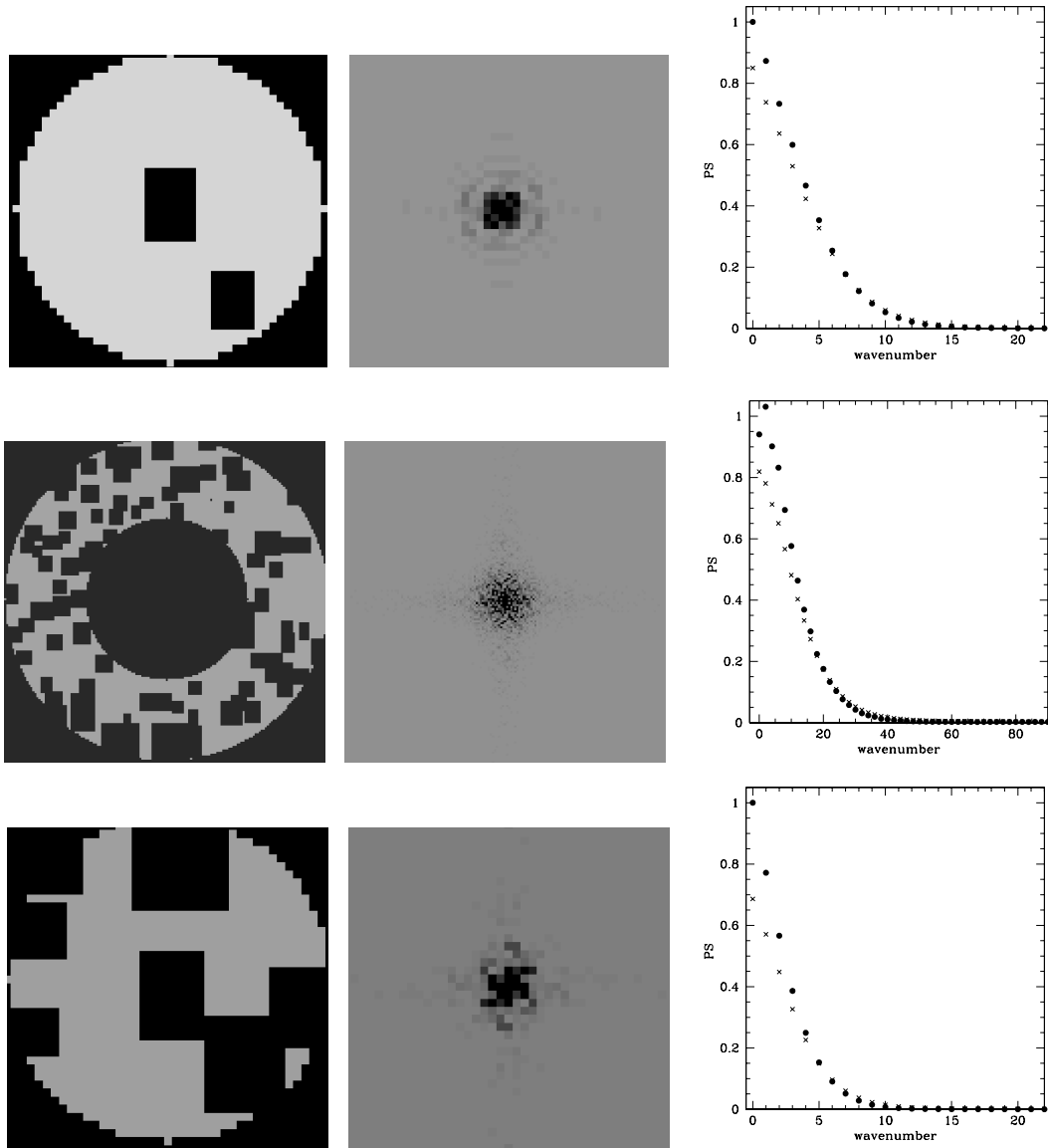


Figure 3.6: Plots illustrating the power spectrum damping effect of the window function used to excize contaminating sources and restrict the measurement area. *Upper panels:* The dE FCC 140 in the Fornax cluster with $M_V \simeq -13$ mag. *Middle panels:* NGC 3311 in the Hydra cluster (see Sect. 4). *Lower panels:* dE 258 in Hydra with $M_V \simeq -15.5$ mag (see Sect. 4). *Left panels:* mask image used to blend out contaminating sources and restrict the measurement region. Masked regions are black. *Middle panels:* Power spectrum of the mask on the left image. *Right panels:* Filled circles: power spectrum of an isolated star, normalised to unity at wavenumber $k=0$. Crosses: the same power spectrum convolved with the mask power spectrum from the middle panels.

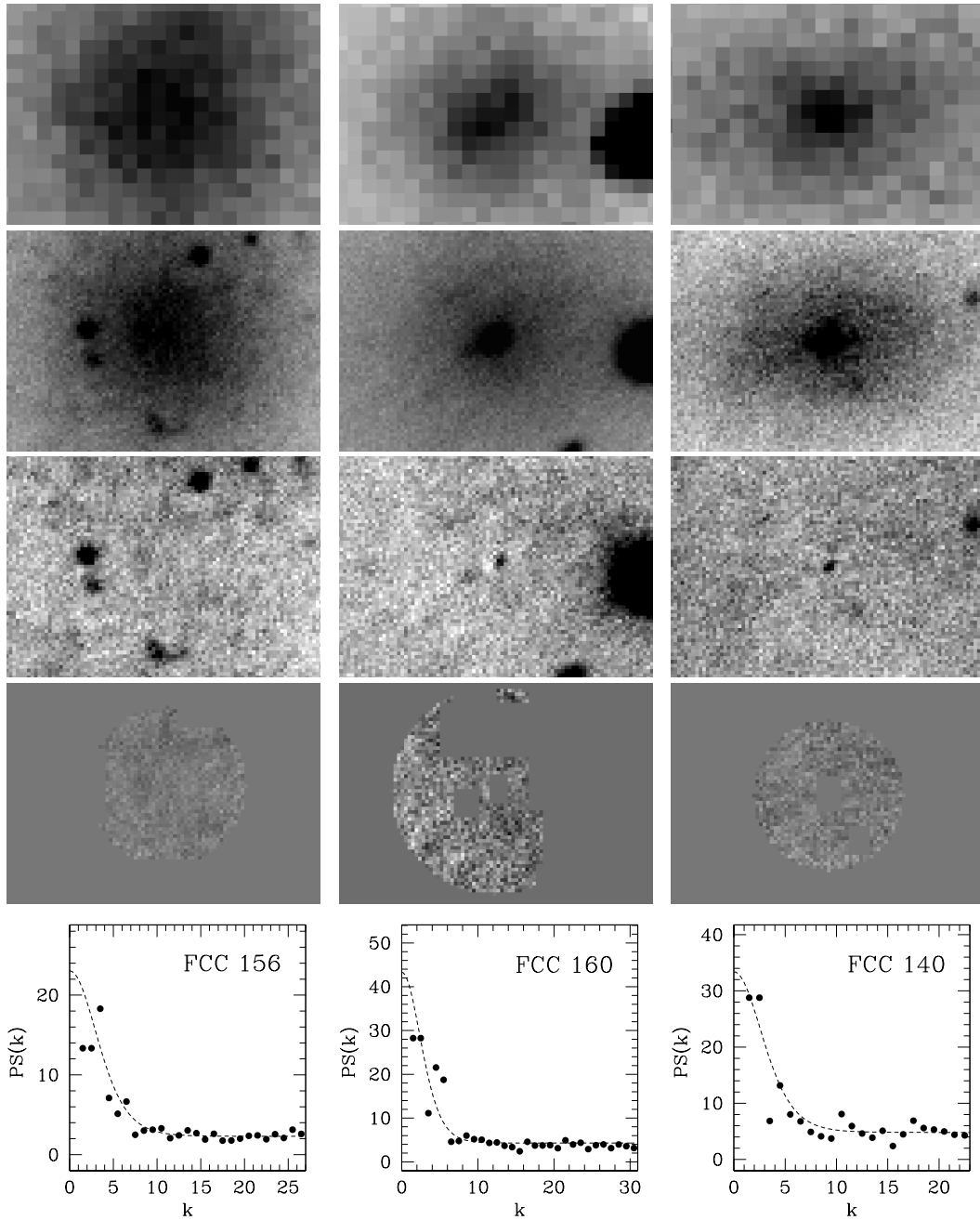


Figure 3.7: Thumbnail images of those galaxies for which cluster membership is confirmed via detecting SBF. Galaxies are ordered by decreasing V -band magnitude from left to right. The galaxy number is indicated in the power spectrum plot in the last line. First line are thumbnails from the WFCCD data of width $15''$, second line thumbnails from the IMACS data of the same size. Third line is the model subtracted IMACS image, 4th line the SBF image. The 5th line gives the azimuthally averaged power spectrum of the SBF image and its fit indicated by a dashed line. The normalised power spectrum of the sky background has already been subtracted, see Sect. 3.3.1. The given power spectrum therefore corresponds to the pure stellar fluctuations in the galaxy itself.

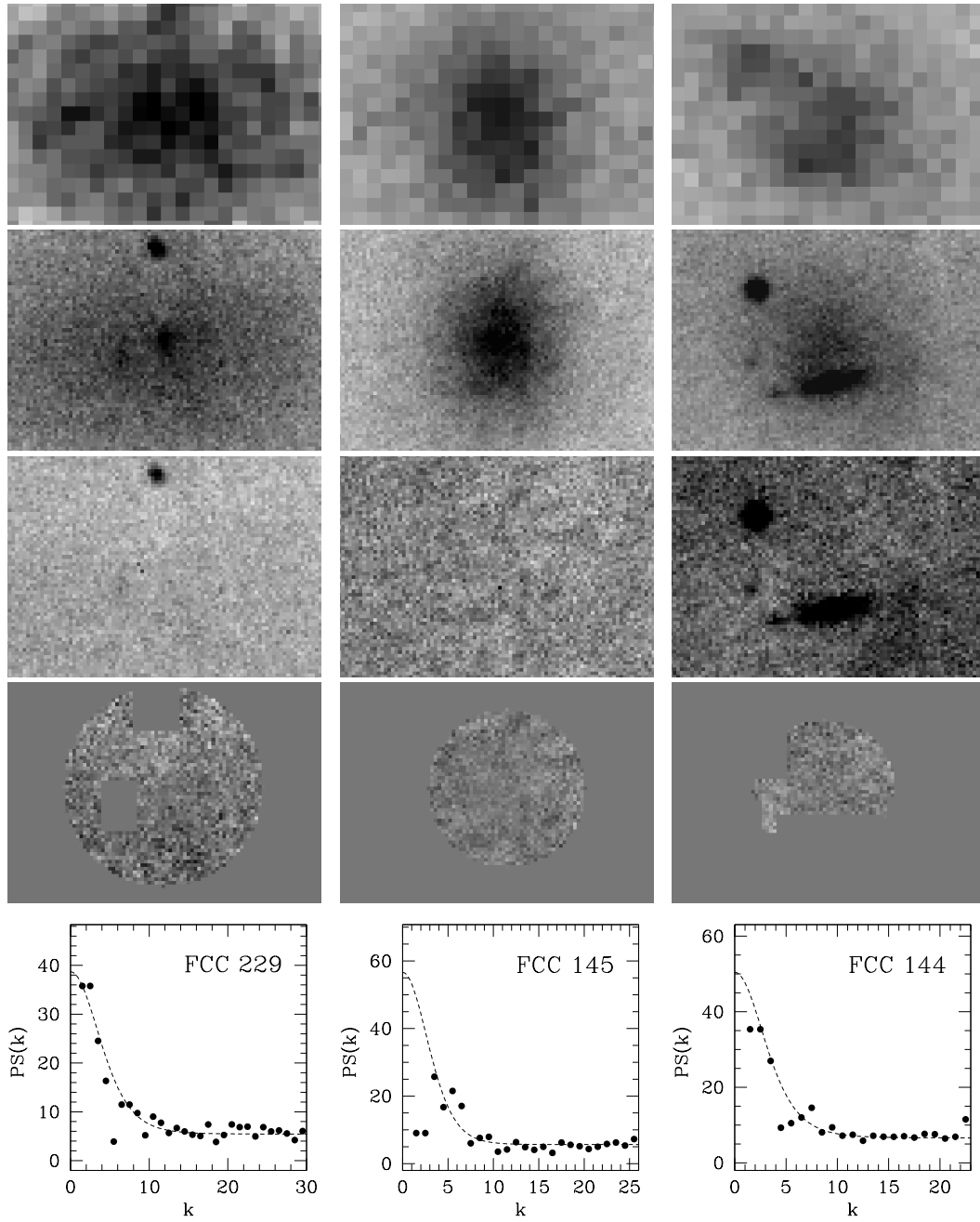


Figure 3.8: Members from SBF, continued from Fig. 3.7.

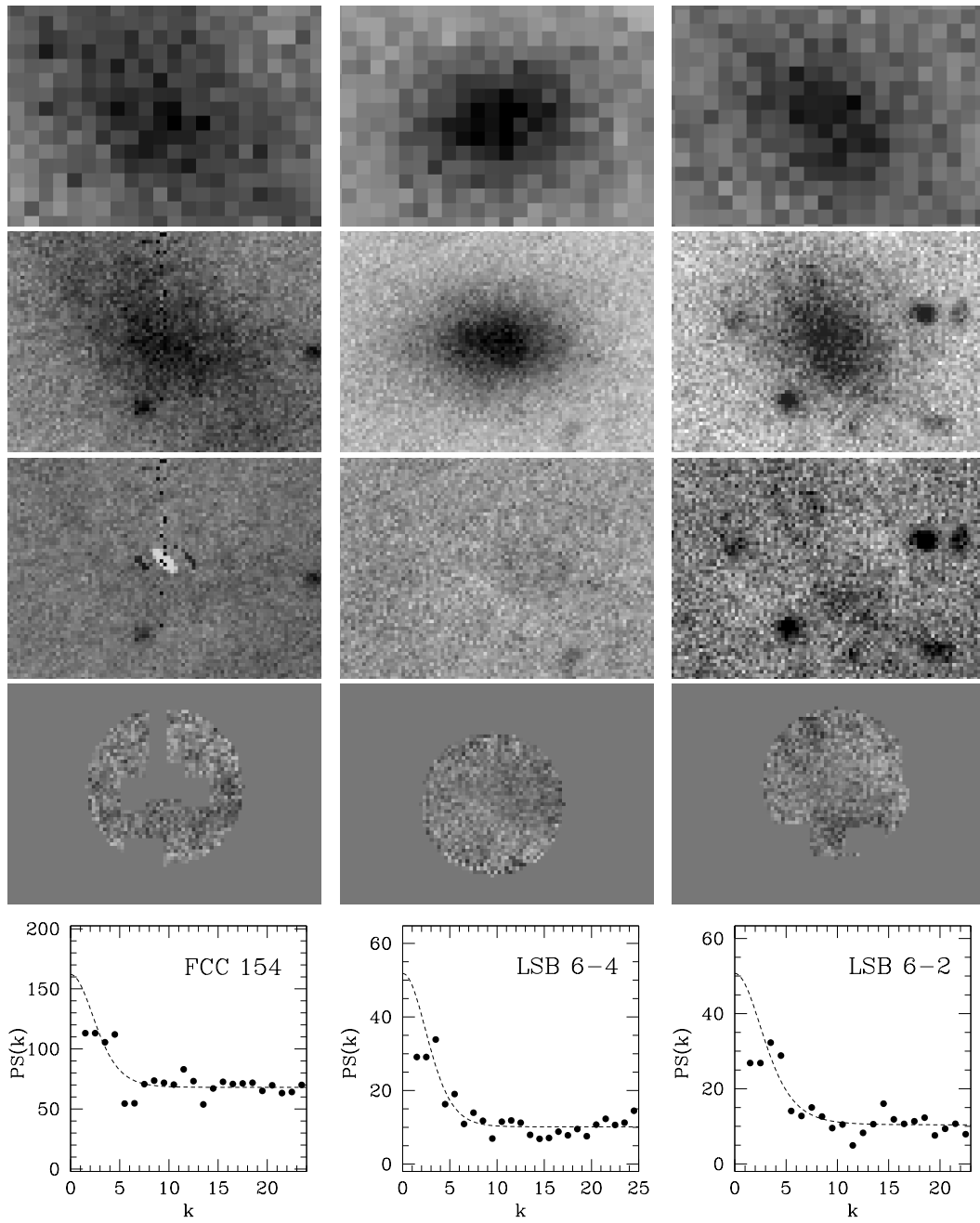


Figure 3.9: Members from SBF, continued from Fig. 3.8.

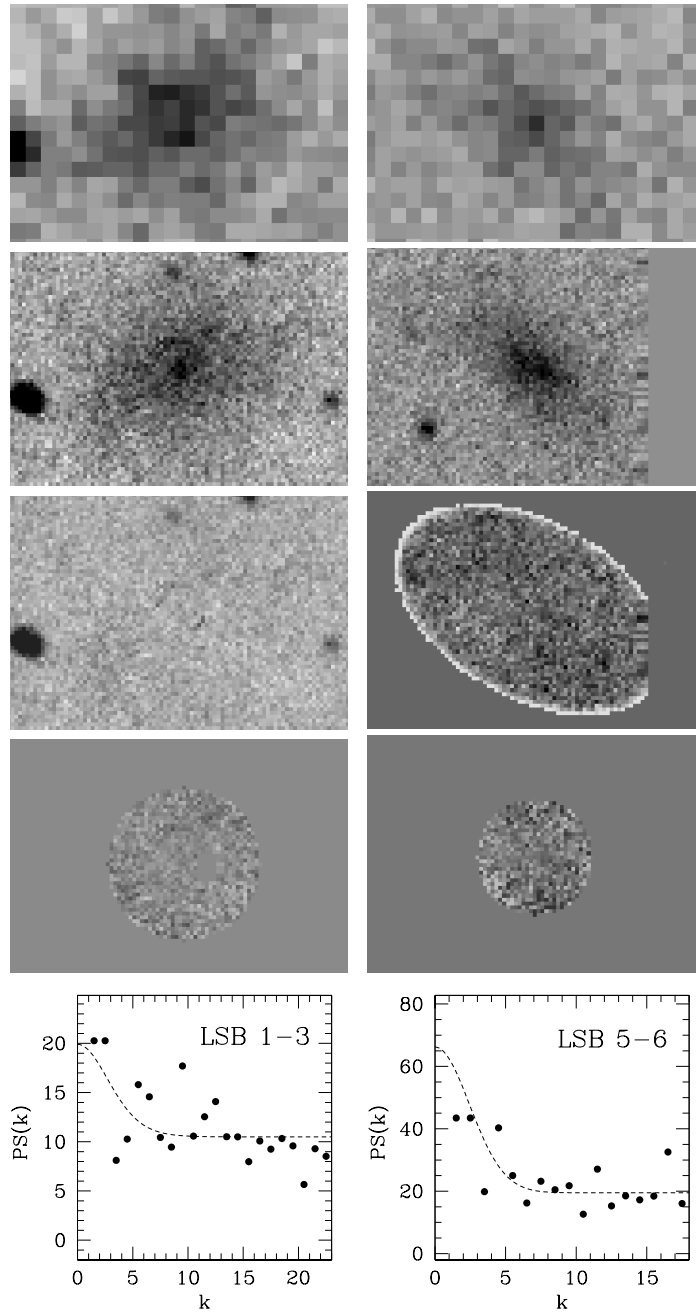


Figure 3.10: Members from SBF, continued from Fig. 3.9. Galaxy 1-3 has a somewhat distorted fluctuation power spectrum, a very low S/N of about 1.0 and a very large contribution from background fluctuations of $\Delta BG = 0.56$ mag. It is classified as a member from morphology (see Fig 3.11) and is not included into the SBF distance estimate to Fornax. Including it in this plot is done to illustrate a limiting case for SBF measurement. In contrast, galaxy 5-6 is included in the SBF distance set. It has a somewhat better shaped power spectrum, a higher S/N of 2.4 and a smaller ΔBG of 0.40 mag (see also Table 3.3).

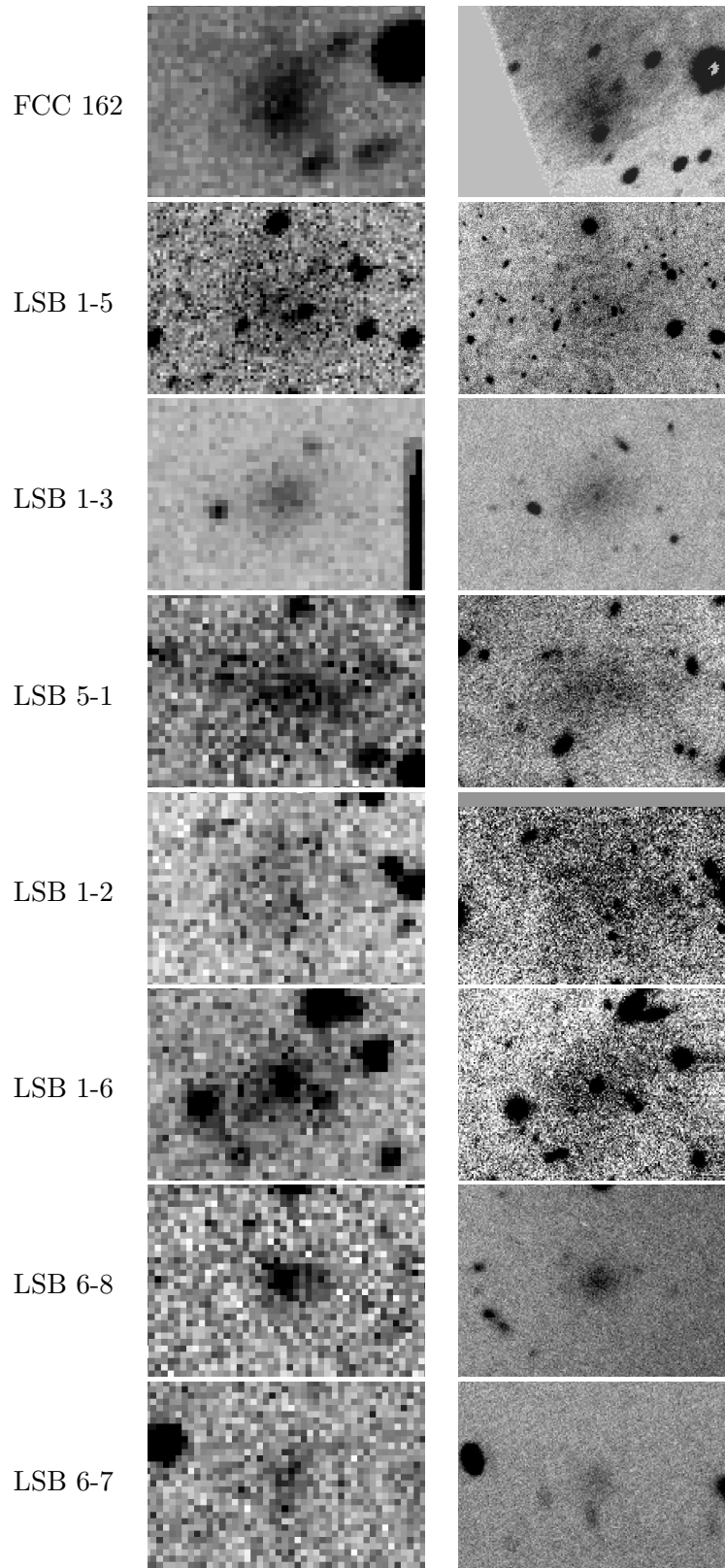


Figure 3.11: Probable members from morphology, ordered by decreasing V -band luminosity from top to bottom. Left WFCCD, Right IMACS. Image width is $30''$ except for the second galaxy from the top where it is $1'$. The two times larger image width with respect to the thumbnails in Figs. 3.7 to 3.10 was chosen because the galaxies plotted here have a lower contrast against the sky background.

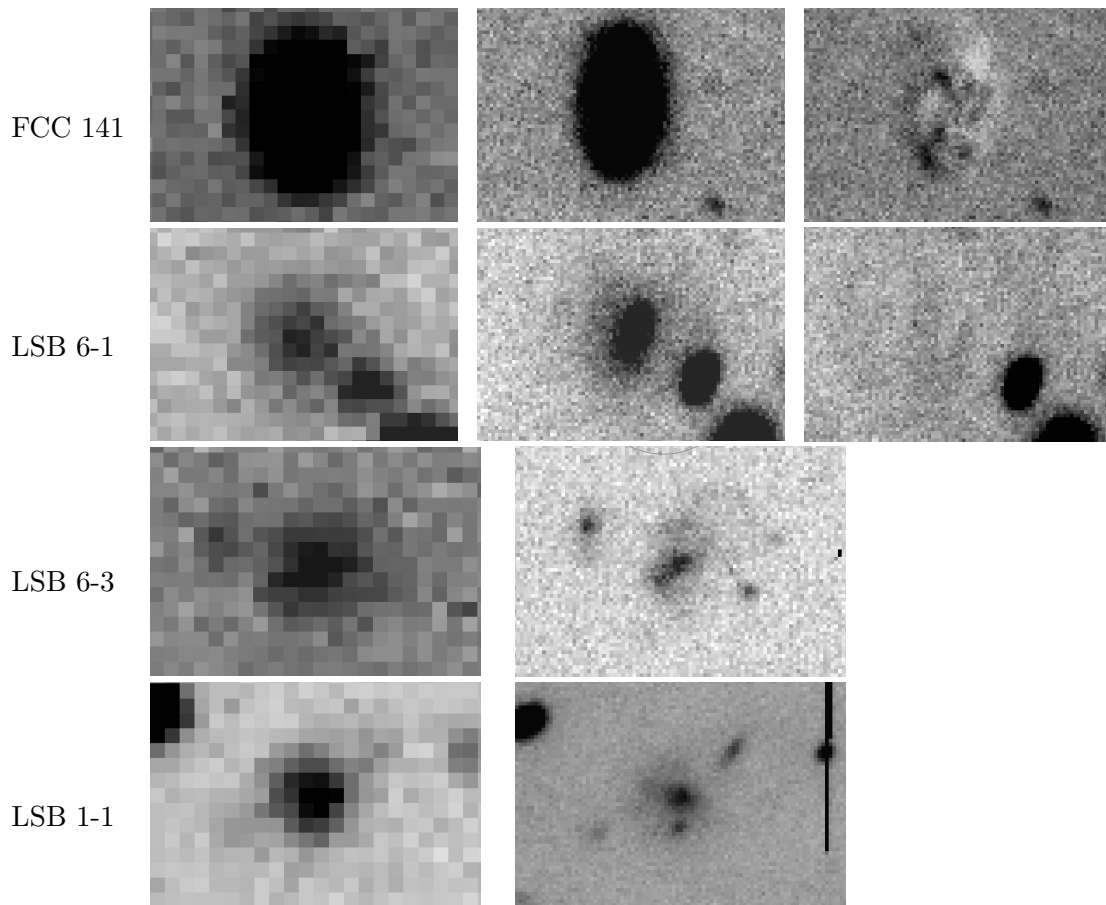


Figure 3.12: Probable background galaxies from morphology. Left panels show images from WFCCD, right panels IMACS images. For the first two galaxies, the IMACS image plus a model subtraction of that image is shown.

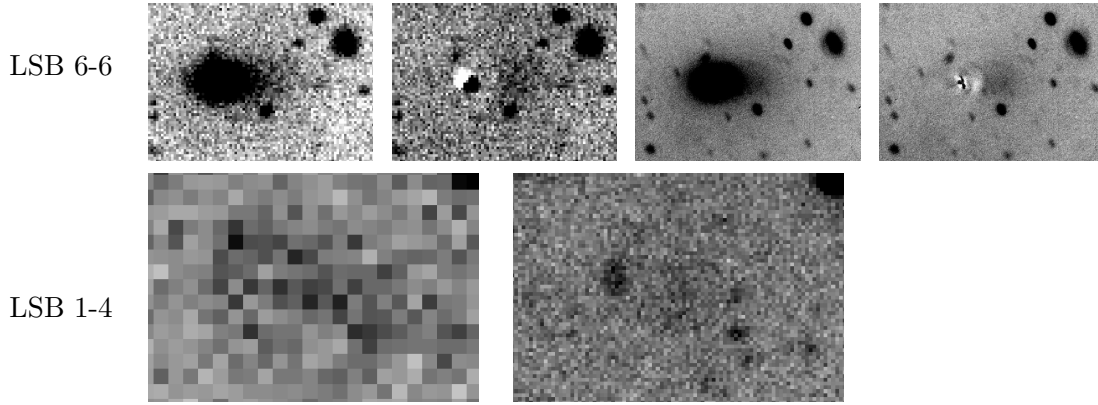


Figure 3.13: Galaxies with uncertain cluster membership assignment. *Top panels:* LSB 6-6, which is located in close projection to a much brighter galaxy and might therefore also be some kind of tidal debris. From left to right: WFCCD image; WFCCD image minus model of the bright companion; IMACS image; IMACS image minus model. *Bottom panels:* LSB 1-4, which at least partially is resolved into several point sources in the IMACS data, putting into question its classification as dE candidate.

There are two reasons for that:

1. The assumed seeing for these calculations was $0.6''$, which was realised for only a couple of dE candidates due to the strongly varying image quality over the field of view. The mean seeing for the 10 dEs with SBF measurement was $0.74''$, it ranged between 0.62 and $1.19''$. Consulting formula (2.6), which gives the limiting absolute magnitude for SBF measurements for observing conditions different to those used for the simulations in Sect. 2, a change in seeing from 0.60 to $0.74''$ corresponds to a 0.6 mag brighter limiting magnitude. This corresponds quite well to the difference between the beforehand calculated and the finally achieved limiting magnitude. We can therefore state that the predictions for SBF measurements deduced from the simulations in Sect. 2, expressed in formula (2.6), prove to be realistic.
2. For the simulations the contribution of background fluctuations ΔBG to the SBF-signal was regarded as negligibly small. While this is almost true for VLT-FORS images (see Sect. 4), the significant CCD-fringing and smaller scale flat-field gradients in the IMACS I -band images cause an increase in the sky noise which slightly decreases the achievable S/N in SBF measurements.

The galaxies for which no SBF signal could be detected but which morphologically classify as probable cluster members are shown in Fig. 3.11. In the IMACS images, these galaxies maintain their smooth morphology and low surface brightness based upon which they were selected as possible cluster members from the lower resolution WFCCD imaging. The brightest of those galaxies, galaxy FCC 162, falls into the magnitude-surface brightness regime where SBF measurement is still possible (see Fig. 3.14). However,

it lies in very close projection to the Fornax cluster giant NGC 1379 (see Fig. 3.4). A proper SBF measurement for FCC 162 is inhibited for two reasons: first, additional photon shot noise introduced by NGC 1379's light reduces the S/N of the SBF; second, FCC 162 is located close to the borders of the IMACS FOV where the image quality is already quite deteriorated.

There are two limiting cases of galaxies that deviate slightly more than 2σ from the magnitude-surface brightness relation, namely the very extended galaxy LSB1-5 (2nd from top in Fig. 3.11) and the rather small galaxy LSB6-7 (first from bottom in Fig. 3.11). We classify both of them as probable cluster members, since their morphological appearance is very similar to the rest of the morphologically confirmed cluster members.

Fig. 3.12 shows thumbnails of the 4 dE candidates from Sect. 3.2 which, based on our higher resolution IMACS imaging, reveal themselves as probable background galaxies. The reasons to classify them as probable background were the following: galaxy FCC 141 is of very high surface brightness and shows clear spiral features after subtracting an elliptical galaxy light model; galaxy 6-1, although not showing spiral-like residuals after model subtraction, also has a typical high surface brightness inner region and an outer low surface brightness like that of spiral galaxies. Galaxies 6-3 and 1-1 appear like interacting background spirals. All these 4 galaxies look clearly more compact than the much dimmer and more extended low surface brightness dEs from Figs. 3.7 to 3.11. This is also reflected in Fig. 3.14: all 4 probable background galaxies lie close to or beyond the bright 2σ limit of the surface-brightness magnitude relation. Indeed, galaxies 6-1 and 6-3 are those for which the re-measurement of μ_0 with the better resolution IMACS data (see Fig. 3.20) yields the largest “jump” towards higher μ_0 . A further reason for classifying spiral/interacting galaxies as background is that the overall dwarf galaxy population in the central Fornax cluster is vastly dominated by early-type galaxies, with only very few dIrrs known (Ferguson & Sandage [1988]).

There are two galaxies (LSB6-6 and LSB1-4) whose classification remains unclear (see Fig. 3.13). LSB6-6 lies in very close projection to a much brighter galaxy and might therefore not be a proper galaxy but rather tidal debris. Major parts of galaxy LSB1-4 are resolved into point sources and leave only a very dim and small low surface brightness part in between them.

Equipped with the revised cluster membership assignments, we can go *in medias res*: how does the Fornax early-type galaxy luminosity function change, when we take into account the SBF cluster membership assignments and improved morphological classifications? 10 of the 24 imaged galaxies could be confirmed as cluster members from SBF, further 8 are confirmed from morphology, 4 are classified as background and two have an uncertain classification. That is, of those 22 galaxies with robust classifications, 18 are probable members and 4 probable background. This already indicates that both the cluster membership classification from the FCC (Ferguson & Sandage [1988]) as the selection of fainter dE candidates from Sect. 3.2 was quite effective. To be more quantitative, Fig. 3.15 shows both the original luminosity function from Fig. 3.3 and a

Galnr.	Ra[2000]	Dec[2000]	V	$\mu_0(V)$	$(V - I)_0$	Membership flag
FCC 156	3:35:42.8	35:20:18.1	16.79	23.12	1.001	1
FCC 160	3:36:04.2	35:23:19.2	17.24	23.20	1.057	1
FCC 140	3:34:56.6	35:11:27.0	18.42	23.51	0.931	1
FCC 229	3:39:55.3	35:39:42.3	18.54	24.20	0.832	1
FCC 145	3:35:05.6	35:13:05.8	18.88	23.47	0.957	1
FCC 141	3:34:57.1	35:12:18.0	18.98	21.70	0.769	4
FCC 162	3:36:06.7	35:25:52.0	19.02	24.11	0.580	3
FCC 144	3:35:00.3	35:19:21.8	19.07	23.83	1.054	1
FCC 154	3:35:30.5	35:15:06.4	19.07	24.27	0.871	1
LSB1-5	3:40:02.8	35:27:54.5	19.50	26.26	0.961	3
LSB6-4	3:35:57.9	35:20:53.8	19.87	23.80	0.929	1
LSB6-2	3:34:57.7	35:13:23.8	20.01	24.15	0.988	1
LSB6-1	3:35:06.1	35:06:25.2	20.30	24.10	0.799	4
LSB6-6	3:35:49.6	35:07:21.9	20.38	25.90	1.661	5
LSB1-3	3:39:41.6	35:31:53.3	20.44	24.57	0.624	3
LSB5-1	3:35:05.4	35:27:03.4	20.51	25.64	0.981	3
LSB6-3	3:34:58.4	35:15:29.7	20.52	23.80	0.739	4
LSB1-2	3:39:28.8	35:34:21.9	20.61	26.39	0.791	3
LSB1-6	3:39:56.4	35:37:19.8	20.65	25.10	0.751	3
LSB1-1	3:39:58.5	35:33:23.8	20.93	23.21	0.759	4
LSB5-6	3:35:47.4	35:21:41.6	21.52	24.91	0.960	1
LSB6-8	3:36:01.8	35:18:38.0	21.69	25.47	1.061	3
LSB1-4	3:39:42.0	35:28:05.0	22.00	25.93	0.661	5
LSB6-7	3:35:38.2	35:05:41.2	22.20	24.95	0.709	3

Table 3.2: Table showing the coordinates and photometric properties of all candidate dEs imaged in the first night of FDF. Galaxy designations FCC and the running numbers are from the Fornax cluster catalog (Ferguson & Sandage [1988]). Designations LSBx-x refer to dE candidates discovered for the first time in Sect. 3.2. The first index refers to the field number of the WFCCD images, the second index is the running number of the LSB candidates in that image. For $\mu_0(V) < 25$ mag/arcsec², $(V - I)_0$ is the value derived from the IMACS photometry minus 0.031 mag, which is half the difference between the mean $(V - I)_0$ colour from IMACS and the WFCCD data (see Sect. 3.3.3 for further details). For $\mu_0(V) > 25$ mag/arcsec², $(V - I)_0$ is the value derived from the WFCCD photometry plus 0.031 mag.

The membership flags mean the following: 1 member from SBF; 2 non-member from SBF; 3 member from morphology; 4 non-member from morphology; 5 uncertain classification. Note that no galaxy has flag=2, indicating that the WFCCD sample has a negligible contamination by giant LSB background galaxies.

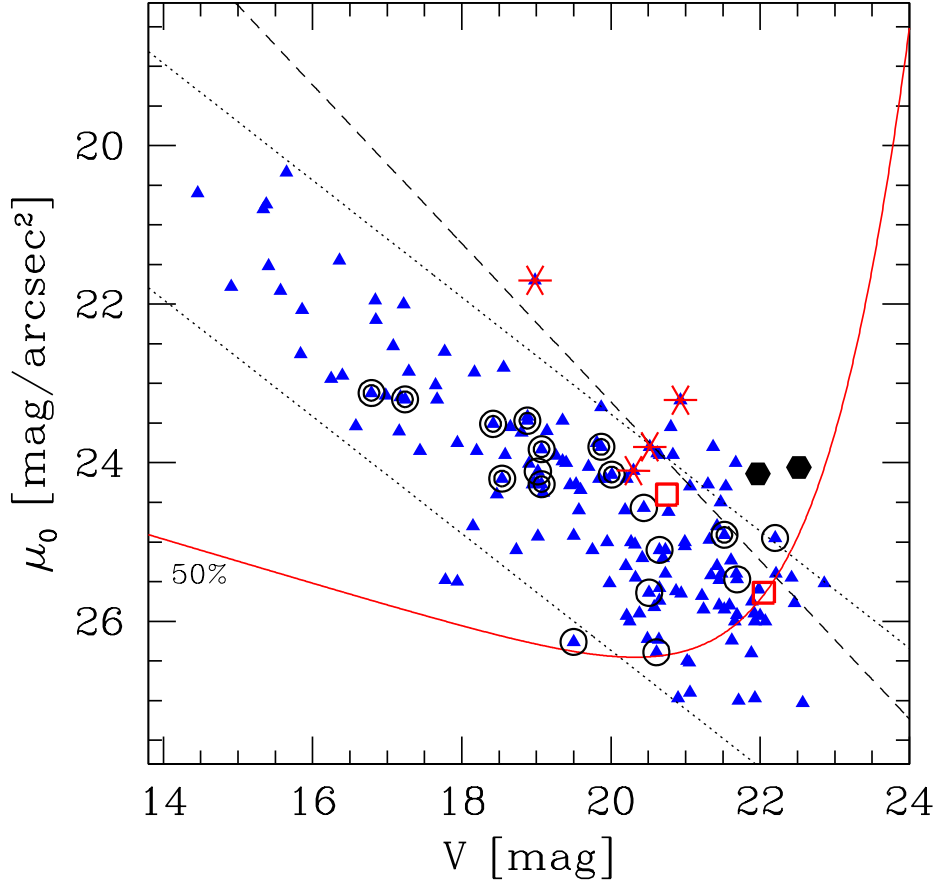


Figure 3.14: Magnitude-surface brightness plot of the same objects as in Fig. 3.2, now with the candidates re-observed in Fornax Deep Field marked according to their revised cluster membership assignment: Double circles indicate cluster membership confirmed with SBF. Single circles indicate probable cluster member from morphology. Small asterisks: probable background galaxy from morphology. The two open squares mark the location of the two morphologically selected dE candidates in a WFCCD background field. The two filled hexagons mark the two additional cluster member candidates found from the IMACS imaging.

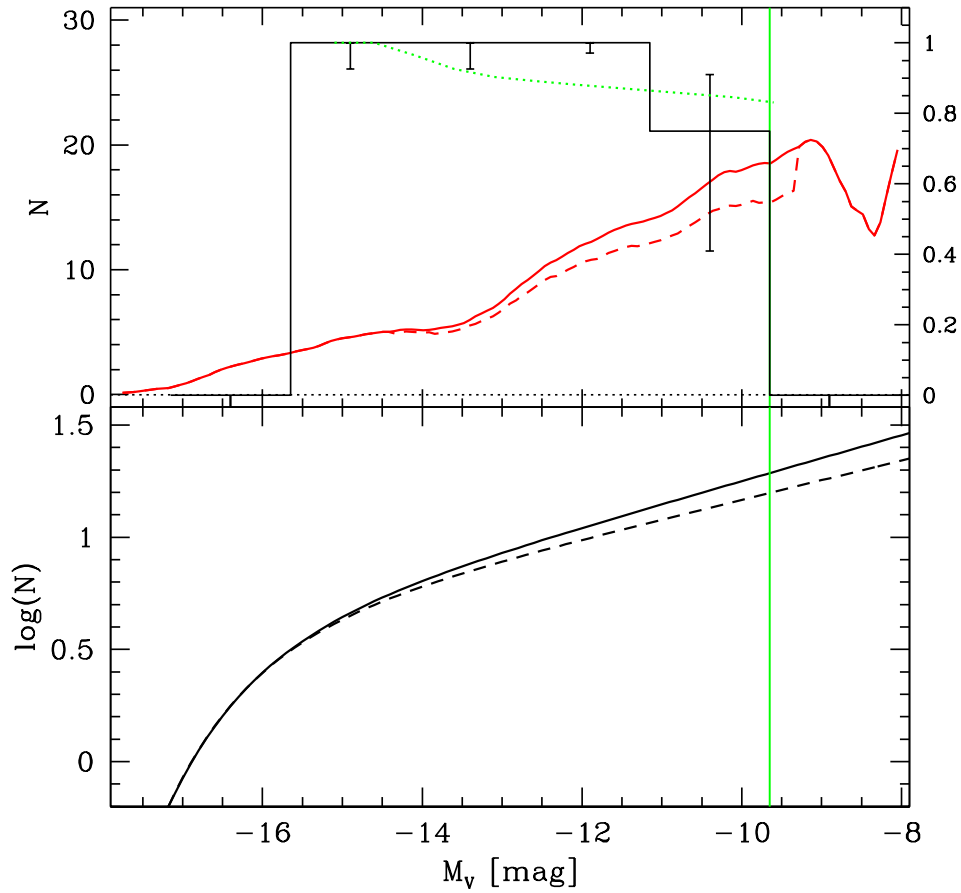


Figure 3.15: Plot of the original galaxy luminosity functions (LFs) from Fig. 3.3 and the corrected LFs derived in Fornax Deep Field (FDF). *Upper panel:* The original LF in linear scale is indicated in the incompleteness corrected, binning independent representation as a solid line. For this LF, only galaxies within 2σ of the magnitude-surface brightness and colour-magnitude relations (see Figs. 3.2 and 3.1) are considered. The histogram shows the ratio of the number of dE candidates with probable cluster membership from SBF and morphology to that of all candidates observed in the FDF that fall within 2σ of the magnitude-surface brightness and colour-magnitude relation, see Fig. 3.14. The histogram error bars are 1σ and were calculated according to Gehrels ([1986]). The dotted line is a binning independent kernel estimator of 1.5 mag kernel width. The dashed line is the product of the solid and dotted line, i.e. the corrected LF, taking into account the SBF cluster membership confirmations and improved morphological classifications of FDF. *Lower panel:* The solid black line is a 1-component Schechter function fit to the original LF in logarithmic scale, having slope $\alpha = -1.102$. The dashed black line is a fit to the corrected LF, having slope $\alpha = -1.087$.

Galaxy	Δ_{mask}	S/N	S/N^*	Δ_{BG}	\bar{m}_I	$(m - M)_{\text{SBF}}$	d [Mpc]
FCC 156	0.093	9.8	15.4	0.188	29.60 ± 0.31	32.00 ± 0.44	25.1 ± 5.2
FCC 160	0.182	9.1	2.3	0.502	28.96 ± 0.31	31.12 ± 0.44	16.7 ± 3.4
FCC 140	0.139	6.0	9.0	0.225	29.37 ± 0.34	32.10 ± 0.46	26.3 ± 5.7
FCC 229	0.113	4.5	8.5	0.387	29.09 ± 0.30	32.27 ± 0.43	28.4 ± 5.7
FCC 145	0.034	9.9	13.6	0.243	28.65 ± 0.29	31.26 ± 0.43	17.9 ± 3.6
FCC 154	0.310	1.4	1.1	0.409	28.03 ± 0.34	31.03 ± 0.46	16.0 ± 3.5
FCC 144	0.175	7.5	10.4	0.271	28.72 ± 0.30	30.90 ± 0.44	15.1 ± 3.1
LSB6-4	0.071	5.2	3.6	0.278	28.69 ± 0.35	31.42 ± 0.47	19.2 ± 4.2
LSB6-2	0.126	5.5	8.6	0.292	28.68 ± 0.30	31.29 ± 0.43	18.1 ± 3.7
LSB5-6	0.142	2.4	2.6	0.403	28.76 ± 0.32	31.36 ± 0.45	18.7 ± 3.9
						31.52 ± 0.15	20.2 ± 1.50

Table 3.3: Table showing the results of the SBF measurements for the 10 dEs with measurable SBF signal. Units are magnitudes except for the last column, S/N and S/N^* . $(m - M)_{\text{SBF}}$ gives the distance modulus when adopting relation (1.10) for all galaxies. S/N^* as defined in Sect. 2.4.2.

new, corrected one. This corrected luminosity function is derived from the original one by multiplying with the ratio of the number of cluster members from SBF and morphology to the number of all galaxies with robust classification. For this calculation only those galaxies are included which fall within 2σ of the colour-magnitude and magnitude-surface brightness relation of all candidates (see Fig. 3.14). This excludes two galaxies which are probable background and two which are probable members from morphology. The slope of the corrected luminosity function is $\alpha = -1.087$, only marginally different to the value of $\alpha = -1.102$ derived in Sect. 3.2. Including the 4 galaxies outside the 2σ limits changes the slope by less than 0.01. We therefore can confirm the very shallow faint end slope for the Fornax galaxy luminosity function derived on pure morphological grounds.

Looking at Fig. 3.15, there might be a small trend in the sense that towards fainter magnitudes the number of misclassifications from the WFCCD data increases, although number counts are certainly too low for more definite statements. Analysis of the second part of FDF will allow a more detailed assessment of this possibility. Such an effect would be consistent with the fact that for galaxies with sizes close to the resolution limit of the WFCCD, details like spiral arms or tidal features can only be detected from our IMACS imaging.

Search for previously undetected dSph candidates

It still remains to be checked whether in our new IMACS image data we can detect more dSph candidates that remained hidden below the resolution limit in the WFCCD data. This is motivated by the fact that several Local Group dSphs would fall close to the resolution limit of the WFCCD data at the Fornax cluster distance (see Fig. 3.2),

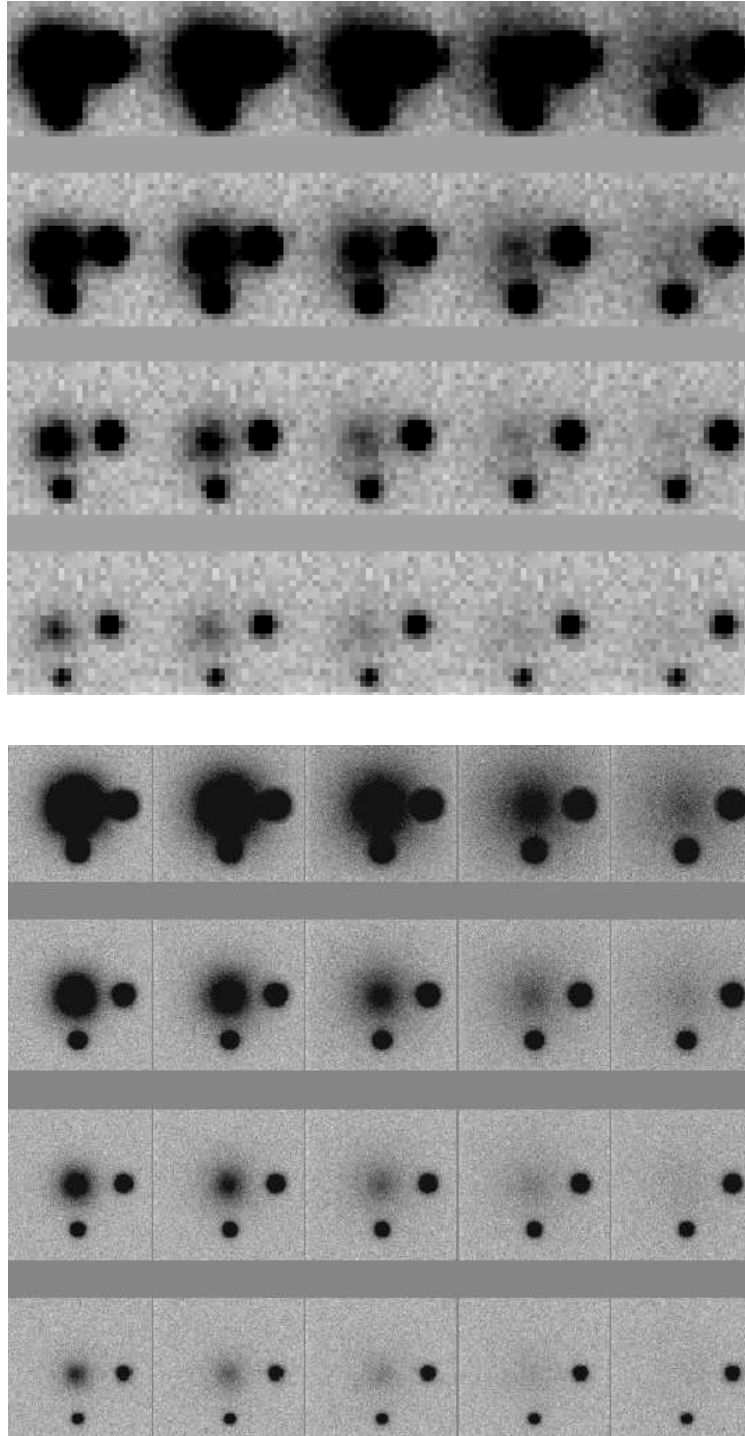


Figure 3.16: Comparison of simulated typical dE candidates at the Fornax cluster distance with an unresolved source of same luminosity (right to the galaxy) and an unresolved source 1 mag fainter (below the galaxy). *Top image*: WFCCD pixel scale of $0.8''/\text{pixel}$ and a seeing of $1.8''$. *Bottom image*: IMACS pixel scale of $0.2''/\text{pixel}$ and a seeing of $0.75''$. In each line, the dEs have the same absolute luminosity, going from $M_V = -13$ mag to $M_V = -10$ mag from top to bottom. From left to right, they have decreasing central surface brightnesses μ_0 as follows: 3σ brighter than μ_0 from the magnitude surface-brightness relation in Fig. 3.2 ($1\sigma = 0.75$ mag), 2σ brighter, 1σ brighter, identical brightness, 1σ fainter.

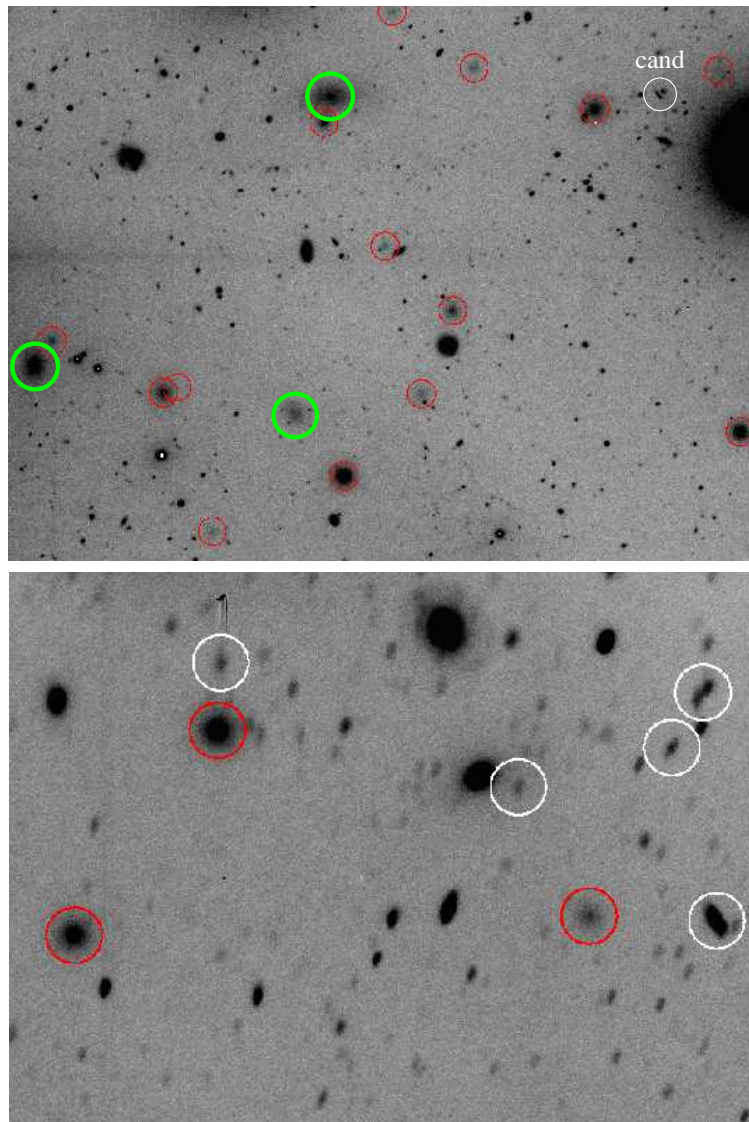


Figure 3.17: *Top panel:* IMACS image excerpt with simulated dEs close to the resolution limit of the WFCCD data indicated as small red circles. Large green circles indicate from left to right the galaxies FCC 145, LSB 6-2, and FCC 140, all confirmed as cluster members via SBF. The white circle indicates the only real source that shares the parameter space of the simulated dEs in the SExtractor output catalog. *Bottom panel:* Another IMACS image excerpt, now without candidate cluster members. Again, small white circles indicate real sources that share the parameter space of the simulated dEs, while red circles are simulated ones. Clearly, the fainter candidates are misclassified due to distortion of the PSF while the brighter ones appear like background spirals.

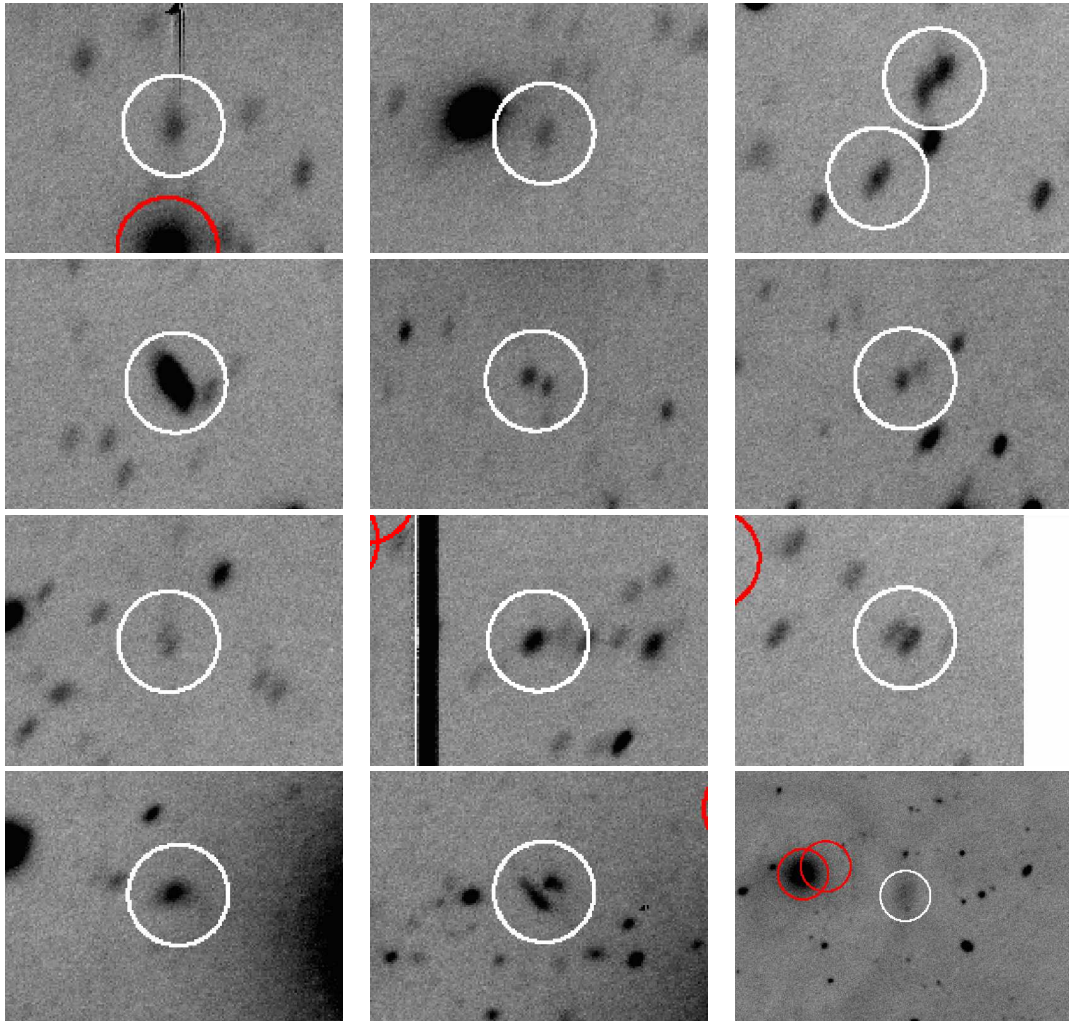


Figure 3.18: Thumbnails of all 13 sources in the entire chip from Fig. 3.17 that share the SExtractor detection parameters of the simulated dEs close to the WFCCD resolution limit. Image width is $30''$. Note the significant image distortion due to which unresolved sources appear elliptical. The candidate in the lower right thumbnail is a false detection due to fringing and telescope structure reflection, as can be recognized from the ring-like structure extending towards the left. This last thumbnail has a width of $1'$.

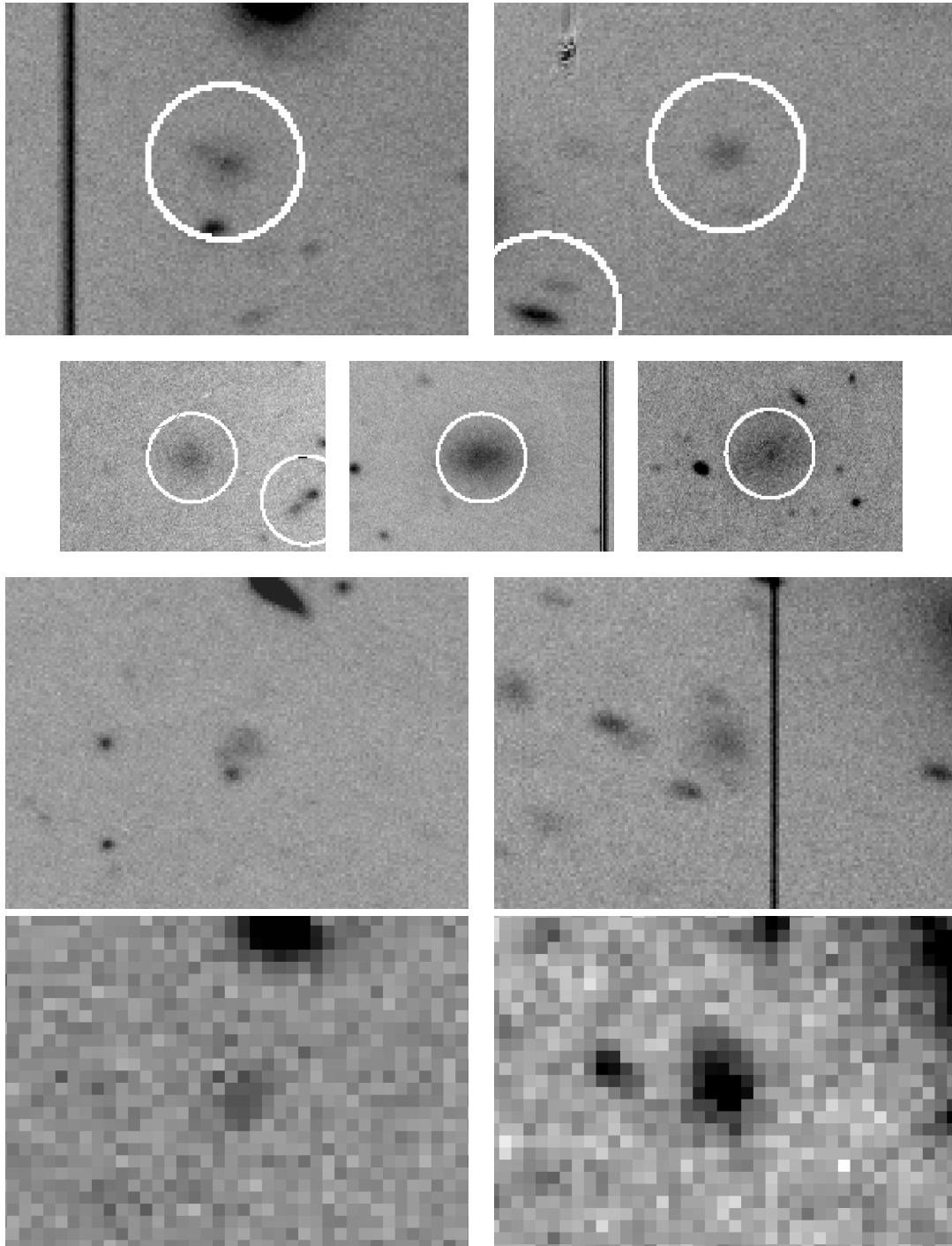


Figure 3.19: Thumbnails of $30''$ width from the IMACS data, showing the seven possible cluster member candidates that were selected by visual inspection from those sources that share the SExtractor detection parameters of the simulated dEs close to the WFCCD resolution limit, see also Figs. 3.17 and 3.18. *Top row*: two candidates outside the FOV of the WFCCD data. *Second row from top*: three candidates that already were selected as candidates in the WFCCD data, namely galaxies LSB 6-8, 6-4 and 1-3. *Second row from bottom*: Two candidates inside the WFCCD-FOV that had previously not been classified as cluster member candidates. *Bottom row*: WFCCD-thumbnails of the two above candidates.

towards brighter μ_0 at about the 3σ limit of the Fornax mag- μ relation. The FWHM of the WFCCD images was between 1.5 and $2''$, corresponding to 140 to 180 pc at the Fornax cluster distance. Local Group dSphs have effective diameters between 150 pc and 1kpc (Mateo [1998]), such that if placed at the Fornax cluster distance, several of them would have gone undetected in the WFCCD images. However, we note that the Fornax dEs are on average significantly larger than their Local Group counterparts of the same luminosity. The magnitude-surface brightness (mag- μ) relation of the Fornax dEs is shifted about 1.1 mag towards higher surface brightness compared to that of the Local Group (see Figs. 3.2 and 3.14). This is not a selection effect caused by missing dE candidates close to the WFCCD resolution limit: only two of the more than 20 Local Group dSphs are at the low surface brightness part of the Fornax mag- μ relation. When restricting the WFCCD data points to $M_V < -11$ mag, which is the approximate magnitude limit fainter than which the mag- μ region of the smallest WFCCD dE candidates overlaps with spurious SExtractor detections of extended sources (see Figs. 3.2 and 3.14), the offset between the LG and Fornax mag- μ relation still is 1.1 mag. If shifting the LG dwarf data points 1.1 mag towards lower surface brightness, none of them falls beyond the 2σ limit of the Fornax dEs. Therefore, it appears unlikely that from the WFCCD data we are missing a substantial number of candidate dEs close to the WFCCD resolution limit.

Fig. 3.16 shows a comparison of typical dE/dSph candidates with unresolved sources, assuming two different pixel scales and resolutions: first the WFCCD pixel scale of $0.8''/\text{pixel}$ and a seeing of $1.8''$, second the IMACS pixel scale of $0.2''$ pixel and $0.75''$ seeing. For the WFCCD data, dEs with $M_V \simeq -10$ to -11 mag and 3σ brighter in $\mu_0(V)$ than the mean magnitude-surface brightness relation are still quite well distinguishable from unresolved point sources. Nevertheless, for the IMACS data a clearer distinction can be made.

In order to search in the IMACS images for dE candidates with sizes close to the WFCCD resolution limit, three steps were performed:

1. Put simulated dEs in the range $-9 > M_V > -12.5$ mag and between 1 and 3σ brighter in μ_0 than the mean magnitude-surface brightness relation onto the IMACS images.
2. Run SExtractor on these images to recover the simulated dEs.
3. Search for objects in the SExtractor output catalog that share the same range of FWHM, peak surface brightness, total luminosity, star-class, Kron-radius and isophotal area than the simulated dEs.
4. Perform a visual inspection of those objects.

Fig. 3.17 shows image excerpts from the IMACS data, indicating some confirmed cluster dEs, simulated dEs close to the WFCCD resolution limit and those real sources that share the parameter space of the simulated dEs with $M_V \leq -10$ mag in the SExtractor output catalog. The restriction to $M_V \leq -10$ mag is made as this is the approximate 50% completeness limit of the WFCCD data. Not only in this excerpt, but in the entire chip (Figs. 3.17 and 3.18), one morphologically rejects each of the 13 sources that

share the simulated dE parameters. The resolved ones clearly resemble compact high surface brightness background galaxies. In the other cases, the significant distortion of the PSF near the image borders makes the candidates appear galaxian, although their shape is identical to the PSF of nearby stars/unresolved sources. In Fig. 3.19, we show thumbnails of those seven sources from the entire two imaged fields that morphologically resemble the simulated small dEs. Two of them were outside the image limits of the WFCCD data and hence are not included in the revision of the WFCCD-LF. Further three of these candidates were already known, while two of them have been imaged in the WFCCD data but had not previously been classified as candidates. The location in the mag- μ plane of these two new candidate cluster members already imaged in the WFCCD data is indicated in Fig. 3.14. Both are fainter than $M_V = -10$ mag and close to the 50% completeness limit of the WFCCD data. When recalculating α with those two now candidates, the result is $\alpha = -1.096$, indistinguishable from the values previously calculated without taking into account the new detections. The simulations and subsequent check of the SExtractor output catalog hence show that the detection of LG dSph candidates in Fornax as done with the WFCCD images was already complete to about 90%, given that only two new possible candidates are added to the 18 probable cluster members imaged in the FDF.

A final check is to compare the location in the mag- μ plane from the WFCCD photometry to that with the FDF photometry. For those galaxies with $\mu_0(V) < 25$ mag/arcsec², such a comparison is shown in Fig. 3.20. The mean difference in total apparent magnitude V between the FDF and WFCCD value is 0.033 ± 0.066 mag, a good agreement. For $\mu_0(V)$, there is a significant difference of -0.17 ± 0.07 mag between the FDF and WFCCD value in the sense that the FDF central surface brightness is higher. This effect occurs most strongly for the smaller dE candidates, as their size approaches the resolution limit of the WFCCD data, and hence any central intensity rise is smeared out by the PSF. This rise in central surface brightness reduces slightly the average difference in $\mu_0(V)$ between Local Group dwarfs and their Fornax cluster counterparts to about 0.9 mag, but it leaves the qualitative statement from above unchanged. Note that the two largest increases in $\mu_0(V)$ between WFCCD and FDF data are for objects that we reclassify as probable background in this section, a finding which supports these morphological classification.

We summarize this section as follows:

1. SBF-cluster memberships and improved morphological classifications do not change the shallow faint end slope of $\alpha \simeq -1.1$ derived from the WFCCD-data by more than 0.02. This is due to the fact that only a small fraction (10-20%) of the previously classified probable cluster members turn out to be probable background.
2. The search for additional dE candidates in the IMACS images possibly overlooked in the WFCCD-data yields only two new candidates, i.e. an increase of about 10%. Also when taking these sources into account, α changes by less than 0.02.
3. The dEs in Fornax are on average slightly larger than the Local Group dSphs.

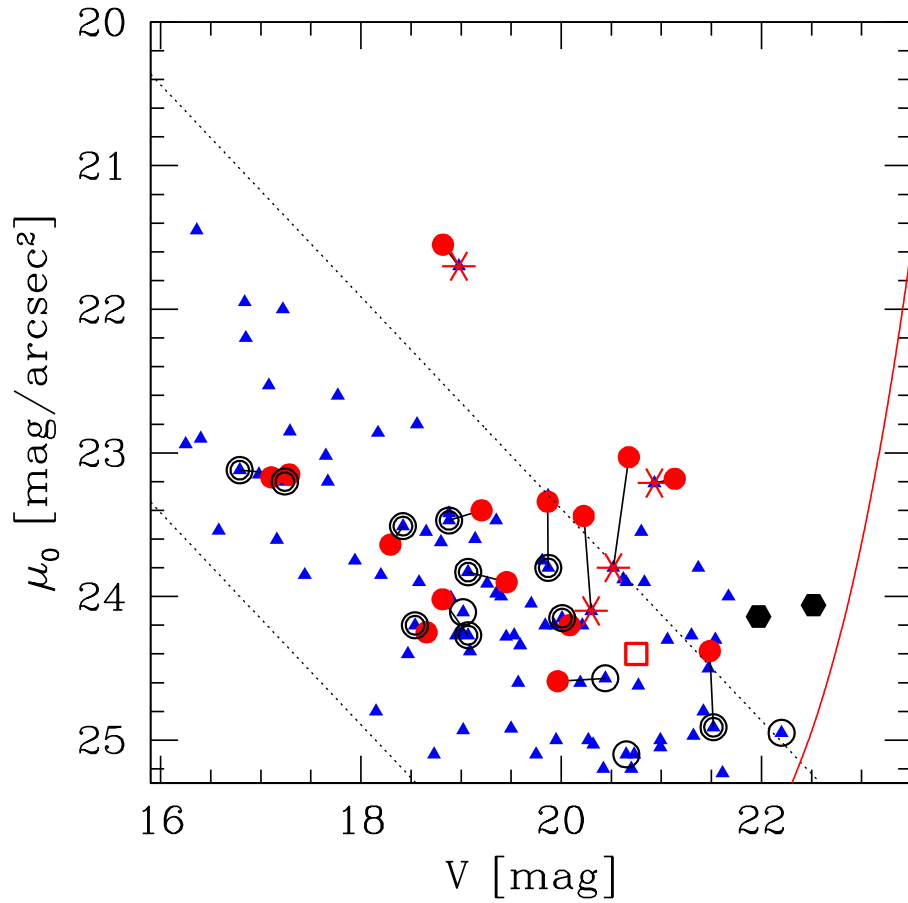


Figure 3.20: Excerpt of the mag- μ plane shown in Fig. 3.14, with the mag- μ values obtained in our follow-up project Fornax Deep Field (FDF) indicated as filled circles. Lines connect the original WFCCD measurements with those from FDF.

The very shallow faint end slope of the early-type galaxy luminosity function in Fornax is in sharp contradiction to the much steeper faint end slope predicted for the mass function of Λ CDM cold dark matter halos (e.g. Kauffman et al. [2000], Moore et al. [1999]). Similar shallow faint end slopes for other galaxy clusters have been found (cf. references in Sect. 2.2). The problem of too shallow faint end slopes for the galaxy luminosity function compared to the CDM mass function is also known as the “substructure crisis” of CDM cosmology. Possible reasons to explain that discrepancy include the accretion scenario (e.g. Hilker et al. [1999b], Côté et al. [1998]), where dwarf galaxies that fall into the cluster centres are tidally disrupted, hence contributing to form the extended cD halos of the most massive cluster galaxies. Another possibility is that the low surface brightness dSphs that we see nowadays originate from tidally stripped originally much more massive dark matter halos (Stoehr et al. [2002], Kravtsov et al. [2004]), while the lower mass halos have not been able to maintain condensed gas to form stars. However, Kazantzidis et al. ([2004]) argue that observed velocity dispersion profiles of Local Group dSph exclude such very massive progenitors, indicating that tidal stripping can only be a part of the picture. Much discussion is going on in this field of research, as it touches the fundamentals of the widely accepted “concordance” cosmological model. The contribution of this chapter is to clearly and unambiguously point out the contradiction between the observed faint end slope of the galaxy luminosity function and the predictions from Λ CDM for the mass function and total number of low-mass dark matter halos.

The fact that Fornax dEs are on average larger than their Local Group counterparts may be explained within a scenario where tidal forces disrupt the smallest and least massive dEs more effectively in a dense environment like the Fornax cluster than in the Local Group (e.g. Hilker et al. ([1999b])). Note that Caldwell & Armandroff ([2000]) report on the discovery of a large population of very low surface brightness dEs in the Virgo cluster whose sizes are on average much larger than that of the Local Group dSphs. This is in agreement with our findings. One possible explanation is that in denser environments, low mass dark matter halos have been able to form stars before reionization (e.g. Ricotti et al. [2002], Dekel & Woo [2003]) more rapidly and efficiently than in low density regions. However, this would also imply that the galaxy luminosity function in Fornax should be somewhat steeper than in the Local Group, which is not supported by our findings. Also, Grebel & Gallagher ([2004]) note that the star formation histories of Local Group dwarfs are very diverse, which is difficult to reconcile with a suppression of star formation after reionization in low mass galaxies. One concern about the comparison between the Local Group and other environments is that the Local Group sample may be highly incomplete. Large and very low surface brightness galaxies ($\mu_0 \simeq 26$ mag/arcsec²) are extremely difficult to detect against the foreground contamination of Milky Way stars. The latest discoveries of more and more faint dSphs (e.g. Armandroff et al. [1999], Whiting et al. [1999], Zucker et al. [2004]) raise the question of how complete the Local Group sample is.

3.3.3 Discussion II: Distance to the Fornax cluster and SBF calibration at blue colours

With the SBF measurements from the previous section, one can in principle make a distance estimate to the Fornax cluster. However, the empirically calibrated colour range for SBF measurements in $(V - I)_0$ has a blue limit of about $(V - I)_0 \simeq 1.05$ mag (Tonry et al. [1997]). Almost all of the dEs from Table 3.3 are clearly bluer than this limit. Furthermore, the SBF survey by Tonry did not include any dwarf galaxy into their calibration. Therefore, it is not clear whether relation (1.10) holds for all the dEs investigated here. In Sect. 2.3 it has been shown that some theoretical models indeed predict a weaker dependence of \overline{M}_I on $(V - I)_0$ for blue colours. This was the reason for adopting relation (2.1) instead of the original relation (1.10) from Tonry et al. ([1997]) for the SBF simulations of galaxies with $(V - I)_0 < 1.0$ in Sect. 2.4. The Worthey models ([1994]) using Padova isochrones predict such a flattening only for the very old and metal-poor stellar populations, while predicting a continuation of relation (1.10) for younger populations. The same holds for the models of Blakeslee et al. ([2001]). The models by Liu et al. ([2000]) and also the original models by Worthey et al. ([1994]) predict a flattening for metal-poor populations of old *and* intermediate ages and do not predict a continuation of relation (1.10). See also Fig. 2.1.

As a consequence, instead of a distance estimate to Fornax, the present measurements can, in combination with literature Fornax cluster distance estimates, be used for a calibration attempt of \overline{M}_I at blue colours, with the additional aim to distinguish between competing stellar population models. We use the value of $(m - M) = 31.41 \pm 0.07$ mag derived in the HST-Key project (Ferrarese et al. [2000]) from Cepheid distances as a reference. Note that the uncertainty of this value is statistical only, as the SBF-distance scale is calibrated using Cepheid distances (Tonry et al. [1997]). As a further control criterion, we demand that there is no significant correlation between the colour $(V - I)_0$ and $(m - M)$. As we aim at a calibration of \overline{M}_I with $(V - I)_0$, this is a very fundamental requirement. Finally, we also require that the scatter of the distance values around their mean are not significantly smaller than the mean single measurement uncertainty. This is to avoid that we over-correct spurious trends in our data.

Fig. 3.21 shows the dependence of the apparent fluctuation magnitude \overline{m}_I on the colour $(V - I)_0$. In the graphs of that figure, 4 different calibration relations are plotted over the data points, each relation shifted to the distance modulus obtained when assuming the relation, compare also Fig. 2.1:

case A: The original, empirically calibrated relation (1.10) for all galaxies.

case B: Relation (1.10) for $(V - I)_0 > 1.0$ mag and relation (2.1) for $(V - I)_0 < 1.0$ mag, as done for the simulations in Sect. 2.4.1.

case C: Relation (1.10) for all galaxies with $\overline{m}_I < 29$ mag and $\overline{M}_I = -2.00$ mag for the three galaxies with $\overline{m}_I > 29$ mag. This is conceptually similar to assuming relation (2.1) for all galaxies with $(V - I)_0 < 1.0$ mag. The difference is that now one horizontal and one steep branch in the theoretical \overline{M}_I - $(V - I)_0$ plane are explicitly associated with two

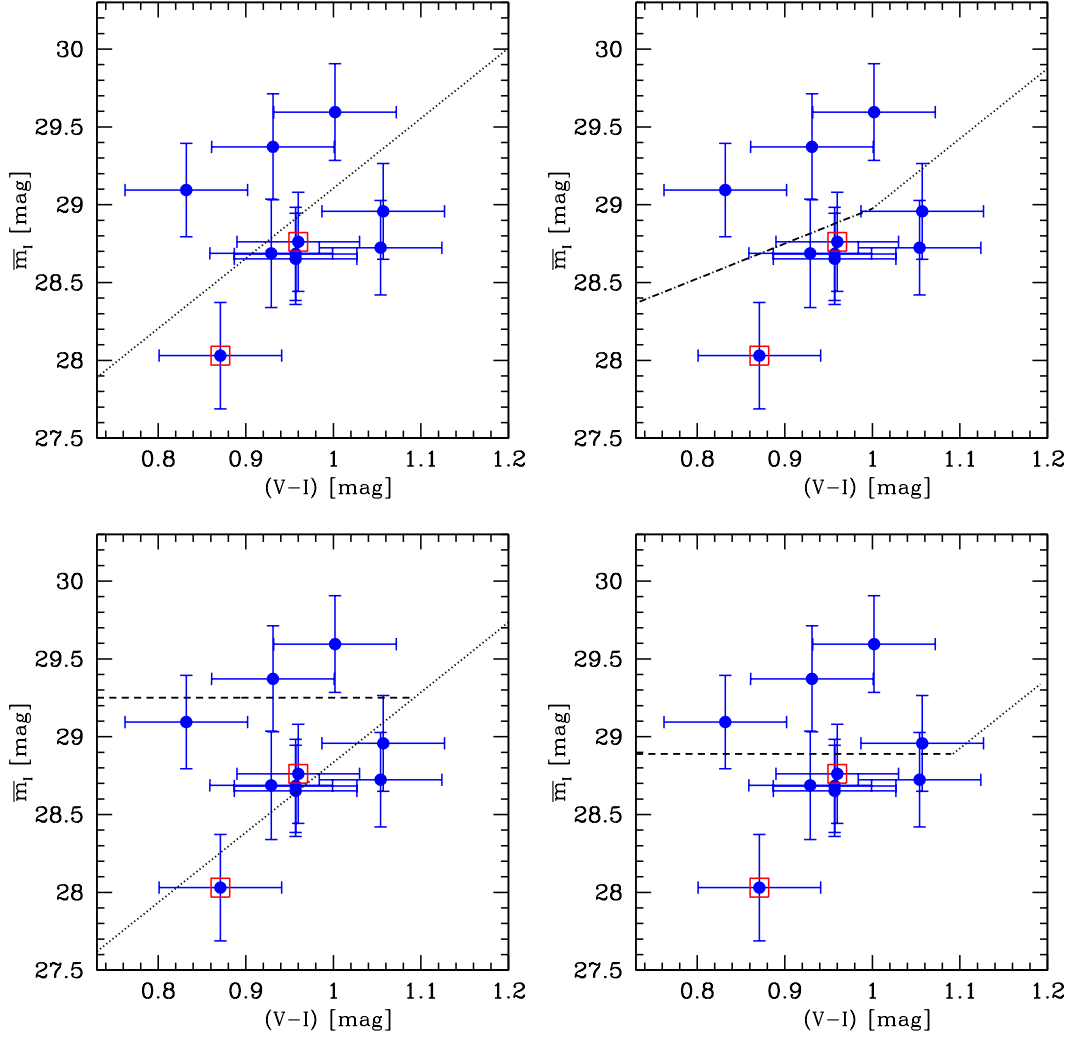


Figure 3.21: Apparent fluctuation magnitude \bar{m}_I plotted vs. $(V - I)_0$ colour with 4 different calibration relations overplotted. For all 4 plots, the calibration relations are shifted to the distance obtained when assuming the respective absolute relation. These figures should be seen in connection with Figs. 2.1, 3.22 and 3.23 and Table 3.4. The two data points with squares indicate a S/N below 3 in the SBF measurement. *Top left panel, case A:* the dotted line indicates equation (1.10) at a distance of $(m - M) = 31.52$ mag. *Top right panel, case B:* the dotted and dashed-dotted lines indicate equations (1.10) and (2.1) at a distance of $(m - M) = 31.39$ mag. *Bottom left panel, case C:* the horizontal dashed line at $\bar{M}_I = -2.00$ mag is assumed as SBF calibration for the galaxies with $\bar{m}_I > 29$ mag. Equation (1.10) is assumed for all other galaxies with $\bar{m}_I < 29$ mag. Assumed distance modulus is $(m - M) = 31.25$ mag. *Bottom right panel, case D:* All galaxies with $(V - I)_0 < 1.09$ – i.e. *all* galaxies – get assigned $\bar{M}_I = -2.00$ mag, as expected from the models of Liu et al. ([2000]) and Worthey ([1994]). Assumed distance modulus is $(m - M) = 30.89$ mag.

Calibration	$(m - M)_{SBF}$	$\sigma_{(m-M)}$	$\delta_{(m-M)}$	$\frac{d(m-M)}{d(V-I)_0}$
Equ. (1.10) (case A)	31.52 ± 0.21	0.48	0.45	-3.30 ± 2.18
Equ. (1.10), no low S/N	31.60 ± 0.22	0.51	0.45	-4.90 ± 2.60
Equ. (1.10) and (2.1) (case B)	31.39 ± 0.17	0.44	0.38	-1.69 ± 1.87
Equ. (1.10) and (2.1), no low S/N	31.47 ± 0.18	0.44	0.39	-3.34 ± 2.33
Equ. (1.10) and constant (case C)	31.25 ± 0.12	$0.21^{+0.08}_{-0.04}$	0.41 ± 0.02	0.54 ± 1.81
Equ. (1.10) and constant, no low S/N	31.27 ± 0.12	$0.22^{+0.09}_{-0.04}$	0.40 ± 0.02	0.28 ± 2.19
Constant (case D)	30.89 ± 0.13	0.43	0.32	1.06 ± 1.52
Constant, no low S/N	31.00 ± 0.12	0.36	0.31	-0.43 ± 1.81
	31.41 ± 0.07			

Table 3.4: Table showing the mean SBF distance moduli for different assumed calibration equations, see also Figs. 3.21 to 3.23. “No low S/N ” means that the two data points with SBF S/N below 3 are not considered. **Case A** (first and second line): equation (1.10) is applied to all galaxies. **Case B** (third and 4th line): equation (1.10) is applied for $(V - I)_0 > 1.0$, and equation (2.1) for $(V - I)_0 < 1.0$. **Case C** (5th and 6th line): equation (1.10) is applied for $\overline{m}_I < 29$ mag, and a constant $\overline{M}_I = -2.00$ mag is assumed for $\overline{m}_I > 29$ mag. **Case D** (last two lines): a constant $\overline{M}_I = -2.00$ mag is assumed for all galaxies. $\sigma_{(m-M)}$ gives the scatter of the measured distance values around their mean. $\delta_{(m-M)}$ gives the mean uncertainty of a single distance measurement. For case C), the error ranges of $\sigma_{(m-M)}$ and $\delta_{(m-M)}$ are indicated, as both values do not agree to within their errors. The last column shows how strong $(m - M)$ depends on $(V - I)_0$, see also Fig. 3.23. The last line gives the Fornax cluster reference distance from the HST-Key project (Ferrarese et al. [2000]).

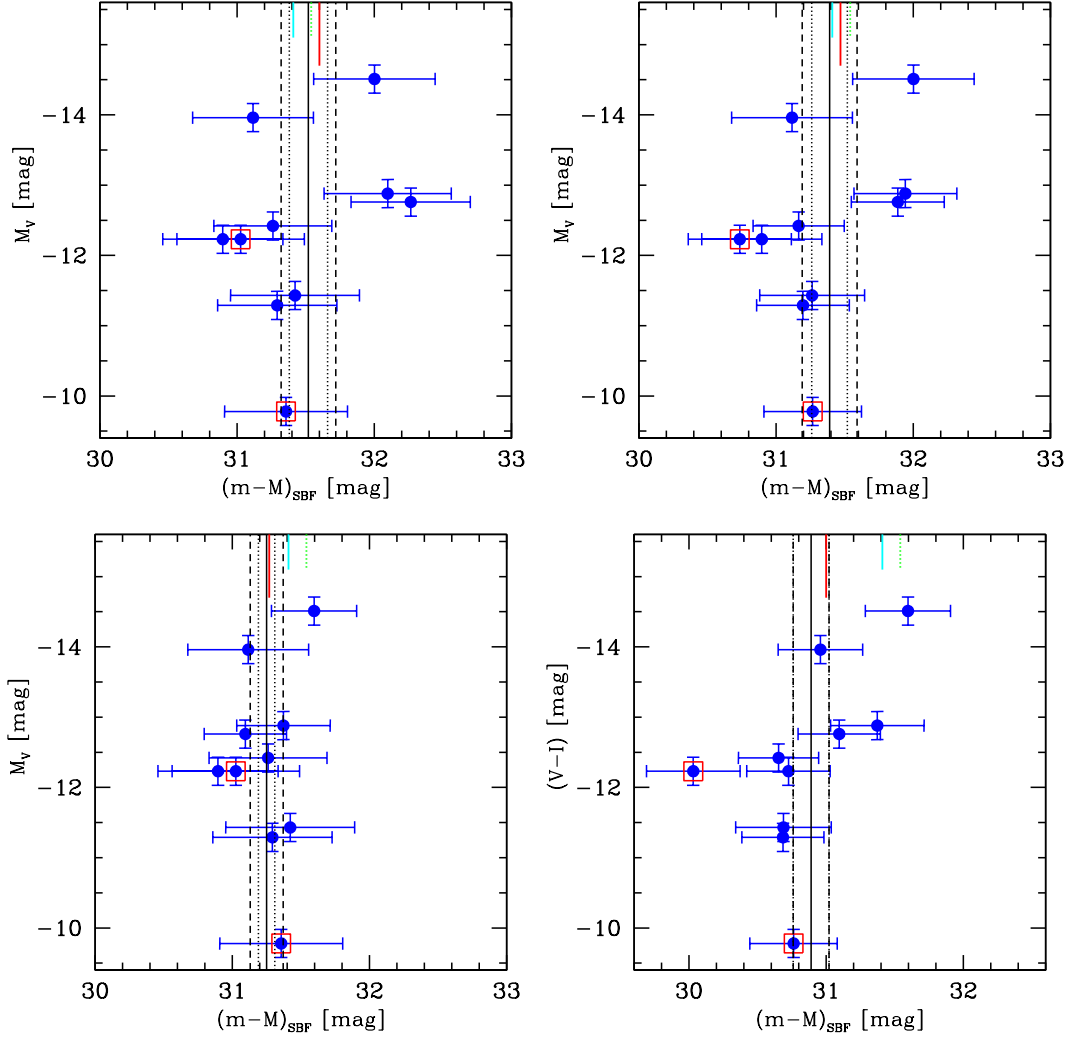


Figure 3.22: SBF-distance modulus plotted vs. absolute luminosity assuming 4 different SBF calibrations, see text, Table 3.4 and Fig. 3.21. The two data points with squares indicate a S/N in the SBF measurement below 3. *Top left panel, case A. Top right panel, case B. Bottom left panel, case C. Bottom right panel, case D.* The vertical solid line indicates the mean distance. The dotted vertical lines indicate the error range of the mean. The dashed vertical lines indicate the total error range when in addition taking into account a 0.031 mag absolute colour uncertainty. Note that this absolute colour error does not go into the distance uncertainty for the colour independent calibration equation adopted in case D). The large vertical tick indicates the mean SBF distance when excluding the two low S/N data points. The small, solid vertical tick marks the Fornax cluster distance of $(m - M) = 31.41$ mag derived in the HST-Key project (Ferrarese et al. [2000]). The small, dotted vertical tick marks the Fornax cluster distance of $(m - M) = 31.54$ mag derived by Jerjen ([2004]) from BR -SBF measurements of brighter Fornax cluster dEs.

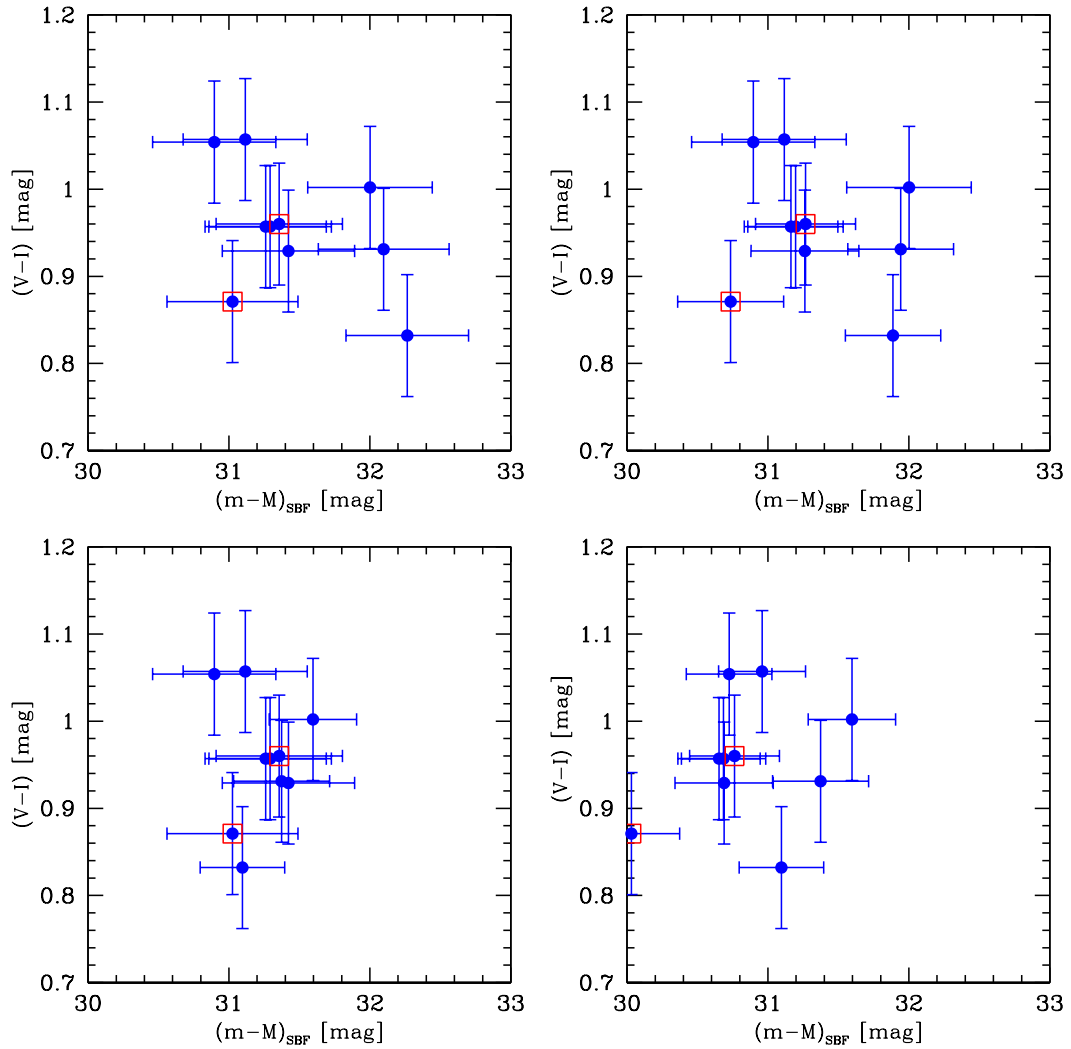


Figure 3.23: SBF distance modulus plotted vs. $(V - I)_0$ colour of the same galaxies as in Figs. 3.21 and 3.22. The two data points with squares indicate a S/N in the SBF measurement below 3. *Upper left panel, case A. Upper right panel, case B. Bottom left panel, case C. Bottom right panel, case D.*

separate sets of galaxies instead of assuming an average flatter relation for *all* galaxies. The specific choice of $\overline{M}_I = -2.00$ mag is about the mean \overline{M}_I of the theoretical data points from the original Worthey ([1994]) models and those of Liu et al. [2000]) in that colour range (see Fig. 2.1).

case D: $\overline{M}_I = -2.00$ mag is assumed for all galaxies. This is a test for the Liu and original Worthey models, as they do not predict a continuation of the steep relation (1.10) for blue colours.

The 4 corresponding distance sets are plotted vs. absolute galaxy luminosity and colour in Figs. 3.22 and 3.23. The resulting mean distances, distance scatters and correlations $\frac{d(m-M)}{d(V-I)_0}$ are given in Table 3.4.

From the mean distances for the various assumed calibration equations, no discriminating conclusion regarding the first two cases A) and B) can be drawn, as all values are consistent with the HST-Key project distance to within their errors. Also case C) is only marginally inconsistent with that reference distance. Only for case D), the derived mean distance is significantly lower than the HST-Key project value. The significance is 3.5σ for the entire sample and 3.0σ when rejecting the low S/N data. For case D) there is also a strong correlation between M_V and $(m-M)$, significant at the 2.0σ level when rejecting the two low S/N data. These two findings indicate that the calibration case D), based on the models by Liu et al. ([2000]) and those of Worthey ([1994]), is probably inadequate. We will therefore not consider case D) for the rest of this section. The assumption of a flat calibration equation applying to all galaxies bluer than about $(V-I)_0 = 1.10$ mag appears to be wrong.

We note that including FCC 160 (which has a high S/N but $S/N^* < 3$) in the low S/N sample does not change these statements. The mean distance rises by 0.06 mag, lowering the difference significance in case D) to 2.5σ and slightly improving the distance agreement in cases B) and C), while rising the difference significance in case A) to 1.1σ . A better criterion to judge on cases A) to C) is $\frac{d(m-M)}{d(V-I)_0}$. For case A) there is a correlation between $(m-M)$ and $(V-I)_0$ significant at the 1.9σ level when rejecting the two low S/N data points. The sign of this correlation gives a trend of too high distance for bluer colours. This is consistent with a flattening of the $\overline{M}_I-(V-I)_0$ relation for blue colours. Consequently in case B), where a flatter relation for $(V-I)_0 < 1.0$ is assumed, the correlation between $(m-M)$ and $(V-I)_0$ becomes less significant. When including all data points, it is 0.9σ significant and increases to only 1.4σ when excluding the two low S/N data points. This significance drops even more to below 0.3σ in case C). Indeed, case C) fits best the observed distribution of \overline{m}_I vs. $(V-I)_0$. This can be seen nicely in Fig. 3.21, where the three galaxies with $\overline{m}_I > 29$ mag appear to populate a different branch in the $\overline{M}_I-(V-I)_0$ plane. In case A) (see also Fig. 3.22) these three galaxies get assigned a comparably large distance, which makes the distance distribution appear somewhat more bimodal than in case C).

The fact that $\frac{d(m-M)}{d(V-I)_0}$ becomes insignificant in case C) indicates that we may have found an acceptable calibration relation for our sample of Fornax dEs. It appears to split up into two different samples: First, three galaxies with very old and metal-poor stellar

populations for which a constant \overline{M}_I is a good approximation; second, the rest of the galaxies which are of more intermediate age and metallicity and for which the original equation (1.10) appears to be a good approximation. This is in agreement with Jerjen et al. ([1998], [2000], [2004]), who have found an analogous bifurcation of the order of 0.5 mag from R -band SBF measurements for blue dEs in the Sculptor and Centaurus A group and a few dEs in the Virgo cluster.

Just as noted by Jerjen et al. for R -band SBF measurements, our finding indicates that there possibly is no unique $\overline{M}_I-(V-I)_0$ relation for very blue colours. The recent SBF calibration by Mei et al. ([2005]) for the Sloan filters ($g-z$) in the course of the ACS Virgo Cluster Survey (Côté et al. [2004]) shows that the blue sub-population of the more than 80 investigated early-type galaxies defines a significantly shallower slope in the $\overline{m}_z-(g-z)$ plane than the red fraction. This is consistent with the findings from this section. However, there is no clear sign for a bifurcation/bimodal distribution in the data of Mei et al. To judge whether a given galaxy possibly lies on the steeper or shallower relation in the SBF-colour plane one would have to measure SBF in several regions of that galaxy with different colours. This requires a significant radial colour gradient within the galaxy. The slope between \overline{m}_I and $(V-I)_0$ in these different regions would then define on which branch the galaxy lies and which calibration needs to be applied. This is done in the papers by Jerjen. For our data this is not a feasible approach as our galaxies have low surface brightnesses that just allow measuring with reasonable accuracy \overline{m}_I for the entire galaxy. That is, instead of judging from different regions within one galaxy we have to judge from different galaxy measurements whether an entire sample of galaxies might lie on the metal-poor or metal-rich branch.

We deal with a rather small sample of galaxies and the error bars of each single measurement is comparable to their spread in the $\overline{M}_I-(V-I)_0$ plane. Therefore, we might also be observing a chance distribution in that plane. As a first test for this we assume a Gaussian distance distribution centered on the mean found for case A) with $\sigma = 0.45$ mag (the mean single measurement uncertainty). Using a KS-test, the hypothesis that the observed distance distribution in case A) is not drawn from this Gaussian unimodal distribution is rejected at the 46% confidence level only. This level is very low and shows that our measurement errors are too large and the number of galaxies investigated too low to support a bimodal distance distribution in case A). Such a bimodal distribution would be expected as a systematic effect if applying the same calibration for all galaxies when instead application of different calibration equations for the two samples would be necessary.

Furthermore, we compare the distance distribution in case C) with a Gaussian centred on the mean distance with $\sigma = 0.40$ mag (the mean single measurement uncertainty). Using a KS-test, the hypothesis that the observed distance distribution in case C) is not drawn from this Gaussian unimodal distribution is rejected at the 41% confidence level only. In other words, the distance distribution in case C) is consistent with a unimodal Gaussian of width corresponding to the mean distance uncertainty.

To get some more feeling for the confidence levels involved, we compare the scatter of

the galaxy distances around their mean to the average single measurement uncertainty. It is evident from Table 3.4 that in case C), the distance scatter is strongly reduced compared to the other cases. This can be verified nicely in Fig. 3.22, where for case C) all but one error bar overlap the mean distance, while for the other cases 5 of the 10 error bars do not. The distance scatter is lower than the mean measurement uncertainty by 2.4σ for the entire sample and by 2.0σ when rejecting the two low S/N data points. These confidence levels are slightly larger than $\frac{d(m-M)}{d(V-I)_0}$ in case B). Of course, if the real single measurement uncertainty would be lower than estimated by us, case C) would become more likely and especially case A) would be rejected at higher confidence due to the then better defined slope $\frac{d(m-M)}{d(V-I)_0}$: the P_0 uncertainty is derived using the simulations from Sect. 2.4.1 and using the scatter from the different background subtractions as a double-check. We estimate that these errors have a statistical fluctuation of about 0.05-0.10 mag from galaxy to galaxy, which reduces to about 0.02-0.03 mag error uncertainty for the entire sample. The $(V-I)_0$ uncertainty is estimated both from the uncertainty in the sky background adjustment as the scatter of the colour differences between the WFCCD and IMACS data, which is 0.10 mag (see Sect. 3.3.2). Assuming that the colour estimates from both runs are equally uncertain, this yields an average $\frac{0.10}{\sqrt{2}} = 0.07$ mag colour uncertainty. The assumption of equal colour uncertainties in both runs is supported by the fact that the colour scatter within the two samples is almost identical: it is 0.127 mag for the WFCCD data and 0.131 mag for the IMACS data. Nevertheless, the statistical uncertainty of these scatters is still sufficient to also be consistent with a slightly lower colour error of about 0.05 mag. This would lower the distance uncertainty by about 0.03-0.05 mag and bring it somewhat closer to the distance scatter derived in case C), reducing the disagreement between distance scatter and measurement uncertainty to about 1.5σ when rejecting the two low S/N data points.

Summarizing: our data indicate that the “classical” calibration by Tonry may not apply for the bluer galaxies, given the quite high significance of $\frac{d(m-M)}{d(V-I)_0}$ in case A) when rejecting the low S/N data points. A modified calibration where for bluer colours \overline{M}_I is fainter than predicted by equation (1.10) is favoured by our data, given the decreasing significance of $\frac{d(m-M)}{d(V-I)_0}$ for cases B) and C). Although case C) shows the weakest correlation between $(m-M)$ and $(V-I)_0$, the scatter of the derived distances around their mean lies significantly below the mean single measurement uncertainty. This indicates that with case C) we may be “overcorrecting” the calibration equation beyond the limits posed by the measurement uncertainty, supported by the non-detection of a bifurcation in SBF calibration of Mei et al. ([2005]). The most secure statement from this section then clearly is: a flat calibration relation for *all* galaxies at blue colours, as predicted by the Liu and original Worthey models, appears to be inadequate to describe our data. Due to the possible “over-correction” and the fact that the mean distance in case C) is slightly below the reference value, we favour case B) as the best approximation to our SBF data for Fornax.

It is beyond the scope of this thesis to discuss in detail the reasons why the Worthey

and Liu models appear to underpredict \overline{M}_I for blue colours. A possible reason might be that the RGB/AGB turn over too much at low metallicities in these models, i.e. the tip of the red giant branch lies at too faint luminosity. Worthey uses an amalgamation of Yale and Vandenberg isochrones (Green et al. [1987], Vandenberg [1985]) and his own population synthesis models. It is interesting to note that with the original Yale isochrones (Green et al. [1987]) the problem existed that the RGB *failed* to turn over at high metallicities, which led to \overline{M}_I incompatible with observations (see Liu et al. [2000] and references therein). This problem was “cured” by Worthey et al. ([1994]) by his amalgamation of the Yale and Vandenberg isochrones. One might speculate that in turn this enforced turnover of the RGB/AGB at high metallicities yields to a too pronounced turn over at low metallicities, which would be consistent with the discrepancy between our SBF data and the Worthey predictions.

Liu et al. use the Bertelli et al. ([1994]) isochrones and the Bruzual & Charlot ([1993]) models. Using the same Bertelli et al. isochrones instead of the Yale-Vandenberg amalgamation, Worthey’s model predictions interestingly do predict a large spread of \overline{M}_I for blue colours (see Fig. 2.1), similar to the predictions of Blakeslee et al. ([2001]) and Cantiello et al. ([2003]). This indicates that not only the input isochrones but also the different stellar synthesis models are responsible for the discrepancy between the different predictions. Note, however that while the Worthey and Liu models seem to be inadequate for blue colours, for red colours they fit somewhat better to the empirical calibration relation (1.10) by Tonry et al. ([1997]) than the Blakeslee and Cantiello models. In that context it is interesting to note that Liu et al. [2002] find the Blakeslee models to provide a significantly worse fit to the available near-IR SBF measurements for metal-rich giant galaxies than those of Liu et al. ([2000]).

Apparently, one single set of population synthesis models is still unable to predict correctly the stellar population properties over the large age-metallicity range covered between blue dwarf galaxies and red giants. Furthermore, empirical SBF calibrations for blue early-type galaxies are just starting to become available (e.g. Mei et al. [2005] and this thesis), while SBF data for red colours have been around for more than a decade. This has enabled modellers to adjust their tracks to the observations in a semi-empirical manner for red colours, while for the blue range this has not yet been possible.

To improve the discrimination between competing models, more data points are needed to better constrain the loci of blue early-type populations in the \overline{M}_I -($V - I$)₀ plane. The second part of FDF, observed in 12/2004, will increase the data sample by a factor of 2-3 and hence allow to better address this issue.

3.4 Summary

In this chapter, the faint end slope of the early-type galaxy luminosity function in the central Fornax cluster was investigated by means of SBF cluster membership confirmation and morphological selection. Furthermore, a tentative SBF calibration at blue colours was presented. These are our findings:

1. We have discovered $\simeq 70$ very faint dE candidates in Fornax based on data obtained with the 2.5m du Pont telescope at Las Campanas Observatory, Chile. Together with the already known dE candidates, these dSphs candidates follow similar magnitude-surface brightness and colour-magnitude relations as their counterparts in the Local Group. The magnitude-surface brightness relation of the Fornax dwarfs is shifted towards larger sizes compared to that of the Local Group.

2. The joint sample of newly found and previously known candidate dEs has a luminosity function with a faint end slope $\alpha \simeq -1.1 \pm 0.1$. This estimate is based on purely morphological cluster membership assignment in the magnitude regime where the faint end slope dominates the luminosity function.

3. From the first part of our follow-up survey Fornax Deep Field using IMACS at Magellan (LCO) with substantially improved spatial resolution, we directly determine the cluster membership for 10 candidate dEs in the magnitude range $-14.2 < M_V < -11.5$ mag using the SBF method. This extends the magnitude range of confirmed cluster members far into the regime where the faint end slope α dominates the luminosity function (LF). We find the predictions for limiting absolute galaxy magnitudes of SBF measurements from our simulations to be in good agreement with the real outcome of our survey. With our IMACS imaging data we improve the morphological cluster membership assignments for fainter galaxies with $M_V < -10$ mag. Combining the SBF cluster membership confirmations with the improved morphological selection, we confirm the probable cluster membership for the vast majority of candidate dEs and find that α changes by less than 0.02. There are only two new dSph candidates detected in our IMACS imaging, inclusion of which does not change α by more than 0.02, either. It is found that Fornax dEs are on average slightly larger than their Local Group counterparts.

4. From the SBF measurements of Fornax dEs we find clear indications for a weaker dependence of the absolute fluctuation magnitude \overline{M}_I on $(V - I)_0$ at blue colours compared to the empirical calibration at redder colours. However, we can also reject at about the 3σ level the theoretical SBF values by Liu et al. ([2000]) and Worthey ([1994]), who predict a colour-independent, flat, relation between \overline{M}_I and $(V - I)_0$ for $(V - I) < 1.10$ mag.

Chapter 4

SBF distances to dEs and Es in the Centaurus and Hydra clusters

This chapter is based on the publications *Mieske, S. & Hilker, M., 2003, A&A, 410, 445* and *Mieske, S., Hilker, M. & Infante, L. 2005, A&A in press, astro-ph/0503647*.

4.1 Abstract

In this chapter, we present *I*-band SBF measurements for 16 early type galaxies in the central Hydra cluster and 15 early-type galaxies in the central Centaurus cluster (mainly dwarfs), based on deep *VI* imaging obtained with VLT FORS1. From the SBF-distances to the galaxies in our sample we estimate a Hydra cluster distance of 41.2 ± 1.4 Mpc ($(m - M) = 33.07 \pm 0.07$ mag) and a Centaurus cluster distance of 45.3 ± 2.0 Mpc ($(m - M) = 33.28 \pm 0.09$ mag). We find a distance difference of 0.26 ± 0.32 mag between the two Centaurus cluster sub-components Cen30 and Cen45, ruling out that both components are separated by their Hubble flow distance, suggesting that Cen45 is falling into the main cluster Cen30. We derive an upper limit of ± 5.7 Mpc radial extension for the Centaurus cluster and ± 3 Mpc for the Hydra cluster, corresponding to a 2-3 times larger radial than tangential extension. Assuming $H_0 = 72 \pm 4$ km s⁻¹ Mpc⁻¹, we estimate a positive peculiar velocity of 1225 ± 235 km s⁻¹ for Hydra and 210 ± 295 km s⁻¹ for Cen30. Allowing for a thermal velocity dispersion of 200 km s⁻¹, this rules out a common peculiar flow velocity for both clusters at 98% confidence. We find that the $9 \times 10^{15} M_\odot$ “Great Attractor” (GA) from the flow study of Tonry et al. ([2000]) at a distance of $\simeq 45$ Mpc can explain the observed peculiar velocities if shifted about 15° towards the Hydra cluster position. Our results are inconsistent at 94% confidence with a scenario where the Centaurus cluster is identical to the GA. In order to better restrict partially degenerate GA parameters like its mass and distance, a recalculation of the local flow model with updated distance information over a larger area than covered by us would be needed.

4.2 Introduction

4.2.1 Peculiar velocities for galaxies

In the past few years, a lot of effort has been put into a precise determination of cosmological parameters. Investigations like the HST Key Project (Freedman et al. [2001]), the Sloan Digital Sky Survey (SDSS) (Abazajian et al. [2003]) or the WMAP mission (Bennett et al. [2003], Spergel et al. [2003]) mark the beginning of a precision era in observational cosmology. The accuracy in determining the Hubble constant H_0 is approaching 5%, most values derived recently by large surveys are consistent with $H_0 = 72 \pm 4 \text{ km s}^{-1} \text{ Mpc}^{-1}$. This enormous improvement in precision has the consequence that deviations from an undisturbed Hubble flow can also be determined to a higher precision. This is of special importance for studying the matter distribution in the nearby universe, as peculiar velocities caused by inhomogeneous matter distribution can be significant compared to the Hubble flow.

There are three main methods that have been applied to estimate the distances and peculiar velocity field in the nearby universe:

1. The SBF method (see Tonry & Schneider [1988], Tonry et al. [2001]). Tonry et al. ([2000]), in the following T00, have performed a study of the local flows using SBF distances obtained in the I -band of about 300 early-type galaxies with $cz < 4000 \text{ km s}^{-1}$. Apart from finding a well defined flow towards the Virgo cluster, attributed to a “Virgo Attractor” with $7 \times 10^{14} M_*$ at about 17 Mpc distance, their model fitting favours an additional “Great Attractor” (GA) of $9 \times 10^{15} M_*$ at a distance of $43 \pm 3 \text{ Mpc}$ in the direction of the Hydra-Centaurus region. According to the SBF flow-model by T00, the gravitational pull exerted by the GA leads to a Local Group peculiar velocity of $300 \pm 200 \text{ km s}^{-1}$ with respect to the Cosmic Microwave Background (CMB).
2. The Fundamental Plane (FP) method (e.g. Dressler et al. [1987c], Blakeslee et al. [2002], Bernardi et al. [2003]). Important early evidence for the presence of a Great Attractor towards the Hydra-Centaurus region had come from an FP analysis performed by Lynden-Bell et al. ([1988]), who proposed a Great Attractor at about a CMB radial velocity of $4350 \pm 350 \text{ km s}^{-1}$ ($\simeq 60 \text{ Mpc}$ for $H_0 = 72 \text{ km s}^{-1} \text{ Mpc}^{-1}$). Later, several studies indicated that the peculiar velocity of the Local Group with respect to the CMB could be only partially explained by the attraction of a nearby GA within $\simeq 100 h^{-1} \text{ Mpc}$, suggesting an additional flow component towards a more distant attractor (e.g. Willick [1990], Hudson [1994], Staveley-Smith et al. [2000], Lauer & Postman [1994]). Not all FP studies found flow components towards the same direction. For instance, the large-scale flow detected by Lauer & Postman was in a direction perpendicular to most other studies. The “Streaming motion of Abell clusters” (SMAC) survey (e.g. Smith et al. [2000], [2001], [2004] and Hudson et al. [2004]) is the most recent example for an application of the FP method to obtain peculiar velocities. In the SMAC survey, FP distances to 56 Abell galaxy clusters with $cz < 12000 \text{ km s}^{-1}$ are presented. In Hudson et al. ([2004]), a flow analysis based on these peculiar velocities is performed, resulting

in the detection of a bulk flow of amplitude $687 \pm 203 \text{ km s}^{-1}$ towards $l=260^\circ$, $b=0^\circ$ (SGL= 170° , SGB= -57°), out to $120 h^{-1} \text{ Mpc}$.

3. The Tully-Fisher method (Tully & Fisher [1977]). Most of the flow studies using this method (e.g. Aaronson et al. [1982] and [1986], Mathewson et al. [1992], Shaya, Tully & Pierce [1992], Courteau et al. [1993], Dale et al. [1999], Willick [1999]) detect a bulk flow of similar amplitude and direction to the one derived in the SMAC (Hudson et al. [2004]) and find no indications for a convergence of this flow within $\simeq 100 h^{-1} \text{ Mpc}$. There are also some studies which find no or much smaller bulk flows, e.g. Giovanelli et al. ([1999]) or Courteau et al. ([2000]).

Distances derived for early-type galaxies with the SBF method and FP analysis are compared in Blakeslee et al. ([2002]), showing an overall good agreement between both methods. The distance differences between both methods are mostly statistical and not correlated with galaxy properties, except for a mild dependence of the FP distance on the Mg_2 index.

4.2.2 Peculiar velocities towards Hydra-Centaurus

Since the first postulation almost 20 years ago of a huge nearby “Great Attractor” in the Hydra-Centaurus region (e.g. Shaya [1984], Tammann & Sandage [1985], Aaronson et al. [1986] and [1989]), most of the local flow studies have agreed that there is a net flow velocity towards that region. However, the radial distance of the mass overdensity responsible for it has been a subject of very lively debate, see the references mentioned above. Is there a huge mass overdensity (“Great Attractor”) at about 40-60 Mpc, or is there only a larger scale flow in the same direction but towards a more distant attractor? This yet unanswered question makes the Hydra ($v_{CMB} \simeq 4100 \text{ km s}^{-1}$, NED database and Lineweaver et al. [1996]) and Centaurus cluster ($v_{CMB} \simeq 3400 \text{ km s}^{-1}$, NED database and Lineweaver et al. [1996]) at Hubble distances of about 50 Mpc ideal test particles for the hypothesis that there is a GA within 40-60 Mpc.

Note that Hudson et al. ([2004]) show that the bulk flow – in which the Local Group participates – points towards the approximate direction of the Hydra-Centaurus region but extends well beyond the proposed position of the Great Attractor. They argue that this flow might mainly be caused by the attractive force of the Shapley Super Cluster ($8000 < cz < 18000 \text{ km s}^{-1}$, see for example Quintana et al. [1995]). However, due to the relatively sparse sampling close to the proposed Great Attractor region, Hudson et al. cannot rule out that an additional massive attractor exists close to the Hydra-Centaurus region.

In this chapter, we will check via SBF-distances to Centaurus and Hydra the GA model by T00, but not test for any additional bulk flow. This is because the projected positions of the Hydra and Centaurus cluster are separated by only 30° and the proposed position of the GA is between the two clusters. Due to this proximity, any other large scale streaming flow should have a negligible effect on their relative velocities.

Note that here and in the following, the term “Great Attractor” (GA) refers to the mass

overdensity whose location was estimated by T00 using the SBF method. Its projected position between the Centaurus and Hydra clusters (Figs. 4.8 and 4.10) is at more than 40 degrees lower galactic longitude than the “Great Attractor region” from the studies of the galaxy density and peculiar velocity field in the Zone of Avoidance (ZOA) (e.g. Woudt et al. [2003], Kolatt et al. [1995]), specifically the massive Norma cluster. This might partially be because T00 did not observe galaxies in the Zone of Avoidance. However, it also reflects the clumpiness of matter distribution in the nearby universe. There might not be only one major “Great Attractor”, but the SBF-GA and ZOA-GA may be distinct substructures of a generally overdense filamentary region (e.g. Fairall & Lahav [2004]).

There is one additional feature that makes the Centaurus cluster even more attractive for peculiar velocity studies – but at the same time more complex –: in redshift space it consists of two well separated sub-clusters, namely the dominating component Cen30 at about 3000 km s^{-1} heliocentric velocity and the smaller component Cen45 at about 4500 km s^{-1} . In several studies this remarkable substructure has been investigated (e.g. Lucey et al. [1980] & [1986], Jerjen et al. [1997], Stein et al. [1997], Churazov et al. [1999], Furusho et al. [2001]), indicating that Cen45 is probably a sub-group falling into the main cluster Cen30. Lucey et al. ([1986]) suggest that Cen45 is located at about the same distance as Cen30, based mainly on a comparison of the cumulative luminosity distribution in both sub-clusters. Churazov et al. ([1999]) propose, based on *ASCA* X-ray temperature measurements, that the two sub-components are merging. They suggest the existence of a large scale filament along the line of sight towards Centaurus in order to explain the discrepancy between the unusually high velocity dispersion of the Cen30 members and the X-ray temperature. Furusho et al. ([2001]) present more extended X-ray measurements and conclude that a major merger in Centaurus rather occurred several Gyrs ago. Stein et al. ([1997]) find that the morphological content of the two sub-clusters differs substantially. Cen30 is more dominated by early-type galaxies, while Cen45 contains more late-type galaxies and fewer dwarfs. This is consistent with Cen30 being the older, main cluster, and Cen45 the more active young infalling sub-cluster.

4.2.3 Aim of this chapter

The aim of this chapter is to improve the distance precision to the Hydra and Centaurus clusters by using SBF-distances from deep and high resolution imaging obtained for both clusters with the same instrument (VLT/FORS1), hence allowing robust relative distance measurements. With the Hydra *and* Centaurus distance in hand, some of Tonry’s flow model parameters (Tonry et al. [2000]) for the Great Attractor can be checked.

This chapter is structured as follows: In section 4.3, the data and their reduction are described. Section 4.4 shows the results of the SBF distance estimates for Hydra and Cen-

Field	RA [2000]	Dec [2000]	ZP _I	ZP _V	CT _I	CT _V	k _I	k _V
1	12:48:45.0	-41:18:20	26.582	27.472	0.00	-0.08	0.093	0.145
2	12:49:18.5	-41:18:20	26.600	27.446	0.00	-0.08	0.093	0.145
3	12:49:52.0	-41:21:02	26.672	27.514	0.088	-0.015	0.093	0.145
4	12:49:52.0	-41:14:50	26.588	27.446	0.00	-0.08	0.093	0.145
5	12:48:45.0	-41:24:32	26.548	27.446	0.00	-0.08	0.093	0.145
6	12:48:45.0	-41:30:44	26.548	27.446	0.00	-0.08	0.093	0.145
7	12:48:45.0	-41:36:56	26.582	27.472	0.00	-0.08	0.093	0.145

Table 4.1: Central coordinates and photometric calibration coefficients for the 7 VLT FORS1 fields observed in Centaurus, as indicated in Fig. 4.1. Calibration equation is: $m = m_{instr} + ZP - CT * (V - I)_0 - k * AIRMASS$.

taurus, including estimates of the cluster depths. All results are discussed in Sect. 4.5, putting special emphasis on a check of Tonry’s Great Attractor model. We finish this chapter with a summary in section 4.6.

4.3 The data

4.3.1 Centaurus

The imaging data for the Centaurus cluster were obtained in service mode at the Very Large Telescope (VLT) of the European Southern Observatory, Chile (Observing Programme 67.A-0358), using UT 1 with the instrument FORS1 in imaging mode. Seven $7 \times 7'$ fields in the central Centaurus cluster were observed in Johnson *V* and *I* passbands. The seeing ranged between 0.4 and 0.6". The total integration time was 1500 seconds for the *V* exposures, divided up into 4 dithered single exposures, and 3000 seconds for the *I* exposures, divided up into 9 dithered single exposures. Fig. 4.1 shows a map of the central Centaurus cluster with the observed fields and cluster galaxies indicated. Table 4.1 gives the coordinates and photometric calibration coefficients of the observed fields. Table 4.2 gives the photometric properties and coordinates of the 15 investigated cluster galaxies. They span a magnitude range of $19.6 > V > 11.5$ mag, corresponding to approximately $-21.5 < M_V < -13.5$.

In the 7 fields, there are located 14 additional galaxies cataloged as early-types in the CCC. These could not be investigated for the following reasons: 5 galaxies showed pronounced spiral features on our high resolution images, revealing that they are probably late-type background galaxies rather than early-type cluster members; 6 galaxies were too faint to detect a significant SBF signal; two galaxies showed pronounced boxy residuals after subtracting an elliptical light model, with the boxy features having a scale size of only a few times that of the seeing; one galaxy was too close to the halo of a bright saturated star to obtain a reliable SBF signal.

CCC-Nr.*	Field	RA* [2000]	Dec* [2000]	V_0^{**}	$(V - I)_0^{**}$	v_{rad} [km s ⁻¹]	Type*
52	1	12:45:44.3	-41:02:58	17.86	1.09	—	dE,N
61	1	12:48:39.7	-41:16:05	16.26	1.14	2910	dE,N
65 (N4696)	1	12:48:49.0	-41:18:39	11.50	1.24	2985	E4,S03(4)
70	1	12:48:53.9	-41:19:09	16.69	1.24	2317	cdE
75	1	12:49:01.9	-41:15:36	17.31	1.12	1958	dE,N
89	2	12:49:18.2	-41:20:07	15.43	1.15	3104	E1
111	3	12:49:40.0	-41:21:59	15.86	1.01	2880	dE,N
115	3	12:49:46.5	-41:22:08	18.15	0.99	—	dE
121	3	12:49:54.2	-41:20:24	17.36	1.07	4739	dE
123	3	12:49:56.1	-41:24:04	17.35	1.03	4661	dS0
124	3	12:49:56.2	-41:23:22	19.09	0.84	—	dE
130 (N4709)	3	12:50:04.0	-41:22:57	12.50	1.35	4650	E3
125	4	12:49:56.4	-41:15:37	16.06	1.08	2880	dE,N
58	5	12:48:36.1	-41:26:25	16.78	1.02	3304	dE
68	6	12:48:52.5	-41:32:25	19.63	0.93	—	dE

Table 4.2: Coordinates and photometric properties of the investigated Centaurus cluster galaxies. The galaxies are ordered by field-number, and within the same field by right ascension. The field number refers to the fields indicated in Fig. 4.1. The radial velocities are taken from Stein et al.'s ([1997]) catalog of radial velocities for the Centaurus cluster.

*As in the Centaurus cluster Catalog (CCC, Jerjen et al. [1997]). Note that galaxy CCC 121 is catalogued in the CCC as being of type Im. Based on our high resolution photometry, we cannot confirm this morphological type but rather find it has a normal, smooth dE-like morphology. Galaxy CCC 70 is catalogued as type E0 due to its relatively high surface brightness. However, it has $M_V \simeq -16.5$ mag, placing it into the dwarf galaxy regime. We therefore adopt the type compact dE (cdE) for CCC 70.

**Based on this thesis.

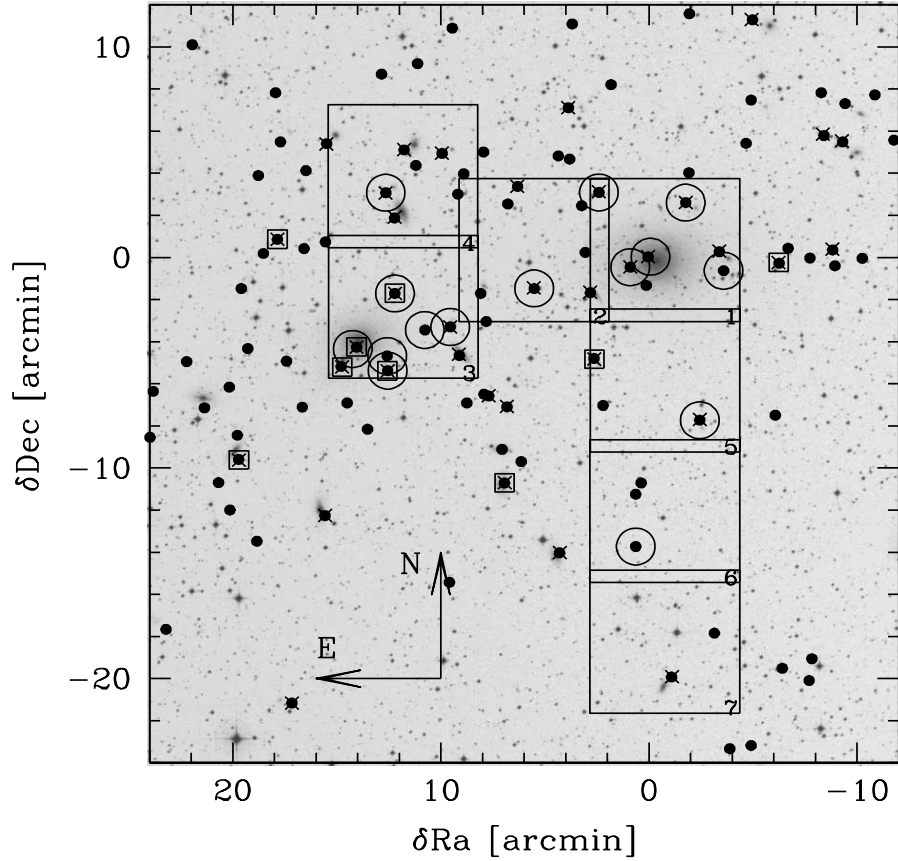


Figure 4.1: Map of the central Centaurus cluster, with distances relative to the main galaxy of Cen30, NGC 4696. Large squares are the observed VLT fields, the field number is indicated in the lower right corner of each square. Dots represent the galaxies listed in Jerjen et al.'s ([1997]) Centaurus Cluster Catalog (CCC) as probable and likely cluster members. Dots marked with crosses are galaxies for which Stein et al. ([1997]) have obtained radial velocity. Small squares indicate galaxies belonging to the sub-cluster Cen45. Galaxies marked with large circles are the ones for which we present new SBF measurements in this thesis. Underlying image from the DSS.

4.3.2 Hydra

The imaging data for Hydra were obtained in service mode at the Very Large Telescope (VLT) of the European Southern Observatory, Chile (Observing Programme 65.N-0459(A)), using UT 1 with the instrument FORS1 in imaging mode. Seven $7 \times 7'$ fields in the central Hydra cluster were observed in Johnson V and I pass-bands. The seeing ranged between 0.6 and 0.7". The total integration time was 1500 seconds for the V exposures, divided up into 4 dithered single exposures, and 3000 seconds for the I exposures, divided up into 9 dithered single exposures. Fig. 4.2 shows a map of the central Hydra cluster with the observed fields and indicating the cluster galaxies. Table 4.3 gives the coordinates and photometric calibration coefficients of the observed fields. Table 4.4 gives the photometric properties and coordinates of the 16 investigated cluster galaxies. They span a magnitude range of $10 < V < 18.5$ mag, corresponding to approximately $-23 < M_V < -14.5$. The galaxies investigated were selected from the radial velocity catalog of Christlein & Zabludoff ([2003]), requiring that they are early-types and have radial velocities within the Hydra cluster range of $2000 < v_{\text{rad}} < 6000$ km s⁻¹. The catalog has a complete spatial coverage over the fields investigated by us. Its faint magnitude limit coincides roughly with the faint magnitude limit for SBF measurements expected at the approximate Hydra cluster distance of 33-33.5 mag (see Table 2.1).

In the 7 fields, there are 8 additional early-type galaxies whose radial velocities correspond to the Hydra cluster but which were not investigated. One of them was too faint to detect a significant SBF signal. The other 7 galaxies showed pronounced boxy or disk residuals after subtracting an elliptical light model with scale sizes of only a few PSF-FWHM.

Note that the dwarf galaxies investigated in Hydra and Centaurus are much brighter than those investigated in Fornax in the previous Sect. 3.3: the faint magnitude limit for the Hydra-Centaurus dwarfs is $M_V \simeq -14.5$ mag, about equal to the bright magnitude limit of the Fornax sample. This is because at the about two times higher distance of Hydra and Centaurus, SBF are twice as weak.

4.3.3 Data reduction before SBF measurement

The pipeline reduced images for both Hydra and Centaurus still showed large scale sky count variations of the order of $\pm 3\%$. To partially compensate for that, a master flat field was constructed by combining all single exposures from all fields, disregarding contribution from astronomical objects to the final master flat using a sigma-clipping-rejection. After division by the smoothed master flat field, the large scale variations were reduced to $\pm 1\%$.

The observational zero points were determined separately for each night. For all fields except for field 3 in Centaurus, which was taken two months after the rest of the

Field	RA [2000]	Dec [2000]	ZP _I	ZP _V	CT _I	CT _V	k _I	k _V
1	10:36:36.0	-27:32:50	26.629	27.477	0.02	-0.05	0.090	0.160
2	10:37:03.4	-27:32:50	26.643	27.529	0.02	-0.05	0.090	0.160
3	10:37:30.7	-27:32:50	26.643	27.529	0.02	-0.05	0.090	0.160
4	10:37:58.6	-27:32:50	26.543	27.529	0.02	-0.05	0.090	0.160
5	10:36:36.0	-27:26:45	26.665	27.532	0.02	-0.05	0.090	0.160
6	10:36:36.0	-27:20:39	26.665	27.532	0.02	-0.05	0.090	0.160
7	10:36:36.0	-27:14:27	26.665	27.532	0.02	-0.05	0.090	0.160

Table 4.3: Central coordinates and photometric calibration coefficients for the 7 VLT FORS1 fields in Hydra as indicated in Fig. 4.2. Calibration equation is: $m = m_{instr} + ZP - CT * (V - I)_0 - k * AIRMASS$.

Nr.	Field	RA [2000]	Dec [2000]	V ₀	(V - I) ₀	v _{rad} [km s ⁻¹]	Type
258	1	10:36:50.1	-27:30:46	17.57	1.02	5251	dE,N
359	1	10:36:49.0	-27:30:00	17.44	1.04	4556	dE
334	1	10:36:45.8	-27:31:24	17.65	1.03	4225	dE,N
357	1	10:36:45.7	-27:30:31	17.30	0.93	3815	dE
140	1	10:36:42.7	-27:35:08	16.15	1.05	3554	dS0,N
N3311	1	10:36:42.7	-27:31:42	10.90	1.15	3713	S0(2) [E+2]
N3309	1	10:36:35.7	-27:31:05	11.90	1.21	4068	E1 [E3]
482	2	10:37:13.7	-27:30:25	16.73	1.06	4439	dE,N
421	2	10:37:00.1	-27:29:53	18.11	1.04	5626	dE,N
123	2	10:36:57.0	-27:34:04	18.51	1.03	2993	dE
172	2	10:36:52.5	-27:32:15	16.28	1.07	3133	dE
252	3	10:37:17.3	-27:35:34	17.19	1.08	3780	dE,N
358	5	10:36:43.0	-27:25:30	17.69	1.06	3936	dE,N
N3308	5	10:36:22.3	-27:26:17	12.10	1.28	3537	SB0(2) [SAB(s)0-]
322	6	10:36:50.7	-27:23:01	18.24	1.02	4306	dE
150	6	10:36:26.8	-27:23:25	15.99	1.07	4158	dE,N

Table 4.4: Coordinates and photometric properties of the investigated galaxies of the Hydra cluster. The galaxies are ordered by field-number, and within the same field by right ascension. The field number refers to the fields indicated in Fig. 4.2. Photometry is taken from this thesis. (V - I)₀ is from the region where SBF are measured, V₀ is the total magnitude of the galaxy derived from a curve-of-growth analysis. Galaxy numbers, coordinates and radial velocities are from the catalog of Christlein & Zabludoff ([2003]), except for the NGC galaxy numbers. Galaxy types are according to the morphology on our Hydra images except for the three NGC galaxies, for which the type is from Richter et al. ([1989]).

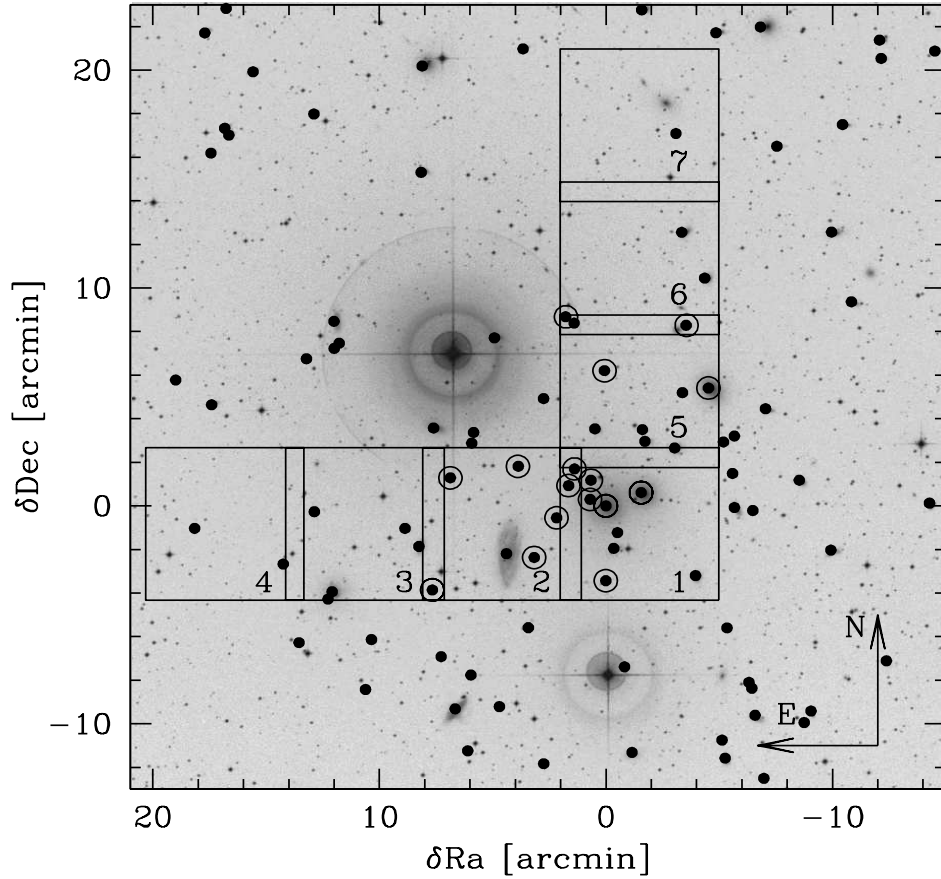


Figure 4.2: Map of the central Hydra cluster, with distances relative to NGC 3311. Large squares are the observed VLT fields, the field number is indicated in the lower right corner of each square. Dots are all Hydra cluster member galaxies from the spectroscopic study of Christlein & Zabludoff ([2003]). Galaxies marked with large circles are the ones for which we present new SBF measurements in this thesis. The cluster members without SBF measurement are 11 late-type and 8 early-type galaxies. Underlying image from the DSS.

Centaurus images, the colour terms were identical to within their errors. For all fields in Hydra and Centaurus, respectively, the extinction coefficients were identical to within their errors. The accuracy of the derived zero points was of the order 1%. For each field and pass-band, the single exposures were brought into a common coordinate system by applying integer pixel shift corrections between the single dithered frames. For SBF measurements, only integer pixel shifts are suitable, as otherwise correlated noise would be introduced. Cosmic rays were removed from the single frames using the IRAF task COSMICRAYS. The registered cleaned single frames were averaged using an average sigma clipping algorithm. For each investigated galaxy, the local background level was determined in both pass-bands via a curve of growth analysis, yielding the total apparent magnitudes in V and I , a surface brightness profile and a colour map.

To correct for galactic reddening and absorption, we used the values from Schlegel et al. ([1998]), who give $A_I = 0.221$ and $E(V - I)_0 = 0.157$ for the coordinates of the Centaurus cluster and $A_I = 0.154$ and $E(V - I)_0 = 0.110$ for the coordinates of the Hydra cluster.

4.3.4 SBF measurement for the dwarfs

For obtaining $(m - M)$ with SBF, one must *measure* the apparent fluctuation magnitude \overline{m}_I and *derive* the absolute fluctuation magnitude \overline{M}_I from $(V - I)_0$.

For the derivation of \overline{M}_I from $(V - I)_0$, equation (1.10) was used for all galaxies with $(V - I)_0 > 1.0$ mag. For $(V - I)_0 < 1.0$, we adopt equation (2.1). This is inspired by the results of Sect. 3.3.3, which indicate that at least some of the dwarf galaxies in the blue colour range have fainter \overline{M}_I than predicted from equation (1.10). In Sect. 3.3.3 it could not be convincingly distinguished between the case where all galaxies follow a shallower $\overline{M}_I - (V - I)_0$ relation and the case where one subset follows the original steep relation and another subset has a colour independent \overline{M}_I . Therefore we consider adoption of equation (2.1) for $(V - I)_0 < 1.0$ the best compromise. Note that this applies to only 4 out of the 31 galaxies investigated, since in comparison to the Fornax dwarfs the galaxies investigated in Hydra/Centaurus are more luminous and hence redder, as a consequence of the colour-magnitude relation for galaxies. For the distance error calculation, a cosmic scatter of 0.10 mag is assumed (Tonry et al. [2001]), adding in quadrature to the error contribution arising from the uncertainty of $(V - I)_0$. From comparing the colour measured for the same galaxies in adjacent fields, we adopt $\Delta(V - I)_0 = 0.015$ mag as the colour uncertainty. This is a much smaller error than for the fainter dwarfs in Sect. 3.3. Reasons for that are the higher surface brightness of the dwarfs investigated in Hydra and Centaurus and the better image quality of the FORS1 data.

The procedure to measure \overline{m}_I of the investigated dwarf galaxies in Hydra and Centaurus was very similar to that already outlined in Sect. 3.3.1. The 4 giant galaxies NGC 3309 and NGC 3311 (Hydra) as NGC 4696 and NGC 4709 (Centaurus) received a “special treatment” explained in Sect. 4.3.5. The steps performed to measure \overline{m}_I for

the dwarfs are listed below. There are two main changes with respect to Sect. 3.3.1: The first change is that the background fluctuations ΔBG are now measured in a large comparison field several degrees away from each cluster and not anymore in three small portions close to each investigated galaxy (point 8). This can be done because of the significantly better and more stable image quality across the entire image. ΔBG was typically about 0.10 mag for both the Hydra and Centaurus galaxies. The second change is that now the contributions of globular clusters to the measured fluctuations ΔGC are of the order 0.2 mag and cannot be neglected anymore (point 11).

The steps for deriving SBF magnitudes are as follows:

1. Model mean galaxy light
2. Detect and subtract remaining contaminating objects from original image.
3. Model mean galaxy light on the cleaned image.
4. Subtract model of original image.
5. Divide resulting image by square root of the model, cut out circular portion with radius typically 20-25 pixel ($4 - 5''$), corresponding to **8-10** seeing disk diameters.
6. Mask out contaminating sources like foreground stars and background galaxies. The completeness limit of the contaminating source detections was determined by artificial star experiments using SExtractor and the ARTDATA package under IRAF. The limiting magnitude for point source detection was about $I = 24.7$ mag for the Hydra images and $I = 25.0$ mag for the Centaurus images.
7. Calculate the power spectrum (PS) of the cleaned image.
8. Calculate the PS of the sky background in a comparison field several degrees away from the clusters. This comparison field had the same observing conditions as the cluster images. Like for the SBF measurement of the dwarf galaxies, all sources above the detection limit were masked out before the PS calculation. The resulting fluctuation amplitude is then divided by the mean galaxy intensity in the region where SBF are measured. This normalised background PS ΔBG is then subtracted from the PS of the SBF image.
9. Obtain the azimuthal average of the resulting PS.
10. Fit equation (3.1) to the result: $P(k) = E(k) \times P_0 + P_1$
11. Obtain the desired observable \bar{m}_I from

$$\bar{m}_I = -2.5 * \log(P_0) + ZP_I - A_I - \Delta k + \Delta GC \quad (4.1)$$

This equation differs from equation (3.2) by one term, namely ΔGC . This is the contribution to the fluctuations caused by Globular Clusters (GCs) below the detection limit and cannot be neglected anymore. This is because the globular cluster luminosity function is sampled only down to its turn-over magnitude (TOM), which is about $I \simeq 24.8$ mag at an assumed distance of 45 Mpc. ΔGC is calculated using equation (15) from Blakeslee & Tonry ([1995]), assuming a TOM of $M_I = -8.46 \pm 0.2$ mag for the globular cluster luminosity function (Kundu & Whitmore [2001]) and a width $\sigma = 1.2$ mag. The specific frequency S_N of the dwarfs' GC systems was estimated by counting the point sources detected in the dwarf galaxy image after subtraction of the elliptical

model, assuming that 50% of the GCs are detected (the completeness magnitude as determined from artificial star experiments roughly corresponds to the apparent turnover magnitude of the GCLF expected at both the distance of Hydra and Centaurus, see Table 4.5 and Fig. 4.5). The number of detected GCs per galaxy is generally below ten. Therefore, only average S_N for sub-samples of GCs could be determined.

For the Centaurus cluster dwarfs, we estimate an average specific frequency of $S_N = 5.4 \pm 1.0$ for all dwarfs, independent on location in the cluster. For Hydra, we find a dependence of S_N on the location in the cluster: for the 5 dwarfs in field 1, which contains the extended halo GC population of the cD galaxy NGC 3311, we find a high average specific frequency of $S_N = 11.5 \pm 2.8$, for the 8 dwarfs in the other fields we find $S_N = 2.3 \pm 0.8$. The apparent TOM of the GCLF was assumed to be equal for all dwarfs, derived from their mean SBF-distance. As ΔGC depends on the fraction of GCs that can be detected and hence correlates somewhat with galaxy distance, the mean ΔGC and mean SBF-distance of the dwarfs were determined iteratively in each cluster, using the mean colour of all dwarfs in each cluster. We note however, that this correlation is not very strong: changing the assumed TOM of the GCLF by 0.1 mag, which as we show in Sect. 4.4 is the uncertainty of the mean Hydra and Centaurus SBF-distance, changes ΔGC by less than 0.01 mag. To obtain ΔGC for a single dwarf, the mean ΔGC was changed according to the specific colour of that galaxy, resulting in a scatter of about 0.03 mag in ΔGC between the different dwarfs. For Centaurus, ΔGC was typically around 0.20 mag. For the Hydra dwarfs, it was about 0.45 mag in field 1 and generally below 0.1 mag for the other fields.

For the dEs, the main error contribution to their SBF-distance comes from the measurement of P_0 . Its error is derived from the Monte Carlo simulations as shown in Sect. 2, Fig. 2.8. At the approximate distance of Hydra/Centaurus ($\simeq 33$ mag), the error of P_0 is found to be about 0.25 mag for dEs with $V_0 < 16.5$ and about 0.40 mag for dEs fainter than that.

4.3.5 SBF measurements for the giants

The SBF measurement procedure was slightly different for the brightest and extended giant galaxies in both clusters, namely NGC 4696 and NGC 4709 in Centaurus and NGC 3309 and NGC 3311 in Hydra.

The first difference was that ΔGC was derived directly from the investigation of the respective globular cluster systems. S_N and the apparent TOM are determined in the regions where SBF are measured, as summarised in Table 4.5 and shown in Fig. 4.5. For this fitting, we keep σ fixed at 1.3 mag (Kundu & Whitmore [2001]), with an error allowance of 0.15 mag. For the Hydra cluster giants, the TOM of these GCLFs is only poorly constrained, due to the relatively low number of GCs present in the images and the somewhat brighter completeness magnitude as compared to the Centaurus data. However, due to the bivariate of σ and TOM, ΔGC is almost independent of both

values. E.g. adopting $\sigma = 1.1$ mag instead of 1.3 mag results in a 0.5 mag brighter TOM and 30% lower S_N for both NGC 3309 and 3311. This gives $\Delta GC = 0.21$ mag for NGC 3311 and $\Delta GC = 0.11$ mag for NGC 3309, lower by only 0.03-0.04 mag than the values obtained from using $\sigma = 1.3$ mag. The S_N of NGC 3311 is lower by 1.7σ than the value of $S_N = 15 \pm 6$ found by McLaughlin et al. [1995], but their study investigated radial distances between 0.5 and $3.5'$, outside the area sampled by us. Our value is in qualitative agreement with previous findings that the local specific frequency decreases significantly in the innermost regions of cD galaxies (e.g. McLaughlin [1994], Forte et al. [2005]). For NGC 4696, our value is consistent with the result of Lee & Geisler ([1997] and Lee, private communication), who obtain $S_N = 6 \pm 1$. For NGC 4709 and NGC 3309, we have not found any literature data on their GC systems. Our results are slightly higher but still consistent with the mean $S_N = 2.4 \pm 1.8$ obtained by Kundu & Whitmore ([2001]) from HST investigations of 28 nearby early-type giants.

The second difference in the SBF measurement procedure as compared to the dwarf galaxies was that \bar{m}_I and $(V - I)_0$ were measured independently in three concentric rings (two for NGC 4709). Those covered the range $8'' < r < 26''$ for NGC 3309, $8'' < r < 32''$ for NGC 3311, $52'' < r < 100''$ for NGC 4696 and $32'' < r < 54''$ for NGC 4709. For each ring, an independent SBF distance estimate was derived. The scatter of those values added in quadrature to the cosmic scatter allowance of 0.10 mag is adopted as the distance error for those 4 giant galaxies.

Note that for NGC 4709, an additional error allowance is added to the distance estimate: for this galaxy we obtain an average colour of $(V - I) = 1.35$ mag in the three rings, significantly redder than the value of Jensen et al. ([2001]) and Tonry et al. ([2001]), who obtain $(V - I)_0 = 1.22$ and 1.21 mag, respectively. Carefully re-analysing our photometry shows that the sky level is the parameter that most influences the colour, given that the halo of NGC 4709 extends to almost the image limits. Systematic errors in the photometric calibration are unlikely as the mean SBF-distance to the 5 other galaxies in the field of NGC 4709 agree to within 2% with the mean of the entire Centaurus sample. We find that the amount of large scale flat field variations present in our images can in the worst case account for a colour shift of up to $\simeq 0.10$ mag for NGC 4709. However, the particular sky values adopted for NGC 4709 is consistent with the large scale flat field variations derived in other fields not dominated by one major galaxy. This translates into a lower colour limit of $(V - I)_0 \simeq 1.30$ mag based on the information available from our data. We therefore add in quadrature an additional error allowance of $0.05 \times 4.5 = 0.225$ mag to the distance error of NGC 4709.

Figs. 4.3 and 4.4 show example images illustrating the SBF measurement procedure for two Centaurus and two Hydra dwarfs and the giants NGC 4696 (Centaurus) and NGC 3311 (Hydra).

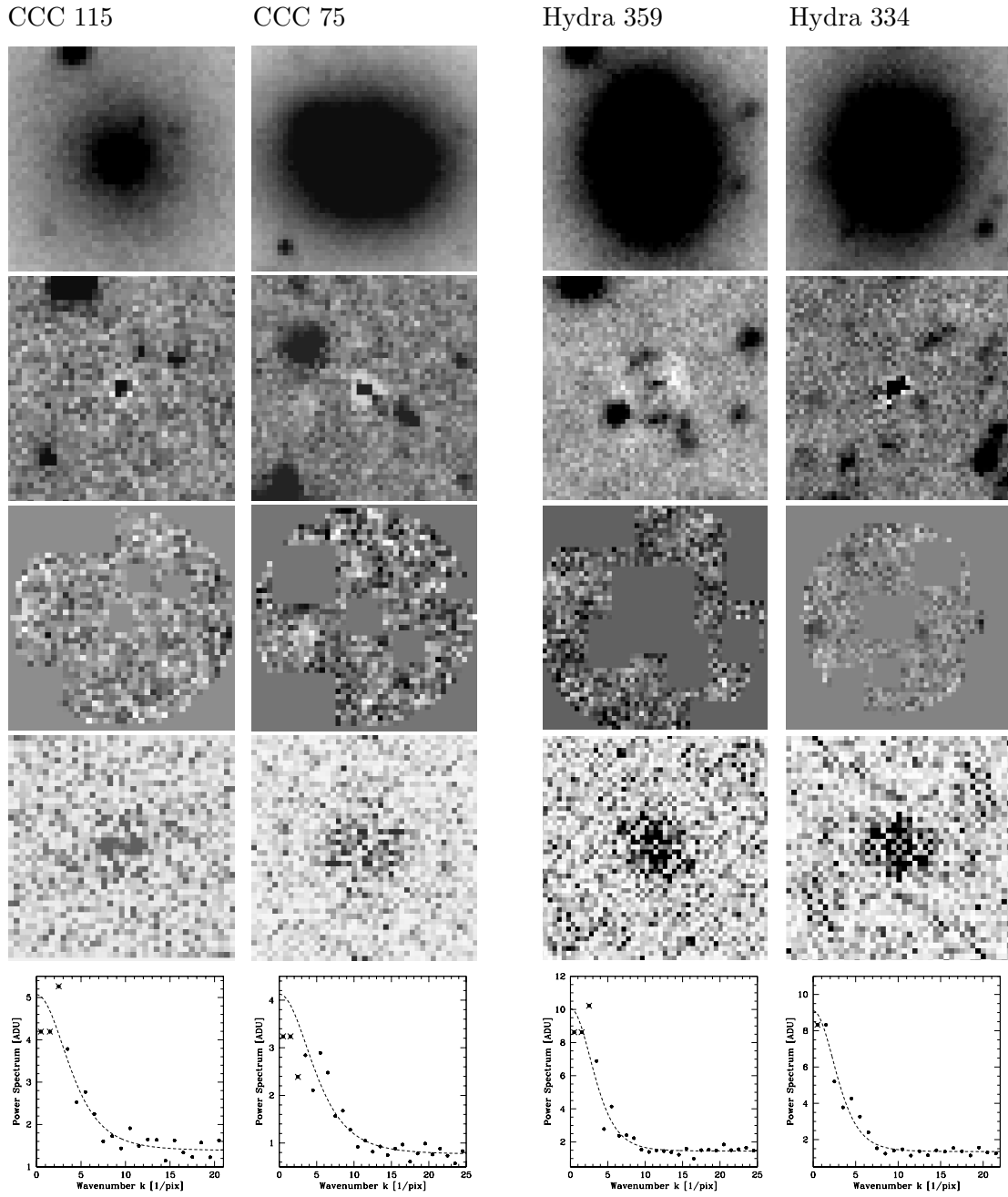


Figure 4.3: Example images and plots for two Centaurus (left) and two Hydra (right) cluster dwarf galaxies, illustrating the SBF measurement procedure. From left to right: CCC 115 (Centaurus field 3); CCC 75 (Centaurus field 1); Hydra 359 (Hydra field 1); Hydra 334 (Hydra field 1). From top to bottom: 1. Original galaxy image; elliptical model subtracted from former image. 2. Former image divided by square root of model, with contaminating sources and region outside measurable circle masked. 3. Power spectrum of the former image. 4. Azimuthal average of the former image with dashed line showing the result of the fit and crosses marking the points rejected in the fit.

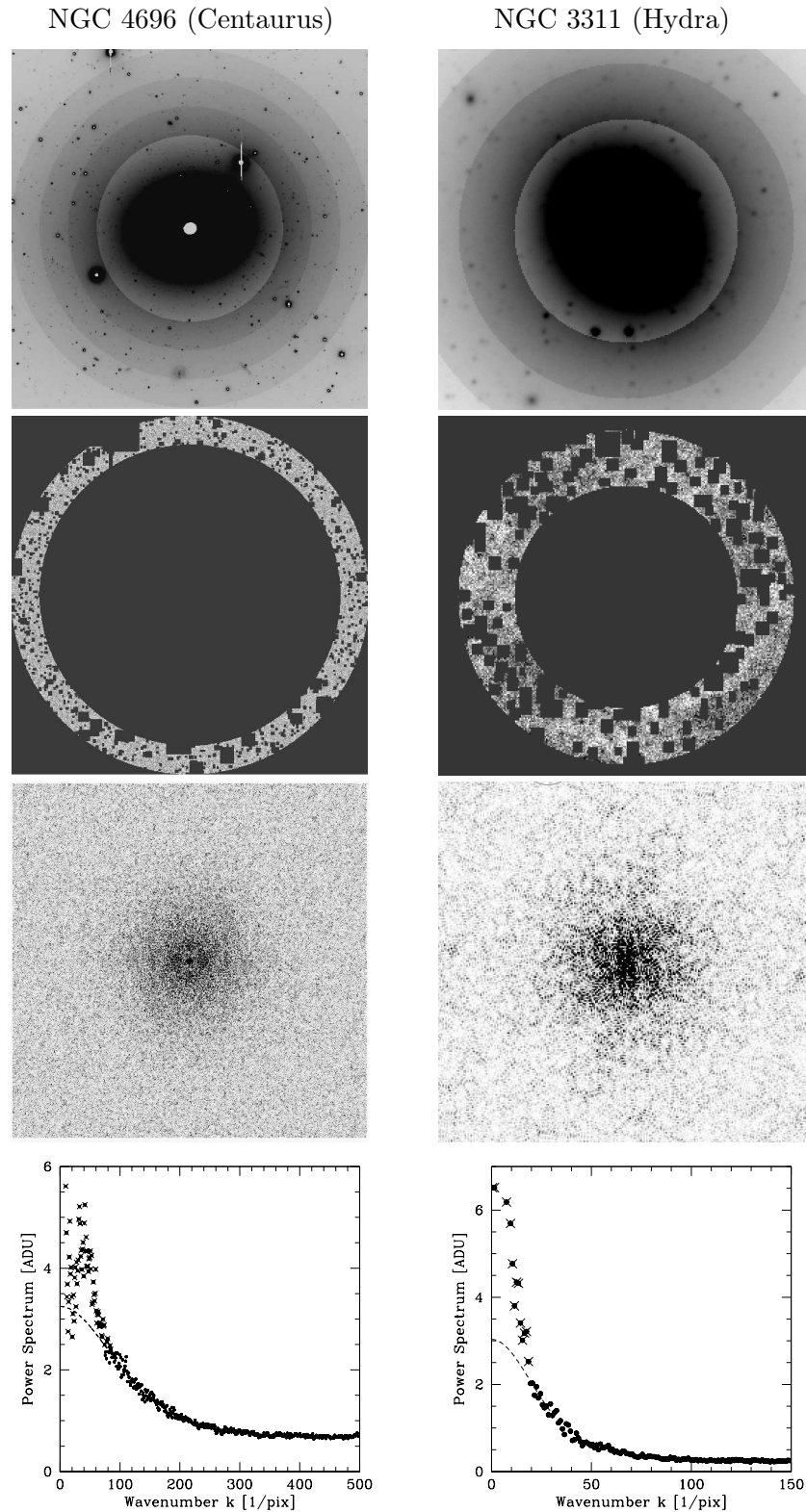


Figure 4.4: Example images and plots illustrating the SBF measurement procedure for NGC 4696, the central galaxy of the Centaurus cluster (left) and NGC 3311, the central galaxy of the Hydra cluster (right). From top to bottom: 1. Original galaxy image. The three rings within which SBF were measured are indicated by different offset intensities. 2. Image showing one of the three rings with all contaminating objects masked. 3. two-dimensional power spectrum of the former image. 4. Azimuthally average of the former image with dashed line showing the result of the fit and crosses marking the points rejected for the measurement.

Gal-Nr.	TOM [mag]	σ	I_{cut} [mag]	$(m - M)_{\text{GC}}$	$(m - M)_{\text{SBF}}$	$N_{\text{GC,rings}}$	$M_{\text{V,rings}}$	$S_{\text{N,rings}}$
NGC 3309	25.49 ± 0.70	1.30	24.70	33.95 ± 0.73	32.81 ± 0.13	430 ± 140	-20.30 ± 0.2	3.5 ± 1.3
NGC 3311	25.09 ± 0.59	1.30	24.70	33.55 ± 0.63	33.09 ± 0.14	810 ± 300	-20.60 ± 0.2	4.6 ± 1.9
NGC 4696	24.49 ± 0.27	1.30	25.05	32.95 ± 0.34	33.14 ± 0.16	2390 ± 300	-21.25 ± 0.2	7.3 ± 1.5
NGC 4709	23.86 ± 0.26	1.30	25.00	32.32 ± 0.33	32.50 ± 0.27	360 ± 60	-19.60 ± 0.2	5.0 ± 1.3

Table 4.5: Details of the globular cluster luminosity function (GCLF) fitting for the Hydra galaxies NGC 3309 and NGC 3311 and the Centaurus galaxies NGC 4696 and NGC 4709, performed in the rings where SBF were measured. A Gaussian with width $\sigma = 1.3$ mag (Kundu & Whitmore [2001]) with an error allowance for σ of ± 0.15 mag is fit to the incompleteness corrected number counts in Fig. 4.5. The error of the turnover magnitude (TOM) is the maximum of the fitting error and the difference in TOM when changing σ to its lower and upper limit of 1.15 and 1.45 mag. I_{cut} is the limiting magnitude for the GCLF fitting, identical to the 50% completeness limit for GC detection. An absolute turn-over magnitude of $M_I = -8.46 \pm 0.2$ mag is assumed (Kundu & Whitmore [2001]). The GCLF-TOMs of the two Hydra galaxies are poorly constrained both because of a brighter cutoff magnitude and lower number of GCs compared to NGC 4696.

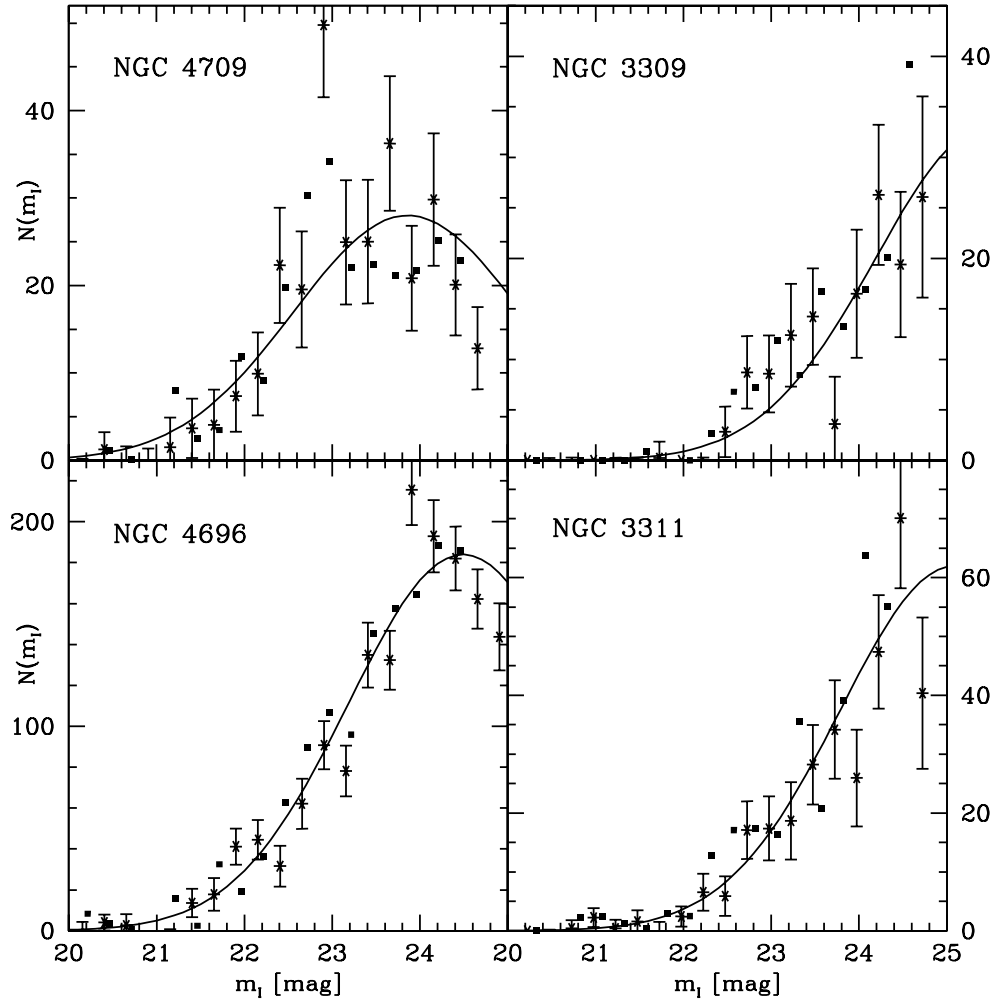


Figure 4.5: Incompleteness corrected globular cluster luminosity functions for the 4 indicated galaxies in the rings where SBF were measured. Asterisks with error bars are counts in the I -band, filled squares are counts in the V -band shifted to I assuming $(V - I)_0 = 1.04$ from Kundu & Whitmore ([2001]). The number counts are corrected for background contamination and shown up to the faintest magnitude bin for which the completeness was above 50%. The solid lines are Gaussian fits, whose parameters are the mean of the values fit independently in V and I . The derived turnover magnitudes and specific frequencies S_N are given in Table 4.5.

4.4 Results

The results of the SBF distance estimates to the Hydra and Centaurus galaxies are shown in Tables 4.6 and 4.7. Note that due to the very good seeing for the Centaurus data (0.4'' FWHM in the *I*-band), the modified S/N^* is substantially higher than the canonical one for all investigated galaxies. Those two galaxies with $S/N < 2$ clearly have $S/N^* > 3$. For the Hydra cluster, for which the seeing was between 0.6 and 0.7'', this effect is not that strong, but still obvious. In the Hydra sample there are two galaxies (No. 150 and 322) with $S/N^* < S/N$, due to the small area used for sampling the SBF. For the giant galaxies NGC 3308, 3309, 3311, 4709 and 4696, S/N^* is extremely high due to the large number of seeing disks sampled.

The simulations from Sect. 2 predict a limiting absolute galaxy magnitude for reliable SBF measurement of about $M_V \simeq -15$ mag for 0.5'' seeing, 33.4 mag distance modulus and 1 hour integration time with the VLT. From Fig. 4.7 it is clear that the actually achieved limiting magnitude with 3000 second integration time is about of that order, even slightly fainter. The about 0.2 mag smaller distance modulus of the joint Hydra/Centaurus sample and the 20% smaller integration time as compared to the simulations have opposite effects on the limiting magnitude. The limiting magnitude for Centaurus is slightly fainter for Centaurus, as the better seeing of about 0.4'' as compared to 0.6'' for Hydra overcompensates the 0.2 mag higher distance and hence weaker SBF signal for Centaurus, in agreement with formula (2.6) and Table 2.1. From all this, we can again confirm that the simulations from Sect. 2 give realistic predictions for the viability of SBF method applications, as already shown in Sect. 3

4.4.1 Relative distance between Hydra and Centaurus from SBF

The mean distance of the Hydra cluster is 41.2 ± 1.4 Mpc, the mean distance of the Centaurus cluster is 45.3 ± 2.0 Mpc. The corresponding mean distance moduli are 33.07 ± 0.07 mag for Hydra and 33.28 ± 0.09 mag for Centaurus. The relative distance in magnitudes then is $(m - M)_{\text{Cen}} - (m - M)_{\text{Hyd}} = 0.21 \pm 0.11$ mag. The relative distance in Mpc is $d(\text{Cen}) - d(\text{Hyd}) = 4.1 \pm 2.4$ Mpc.

When excluding distances to galaxies with colours outside the empirically calibrated range $1.0 < (V - I)_0 < 1.30$ mag, the Hydra and Centaurus distances change by less than 1%. The relative distance between the central Centaurus galaxy NGC 4696 and the three Hydra giants NGC 3308, 3309, 3311 is 0.16 ± 0.19 mag, consistent with the relative distance derived using all galaxies. NGC 4709 was not included in that comparison, as it is redder than the empirically calibrated range and might be located somewhat in front of Centaurus, see also Sect. 4.5.6.

Nr.	Field	S/N	S/N^*	Δ_{mask}	Δ_{BG}	Δ_{GC}	\bar{m}_I	$(m - M)$	d [Mpc]
258	1	4.46	6.82	0.393	0.115	0.43	31.16 ± 0.46	33.50 ± 0.47	50.19 ± 11.0
359	1	6.28	12.1	0.305	0.122	0.46	30.44 ± 0.46	32.68 ± 0.47	34.29 ± 7.5
334	1	6.83	11.7	0.268	0.116	0.45	30.67 ± 0.45	32.94 ± 0.47	38.76 ± 8.5
357	1	9.87	16.6	0.210	0.065	0.38	30.25 ± 0.45	32.83 ± 0.49	36.74 ± 8.4
140	1	6.31	14.5	0.217	0.100	0.47	31.52 ± 0.49	33.71 ± 0.51	55.15 ± 13.0
N3309	1	12.90	92.2	0.175	0.042	0.14	31.30 ± 0.09	32.81 ± 0.13	36.47 ± 2.1
N3311	1	10.30	78.2	0.208	0.030	0.25	31.33 ± 0.10	33.09 ± 0.14	41.42 ± 2.6
482	2	3.32	3.78	0.204	0.241	0.07	30.65 ± 0.42	32.96 ± 0.44	39.02 ± 8.0
421	2	6.78	10.92	0.203	0.073	0.08	30.83 ± 0.27	32.93 ± 0.30	38.54 ± 5.3
123	2	5.04	5.54	0.255	0.121	0.08	31.02 ± 0.43	33.15 ± 0.44	42.69 ± 8.8
172	2	4.94	5.48	0.108	0.135	0.07	30.64 ± 0.42	32.85 ± 0.44	37.22 ± 7.6
252	3	3.90	8.3	0.221	0.189	0.08	31.07 ± 0.42	33.12 ± 0.42	42.05 ± 8.3
358	5	4.91	7.2	0.119	0.145	0.06	31.03 ± 0.42	33.16 ± 0.44	42.84 ± 8.8
N3308	5	13.20	72.5	0.130	0.028	0.24	31.88 ± 0.28	33.04 ± 0.30	40.63 ± 5.7
322	6	8.86	5.2	0.248	0.142	0.04	30.42 ± 0.42	32.73 ± 0.44	35.13 ± 7.2
150	6	6.63	5.9	0.238	0.109	0.05	31.30 ± 0.27	33.40 ± 0.29	47.85 ± 6.5
								33.07 ± 0.07	41.20 ± 1.4

Table 4.6: Result of the SBF measurements for the investigated Hydra cluster galaxies. The error in metric distance d is the mean of the upper and lower distance error range corresponding to the magnitude error in $(m - M)$. The columns Δ_{mask} , Δ_{BG} , Δ_{GC} , \bar{m}_I and $(m - M)$ are given in magnitudes. For the two giant galaxies NGC 3309 and NGC 3311, the results shown are the averaged means over the three rings investigated. S/N^* as defined in Sect. 2.4.2. In the lowest row, the mean distance d and the corresponding distance modulus $(m - M)$ of all galaxies are given.

Nr.	Field	S/N	S/N^*	Δ_{mask}	Δ_{BG}	Δ_{GC}	\bar{m}_I	$(m - M)$	d [Mpc]
N4696	1	4.78	228	0.090	0.090	0.23	31.840 ± 0.120	33.14 ± 0.17	42.5 ± 3.20
75	1,2	3.84	13.7	0.178	0.079	0.18	31.289 ± 0.430	33.60 ± 0.45	52.5 ± 11.0
61	1	5.76	30.0	0.174	0.068	0.26	31.456 ± 0.290	33.23 ± 0.32	44.2 ± 6.50
70	1	11.1	42.6	0.20	0.012	0.34	31.260 ± 0.310	32.58 ± 0.33	32.8 ± 5.10
52	1	4.39	12.3	0.168	0.072	0.22	31.473 ± 0.430	33.47 ± 0.45	49.4 ± 10.0
89	2	7.45	44.2	0.150	0.020	0.25	31.772 ± 0.290	33.50 ± 0.31	50.1 ± 7.30
N4709	3	5.00	156	0.140	0.089	0.06	31.623 ± 0.083	32.50 ± 0.27	31.6 ± 3.9
124	3	1.87	6.40	0.153	0.199	0.13	30.561 ± 0.430	33.33 ± 0.57	46.3 ± 12.0
123	3	8.68	29.5	0.151	0.041	0.19	30.594 ± 0.430	32.86 ± 0.45	37.3 ± 7.70
121	3	3.49	13.1	0.183	0.116	0.24	31.454 ± 0.460	33.54 ± 0.47	51.1 ± 11.0
115	3	3.00	10.7	0.145	0.169	0.17	31.063 ± 0.430	33.49 ± 0.45	50.0 ± 10.0
111	3	13.1	67.9	0.122	0.035	0.18	30.527 ± 0.280	32.88 ± 0.30	37.7 ± 5.30
125	4	11.2	20.7	0.166	0.028	0.65	31.198 ± 0.380	33.24 ± 0.40	44.5 ± 8.30
58	5	2.85	16.1	0.184	0.096	0.13	31.419 ± 0.430	33.73 ± 0.44	55.7 ± 11.0
68	6	1.22	3.50	0.144	0.396	0.13	31.058 ± 0.430	33.62 ± 0.47	53.1 ± 12.0
								33.28 ± 0.09	45.3 ± 2.0

Table 4.7: Result of the SBF measurements for the investigated Centaurus cluster galaxies. Columns as in Table 4.6.

4.4.2 Peculiar velocities of Hydra and Centaurus

To estimate the distortion of the Hubble flow between us and Hydra, we adopt the mean heliocentric radial velocity $3853 \pm 128 \text{ km s}^{-1}$ of the 44 Hydra cluster members within the inner $10'$ of the cluster center, based on the catalog of Christlein & Zabludoff ([2003]). This velocity is corrected for the relative motion of the Sun with respect to the CMB. We adopt the value derived by Lineweaver et al. ([1996]) from the COBE dipole CMB anisotropy, who find the Sun moving at 369 km s^{-1} toward galactic coordinates $l = 264.^{\circ}31$, $b = 48.^{\circ}05$. This results in a CMB dipole velocity component of $+336 \text{ km s}^{-1}$ towards the Hydra cluster and of $+281 \text{ km s}^{-1}$ towards the Centaurus cluster. The mean CMB rest-frame radial velocity of the Hydra cluster then becomes $4190 \pm 128 \text{ km s}^{-1}$. We assume a cosmological value of $H_0 = 72 \pm 4 \text{ km s}^{-1} \text{ Mpc}^{-1}$ (e.g. Freedman et al [2001], Spergel et al. [2003], Tegmark et al. [2004]). Then, our mean Hydra cluster distance of $41.2 \pm 1.4 \text{ Mpc}$ corresponds to a peculiar velocity of $1225 \pm 235 \text{ km s}^{-1}$.

Regarding the Centaurus cluster, we restrict our considerations to the dominant component Cen30. Its heliocentric radial velocity is $3170 \pm 174 \text{ km s}^{-1}$ (Stein et al. [1997]), yielding a CMB velocity of $3450 \pm 174 \text{ km s}^{-1}$. The mean distance of the 8 Cen30 members investigated by us is $45.0 \pm 2.7 \text{ Mpc}$. The cosmological CMB velocity value corresponding to $H_0 = 72 \text{ km s}^{-1} \text{ Mpc}^{-1}$ is $3240 \pm 240 \text{ km s}^{-1}$. The peculiar velocity of Cen30 then is $210 \pm 295 \text{ km s}^{-1}$, much smaller than for Hydra and consistent with an undistorted Hubble flow towards Centaurus. If we include the Cen45 component in our analysis, the peculiar velocity rises slightly to $450 \pm 300 \text{ km s}^{-1}$, still lower than the Hydra velocity by about 800 km s^{-1} at 2σ significance. Using only the giant galaxies for the peculiar velocity calculation, we obtain $395 \pm 345 \text{ km s}^{-1}$ for NGC 4696 in Cen30 and $1345 \pm 240 \text{ km s}^{-1}$ for Hydra, agreeing very well with the values obtained from the entire sample.

In Fig. 4.6, a Hubble diagram for Hydra and Centaurus is shown, illustrating the higher peculiar velocity for Hydra. Within the uncertainties of the measured distances, we cannot detect a negative slope between distance and radial velocity as it would be the case if the more distant galaxies in the sample would be falling into the Great Attractor from behind. See also the next section for a discussion on the depth of both clusters.

In Sect. 4.5.1, it will be discussed whether the high peculiar velocity for Hydra together with the lower one found for Centaurus is consistent with the Great Attractor model as proposed by T00.

4.4.3 Depth of the Hydra and Centaurus clusters

The mean single measurement uncertainty for the Hydra cluster SBF-distances as shown in Table 4.6 is 7.4 Mpc , whereas the scatter of these distances around their mean is 5.7 Mpc . For the Centaurus cluster (Table 4.7), the mean single measurement uncertainty is 8.3 Mpc , whereas the distance scatter is 7.5 Mpc . These values are consistent with the assumption of a δ -distribution for the real distances in both clusters. We derive an upper

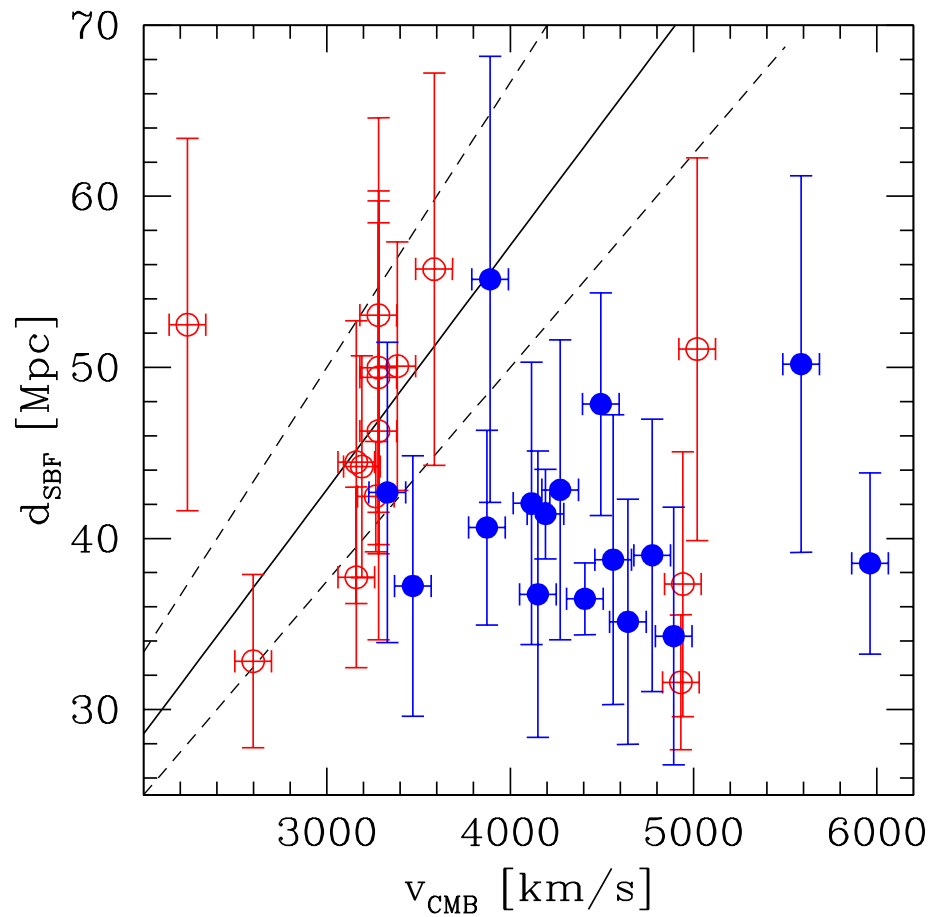


Figure 4.6: CMB rest-frame radial velocity is plotted vs. SBF distance for the Hydra galaxies (filled circles) and the Centaurus galaxies (open circles). The solid line gives the Hubble flow for $H_0=70 \text{ km s}^{-1} \text{ Mpc}^{-1}$. The upper dashed line corresponds to $H_0=60$, the lower dashed line to $H_0=80$.

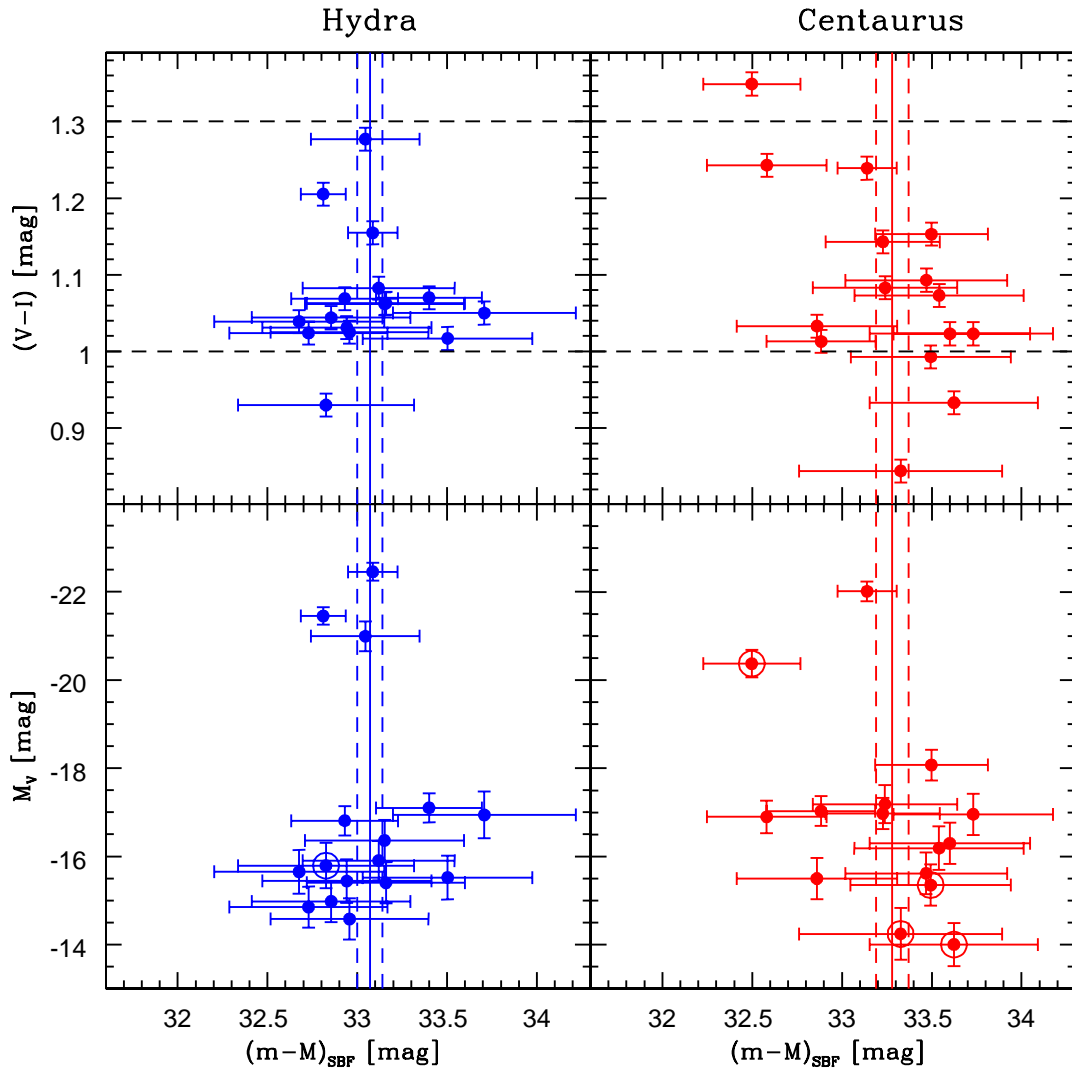


Figure 4.7: *Left panels:* Distance modulus $(m - M)_{\text{SBF}}$ of the Hydra galaxies plotted vs. their absolute magnitude M_V (bottom) and colour $(V - I)_0$ (top). The mean distance modulus with its 1σ error is indicated by the solid and dashed vertical lines. The dashed horizontal lines in the top panel indicate the colour range of the empirical SBF calibration (1.10) by Tonry et al. ([2001]). The data points outside this colour range – for which calibration equation (2.1) was used – are marked by open circles in the lower panel. *Right panels:* Plot of the same entities as in the left panels for the Centaurus cluster distances.

limit for the depth of both clusters applying the inequality $\frac{(n-1)(\Delta x)^2}{\chi^2_{1-\frac{\alpha}{2}}} \leq \sigma^2 \leq \frac{(n-1)(\Delta x)^2}{\chi^2_{\frac{\alpha}{2}}}$ to obtain the confidence interval at probability α for the real variance σ^2 of a distribution of n measurements with a measured variance Δx^2 (Hackbusch et al. [1996]). From tabulated χ^2 values we find that the Hydra cluster would have to be radially extended over 3.5 Mpc to both sides in order to exclude with 95% confidence a δ -distribution for the distance of our sample galaxies. For the Centaurus cluster, this radial extension is 5.7 Mpc.

We therefore derive a formal upper limit of ± 3.5 Mpc radial extension for the Hydra cluster and ± 5.7 Mpc for the Centaurus cluster. The Hydra cluster's extension on the sky is about 3 degrees (Tonry et al. [2000]). At 41 Mpc distance this corresponds to about 2 Mpc. In case of a spherically symmetric distribution we would therefore expect a radial distance scatter of the order of ± 1 Mpc. I.e. for Hydra we can only exclude a cigar-shape with the major axis at least 3–4 times larger than the minor axis. This is quite unlikely for a relaxed or nearly relaxed cluster as it is the Hydra cluster (e.g. Tamura et al. [1996] and [2000], Yamasaki et al. [2003]). The Centaurus cluster's angular extension on the sky of 6 degrees (Lucey et al. [1986]) corresponds to a diameter of 4.7 Mpc at 45 Mpc distance. This would make us expect a distance scatter of about 2-2.5 Mpc around the mean in case of a spherical cluster shape. I.e. for the Centaurus cluster we can exclude a cigar-shape with the major axis being at least 2.5 times larger than the minor axis, leaving some space for a possible filamentary structure as discussed in Sect. 4.5.6.

4.5 Discussion

4.5.1 The Great Attractor acting upon Hydra and Centaurus

With the Hydra and Centaurus cluster distances derived in this chapter, some parameters of the Great Attractor (GA) model derived by T00 can be checked. The distance to the Cen30 component of Centaurus derived by us implies a rather low peculiar velocity of $210 \pm 295 \text{ km s}^{-1}$ with respect to an undisturbed Hubble flow. This has several possible implications for the Great Attractor model: the mass of the GA is much smaller than the $9 \times 10^{15} M_{\odot}$ determined by T00; the GA is very massive but the Centaurus cluster falls into the GA almost perpendicular to the line of sight; or, the Centaurus cluster *is* the Great Attractor.

The large peculiar velocity of $1225 \pm 235 \text{ km s}^{-1}$ that we derive for the Hydra cluster and the fact that a possible Hydra cluster infall into Centaurus has only a negligible radial component (see Fig. 4.10) supports the second possibility: a massive GA with its center of mass slightly behind the Hydra-Centaurus plane, in closer projection to Hydra than to Centaurus. Such a location, just like the position determined by T00, implies that the GA is not directly associated with any prominent galaxy cluster, see Figs. 4.8 and 4.10.

Before proceeding to a more detailed investigation of this possibility, it is useful to test

the null hypothesis that Hydra and Centaurus in reality share a common flow velocity. To do so, it is necessary to add in quadrature a “thermal” velocity dispersion component to the peculiar velocity errors of both clusters. The best fitting rms peculiar velocity from the SBF survey of T00 is 187 km s^{-1} . Padilla & Baugh ([2002]) give as the *pair-wise* line-of-sight cluster velocity dispersion expected in a Λ CDM universe a value of 250 km s^{-1} , corresponding to 175 km s^{-1} thermal component for a single cluster. We adopt as a somewhat conservative estimate of 200 km s^{-1} additional error contribution for each cluster. Then, we subtract in quadrature the mean error contribution from the uncertainty in H_0 from the error of the peculiar velocity difference, as we want to define the uncertainty of the relative peculiar velocity. This yields a relative peculiar velocity between Hydra and Centaurus of $1015 \pm 440 \text{ km s}^{-1}$. The null hypothesis of a common flow velocity for Hydra and Centaurus is therefore rejected at 2.3σ significance (98% confidence).

When including the Cen45 galaxies into the peculiar velocity estimate for Centaurus, one gets a relative peculiar velocity between Hydra and Centaurus of $775 \pm 440 \text{ km s}^{-1}$, less significant at the 1.8σ level (93% confidence). We note, however, that no Cen45 galaxy was included in Tonry et al.’s calculation of the local flow model, due to the peculiar nature of that sub-cluster. Inclusion of Cen45 into the peculiar velocity estimate uses as implicit condition that the masses of Cen30 and Cen45 have the same ratio as the number of galaxies in both clusters. Based on X-ray data from ROSAT, Reiprich & Böhringer ([2002]) estimate a mass of $\simeq 2.7 \times 10^{14} M_*$ for the Centaurus cluster ($M_* = 2 \times 10^{30} \text{ kg}$, the mass of the Sun). This would require that the infalling sub-component Cen45 has a mass of almost $1 \times 10^{14} M_*$, inconsistent with the very narrow velocity distribution of this sub-component (e.g. Stein et al. [1997], Lucey et al. [1986]). Taking the mean of the values obtained by Stein et al. and Lucey et al., Cen30 has a velocity dispersion of $\sigma \simeq 750 \text{ km s}^{-1}$, while Cen45 has $\sigma \simeq 200 \text{ km s}^{-1}$. Mass scales quadratically with velocity dispersion, and therefore one would expect a Cen45 mass more than an order of magnitude lower than that of the main component Cen30. Because of its quite low velocity dispersion, Stein et al. ([1997]) come to the conclusion that Cen45 can only be a loosely bound group of galaxies rather than a proper galaxy cluster. Therefore, we will in the following not include the Cen45 radial velocities for the calculation of the Centaurus peculiar velocity.

Fig. 4.8 shows the projected positions of the Hydra and Centaurus cluster and the Great Attractor from T00. The Great Attractor in this flow model is defined by its 3D-position between Centaurus and Hydra at a distance $d=43\pm 3 \text{ Mpc}$, over-density δ , infall exponent γ , core radius r_c and cutoff radius r_{cut} . T00 provide a FORTRAN program which implements their flow model including the Virgo Attractor, Great Attractor and a quadruple component. It gives as an output the expected CMB radial velocity at an input 3D-position. The parameters of all components and the cosmological parameters $H_0 = 78 \text{ km s}^{-1} \text{ Mpc}^{-1}$ and $\Omega_m = 0.2$ go into the calculation. Fig. 4.9 shows these expected CMB radial velocities at the 3D-positions of Hydra and Centaurus, for varying projected GA positions and at 4 different GA distances between 43 and 49 Mpc.

Except for the 3D-positions, all other GA parameters were adopted as determined by T00, because we only trace the peculiar velocity field at two 3D positions, which makes it senseless to fit a larger number of parameters. An updated distance set in a much larger area would be needed for that. The 4 different GA distances assumed are almost within the error range of 43 ± 3 Mpc given by Tonry for the GA distance. Also, the angular changes of the GA positions in Fig. 4.8 are only between Hydra and Centaurus and of the order of 20-30 degrees. They do not significantly affect the gravitational pull of the GA on the Local Group.

Figs. 4.8 and 4.9 show that the Hydra and Centaurus distances derived by our group can be explained by Tonry's GA model if the GA is shifted at least 10° towards lower super-galactic longitude and 10° towards lower latitude with respect to the original projected GA position determined by T00. This is illustrated also in Fig. 4.10. At an assumed GA distance of 43 Mpc, the GA would have to be directly behind the Hydra cluster in order to exert a sufficient gravitational pull. Already at 45 Mpc GA distance, GA projected positions up to 10° away from Hydra are possible. At GA distances of 47 and 49 Mpc – slightly outside the error range of T00's GA distance – the expected peculiar velocities rise and start to exclude a GA position directly behind Hydra. Note that at the original GA position from T00, the expected radial velocity for Hydra is below its measured velocity by about 1000 km s^{-1} , ruling out this position.

The expected peculiar velocity of Centaurus matches the observed one as soon as the projected GA position is several degrees away from Centaurus, see Figs. 4.8 and 4.9. It also matches the observed one if the GA is identical to the Centaurus cluster (position 1 at 45 Mpc distance). However, this latter possibility fails to explain the very large peculiar velocity measured for Hydra. If GA=Centaurus, then it would exert only a very small radial gravitational pull on Hydra, because Hydra's infall vector would be mainly tangential (see Fig. 4.10): Assuming GA=Centaurus and the T00 GA mass of $9 \times 10^{15} M_\odot$ yields a radial infall velocity for Hydra of $130 \pm 70 \text{ km s}^{-1}$, where the uncertainty arises from the error in relative distance between Hydra and Centaurus. The assumption that in addition to a common flow of both clusters – which is rejected at 98% confidence – there is a 200 km s^{-1} Hydra infall into Centaurus (=GA) is still rejected at 94% confidence. In this context one important notion is that the mass of the Centaurus cluster derived from X-ray temperature maps ($\simeq 3 \times 10^{14} M_\odot$, see for example Reiprich & Böhringer [2002]) is about a factor of 30 lower than the $10^{16} M_\odot$ estimated for the GA in T00. This a priori makes the Centaurus cluster an improbable GA candidate. We note that only in the case of an unrealistically massive GA at the Centaurus position with $5 \times 10^{16} M_\odot$ - which is totally inconsistent with the amount of peculiar velocities observed in the nearby universe and a factor of 100 more massive than Centaurus -, the confidence level of rejecting a common flow for Hydra and Centaurus drops to 1σ . A radial infall velocity for Hydra of $500 \pm 270 \text{ km s}^{-1}$ into the GA would be expected in this case.

It is clear that a simultaneous check of more than one parameter (mass, distance, infall parameter, etc.) of the Tonry GA can only be performed with an updated distance

set extending over a much larger area and distance range than sampled by us. Note, however, that only a change in projected position is *necessary* to explain the peculiar velocities of Hydra and Centaurus observed by us. To nevertheless get an idea on the order of the degeneracies involved when using only two 3D positions, we estimate the GA mass-distance degeneracy for projected GA positions close to Hydra (positions 6 to 11 in Fig. 4.9): at a GA distance of 47 Mpc, a smaller GA mass by a factor of two would still not underpredict the peculiar velocity for Hydra, while at a GA distance of 43 Mpc, a larger GA mass by a factor of two would still not overpredict the Hydra peculiar velocities.

The shift of the projected GA position that is required to obtain consistency with our peculiar velocity measurements is almost three times larger than its 3σ confidence range from T00. Note, however, that T00 did not include any Hydra cluster galaxy into their model calculations. This again stresses that a recalculation of the flow model might become necessary in the light of increasingly more high-quality SBF data being published.

Summarising, the two SBF-distances for Hydra and Centaurus derived by our group rule out a common flow velocity for these two clusters at 98% confidence. Within the scenario of a Great Attractor (GA) somewhere in the Hydra-Centaurus region, our results are inconsistent at 94% confidence with a picture where Centaurus is identical to the GA, both Centaurus and Hydra share a common flow and Hydra has an additional infall into the GA. Our results are consistent with a shift in projected GA position by at least 15° towards the Hydra cluster compared to the position determined by Tonry et al. ([2000]), see Figs. 4.8 and 4.10. A change in the GA mass or distance within the error ranges of Tonry’s flow model is not required.

Our results increase the angular distance between the Hydra-Centaurus GA and the overdense region in the Zone of Avoidance (ZOA), especially the Norma cluster, to about 50° . As the Norma cluster has also been proposed as the possible center of a “Great Attractor” region (Woudt et al. [2003], Kolatt et al. [1995]), this large angular separation supports the idea that the SBF-GA and the ZOA-GA might be different substructures within a generally overdense region of the universe.

4.5.2 Some other ideas

The main result of the previous section is that the Great Attractor is probably not identical to neither the Hydra nor Centaurus clusters. At face value this implies the existence of a super-massive invisible dark halo, in contradiction to the widely accepted paradigm that light traces matter reasonably well on large scales. We note that the same problem also holds for the position of the Great Attractor from the study of Tonry et al. ([2000]). However, one must keep in mind that this scenario is a rather simplified picture of reality. The mass distribution in the universe is continuous and the formal position of the Great Attractor is the center of mass of the entire – continuous – mass distribution in that particular region. Nevertheless, the absence of a prominent galaxy cluster in the background of Hydra and Centaurus is puzzling with respect to

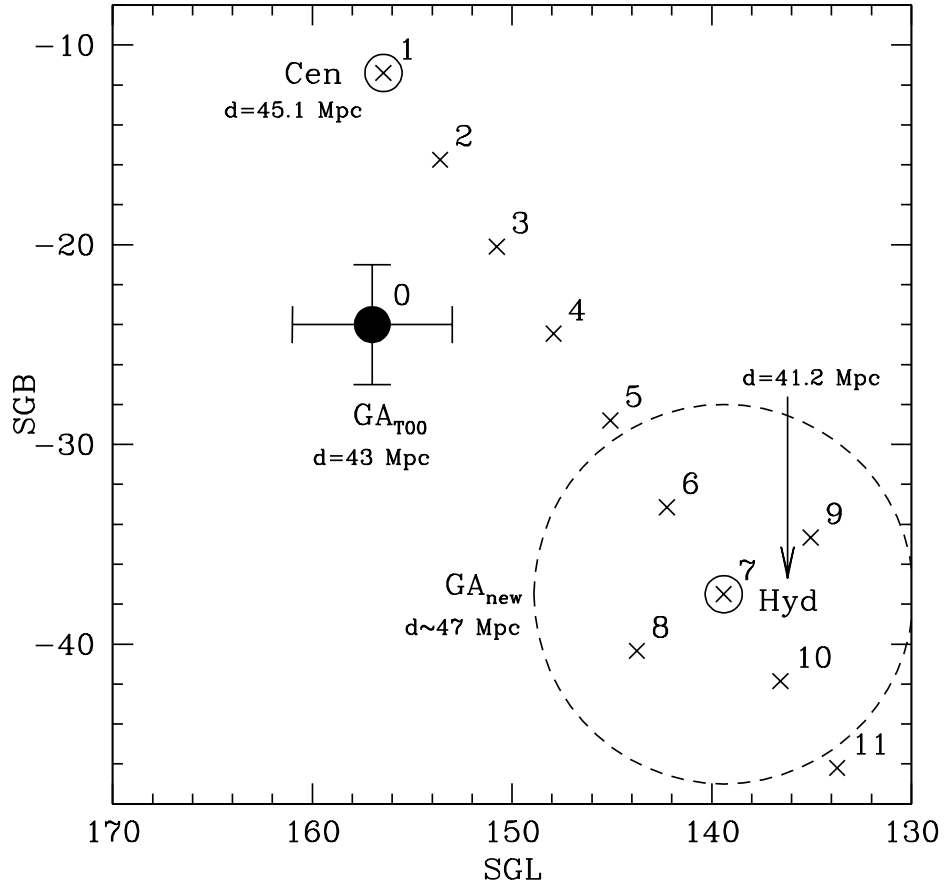


Figure 4.8: Positions in super-galactic coordinates of the following objects: Great Attractor (GA) according to Tonry et al. ([2000], T00 in the following) as filled circle; Hydra cluster as open circle at $\simeq (140, -38)$; Centaurus cluster as open circle at $\simeq (156, -12)$. Crosses and the attributed numbers indicate assumed projected positions of the GA for which the expected CMB radial velocities of Hydra and Centaurus are shown in Fig. 4.9, as calculated with the flow model by T00. The dashed circle delimits the region into which the projected position of the GA from T00 must be shifted to explain the observed distances and CMB velocities for Hydra and Centaurus, see Figs. 4.9 and 4.10. The GA can be accommodated in the entire circle region for a distance of $\simeq 47$ Mpc.

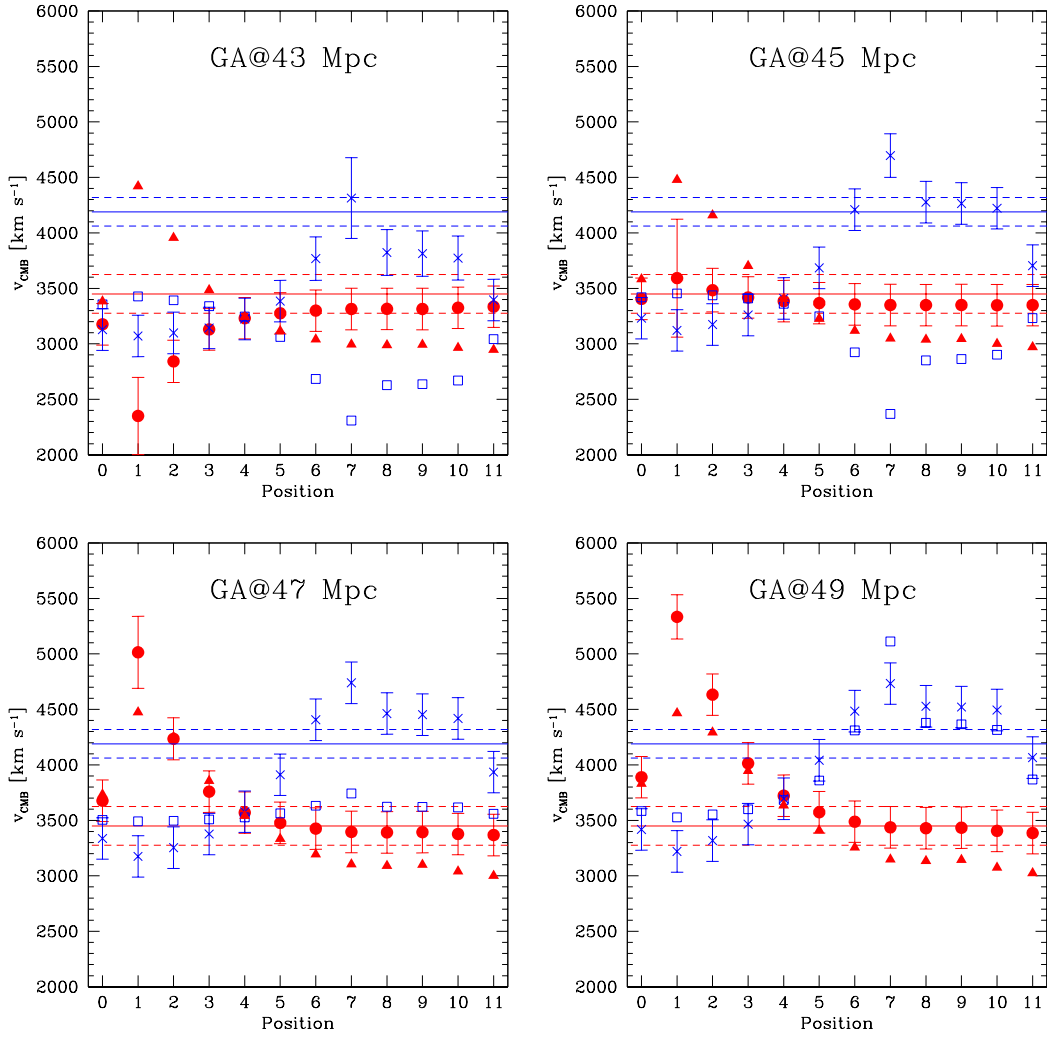


Figure 4.9: Comparison between expected and measured CMB radial velocities for 4 different GA distances of 43, 45, 47 and 49 Mpc, see also Fig. 4.10. The x-axes indicates the different projected GA positions from Fig. 4.8. *Filled circles:* expected CMB radial velocity for the Centaurus cluster based on the flow model by Tonry et al. ([2000]), using the Centaurus distance of this thesis. *Crosses:* expected CMB radial velocities for Hydra, using the Hydra distance of this thesis. *Open squares:* expected CMB radial velocities for Hydra assuming a 15% higher Hydra distance of 47 Mpc. *Filled triangles:* expected CMB radial velocities for Centaurus assuming a 15% lower Centaurus distance of 39 Mpc. Error bars have been omitted for these two sets of expected velocities. *Upper horizontal solid line:* CMB rest-frame radial velocity of the Hydra cluster (Christlein & Zabludoff [2003]). *Lower horizontal solid line:* CMB rest-frame radial velocity of the Centaurus clusters's Cen30 component (Stein et al. [1997]). The dashed horizontal lines indicate the respective error ranges.

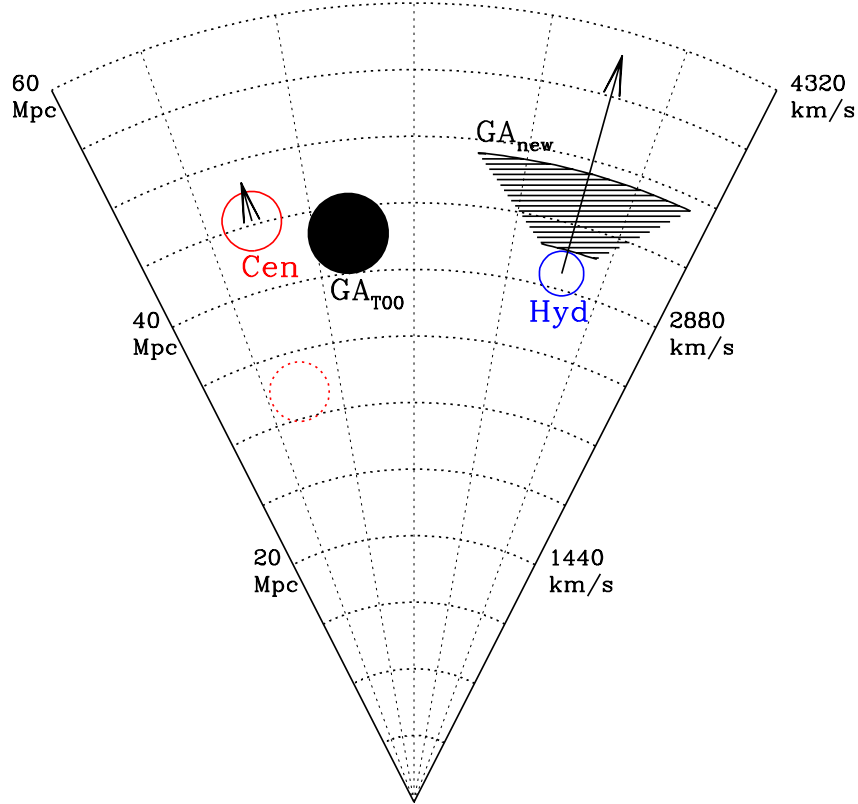


Figure 4.10: Pie slice distance-redshift diagram of a plane defined by the positions of the Centaurus and Hydra cluster and the Sun, with the Sun being the origin. We assume $H_0 = 72 \text{ km s}^{-1} \text{ Mpc}^{-1}$ to convert distance to CMB redshift. The dotted meridian lines are separated by 10° . The positions of the Centaurus and Hydra cluster are indicated as circles with solid lines, using the distances derived in this thesis. The dotted circle indicates the Cen30 distance derived by Tonry et al. ([2001]). The symbol sizes corresponds to the distance uncertainties. The position of the Great Attractor from Tonry et al. ([2000]) is indicated by the filled circle. The peculiar velocities derived in this thesis for Hydra and Centaurus are indicated by the arrows. The area within which the Tonry et al. Great Attractor can be accommodated in the light of our new peculiar velocity measurements is indicated by the shaded area, see also Figs. 4.8 and 4.9.

our results. We note that there have been some potential detections of extended “dark” structures in the nearby universe, such as a massive ($M_{\text{dyn}} \simeq 10^{11} M_*$) hydrogen cloud in Virgo (Minchin et al. [2005]) that has no optical counterparts, or the so-called “dark clumps” with implied masses $\simeq 10^{14} M_*$ that come out of weak lensing studies as matter overdensities with no optical counterparts (e.g. von der Linden et al. [2005], Dahle et al. [2003], Umetsu & Futamase [2000]). However, these potentially massive dark halos still have lower masses than that estimated for the GA by T00, and possible misinterpretations due to chance alignment and noise in the weak lensing analyses (von der Linden et al. [2005]) make “dark clumps” quite uncertain dark halo candidates.

One possibility to explain a high Hydra cluster peculiar velocity without the need for a “dark” Great Attractor would be infall along a filamentary structure. However, this scenario would require that our sample of galaxies in the direction and within the redshift range of Hydra be strongly biased towards those with lower distances. In Sect. 4.5.4 we show that this is not the case. Furthermore, Hydra is the prototype of a relaxed cluster (Tamura et al. [2000], Yamasaki et al. [2003]) and is therefore unlikely to have a radial extension significantly longer than the tangential one.

As shown in Sect. 4.5.1, one improbable (2%) – but not impossible – scenario is that both Hydra and Centaurus take part in a common bulk flow and that the large measured difference in peculiar velocity is caused by the thermal velocity field and our measurement errors. This scenario becomes more likely if in addition to the random peculiar velocity field we assume that both clusters were formed in the same primordial dark matter halo which carried away a net angular momentum which then was distributed among the Hydra and Centaurus sub-clumps. A crude estimate of additional peculiar velocity introduced into the Hydra-Centaurus system can then be obtained by assuming pure Keplerian rotation of both clusters around their centre of mass. Assuming the X-ray M_{200} mass estimates for Hydra and Centaurus by Reiprich & Böhringer ([2002]) yields a total mass of $\simeq 6 \times 10^{14} M_*$. The projected distance between both clusters is about 20 Mpc. The rotational velocity on a circular orbit of radius 10 Mpc with a central mass of $6 \times 10^{14} M_*$ is about 510 km s^{-1} . This is of the order of the peculiar velocity difference measured by us. However, the Hydra-Centaurus system is much too large to assume that both clusters are gravitationally bound to each other: the time for one revolution on a circular orbit would be around 90 Gyrs. Furthermore, one crossing time is about 30 Gyrs, about twice the age of the universe. Due to these large distances and long time-scales, it seems inadequate to consider Hydra and Centaurus as correlated sub-clumps of one main primordial dark matter halo. Therefore, adding in quadrature a thermal peculiar velocity component to the peculiar velocity errors of both Hydra and Centaurus (see Sect. 4.5.1) seems to be the proper way to account for primordial inhomogeneities in the matter and momentum distribution.

4.5.3 Comparison with literature distances

As our distances to the Hydra and Centaurus clusters imply large peculiar velocity differences between the two clusters, we compare both derived distances with values obtained by other authors.

Centaurus

There are 4 recent publications that present distances to either the entire Centaurus cluster or single cluster galaxies:

1. Tonry et al. ([1997]) obtained a significantly smaller distance of 32.51 ± 0.11 mag for Cen30 and 32.80 ± 0.09 mag for Cen45 in the course of their *I*-band SBF survey. However, already in Tonry et al. ([2001]) and Blakeslee et al. ([2002]) it has been pointed out that these results are subject to a Malmquist-like selection effect (Malmquist [1920]) biasing towards closer distances by up to 0.3 mag: the sensitivity of Tonry's survey is reached at about the distance of the Centaurus cluster. This makes those galaxies whose observational and statistical errors place them closer than the mean cluster distance more probable to be included in their survey than those who fall behind the cluster for their errors. Adding this 0.30 mag to Tonry's distances yields a Centaurus cluster mean distance of $\simeq 32.9 \pm 0.10$ mag. This is still significantly lower than our value. For the two galaxies NGC 4696 and NGC 4709 common to both surveys, our mean distance is 32.825 mag, less than 0.1 mag higher than the mean Tonry distance. As will be discussed in Sect. 4.5.6, NGC 4709 appears to be located in front of the Centaurus cluster, which is why our mean distance of NGC 4696 and NGC 4709 is significantly lower than the mean cluster distance.
2. For the Centaurus cluster galaxy NGC 4373, Pahre et al. ([1999]) obtain $(m - M) = 32.99 \pm 0.11$ mag from WFPC2 images, slightly lower than both our distance to NGC 4696 and the entire cluster.
3. An SBF-distance to NGC 4709 in the Centaurus cluster comes from Jensen et al. [2001], using *I*-band HST data. They obtain a distance modulus of 33.04 ± 0.17 mag, higher than our distance estimate at the 1.7σ level. This difference is entirely due to the significant colour difference between our rather red value of $(V - I)_0 = 1.35$ mag and that of Jensen et al., who obtain $(V - I)_0 = 1.22$ mag for NGC 4709. Adopting this bluer colour results in a 0.6 mag higher distance of 33.10 ± 0.15 mag for NGC 4709. This gives a significant disagreement with the GCLF-distance for that galaxy (see Table 4.5) at the 2.2σ level, but at the same time a nice agreement with the SBF-distance to NGC 4696. As already mentioned, the sky background fitting for NGC 4709 might partially cause this colour discrepancy, which is why we added an additional error allowance to the NGC 4709 distance estimate in Sect. 4.3.5. In any case, NGC 4709 is the main galaxy of the infalling sub-component Cen45. As we restrict our peculiar velocity estimates to the dominating Cen30 component of Centaurus due to the probably infalling nature of Cen45, the discrepancy for NGC 4709 does not influence the discussion on the Great Attractor hypothesis. A more detailed discussion on the Cen30-Cen45 relative distance

is given in Sect. 4.5.6.

Jensen et al. [2001] also obtain NICMOS F160W SBF measurements of 16 distant galaxies with $cz < 10000 \text{ km s}^{-1}$, among them NGC 4709 as the only Centaurus cluster member. For this galaxy they measure an apparent fluctuation magnitude of $\overline{m}_{\text{F160W}} = 28.51 \pm 0.07 \text{ mag}$. To convert this into $\overline{M}_{\text{F160W}}$, we use the revised calibration of Jensen et al. ([2003]). For the colour range $1.05 < (V - I)_0 < 1.24 \text{ mag}$, they derive

$$\overline{M}_{\text{F160W}} = (-4.86 \pm 0.03) + (5.1 \pm 0.5) \times [(V - I)_0 - 1.16] \quad (4.2)$$

This is equation (1) of their paper. Using the converted $(V - I)_0$ colour of 1.22 mag from their HST-data, a distance of $33.06 \pm 0.08 \text{ mag}$ for NGC 4709 is obtained.

4. Another distance estimate for the Centaurus cluster comes from the Fundamental Plane (FP) analysis presented within the SMAC survey (e.g. Smith et al. [2000], [2001], [2004] and Hudson et al. [2004]), which includes peculiar velocity measurements for both the Hydra and Centaurus cluster. In the framework of this FP analysis, the difference between cz_{FP} from the FP analysis and the measured cz_{CMB} of the cluster yields its peculiar radial velocity with respect to the Hubble flow. For comparison of the SMAC results with our metric distances, we adopt $H_0 = 72 \pm 4 \text{ km s}^{-1} \text{ Mpc}^{-1}$. For Centaurus, the revised mean SBF distance is $45.3 \pm 2.0 \text{ Mpc}$, while the SMAC result (Smith et al. [2004], priv. comm.) is $cz_{\text{FP}} = 3019 \pm 158 \text{ km s}^{-1}$, corresponding to $41.9 \pm 3.2 \text{ Mpc}$ ($33.11 \pm 0.16 \text{ mag}$) for $H_0 = 72 \pm 4 \text{ km s}^{-1} \text{ Mpc}^{-1}$. Both values agree to within their errors.

For the Centaurus cluster we summarise that the SMAC FP-distance is consistent with our SBF-distance, implying a small peculiar velocity for Centaurus. Literature SBF-distances are slightly below our value by about 0.3 mag. Fig. 4.11 illustrates this. The plotted literature distances have an average of 33.02 mag, $0.26 \pm 0.12 \text{ mag}$ smaller than our distance value. The error weighted mean of all distances is 0.18 mag lower than our value.

Hydra

There are 4 recent publications that present distances to either the entire Hydra cluster or single cluster galaxies, see also Fig. 4.11:

1. Blakeslee et al. ([2002]), who perform a comparison between SBF and Fundamental Plane distance for early-type galaxies, including the Hydra giant ellipticals NGC 3309 and NGC 3311. The SBF distances are $33.66 \pm 0.68 \text{ mag}$ for NGC 3309 and $33.23 \pm 0.52 \text{ mag}$ for NGC 3311 (Blakeslee, private communications). This corresponds to a mean distance of $49.1 \pm 10 \text{ Mpc}$, which is larger than but still consistent with our mean Hydra distance. The FP distances are $33.33 \pm 0.41 \text{ mag}$ for NGC 3309 and $32.93 \pm 0.41 \text{ mag}$ for NGC 3311. This corresponds to a mean distance of $42.4 \pm 5.8 \text{ Mpc}$ and is in good agreement with our results.

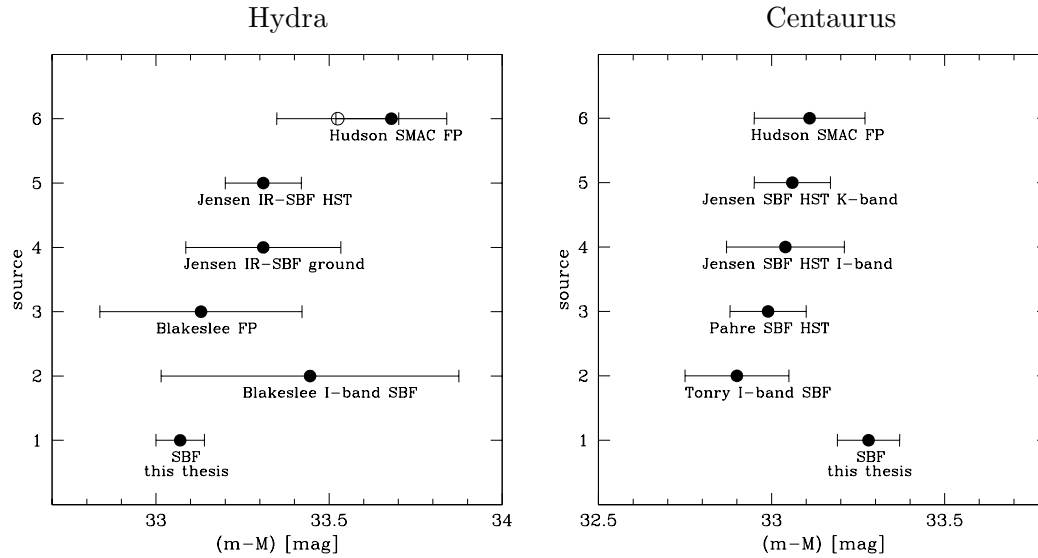


Figure 4.11: Literature comparison of distances to the Hydra cluster (left) and Centaurus cluster (right). Numbers for the Hydra distances refer to the following sources: 1 SBF distance from this thesis; 2 mean I -band SBF distance to NGC 3309 and NGC 3311 from Blakeslee et al. ([2002], and priv. comm.); 3 mean FP distance to NGC 3309 and NGC 3311 from Blakeslee et al. ([2002]); 4 mean K -band SBF distance to NGC 3309 and NGC 3311 from Jensen et al. ([1999]); 5 NICMOS F160W SBF-distance to NGC 3309 from Jensen et al. ([2001]) using the revised calibration by Jensen et al. ([2003]); 6 FP distance to the Hydra cluster from Hudson et al. ([2004]), open symbol refers to the distance when including the Mg_2 term in the FP-relation fit. Numbers for the Centaurus distances refer to the following sources: 1 SBF distance from this thesis; 2 mean I -band SBF distance of 8 Centaurus cluster galaxies from Tonry et al. [1997], corrected for a Malmquist-like selection bias by adding 0.30 mag, see text; 3 I -band SBF distance to NGC 4373 from Pahre et al. [1999]; 4 I -band HST SBF distance to NGC 4709 from Jensen et al. [2001]; 5 NICMOS F160W SBF-distance to NGC 4709 from Jensen et al. ([2001]) using the revised calibration by Jensen et al. ([2003]); 6 FP distance to the Centaurus cluster from Hudson et al. ([2004])

2. Another distance estimate for the Hydra cluster comes from the SMAC survey. For the Hydra cluster, Smith et al. ([2004] and priv. comm.) obtain $c z_{FP} = 3919 \pm 206$ km s⁻¹. This corresponds to a distance of 54.4 ± 4.2 Mpc when assuming $H_0 = 72 \pm 4$ km s⁻¹ Mpc⁻¹. This is inconsistent with our distance of 41.2 ± 1.4 Mpc at the 3.0σ level and corresponds to a difference of 0.60 ± 0.18 mag in distance modulus.
3. Jensen et al. ([1999]), who measure IR-SBF distances for NGC 3309 and NGC 3311 in the K' -band using the Hawaii 2.24m telescope. They obtain identical distances to NGC 3309 and NGC 3311 of 46 ± 5 Mpc, using $\overline{M}_{K'} = -5.61 \pm 0.12$ as derived in Jensen et al. ([1998]). This is higher than our Hydra cluster distance by about 10%, but still marginally consistent. It is about 20% higher than our mean distance to NGC 3309 and NGC 3311. A possible reason for the higher distance may be that the SBF signal measured by Jensen et al. was in some parts dominated by background spatial variance, whose removal was estimated to introduce errors of up to 0.4 mag in the finally adopted value for $\overline{m}_{K'}$. Also, the more recent calibration of $\overline{M}_{K'}$ by Liu et al. ([2002]) shows an intrinsic scatter of about 0.25 mag in $\overline{M}_{K'}$ for the galaxies observed, about twice as large as assumed by Jensen et al. ([1999]).
4. Jensen et al. ([2001]), from their NICMOS F160W SBF distances of 16 distant galaxies, among them NGC 3309 as the only Hydra cluster member. For this galaxy they measure an apparent fluctuation magnitude of $\overline{m}_{F160W} = 28.86 \pm 0.07$ mag. In Jensen et al. ([2001]), $(V - I)_0$ of NGC 3309 is estimated from $(B - R)$ colours by Postman & Lauer ([1995]) to be 1.28 mag. This is slightly redder than the value of 1.21 mag determined by us directly via VI photometry in this thesis. From our photometry we detect a slight colour gradient with redder colour towards the centre of NGC 3309. The region sampled by Jensen et al. ([2001]) for SBF measurement is a ring region with $2.4'' < r < 4.8''$, which is closer to the centre than even our innermost ring. Our photometry indicates a colour of $(V - I)_0 \simeq 1.23$ -1.24 mag in this area. Adopting 1.24 ± 0.02 mag and plugging this value into equation (4.2) results in $\overline{M}_{F160W} = -4.45 \pm 0.05$ mag for NGC 3309. This yields a distance estimate of $(m - M) = 33.31 \pm 0.11$ mag. This is higher than our mean distance for Hydra by 0.24 mag (12%) and higher than the distance to NGC 3309 by about 0.5 mag.

For the Hydra cluster we summarise that recent literature distance estimates have a mean of 33.37 ± 0.08 mag. This is 0.30 ± 0.11 mag higher than our result. Fig. 4.11 illustrates this. The error weighted mean of all distances is 0.11 mag higher than our result.

Systematic biases in literature distances?

It is worth having a closer look at the literature distances to see to which extent systematic biases might influence their results. The different direction of the distance differences for Centaurus and Hydra make it appear likely that there might be some intrinsic properties of Centaurus and Hydra that could bias different distance measure-

ment techniques in opposite ways.

The first remarkable thing is that although for the Hydra cluster there is a substantial disagreement between our SBF distances and the SMAC FP distances, both methods yield very similar results for the Centaurus cluster. In that context it is very interesting to note that the SMAC value of cz_{FP} for Hydra implies a very small peculiar velocity for Hydra, almost consistent with zero. Hudson et al. ([2004]) show that for the determination of the bulk flow velocity amplitude, the Hydra cluster is the most significant outlier of all 56 investigated clusters. Excluding this single cluster from the bulk-flow analysis increases the bulk flow velocity by more than 100 km s^{-1} up to almost 800 km s^{-1} .

The question arises whether the Hydra (and also the Centaurus) cluster exhibits peculiarities in the stellar populations of its galaxies that may have a biasing effect on SBF distances and/or FP distances.

Already Jensen et al. ([2003]) have noted that IR-SBF measurements are more sensitive to age-metallicity effects than I -band SBF. Tonry et al. [2001] have shown that the I -band cosmic scatter in \overline{M}_I is between 0.05 and 0.10 mag. The spread of \overline{M}_{F160W} at a given colour can be up to 0.2 mag according to the calibration of Jensen et al. ([2003]). Stellar population models (e.g. Liu et al. [2000] and [2002], Blakeslee et al. [2001]) indicate that at red colours ($(V - I)_0 \geq 1.2$), the \overline{M}_{F160W} values used for the calibration correspond to very old galaxies with age ~ 15 Gyr. This means that there is little room for fainter \overline{M}_{F160W} at red colours. Indeed, Jensen et al. ([2003]) attribute the spread in \overline{M}_{F160W} largely to the distance uncertainty from the I -band SBF distances used to calibrate the \overline{M}_{F160W} values. The age-metallicity spread could therefore contribute not more than 0.2 mag to the 0.2-0.5 mag difference between our I -band SBF distances and the IR-SBF-distances for NGC 3309 and 3311. Both galaxies would need to be several Gyrs older and slightly more metal-poor than the galaxies at comparable colours used in Jensen et al.'s calibration. It is an interesting coincidence, that from X-ray observations Hydra is the prototype of a relaxed cluster (e.g. Tamura et al. [1996] and [2000], Yamasaki et al. [2003]), not having undergone a major merger in the last several Gyrs. Such a quieter evolution as compared to other environments could result in an older and more metal-poor population.

For the Centaurus cluster, the opposite effect would be needed to reduce the discrepancy between Jensen's IR-SBF distance to NGC 4709 and our Centaurus cluster distance. I.e., its galaxies should be more metal-rich and younger than the average ones used in Jensen's calibration. Indeed, X-ray observations (Furusho et al. [2001]) and the double-peaked velocity structure (Stein et al. [1997]) indicate that the Centaurus cluster has recently undergone or is still experiencing a major merger. This might have triggered to some degree new star formation in the cluster and hence created a younger, more metal-rich population of stars. It must be kept in mind, however, that we are investigating early-type galaxies with the SBF-technique. These galaxies are not expected to harbour a large amount of gas and should therefore not be places of strong star formation in the case of cluster-cluster mergers. What complicates the reasoning further is that our

distance to NGC 4709 is significantly *lower* than Jensen’s distance, mainly due to the large $(V - I)_0$ colour difference. One has to assume that our colour estimate for NGC 4709 is wrong to make the arguments above work.

Under this condition, the discrepancy between our I -band SBF distance and the IR-SBF distances by Jensen et al. can be explained if the Hydra cluster is older and more metal-poor, while the Centaurus cluster is younger and more metal-rich than “average” early-type galaxies entering Jensen’s calibration.

The opposite effect would be needed to reconcile the Hudson et al. ([2004]) FP-distances with our values, especially for the Hydra cluster. Hudson et al. ([2004]) remark that if there are systematic age-metallicity differences between different clusters, this could significantly bias the derived FP distance values. As an increase of metallicity tends to fainten a galaxy’s surface brightness, a *metal-rich* outlier would imply a *too large* distance. A bias like that can be partially corrected for by including the Mg_2 index in the inverse FP analysis. When doing so, Hudson et al. ([2004]) get $cz_{FP} = 3648 \pm 229$ km s⁻¹ for the Hydra cluster. This corresponds to a distance of 50.7 ± 4.3 Mpc, about 4 Mpc less than without the Mg_2 index. The disagreement with our result decreases to 0.45 ± 0.18 mag, still significant at the 2.1σ level. The direction of this correction indicates that the Hydra cluster might be a metal-rich outlier, the opposite of what would be needed to explain the discrepancy with the IR-SBF distances.

The I -band SBF distance estimates by Blakeslee et al. ([2002], and priv. comm.) for the Hydra galaxies are higher than our values, but still agree to within their (large) errors. For the Centaurus cluster, the Tonry et al. [1997] values are significantly below our estimate. A possible reason for that are the different cutoff magnitudes for investigating the globular cluster systems. While we are able to map both GCSs well beyond their TOM (down to 25 mag in I), Tonry et al. have a significantly brighter dereddened cutoff-magnitude for their investigations, which is 23.6 ± 0.2 mag for NGC 4696 and 23.8 ± 0.3 mag for NGC 4709 in I (Blakeslee & Tonry, private communication). They obtain a contribution ΔGC of about 50% to the SBF-signal from undetected globular clusters, which causes an additional distance error of almost the same order (Blakeslee & Tonry, private communication). Tonry et al. [1997] derived ΔGC by assuming a GCLF-TOM corresponding to the approximate cluster distance. In other words, GCLF-TOM (and hence ΔGC) and SBF-distance are somewhat interrelated. This has already been mentioned in Sect. 4.3.4 when discussing our SBF measurement procedure. Our approach to overcome this problem is to iteratively determine the TOM, ΔGC and the SBF-distance. If one fixes the TOM and width σ (as it was done by Tonry et al.), hence fitting only the total number of GCs, a larger SBF-distance uncertainty is the result. If one uses a too low cluster distance estimate for calculating ΔGC , one systematically underpredicts the distance, as a larger fraction of the measured fluctuations is contributed to the stellar fluctuations.

To get an idea on the amount of this bias, we use equation (15) from Blakeslee & Tonry ([1995]), assume a TOM of $M_I = -8.5$ mag for the globular cluster luminosity function, a width $\sigma = 1.3$ mag, $S_N = 6$ (the mean of our values for NGC 4696 and NGC

4709) and $(V - I)_0 = 1.24$ mag. Then, we calculate ΔGC for two different cases, for both of which we assume a limiting magnitude for GC detection of $I = 23.7$ mag. First, for $(m - M) = 32.75$ mag and hence apparent TOM=24.25 mag (Tonry’s distance to NGC 4696); second, for $(m - M) = 33.25$ mag and hence apparent TOM=24.75 mag (our distance to Centaurus). The contribution ΔGC in the first case is 1.00 mag, in the second case 1.63 mag. This means that in the first case, the contribution of globular clusters to the fluctuation signal is about 70%, in the second case it even is 82%. Furthermore, only from assuming a 0.5 mag lower distance for the calculation of ΔGC , ΔGC itself is changed by 0.63 mag. This indicates that the Tonry et al. SBF-distances to Centaurus may be underestimated due to them assuming a too low “guess” for the correct Centaurus cluster distance. The reason for the large amplitude of this effect is the rather bright completeness magnitude, more than 1 mag brighter than ours. In our GCLF fitting for the giants, we only keep the width σ fixed and determine the TOM directly. This gives us a much more accurate estimate of ΔGC , which also is much smaller (0.2 mag) due to the much higher depth of our data.

Regarding the HST I -band distance from Pahre et al. [1999], which is lower than our Centaurus distance by 0.29 ± 0.15 mag, there is not much room for a possible underestimation of ΔGC , since these data are very deep and allow mapping the GCLF to fainter magnitudes than our data. One possible reason for the discrepancy with our result is that NGC 4373 (SGL=154.13°, SGB=-15.60°) is located several degrees in projection away from the Centaurus cluster centre and might therefore not be directly associated to the main cluster.

Summarising this subsection, possible systematic effects biasing the results of other authors that get a lower Centaurus cluster and higher Hydra cluster distance than we do are probably not larger than 0.20 mag (except for Tonry’s I -band SBF distances). Specifically, IR-SBF distances and FP distances require opposite stellar population peculiarities to bring them closer to our value.

4.5.4 Systematic effects in our data?

Having discussed possible systematic effects in the data of other authors, we discuss in this section whether and to what extent any systematic biases in our data set may influence our SBF distance estimates to Hydra and Centaurus.

Selection bias?

One possible effect inherent in our data might be a selection bias towards brighter SBF magnitudes at the faint magnitude limit of our survey. Galaxies whose observational uncertainties or stellar populations place them at seemingly low distances will have a higher S/N in the SBF measurement than galaxies of the same apparent brightness who fall behind the observed cluster due to observational errors. Fig. 4.7 shows the absolute brightness M_V of the Hydra and Centaurus galaxies plotted vs. $(m - M)_{SBF}$.

Applying a linear fit to the Hydra M_V vs. $(m - M)_{SBF}$ data points results in a non-zero slope at 0.4σ significance. When rejecting the three faintest data points, the significance changes to 0.6σ . The mean distance of the three giants is 39.5 ± 1.5 Mpc, while for the 13 dwarfs it is 41.6 ± 1.7 Mpc, i.e. a difference of $5 \pm 6\%$. Rejecting the three faintest data points, the mean distance rises by about 2% to 42.1 ± 2.4 Mpc. Excluding the two brightest dwarfs lowers the mean distance by about 3% to 39.8 ± 1.1 Mpc. All the mean distances for the sub-samples mentioned are within the error ranges of the entire sample. As noted in Sect. 4.3, there is only one faint early-type Hydra cluster member from the spectroscopic sample of Christlein & Zabludoff ([2003]) for which SBF could not be measured due to an undetectable SBF signal. This galaxy would have $M_V \simeq -13.5$ mag at the Hydra cluster distance, about 1 mag fainter than the magnitude regime investigated here. Our results do therefore not support a selection bias for the Hydra galaxies larger than 0.10 mag, neither towards too bright nor too faint SBF magnitudes.

Applying a linear fit to the Centaurus data points results in a non-zero slope at 1.4σ significance. However, this slope is solely driven by the very low distance for NGC 4709, which might be located somewhat in front of Centaurus (see further discussion in Sect. 4.5.6 and on page 111) and for which our colour estimate is significantly redder than that of other authors, leading to the comparably low distance. When disregarding the NGC 4709 data point, the mean distance of the entire sample rises by 2% to 46.2 Mpc and the slope between M_V vs. $(m - M)_{SBF}$ reduces to 0.8σ significance. When rejecting in addition the three faintest data points, the significance decreases more to 0.2σ . The mean distance of the 13 dwarfs is 46.5 ± 1.9 Mpc, 4.0 ± 3.7 Mpc larger than that of NGC 4696. The mean distance of the seven dwarfs with redshifts corresponding to Cen30 is 45.4 ± 3.1 Mpc, identical to the mean distance of the entire sample and only 2.9 ± 4.5 Mpc different to that of NGC 4696. Rejecting the three faintest data points, the mean distance falls by about 3% to 44.1 ± 2.3 Mpc. Excluding the two brightest dwarfs leaves the mean distance practically unchanged at 44.9 ± 3.6 Mpc. All the mean distances for the sub-samples mentioned are within the error range of 0.10 mag of the entire sample. Our results do therefore not support a selection bias larger than 0.10 mag for the Centaurus galaxies, neither towards too bright nor too faint SBF magnitudes.

A final check is to calculate the two measures of the observation quality for SBF-data 'Q' and 'PD', defined in T00. SBF-Measurements with $Q < 0$ or $PD > 2.7$ are considered as potentially affected by low quality. PD , which is the product of the seeing-FWHM in arcsec and the radial velocity in units of 1000 km s^{-1} , is about 2.0 for Hydra and about 1.5 for Centaurus (using the undisturbed Hubble flow radial velocity that corresponds to our distance value). The parameter 'Q', which is the logarithm to the basis of 2 of the ratio of the detected electron number corresponding to \bar{m}_I and PD^2 , is below 0 for seven Centaurus cluster galaxies. The mean SBF-distance of these seven galaxies is 46.4 ± 3 Mpc, in perfect agreement with the overall mean. In the Hydra sample, 5 galaxies have $Q < 0$. Their mean distance is 44.1 ± 3.4 Mpc, also consistent with the overall

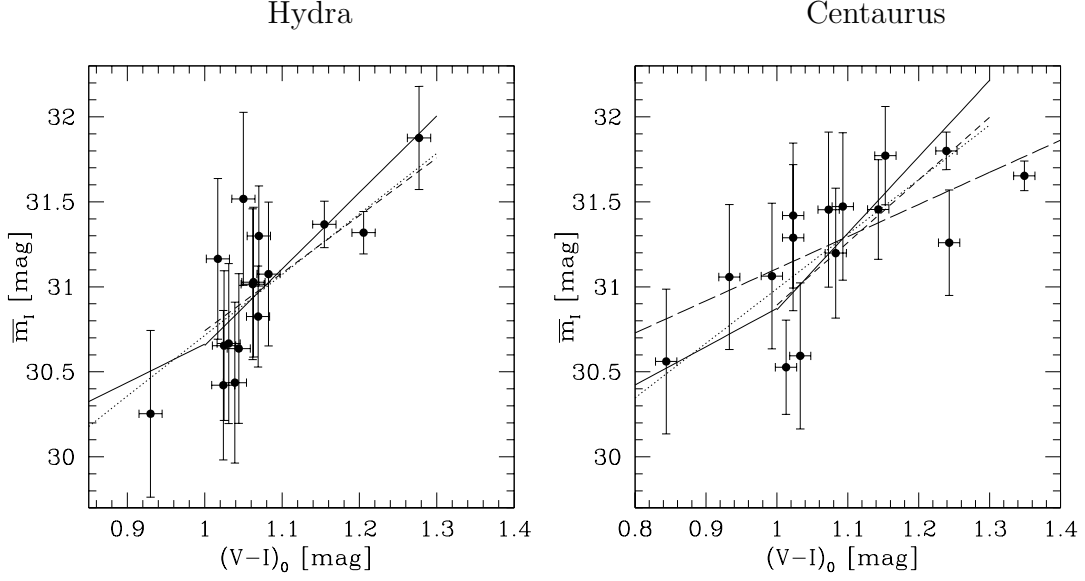


Figure 4.12: Dereddened colour $(V - I)_0$ plotted vs. apparent fluctuation magnitude \overline{m}_I for the investigated Hydra (left) and Centaurus (right) galaxies. The solid lines indicates the calibration relations (1.10) for $(V - I)_0 > 1.0$ and (2.1) for $(V - I)_0 < 1.0$ adopted between \overline{M}_I and $(V - I)_0$, shifted to $(m - M) = 33.07$ mag for Hydra and $(m - M) = 33.28$ mag for Centaurus. The short dashed line are linear fits to the data points in the empirically calibrated colour regime $1.0 < (V - I)_0 < 1.3$ mag, allowing both the zero-point and slope to vary. The fitted slope is lower by 1.2σ (Hydra) and 0.9σ (Centaurus) than the slope of 4.5 of relation (1.10). The dotted lines are fits for $(V - I)_0 < 1.3$ mag, including all Hydra galaxies and all Centaurus galaxies except NGC 4709. The long dashed line for Centaurus is the fit when including NGC 4709.

mean.

Calibration bias?

Another possible systematic effect could be that the calibration between \overline{M}_I and $(V - I)_0$ adopted in this thesis might not be valid for the entire investigated colour range. In Sect. 3.3.3 it has been shown that \overline{M}_I appears to depend less strongly on $(V - I)_0$ for blue colours, as predicted by stellar population models (Blakeslee et al. [2001], Worthey [1994]) and also found by other authors for different colours (Jerjen et al. [2004], Mei et al. [2005]). This was the reason for adopting relation (2.1) for the SBF calibration of galaxies with $(V - I)_0 < 1.0$. For $(V - I)_0 > 1.0$ we still assume Tonry's empirical relation (1.10). Fig. 4.12 shows the apparent fluctuation magnitude \overline{m}_I plotted vs. $(V - I)_0$. Overplotted are the calibration relations (1.10) and (2.1) as well as the linear relations obtained from fits to the data points in various colour ranges.

The dwarf galaxies investigated in Hydra and Centaurus are on average brighter than

those in Fornax, and therefore also redder due to the colour-magnitude relation (see Sect. 3.2). Only one Hydra dwarf and three Centaurus dwarfs have $(V - I)_0 < 1.0$. Fig. 4.12 shows that their data points are all consistent with relation (2.1). Switching from relation (2.1) to the empirical calibration (1.10) for $(V - I)_0 < 1.0$ changes the mean distance of the entire samples by +0.01 mag for Hydra and -0.035 for Centaurus. These changes are in the right direction to reduce the discrepancy with literature results, but their amount is insignificant.

Excluding the SBF-distances for galaxies with colours outside the empirically calibrated range $1.0 < (V - I)_0 < 1.3$ mag does not change the mean distance by more than 1%, neither for Centaurus nor for Hydra, see Sect. 4.4.1. For a more conservative colour cut, one can also exclude all galaxies with $(V - I)_0 < 1.05$ mag. The resulting mean distance for the Hydra sample then is 43.1 ± 1.9 mag, about 5% or 0.1 mag higher than for the entire sample. Doing the same for Centaurus lowers its mean distance by 0.09 mag to 43.3 ± 2.7 Mpc. This brings our distance estimates closer to the other values in the literature. The amount of these changes is about equal to the mean distance error for both clusters. A linear fit to the $(m - M)_{SBF} - (V - I)_0$ Hydra data points in Fig. 4.7 yields a slope significant at exactly the 1.0σ limit. For Centaurus, the slope is significant at the 2.6σ level when including NGC 4709 and reduces to 1.2σ when rejecting it. This shows again that this galaxy should be considered separately from the rest of the sample (see further discussion in Sect. 4.5.6 and on page 111). The fact that the confidence levels of the Hydra and Centaurus slopes are about 1σ , fits nicely to the fact that the colour restriction of our samples to $(V - I)_0 > 1.05$ mag also yields a 1σ change of the mean distance.

Fig. 4.12 shows that the slope in the $\overline{m_I} - (V - I)_0$ plane for the Hydra and Centaurus samples is slightly shallower than the value of 4.5 used for the calibration, although only at about the 1σ significance level. When forcing those fits to match with relation (1.10) at the respective mean colours of the samples, this yields a -0.01 mag distance shift for Hydra and -0.04 mag shift for Centaurus.

Summarizing this subsection, we do not find indications for stellar population effects in our data biasing our distance estimates by more than the distance error to both clusters, which is 0.10 mag.

Malmquist bias?

Blakeslee et al. ([2002]) note that both their SBF survey as the FP distances from the SMAC survey are subject to the so-called 'Malmquist-bias' (Malmquist [1920]). In this context, 'Malmquist-bias' refers to the fact that the expectation value for the true distance r of a galaxy tends to be higher than its measured distance d , the higher the observational errors are and the closer it lies to the survey limit (Blakeslee et al. [2002], Strauss & Willick [1995], Lynden-Bell et al. [1988]). The Malmquist bias is most severe for distance estimates to field galaxies that are not bound in a cluster.

To investigate whether this might significantly bias our distance estimate to the Hydra cluster towards too low distance, we use the formula given by Blakeslee et al. ([2002]) for the calculation of r at a measured value of d , based on the notation of Strauss & Willick ([1995]):

$$E(r|d) = \int_0^\infty \frac{r^3 n(r) \exp\left(\frac{[\ln(r/d)]^2}{2\Delta^2}\right)}{r^2 n(r) \exp\left(\frac{[\ln(r/d)]^2}{2\Delta^2}\right)} dr \quad (4.3)$$

$n(r)$ is the real-space density distribution of galaxies in the direction of the given sample galaxy, and Δ is the fractional error in the distance measurement of this galaxy.

For the radial density distribution of the Hydra cluster galaxies we adopt:

$$n(r) = \exp\left(\frac{-(d - d_0)^2}{2\sigma^2}\right) + b. \quad (4.4)$$

The first term is the density distribution within the cluster, parametrised by the mean distance d_0 and width σ . The constant b is included to allow for a uniformly distributed population of back- and foreground galaxies. Plugging equation (4.4) into equation (4.3) allows one to iteratively determine the magnitude of the Malmquist bias. Evaluating equation (4.3) with $\sigma = 1$ Mpc (expected for the Hydra cluster galaxies if they are distributed in a spherically symmetric manner, see Sect. 4.4.3) yields a vanishing Malmquist bias for $b = 0$ and only 2% bias for 25% background contamination. This is negligible compared to the error of Hydra's mean distance. The negligible Malmquist bias for $\sigma = 1$ Mpc still holds if we multiply our distance errors by 1.5, matching the errors of the SBF-distances to NGC 3309 and NGC 3311 by Blakeslee et al. ([2002]).

Therefore, it is likely that neither in our investigation nor in that by Blakeslee et al., a Malmquist bias artificially decreases the distance values to the Hydra galaxies.

SBF-distance vs. GCLF distance

An interesting consistency check of our SBF-distances is to compare them with the GCLF distances derived for the 4 giant galaxies NGC 3309, NGC 3311 (Hydra), NGC 4696 and NGC 4709 (Centaurus), see Table 4.5. For NGC 4696 and 4709, GCLF- and SBF-distances agree to within 0.2 mag. The relative distance between both galaxies from their SBF-measurements is also recovered well by the GCLF-distances. The mean difference $(m - M)_{SBF} - (m - M)_{GCLF}$ for all 4 giants is 0.31 ± 0.54 mag. The large error in that value is because the GCLF-distances to NGC 3309 and 3311 are only very poorly constrained, with formal uncertainties around 0.6-0.7 mag. This inhibits a thorough comparison of GCLF- and SBF-distances for the Hydra galaxies. Note, however, that in spite of these poor constraints, the variance contribution ΔGC of unresolved GCs to the SBF-signal is quite well determined: the uncertainties in σ and TOMs for the Hydra giants translate to rather small uncertainties below 0.05 mag for ΔGC , see Sect. 4.3.5, due to the bivariate between σ and TOM.

Summarising the discussion on possible systematic effects within our Hydra and Centaurus data, we find an upper limit of about 0.1 mag for too low Hydra distances and too high Centaurus distances with bluer colour. We find that Malmquist like biases are unlikely to cause a bias larger than 0.05 mag.

4.5.5 Consequence of a higher Hydra and lower Centaurus distance for the GA model

Due to the difference between our distance estimates to Hydra and Centaurus to those of other authors we check the peculiar velocity predicted for a 15% larger Hydra and 15% smaller Centaurus distance within the flow model of Tonry et al. ([2000]), see Fig. 4.9. The expected CMB radial velocity for a higher Hydra distance remains well below the actually measured ones for GA distances between 43 and 47 Mpc. This is because a 15% higher distance places Hydra behind the GA, resulting in negative peculiar velocities. However, for a GA distance of 49 Mpc and a projected position within about 10° of the Hydra cluster, the expected CMB radial velocity of a 15% more distant Hydra cluster matches the observations. This GA distance is 15% higher than determined by T00, different at 2σ significance. Note that even for this larger assumed Hydra distance, the Hydra peculiar velocity is still significant and requires a strong gravitational pull from behind, consistent with a GA in closer projected position to Hydra than to Centaurus. When in addition assuming a 15% lower distance to the Centaurus cluster, the Hydra and Centaurus peculiar velocities become comparable. This can be explained by a 49 Mpc distant GA at approximately equal projected distance between Hydra and Centaurus, but also by a common motion towards a more distant attractor, whose amplitude is consistent with that found in the SMAC (Hudson et al. [2004]).

Although a check of the predicted peculiar velocities using literature distances is a valuable exercise, we note that it is difficult to imagine that any systematic effect biases our SBF-distances by 15% (0.3 mag) in *opposite* directions for Hydra and Centaurus, see Sect. 4.5.4. That is, the significant *difference* between the Hydra and Centaurus peculiar velocity should be less affected by systematics than their absolute distances. This is especially true given that both data sets were observed with the same instrument.

4.5.6 Cen30 and Cen45

In our sample of 15 Centaurus cluster galaxies, eleven have measured redshifts. Of those, 8 have radial velocities below 4000 km s^{-1} , hence are members of the Cen30 components, among them NGC 4696. The remaining three, among them NGC 4709, have radial velocities above 4500 km s^{-1} , hence belong to the Cen45 component (see Fig. 4.6). What can we say about the relative distance between these two sub-components?

The mean distance of the 8 Cen30 members is $45.0 \pm 2.7 \text{ Mpc}$. That of the three Cen45 members is $40.0 \pm 5.8 \text{ Mpc}$, slightly lower but still consistent with the Cen30 distance. The relative distance modulus of the two components then is $(m - M)_{Cen30} - (m - M)_{Cen45} = 0.26 \pm 0.32 \text{ mag}$. This excludes that both components are separated by

their Hubble flow distance of approximately -0.9 mag. Our finding is consistent with suggestions that the Centaurus cluster is undergoing or has recently undergone a major merger (Churazov et al. [1999], Furusho et al. [2001]), with Cen45 being the infalling sub-component. The distance difference between the two main galaxies NGC 4696 and NGC 4709 is significant at the 2σ level, being $(m-M)_{N4696} - (m-M)_{N4709} = 0.64 \pm 0.31$ mag. However, due to the very red colour measured for NGC 4709, the mean distance of all three Cen45 member might be a more reliable distance estimate. A significant relative distance between Cen30 and Cen45 is supported by the different TOM of the GCLFs, see Table 4.5: $(m-M)_{N4696} - (m-M)_{N4709} = 0.63 \pm 0.47$ mag. However, the error bars are still too large to tell whether or not Cen45 has already reached Cen30 in its in-fall process.

Going back to the flow model of Tonry et al. ([2000]), it is worth checking at what distance in front of the GA one would expect an infall velocity of about 1500 km s^{-1} , i.e. the velocity difference between Cen30 and Cen45. Assuming Cen30=GA at $\simeq 3000 \text{ km s}^{-1}$, a velocity of 4500 km s^{-1} is reached if Cen45 is located 5 Mpc in front of Cen30, i.e. at 40 Mpc distance. A larger relative distance of 10 Mpc – i.e. a distance of 35 Mpc from us – would result in a velocity well below 4000 km s^{-1} . If one was to explain the large Cen45 in-fall into Centaurus by the Great Attractor, the small distance of about 32 Mpc that we derive for NGC 4709 does not fit into the picture while the mean distance for all three Cen45 galaxies does. However, we can exclude with 94% confidence the assumption that Centaurus=GA from the analysis of the peculiar velocities, a conclusion which is supported by the substantially smaller mass estimated for the Centaurus cluster ($\simeq 3 \times 10^{14} M_*$, see Eiprich & Böhringer [2002]) as compared to that proposed for the GA ($\simeq 9 \times 10^{15} M_*$, see T00).

The more probable picture seems that Cen45 – as an only loosely bound group of galaxies – is right now in the merging process with Cen30. Relative velocities of 1500 km s^{-1} between merging clusters are not unusual. For example, the massive galaxy cluster Abell 1689 ($M \simeq 1 - 2 \times 10^{15} M_*$, see King et al. [2002], Broadhurst et al. [2005]) exhibits a very broad velocity distribution with a central velocity dispersion of $\sigma \simeq 2000 \text{ km s}^{-1}$ (Czoske [2004]) and various radial velocity sub-clumps (Girardi et al. [1997]). This shows that for a relative velocity of 1500 km s^{-1} a mass of $\simeq 10^{16} M_*$ – as derived by T00 for the GA – is not necessary.

It has been suggested by Churazov et al. ([1999]) that in the direction of the Centaurus cluster we are looking into a large scale filamentary structure. They bring this scenario forward in order to explain an unusually extreme “ β -problem”, i.e. a substantial disagreement between the energy-ratio per unit mass for galaxies to that in the gas derived from X-ray temperatures and from galaxy velocity dispersion. Colberg et al. ([1999]) have shown in numerical simulations that clusters accrete matter from a few preferred directions, defined by filamentary structures, and that the accretion persists over cosmologically long times.

This scenario of a filamentary structure cannot be rejected with our data, since we do see some indications for Cen45 being located slightly in front of Cen30. However, we

have also found an upper limit of about a factor of 2.5 for the ratio of radial to tangential depth of the Centaurus cluster, putting an upper limit of $\simeq 6$ Mpc to the radial extent of such a filament.

4.6 Summary

In this chapter, we have presented *I*-band SBF measurements for 16 early-type galaxies in the central Hydra cluster and 15 early-type galaxies in the central Centaurus cluster (mainly dwarfs), based on deep photometric data obtained with VLT FORS1.

The following results were obtained:

1. The mean SBF-distance of the investigated Hydra galaxies is 41.2 ± 1.4 Mpc (33.07 ± 0.07 mag). The mean SBF-distance of the investigated Centaurus galaxies is 45.3 ± 2.0 Mpc ($(m - M) = 33.28 \pm 0.09$ mag). This gives a relative distance between Centaurus and Hydra of $(m - M)_{\text{Cen}} - (m - M)_{\text{Hyd}} = 0.21 \pm 0.11$ mag, or 4.1 ± 2.4 Mpc. As already found in Sect. 3 for the SBF measurements of Fornax cluster dEs, the limiting absolute galaxy magnitude for SBF application is in excellent agreement with predictions based on the simulations in Sect. 2.

2. In the CMB rest-frame and assuming $H_0 = 72 \pm 4$ km s⁻¹ Mpc⁻¹, the distance obtained for the Hydra cluster yields a high positive peculiar velocity of 1225 ± 235 km s⁻¹, for the Centaurus cluster 210 ± 295 km s⁻¹. Allowing for a thermal velocity error component of 200 km s⁻¹, this rules out a common flow velocity for both clusters at 98% confidence. We find that the $9 \times 10^{15} M_\odot$ “Great Attractor” from the flow study of Tonry et al. ([2000]) at a distance of 43 ± 3 Mpc can explain the observed peculiar velocities if shifted about 15° towards the Hydra cluster position. Our results are inconsistent at 94% confidence with a scenario where the Centaurus cluster is the GA. The difference between the mass of the Centaurus cluster as derived from X-ray observations and that proposed for the Great Attractor is about a factor of 30, making that hypothesis even more unlikely. The possibility of a large Hydra peculiar velocity due to infall along a filament is inconsistent with our data. The idea of a net angular momentum of the Hydra-Centaurus system in addition to the cosmic thermal velocity field is found to be inadequate due to the large timescales and distances involved.

3. The Hydra cluster SBF-distance derived by us is about 0.3 mag lower than the mean of distances published in the last 5 years, while the estimated Centaurus distances agree well with FP-distances, but are about 0.3 mag higher than previous SBF-estimates. Several possible reasons for these differences are discussed. We find that peculiarities in the stellar population of the bluest galaxies in our sample might bias our sample towards low (Hydra) or high (Centaurus) distances by up to 0.1 mag, i.e. within the statistical distance errors. Peculiarities in the stellar population of the brightest cluster galaxies may bias the distance measurements for IR-SBF or Fundamental Plane measurements by up to 0.2 mag.

4. From the scatter of the SBF-distances around their mean we derive upper

limits of ± 3.5 Mpc depth for the Hydra cluster and ± 5.7 Mpc for Centaurus. For both clusters, these upper limit correspond to a cigar shape with about three times longer radial than tangential extension.

5. We find a distance difference of 0.26 ± 0.32 mag between the two Centaurus cluster sub-components Cen30 and Cen45, ruling out that both components are separated by their Hubble flow distance, consistent with a picture where Cen45 is falling into the main cluster Cen30. The marginally significant relative SBF and GCLF-distances between the main galaxies of both sub-components suggest that Cen45 may not yet have reached Cen30.

Chapter 5

Conclusions and Outlook

In this thesis, we have presented two applications of the SBF method to estimate distances to dwarf elliptical galaxies (dEs) in nearby galaxy clusters, preceded by simulations quantifying the potential of the method.

- The simulations (chapter 2) allowed us to estimate limiting absolute galaxy magnitudes for the application of the SBF method as a function of galaxy distance, telescope mirror size, integration time and seeing. These estimates agreed very well with the limiting magnitudes achieved in the observations of Fornax, Hydra and Centaurus cluster dEs presented in this thesis. Therefore, they provide a valuable tool to efficiently design future SBF surveys.
- The first application of the SBF method was made to dEs in the Fornax cluster (chapter 3). The aim was to obtain reliable distance estimates to unconfirmed dE candidates in order to establish their membership in the Fornax cluster. A further task was to improve the morphological classification of fainter candidate dEs that had been detected by our group in earlier lower resolution imaging. There were only few “surprises”, i.e. galaxies that turned out to be probable background galaxies although being classified as probable members in the lower resolution imaging (or vice versa). This is because the counterparts of the faintest Local Group galaxies would almost all have been resolved at the Fornax cluster distance in the lower resolution images. Furthermore, there was no case where a probable candidate was *rejected* based on not detecting SBF. This indicates that in the direction of Fornax, the space density of large, low surface brightness background galaxies is small compared to the cluster population. We confirm the very shallow faint end slope $\alpha \simeq -1.1$ for the Fornax cluster galaxy luminosity function as derived from the lower resolution photometry. Our finding provides further support for the strong discrepancy between the number of low luminosity galaxies and that of low mass dark matter halos as expected from Λ CDM structure formation models. Conceptually, the great advantage of getting cluster memberships per SBF compared to getting radial velocities is that one requires only a photometric

imaging run (no follow-up with spectroscopy). A further advantage is that there is a considerable range of useful “byproducts” when doing a deep imaging survey in two bands, like investigation of globular cluster systems for giants, dwarfs and the intracluster space or detection and photometry of very low surface brightness galaxies.

We also addressed the *I*-band SBF calibration at blue colours because of the faintness and hence blue colours of the dEs investigated. We find that the absolute fluctuation magnitude depends less strongly on colour ($V - I$) than in the already calibrated red range. This agrees with literature results for SBF measurements in other pass-bands, including the HST SBF-calibration in the Sloan z , ($g - z$) filters.

- The second SBF application to dwarf galaxies in the Hydra and Centaurus clusters (chapter 4) was aimed at estimating the absolute distance to each cluster and the relative distance between them. Therefore, also brighter giant galaxies were included in the SBF sample. SBF calibration uncertainties were of minor concern, since the galaxies investigated were much brighter than the Fornax dwarfs and hence also redder, falling into the empirically well calibrated colour range. We obtained a relative distance of 0.20 ± 0.12 mag between Centaurus and Hydra, indicating that the Hydra cluster ($d \simeq 41$ Mpc) is somewhat closer to us than Centaurus ($d \simeq 45$ Mpc). Since the CMB radial velocity of the Hydra cluster is about 700 km s^{-1} higher than that of Centaurus, this implies a large difference in peculiar velocity between both clusters: the Centaurus cluster lies approximately within the Hubble flow, while the Hydra cluster’s peculiar velocity is more than 1000 km s^{-1} . This difference can be explained by a significant mass overdensity – the “Great Attractor” – in close projection to and slightly behind ($\simeq 5\text{-}10$ Mpc) the Hydra cluster. This position is about 15° away in projection to that estimated in the SBF flow study by Tonry and collaborators. Those authors had not included the Hydra cluster into their study and generally investigated more nearby galaxies. The Great Attractor distance ($\simeq 45$ Mpc) and mass ($\simeq 10^{16} M_*$) determined by Tonry and collaborators does not need to be changed to explain our observed peculiar velocities, although mass-distance degeneracies of a factor of a few exist. Both at the location determined by us and that from Tonry et al., the Great Attractor is not directly associated with any prominent galaxy cluster. This is consistent with the Great Attractor being a super-massive dark halo that has not been able to form a significant number of stars/galaxies. While in the literature there have been some claims for very massive dark halos, their proposed masses are still at least a factor of 10-20 below that estimated for the Great Attractor. Some cautionary remarks regarding the interpretation of peculiar velocity differences seem appropriate: While our results are certainly inconsistent with the Hydra and Centaurus cluster participating in a pure Hubble flow, they do not firmly discard an equal distance for Hydra and Centaurus, which would also be

in better agreement with literature distance estimates. In this case the peculiar velocity difference between both clusters would be about 700 km s^{-1} . This is still considerable, but can with a slightly higher probability (5-10%) be explained by a chance superposition of thermal peculiar velocities, without the need for a massive “Attractor” in the background.

We suggest that an updated modelling of the local peculiar velocity field is necessary in the light of more and more high quality data arriving for distance estimates to nearby galaxies. The discovery of very massive galaxy clusters in the Zone of Avoidance in the last few years at substantial angular separation from the Hydra-Centaurus region supports the impression that there is not one single “Great Attractor”, but rather several substructures within a generally overdense filamentary region of the nearby universe.

Outlook

Our first application “Fornax Deep Field” has shown that the SBF method can significantly improve the constraints on the faint end of the galaxy luminosity function in nearby ($d < 20 \text{ Mpc}$) galaxy clusters. This especially holds for those clusters that are less dense than Fornax and hence require a more rigorous background decontamination, which the SBF method can easily achieve down to very faint magnitudes. Requirements for this are that like in the Fornax case the galaxy population be dominated by early-types, that the area for SBF sampling be large enough, comprising at least about 20×20 PSF-FWHM, and that the cluster be close enough such that the SBF are reliably detected above the sky noise for faint surface brightnesses. Nearby groups of galaxies within 20 Mpc like Virgo, Leo I, Dorado or Antlia are feasible follow-up candidates for surveys similar to “Fornax Deep Field”. Evaluation of the second part of “Fornax Deep Field” will allow us to further improve the restrictions on the galaxy luminosity function in Fornax and to address more precisely the SBF calibration at blue colours.

Regarding the possible existence of a Great Attractor in the Hydra-Centaurus region – which is consistent with the results of our second SBF application – it is necessary to continue with SBF surveys in the distance range 40-60 Mpc over a much larger area than investigated by us, given that we sample the peculiar velocity field at only two positions. The technical requirement for such surveys clearly is a sufficient depth of the data that reliably allows to calculate the contribution of undetected globular clusters to the measured fluctuations. As soon as this contribution constitutes the major fraction of the measured fluctuation signal (like in Tonry’s SBF measurements for the Centaurus cluster), SBF distances are not reliable any more. A deep and wide field SBF survey in the extended Hydra-Centaurus region, using for example IMACS at Magellan, the same instrument used for obtaining data in Chapt. 3, would be an appropriate next step.

Chapter 6

Zusammenfassung

Diese Arbeit beschäftigt sich mit zwei Anwendungen einer speziellen Methode zur Entfernungsbestimmung auf zwergelliptische Galaxien, nämlich der Methode der “surface brightness fluctuations” (SBF, auf deutsch “Fluktuationen der Flächenhelligkeit”). Die SBF Methode beruht auf der trivialen Tatsache, daß auf dem astronomischen Bild einer Galaxie die Anzahl der in einem Bildelement (=Pixel) abgebildeten Sterne *endlich* ist. In Bereichen konstanter Flächenhelligkeit gibt es daher statistische Fluktuationen der Flächenhelligkeit von Pixel zu Pixel – die “surface brightness fluctuations” –, deren Amplitude proportional zur Quadratwurzel der Anzahl der Sterne pro Pixel ist. Diese Anzahl ist aus geometrischen Gründen quadratisch proportional zur Entfernung der Galaxie. Die Amplitude der auf die mittlere Flächenhelligkeit normierten Fluktuationen (SBF Amplitude) ist daher umgekehrt proportional zur Entfernung und kann zur Entfernungsbestimmung genutzt werden.

- In Kapitel 1 dieser Arbeit wird ein kurzer Überblick über verschiedene Methoden zur astronomischen Entfernungsbestimmung gegeben. Daraufhin werden die mathematischen Grundlagen und verschiedene praktische Aspekte der SBF Methode erläutert.
- In Kapitel 2 beschreiben wir Simulationen, die das Potenzial der SBF Methode quantifizieren, Entfernungen zu den intrinsisch leuchtschwachen zwergelliptischen Galaxien (dEs) in nahegelegenen Galaxienhaufen zu bestimmen. Das zugrundeliegende wissenschaftliche Problem ist, dass es bei Beobachtungen nahegelegener Galaxienhaufen sehr schwierig ist zu erkennen, ob leuchtschwache Objekte, die dem erwarteten Aussehen von dEs im Haufen entsprechen, wirklich dem Haufen angehören. Um diese Unsicherheit zu überwinden, sind direkte Entfernungsmessungen nötig. Die Kenntnis der Haufenmitgliedschaft ist notwendig, um die Galaxienleuchtkraftfunktion (“galaxy luminosity function”, GLF) zu bestimmen, definiert als die Anzahl an Galaxien pro logarithmischen Helligkeitsintervall. Der Vergleich der GLF mit der aus kosmologischen Modellrechnungen hervorgehen-

- den Massenfunktion sogenannter “Dunkle Materie Halos” (“Dark Matter Halos”) ermöglicht dann eine Bewertung gängiger Theorien zur Struktur- und Galaxienbildung. Die Simulationen in Kapitel 2 zeigen, dass für dEs in nahegelegenen Galaxienhaufen wie Virgo oder Fornax verlässliche Haufenmitgliedschaftbestimmungen mittels der SBF Methode bis hin zu sehr geringen absoluten Helligkeiten ($M_V \simeq -11$ mag) möglich sind.
- In Kapitel 3 wird die Anwendung der SBF Methode auf leuchtschwache dE Kandidaten im Fornax Galaxienhaufen beschrieben, welche anhand von früheren Aufnahmen mit geringerer Auflösung als mögliche Haufenmitglieder klassifiziert worden waren. Von 24 dEs im Helligkeitsbereich $-14 < M_V < -9$ mag konnten 10 dEs per SBF Messung als Haufenmitglieder identifiziert werden, weitere 8 dEs konnten anhand ihrer Morphologie als wahrscheinliche Haufenmitglieder bestätigt werden. Nur 4 dEs wurden als wahrscheinliche Hintergrundobjekte klassifiziert. Zwei dEs hatten eine unklare Klassifikation, und zwei zusätzliche Kandidaten wurden neu entdeckt. Diese Ergebnisse bedeuten die klare Bestätigung einer sehr flach ansteigenden GLF in Fornax, in deutlicher Diskrepanz zu der viel steiler zu erwartenden Massenfunktion Dunkler Materie Halos. Solche im Vergleich zu kosmologischen Modellen zu flach ansteigenden GLFs sind bereits für die Umgebung der Milchstraße wie auch für andere Galaxienhaufen gemessen worden. Dies wird auch als das “Substrukturproblem” der modernen Kosmologie bezeichnet. Eine anhand von existierenden Beobachtungen testbare Erklärung für das Substrukturproblem steht bislang noch aus.
 - In Kapitel 4 wird die Anwendung der SBF Methode auf 31 Galaxien (davon 26 dEs) im Centaurus und Hydra Galaxienhaufen beschrieben. Für den Hydrahaufen wird eine etwas geringere Entfernung von 41.2 ± 1.4 Mpc abgeschätzt als für Centaurus (45.3 ± 2.0 Mpc). Dies bedeutet, dass der Hydrahaufen sich im Vergleich zu Centaurus um ca. 1000 km s^{-1} schneller von uns entfernt als für den Fall eines vollkommen gleichmäßigen Auseinanderdriftens aller Objekte im Universum (dem sog. “Hubble flow”, d.h. Hubblefluß). Eine mögliche Erklärung für eine solch hohe “Pekuliargeschwindigkeit” ist, dass sich wenige Mpc hinter Hydra der Schwerpunkt einer ausgeprägten überdichten Region im nahen Universum befindet, welche den Hydrahaufen aufgrund ihrer gravitativen Wirkung von uns weg zieht. Hinweise auf eine solche Überdichte in Richtung Hydra/Centaurus hat es schon seit mehreren Jahrzehnten gegeben, man bezeichnet sie gemeinhin als “Great Attractor”. Die mit unseren Daten konsistente Position des Great Attractors am Himmel ist ca. 15° entfernt von der Position, die in einer vorhergehenden SBF-Studie von Tonry und Mitarbeitern abgeschätzt wurde. Jene Studie beinhaltete allerdings keine Entfernungsabschätzung zum Hydrahaufen und beschränkte sich generell auf nahegelegene Galaxien. Die Entfernung ($\simeq 45$ Mpc) und Masse ($\simeq 10^{16} M_*$, mit $M_* = 2 \times 10^{30}$ kg der Masse der Sonne) des Great Attractors aus der Tonry-Studie muß nicht geändert werden, um unsere Resultate zu

erklären. Das interessante am Great Attractor ist, dass sich weder an der in dieser Arbeit noch an der von Tonry abgeschätzten Position ein deutlich sichtbarer Galaxienhaufen befindet. Damit entspricht der Great Attractor der Vorstellung eines sehr massereichen Halos aus dunkler Materie, in dem sich nur sehr wenige Sterne/Galaxien gebildet haben. In der Literatur gibt es Hinweise auf die mögliche Existenz solcher Halos, welche aber alle mindestens 10-20 mal masseärmer sind als man für den Great Attractor abschätzt. Es bleibt zu bemerken, dass unsere Daten noch marginal konsistent mit einer gleichen Entfernung für Hydra und Centaurus sind, was auch näher an bisherigen Abschätzungen aus der Literatur liegt. In solch einem Fall wäre der Unterschied an Pekuliargeschwindigkeit zwischen beiden Haufen ca. 700 km s^{-1} , was mit einer gewissen Wahrscheinlichkeit (5-10%) auch das Produkt einer zufälligen Überlagerung von "thermischen" Geschwindigkeitsvektoren sein könnte, also keines "Great Attractors" bedürfte.

Ausblick

Die Ergebnisse von Kapitel 3 haben gezeigt, dass die SBF Methode sehr gut dazu geeignet ist, die Form der Galaxienleuchtkraftfunktion im leuchtschwachen Bereich in nahen Galaxienhaufen mit größerer Genauigkeit zu bestimmen als durch reine morphologische Selektion. Dies gilt besonders auch für solche Galaxienhaufen, die weniger dicht als der hier betrachtete Fornaxhaufen sind und deshalb einen höheren Anteil an Hintergrundobjekten unter morphologisch vorselektierten möglichen Haufenmitgliedern haben. Lohnende Ziele für zukünftige Untersuchungen analog zu der hier präsentierten sind nahegelegene Galaxienhaufen/-gruppen wie z.B. Leo, Dorado, Virgo und Antlia. Bzgl. der Hypothese eines nahegelegenen "Great Attractors" (Kapitel 4) wird es nötig sein, in einem weiter ausgedehnten Bereich am Himmel akkurate Entfernungen zu Galaxien im Entfernungsbereich 40-60 Mpc mittels SBF (oder anderen Methoden) zu messen, da unsere Untersuchung das Pekuliargeschwindigkeitsfeld nur an zwei Punkten misst. Eine solche weiter ausgedehnte Untersuchung wird eine genauere Abschätzung der Gesamtmasse und Entfernung des Great Attractors ermöglichen. Ein geeignetes Instrument ist IMACS am Magellan-Teleskop in Las Campanas, Chile, welches bereits für die Datengewinnung in Kapitel 3 benutzt wurde.

Bibliography

- [1982] Aaronson, M., Huchra, J., Mould, J., Schechter, P.L., & Tully, R.B. 1982, *ApJ*, 258, 64
- [1986] Aaronson, M., Bothun, G., Mould, J., Huchra, J., Schommer, R.A., & Cornell, M.E. 1986, *ApJ*, 302, 536
- [1989] Aaronson, M., Bothun, G.D., Cornell, M.E. et al. 1989, *ApJ*, 338, 654
- [2003] Abazajian, K., Adelman-McCarthy, J.K., Agueros, M.A. et al. (SDSS collaboration), 2003, *AJ*, 126, 2081
- [1994] Ajhar, E.A., & Tonry, J.L. 1994, *ApJ*, 429, 557
- [2001] Ajhar, E.A., Tonry, J.L., Blakeslee, J.P., Riess, A.G., & Schmidt, B.P. 2001, *ApJ*, 559, 584
- [1993] Aragon-Salamanca, A., Ellis, R.S., Couch, W.J., & Carter, D. 1993, *MNRAS*, 262, 764
- [1999] Armandroff, T.E., Jacoby, G.H., & Davies, J.E. 1999, *AJ*, 118, 1220
- [2002] Arnaboldi, M., Aguerri, J.A.L., Napolitano, N.R. et al. 2002, *AJ*, 123, 760
- [2003] Barrientos, L.F., & Lilly, S.J. 2003, *ApJ*, 596, 129
- [2002] Bartelmann, M., & White, S.D.M. 2002, *A&A*, 388, 732
- [2001] Bellazzini, M., Ferraro, F.R., & Pancino, E., 2001, *ApJ*, 556, 635
- [1992] Bender, R., Burstein, D., & Faber, S.M. 1992, *ApJ*, 399, 462
- [2002] Benedict, G.F., McArthur, B.E., Fredrick, L.W et al. 2002, *AJ*, 123, 473
- [2003] Bennett, C.L., Halpern, M., Hinshaw, G. et al. 2003, *ApJS*, 148, 1
- [2003] Bernardi, M., Sheth, R.K., Annis, J. et al., 2003, *AJ*, 125, 1866
- [1994] Bertelli, G., Bressan, A., Chiosi, C., Fagotto, F., & Nasi, E. 1994, *A&AS*, 106, 275

- [1996] Bertin, E., & Arnouts, S. 1996, *A&AS*, 117, 393
- [1995] Blakeslee, J.P., & Tonry, J.L. 1995, *ApJ*, 442, 579
- [1999] Blakeslee, J.P., Ajhar, E.A., & Tonry, J.L. 1999, in *Post-Hipparcos Cosmic Candles*, ed. A. Heck & F. Caputo (Boston: Kluwer), 181
- [2001] Blakeslee, J.P., Vazdekis, A., & Ajhar, E.A. 2001, *MNRAS*, 320, 193
- [2002] Blakeslee, J.P., Lucey, J.R., Tonry, J.L. et al. 2002, *MNRAS*, 330, 443
- [1997a] Bono, G., Caputo, F., Cassisi, S., Castellani, V., & Marconi, M. 1997a, *ApJ*, 479, 279
- [1997b] Bono, G., Caputo, F., Cassisi, S., Castellani, V., & Marconi, M. 1997b, *ApJ*, 489, 822
- [1991] Bothun, G.D., Impey, C.D., & Malin, D.F. 1991, *ApJ*, 376, 404
- [2005] Broadhurst, T., Benítez, N., Coe, D. et al. (ACS-team) 2005, *ApJ*, 621, 53
- [1999] Brocato, E., Castellani, V., Raimondo, G., & Romaniello, M. 1999, *A&AS*, 136, 65
- [2000] Brocato, E., Castellani, V., Poli, F.M., & Raimondo, G. 2000, *A&AS*, 146, 91
- [1993] Bruzual, G., & Charlot, S. 1993, *ApJ*, 405, 538
- [2000] Caldwell, N., & Armandroff, T.A. 2000, 197th AAS Meeting, #106.05; *Bulletin of the American Astronomical Society*, Vol. 32, p.1579
- [2003] Cantiello, M., Raimondo, G., Brocato, E., & Capaccioli, M. 2003, *AJ*, 125, 2783
- [1991] Castellani, V., Chieffi, A., & Pulone, L. 1991, *ApJS*, 76, 911
- [1992] Castellani, V., Chieffi, S., & Straniero, O. 1992, *ApJS*, 78, 517
- [2004] Catelan, M., Pritzl, B.J., & Smith, H.A. 2004, *ApJS*, 154, 633
- [2003] Christlein, D., & Zabludoff, A.I., 2003, *ApJ*, 591, 764
- [1999] Churazov, E., Gilfanov, M., Forman, W., & Jones, C. 1999, *ApJ*, 520, 105
- [1993] Ciardullo, R., Jacoby, G.H., & Tonry, J.L. 1993, *ApJ*, 419, 479
- [1999] Colberg, J.M., White, S.D.M., Jenkins, A., & Pearce, F.R. 1999, *MNRAS*, 308, 593
- [2003] Costa, E., & Méndez, R.A. 2003, *A&A*, 402, 541
- [1998] Côté, P., Marzke, R.O., & West, M.J. 1998, *ApJ*, 501, 554

- [2004] Côté, P., Blakeslee, J.P., Ferrarese, L. et al. (ACS VCS team) 2004, *ApJS*, 153, 223
- [1993] Courteau, S., Faber, S.M., Dressler, A., & Willick, J.A. 1993, *ApJ*, 412L, 51
- [2000] Courteau, S., Willick, J.A., Strauss, M.A., Schlegel, D., & Postman, M. 2000, *ApJ*, 544, 636
- [2004] Czoske, O. 2004, astro-ph/0403650, to appear in Proc. of IAU Colloq. 195, ed. A. Diaferio et al., in preparation
- [2003] Dahle, H., Pedersen, K., Lilje, P.B., Maddox, S.J., & Kaiser, N. 2003, *ApJ*, 591, 662
- [1999] Dale, D.A., Giovanelli, R., Haynes, M.P., Campusano, L.E., & Hardy, E. 1999, *AJ*, 118, 1489
- [2003] Dekel, A., & Woo, J. 2003, *MNRAS*, 344, 1131 *ApJ* 438L, 13
- [1987c] Dressler, A., Faber, S.M., Burstein, D. et al. 1987, *ApJ*, 313L, 37
- [1987a] Dressler, A., Lynden-Bell, D., Burstein, David et al. (7 samurai) 1987, *ApJ*, 313, 42
- [1987b] Dressler, A. 1987, *ApJ*, 317, 1
- [2000] Drinkwater M.J., Phillipps S., Jones J.B. et al. 2000b, *A&A* 355, 900
- [2001a] Drinkwater, M.J., Gregg M.D., Holman B.A., & Brown M.J.I., 2001a, *MNRAS* 326, 1076
- [2001b] Drinkwater, M.J., Gregg, M.D., & Colless, M. 2001b, 2001, *ApJ*, 548, 139
- [1997] ESA, 1997, The Hipparcos and Tycho Catalogues, *yCat* 1239, 0
- [1976] Faber, S.M., & Jackson, R.E. 1976, *ApJ*, 204, 668
- [2004] Fairall, A., & Lahav, O. 2004, astro-ph/0411436, conference summary; to appear in ‘Nearby Large-Scale Structures and the Zone of Avoidance’, eds. A.P. Fairall and P.A. Woudt, ASP Conf. Series
- [1988] Ferguson, H.C., & Sandage A. 1988, *AJ*, 96, 1520
- [2000] Ferrarese, L., Ford, H.C., & Huchra, J., 2000, *ApJS* 128, 431
- [2005] Forte, J.C., Faifer, F., & Geisler, D. 2005, *MNRAS*, 357, 56
- [2001] Freedman, W.L., Madore, B.F., Gibson, B.K. et al., 2001, *ApJ*, 553, 47
- [2001] Furusho, T., Yamasaki, N.Y., Ohashi, T. et al. 2001, *PASJ*, 53, 421

- [1986] Gehrels, N. 1986, *ApJ* 303, 336
- [2000] Gibson, B.K., Stetson, P.B., Freedman, W.L. et al. 2000, *ApJ*, 529, 723
- [1999] Giovanelli, R., Dale, D.A., Haynes, M.P., Hardy, E., & Campusano, L.E. 1999, *ApJ*, 525, 25
- [1996] Girardi, L., Bressan, A., Chiosi, C., Bertelli, G., & Nasi, E. 1996, *A&AS*, 117, 113
- [1997] Girardi, M., Fadda, D., Escalera, E., et al. 1997, *ApJ*, 490, 56
- [2000] Girardi, L., Bressan, A., Bertelli, G., & Chiosi, C. 2000, *A&AS*, 141, 371
- [2002] Girardi, L., Bertelli, G., Bressan, A. et al. 2002, *A&A*, 391, 195
- [2002] Gonzalez, A.H., Zaritsky, D., Simard, L., Clowe, D., & White, S.D.M. 2002, *ApJ*, 579, 577
- [2003] Graham, A.W., & Guzman, R. 2003, *AJ*, 125, 2936
- [2001] Grebel, E.K. 2001, *Ap&SSS*, 277, 231
- [2003] Grebel, E.K., Gallagher, J.S., & Harbeck, D. 2003, *AJ*, 125, 1926
- [2004] Grebel, E.K., & Gallagher, J.S. 2004, *ApJ letters*, 610, 89
- [1987] Green, E.M., Demarque, P., & King, C.R. 1987, *The revised Yale isochrones and luminosity functions*, New Haven: Yale Observatory, 1987
- [1996] Hackbusch, W., Schwarz, H.R., & Zeidler, E., 1996, *Teubner-Taschenbuch der Mathematik* (founded by Bronstein/Semendjajew, continued by Grosche), B.G. Teubner Verlagsgesellschaft Leipzig 1996
- [1999] Hilker, M., Infante L., Vieira G., Kissler-Patig M., & Richtler T., 1999, *A&AS* 134, 75
- [1999b] Hilker, M., Infante, L., & Richtler, T. 1999b, *A&AS*, 138, 55
- [1929] Hubble, E. 1929, *PNAS*, 15, 168
- [1994] Hudson, M.J., 1994, *MNRAS*, 266, 475
- [2004] Hudson, M.J., Smith, R.J., Lucey, J.R., & Branchini, E., 2004, 352, 61
- [1990] Irwin, M.J., Davies, J.I., Disney, M.J., & Phillipps, S. 1990, *MNRAS*, 245, 289
- [1992] Jacoby, G.H., Branch, D., Ciardullo, R. et al., 1992, *PASP*, 104, 599
- [1996] Jensen, J.B., Luppino, G.A., & Tonry, J.L., 1996, *ApJ*, 468, 519

- [1998] Jensen, J.B., Tonry, J.L., & Luppino, G.A. 1998, ApJ, 505, 111
- [1999] Jensen, J.B., Tonry, J.L., & Luppino, G.A. 1999, ApJ, 510, 71
- [2001] Jensen, J.B., Tonry, J.L., Thompson, R.I. et al., 2001, ApJ, 550, 502
- [2003] Jensen, J.B., Tonry, J.L., & Barris, B.J., 2003, ApJ 583, 712
- [1997] Jerjen, H., & Dressler, A., 1997, A&AS 124, 1
- [1998] Jerjen, H., Freeman, K.C., & Binggeli, B. 1998, AJ 116, 2873
- [2000] Jerjen, H., Freeman, K.C., & Binggeli, B. 2000, AJ 119, 166
- [2001] Jerjen, H., Rekola, R., Takalo, L., Coleman, M., & Valtonen, M., 2001, A&A 380, 90
- [2003] Jerjen, H. 2003, A&A, 398, 63
- [2004] Jerjen, H., Binggeli, B., & Barazza, F.D. 2004, AJ, 127, 771
- [2000] Kambas, A., Davies, J. I., Smith, R. M., Bianchi, & S., Haynes, J. A., 2000, AJ 120, 1316
- [2000] Kauffmann, & G., Haehnelt, M., 2000, MNRAS 311, 576
- [2004] Kazantzidis, S., Mayer, L., Mastropietro, C., Diemand, J., Stadel, J., & Moore, B. 2004, ApJ, 608, 663
- [2002] King, L.J., Clowe, D.I., & Schneider, P. 2002, A&A, 383, 118
- [1998] Kissler-Patig, M., Brodie, P.B., Schroder, L.L., et al. 1998, AJ, 115, 105
- [2004] Kravtsov, A.V., Gnedin, O.Y., & Klypin, A.A. 2004, ApJ, 609, 482
- [1995] Kolatt, T., Dekel, A., & Lahav, O. 1995, MNRAS, 275, 797
- [2001] Kundu, A., & Whitmore, B.C. 2001, AJ, 121, 2950
- [1994] Landolt, A.U. 1992, AJ, 104, 340
- [1994] Lauer, T.R., & Postman, M., 1994, ApJ, 425, 418
- [1998] Lauer, T.R., Tonry, J.L., Postman, M., Ajhar, E.A., & Holtzman, J.A. 1998, ApJ, 499, 577
- [1997] Lee, M., & Geisler, D. 1997, IAU symposium 186, abstract 62, <http://www.ifa.hawaii.edu/iau-s186/abstracts/html/062P.html>
- [1996] Lineweaver, C.H., Tenorio, L., Smoot, G.V. et al., 1996, ApJ 470, 38

- [2000] Liu, M.C., Charlot, S., & Graham, J. 2000, ApJ, 543, 644
- [2001] Liu, M.C., & Graham, J.R. 2001, ApJ letters, 557, 31
- [2002] Liu, M.C., Graham, J.R., & Charlot, S. 2002, ApJ, 564, 216
- [1980] Lucey, J.R., Dickens, R.J., & Dawe, J.A. 1980, Nature, 285, 305
- [1986] Lucey, J.R., Currie, M.J., & Dickens, R.J., 1986, MNRAS 221, 453
- [1993] Luppino, G.A., & Tonry, J.L. 1993, ApJ, 410, 81
- [1988] Lynden-Bell, D., Faber, S.M., Burstein, D. et al. 1988, ApJ, 326, 19
- [1991] Madore, B.F., & Freedman, W.L. 1991, PASP, 103, 933
- [1920] Malmquist, K.G. 1920, Medd. Lund. Astron. Obs., Ser.2, No.22
- [1998] Mateo, M.L., 1998, ARA&A 36, 435
- [1992] Mathewson, D.S., Ford, V.L., & Buchhorn, M. 1992, ApJ, 389L, 5
- [1994] McLaughlin, D.E. 1994, PASP, 106, 47
- [1995] McLaughlin, D.E., et al. 1995
- [2000] Mei, S., Silva, D., & Quinn, P.J. 2000, A&A, 361, 68
- [2001] Mei, S., Silva, D.R., & Quinn, P.J. 2001, A&A, 366, 54
- [2003] Mei, S., Scodreggio, M., Silva, D.R., & Quinn, P.J. 2003, A&A, 399, 441
- [2005] Mei, S., Blakeslee, J.P., Tonry, J.L. et al. (ACS VCS team) 2005, ApJ in press
- [1998] Miller, B.W., Lotz, J., Ferguson, H.C., Stiavelli, M., & Whitmore, B.C. 1998, ApJ, 508L, 133
- [2005] Minchin, R., Davies, J., Disney, M. et al. 2005, ApJ letters, 622, 21
- [1999] Moore, B., Ghigna, S., Governato, F. et al. 1999, ApJL, 524, 19
- [1998] Morris, P.W., & Shanks, T. 1998, MNRAS, 298, 451
- [1997] Neilsen, E.H., Jr., Tsvetanov, Z.I., & Ford, H.C. 1997, ApJ, 483, 745
- [2000] Neilsen, E.H., Jr., & Tsvetanov, Z.I. 2000, ApJ, 536, 255
- [2002] Padilla, N.D., & Baugh, C.M. 2002, MNRAS, 329, 431
- [1994] Pahre, M.A., & Mould, J.R. 1994, ApJ, 433, 567
- [1999] Pahre, M.A., Mould, J.R., Dressler, A. et al. 1999, ApJ, 515, 79

- [1998] Phillipps, S., Parker, Q.A., Schwartzberg, J.M., & Jones, J.B., 1998 ApJ 493L, 59
- [2001] Poggianti, B., Bridges, T.J., Carter, D., Mobasher, B., et al. 2001, ApJ, 563, 118
- [1995] Postman, M., & Lauer, T.R., ApJ, 440, 28
- [1974] Press, W.H., & Schechter, P., 1974, ApJ 187, 425
- [1999] Pritchet, C.J., & van den Bergh, S., 1999, AJ 118, 883
- [1995] Quintana, H., Ramirez, A., Melnick, J., Raychaudhury, S., & Slezak, E., 1995, AJ, 110, 463
- [2002] Reiprich, T.H., & Böhringer, H. 2002, ApJ, 567, 716
- [2004] Rejkuba, M. 2004, A&A, 413, 903
- [1989] Richter, O.G., 1989, A&AS, 77, 237
- [2002] Ricotti, M., Gnedin, N.Y., & Shull, J.M. 2002, ApJ, 575, 49
- [2004] Riess, A.G., Strolger, L., Tonry, J. et al. 2004, ApJ, 607, 665
- [1985] Sandage, A., Binggeli, B., & Tammann, G.A., 1985, AJ 90, 1759
- [1988] Sandage, A. 1988, ARA&A, 26, 561
- [2002] Sandage, A., & Saha, A. 2002, AJ, 123, 2047
- [1976] Schechter, P. 1976, ApJ, 203, 297
- [1998] Schlegel, D.J., Finkbeiner, D.P., & Davis, M. 1998, ApJ, 500, 525
- [1997] Secker, J., Harris, W.E., & Plummer, J.D. 1997, PASP, 109, 1377
- [1984] Shaya, E.J. 1984, ApJ, 280, 470
- [1992] Shaya, E.J., Tully, R.B., & Pierce, M.J. 1992, ApJ, 391, 16
- [2002] Siegel, M.H., Majewski, S.R., Reid, I.N., & Thompson, I.B. 2002, ApJ, 578, 151
- [1994] Simard, L., & Pritchet, C. 1994, AJ, 107, 503
- [2000] Smith, R.J., Lucey, J.R., Hudson, M.J., Schlegel, D.J., & Davies, R.L. 2000, MNRAS, 313, 469
- [2001] Smith, R.J., Lucey, J.R., Schlegel, D.J., Hudson, M.J., Baggley, G., & Davies, R.L. 2001, MNRAS, 327, 249
- [2004] Smith, R.J., Hudson, M.J., Nelan, J.E. et al. 2004, AJ, 128, 1558

- [1995] Sodemann, M., & Thomsen, B. 1995, *AJ*, 110, 179
- [1996] Sodemann, M., & Thomsen, B. 1996, *AJ*, 111, 208
- [2003] Spergel, D.N., Verde, L., Peiris, H.V. et al. 2003, *ApJS*, 148, 175
- [2000] Staveley-Smith, L., Juraszek, S., Koribalski, B.S., Henning, P.A., & Kraan-Korteweg, R.C. 2000, in Kraan-Korteweg R.C., Henning P.A., Andernach H., eds, *ASP Conf. Ser. Vol. 218*, p. 207
- [1997] Stein, P., Jerjen, H., & Federspiel, M. 1997, *A&A*, 327, 952
- [2002] Stoehr, F, White, S.D.M., Tormen, G., & Springel, V. 2002, *MNRAS letters*, 335, 84
- [1995] Strauss, M.A., & Willick, J.A., 1995, *Phys. Rep.*, 261, 271
- [1985] Tammann, G.A., & Sandage, A. 1985, *ApJ*, 294, 81
- [1996] Tamura, T., Day, C.S., Fukazawa, Y. et al., 1996, *PASJ*, 48, 671
- [2000] Tamura, T., Makishima, K., Fukazawa, Y., Ikebe, Y., & Zu, H., 2000, *ApJ*, 535, 602
- [2004] Tegmark, M., Strauss, M.A., Blanton, M.R. et al., 2004, *PhRvD*, 69j, 3501
- [1997] Thomsen, B., Baum, W.A., Hammergren, M., & Worthey, G. 1997, *ApJ letters*, 483, 37
- [1988] Tonry, J.L., & Schneider, D.P. 1988, *AJ*, 96, 807
- [1990] Tonry, J.L., Ajhar, E.A., & Luppino, G.A. 1990, *AJ*, 100, 1416
- [1991] Tonry, J.L. 1991, *ApJ letters*, 373, 1
- [1997] Tonry, J.L., Blakeslee, J.P., Ajhar, E.A., & Dressler, A. 1997, *ApJ*, 475 399
- [2000] Tonry, J.L., Blakeslee, J.P., Ajhar, E.A., & Dressler, A. 2000, *ApJ*, 530, 625 (T00)
- [2001] Tonry, J.L., Dressler, A., Blakeslee, J.P. et al. 2001, *ApJ*, 546, 681
- [2001] Trentham, N., Tully, R.B., & Verheijen, M.A.W., 2001, *MNRAS* 325, 385
- [2002a] Trentham, N., & Hodgkin, S., 2002, *MNRAS* 333, 423
- [2002b] Trentham, N., & Tully, R.B., 2002, *MNRAS* 335, 712
- [1977] Tully, R.B., & Fisher, J.R. 1977, *A&A*, 54, 661
- [2000] Umetsu, K., & Futamase, T. 2000, *ApJ letters*, 539, 5

- [1985] Vandenberg, D.A. 1985, *ApJS*, 58, 711
- [2000] Van den Bergh, S., 2000, *PASP* 112, 529
- [1996] Vazdekis, A., Casuso, E., Peletier, R.F., & Beckman, J.E. 1996, *ApJS*, 106, 307
- [2005] von der Linden, A., Erben, T., Schneider, P., & Castander, F.J. 2005, submitted to *A&A*, astro-ph/0501442
- [1999] Whiting, A.B., Hau, G.K.T., & Irwin, M.J. 1999, *AJ*, 118, 2767
- [1990] Willick, J.A., 1990, *ApJL*, 351, 5
- [1999] Willick, J.A., 1999, *ApJ*, 522, 647
- [1994] Worthey, G. 1994, *ApJS*, 95, 107
- [2003] Woudt, P.A., Kraan-Korteweg, R.C., Cayatte, V., Balkowski, C., & Felenbok, P. 2003, *A&A*, 415, 9
- [2003] Yamasaki, N.Y., Ohashi, T., & Furusho, T., 2003, *ApJ*, 578, 833
- [2004] Zucker, D.B., Kniazev, A.Y., Bell, E.F. et al. 2004, *ApJ letters*, 612, 121

Appendix A

Appendix

A.1 Danksagung

Diese Arbeit entstand in der Zeit vom März 2002 bis März 2005 an der Sternwarte der Universität Bonn und dem Departamento de Astronomía y Astrofísica de la Pontificia Universidad Católica de Chile, Santiago. Allen Mitarbeitern der beiden Institute danke ich an dieser Stelle für die Hilfsbereitschaft und das angenehme Arbeitsklima.

Dem DAAD danke ich für das bereitgestellte Stipendium, welches mir den Aufenthalt in Santiago ermöglicht hat. Der DFG danke ich für die Bewilligung des SBF Projektes HI855/1.

Den folgenden Personen gilt mein besonderer Dank:

Prof. Dr. L. Infante für die Hilfe bei der Vorbereitung meines Aufenthalts in Santiago, für die vertrauensvolle und engagierte Betreuung in Santiago sowie für seine Empfehlungsschreiben.

Prof. Dr. K. S. de Boer für die Hilfe bei der Vorbereitung meiner beiden Aufenthalte in Santiago, für die Übernahme des Referats, für seine Empfehlungsschreiben und für seine unkomplizierte Art, die Sternwarte zu leiten.

Michael Hilker für die hervorragende wissenschaftliche Betreuung in Bonn und auch vorher in Santiago, der Einführung in das Thema und die tolle Kameradschaft.

John P. Blakeslee, Simona Mei, Narcizo Benitez und Holland Ford für viele interessante Diskussionen.

In Santiago: Matías Gomez und seiner Familie, Thomas Hilker, Martin Altmann, Marcelo Mora, José Gallardo, Erika Labbé, Jura Borrisova.

In Bonn: Manuel Metz, Ole Marggraf, Oliver Cordes, Pavel Kroupa, Mike Fellhauer, Philip Willemsen für die vielen guten Gespräche und ihre Lockerheit.

Der Mannschaft des Las Campanas Observatoriums in Chile für die gute Arbeitsatmosphäre und freundlichen Umgangformel in drei Beobachtungskampagnen.

Un agradecimiento muy especial le quiero dar a mi esposa Katherine por apoyarme en todos esos tiempos y para estar siempre a mi lado. Debo muchas gracias a mis dos hijos Maximiliano y Johannes para inspirarme a dar todos los días lo mejor para ellos. Quiero agradecer a toda mi familia suegra en Santiago, quienes con su incondicional apoyo a nosotros siempre me han hecho sentir parte de la familia. Un gracias especial doy a mi suegra Olga para cuidar a mis chiquillos y Katy en los últimos dos meses.

Ein besonderer Dank geht an meine Familie, ganz besonders meine Mutter, meine Oma und meine Schwester, die mich in den vielen Jahren des Hin- und Herreisens zwischen Chile und Deutschland immer unterstützt haben. Ohne Eure Hilfe hätte ich es nicht geschafft.

Neuwied, im März 2005

A.2 Versicherung

Ich versichere, daß ich diese Arbeit selbständig verfaßt und keine anderen als die in Abschnitt "Bibliography" angegebenen Quellen und Hilfsmittel benutzt sowie die Zitate kenntlich gemacht habe.

Bonn, den 30.3.2005

1. Referent: Prof. Dr. L. Infante
2. Referent: Prof. Dr. K. S. de Boer

A.3 Curriculum vitae

Personal dates:

Name: Steffen Mieske
 Nationality: German
 Date of Birth: 12. January 1976
 Place of birth: Neuwied, Germany
 Civil status: Married, two children

School education:

1982 – 1986 Primary School Friedrich-Ebert-Grundschule Oberbieber
 1986 – 1995 Secondary School, Rhein-Wied-Gymnasium Neuwied
 June 1995 Abitur (High school examination)

Civil service:

Sept. 1995 – Sept. 1996 Landesgehörlosenschule Neuwied

Studies:

Oct. 1996 – August 2001 Study of Physics at Bonn University
 Oct. 1998 Vordiplom (pre-exam) in Physics, mark: “Sehr gut” (very good).
 Oct. 1998 Enter BIPP (Bonn International Physics Programme)
 March – April 1999 Student assistant at MPIfR Bonn with Prof. Schmid-Burgk
 May – July 2000 Student assistant as tutor of the
 physics lab course for medicine students
 Sept. 2000 – Aug. 2001 Diploma thesis in physics, subject of choice astronomy. Topic:
*Towards the understanding of ultra compact object in Fornax:
 Results of a recent spectroscopic survey*
 In the framework of the BIPP stay at the astronomical
 institute of the Pontificia Universidad Católica de Chile (PUC)
 August 2001 Diploma in physics
 Total mark: “Mit Auszeichnung” (with distinction)
 Oct. 2001 – Feb. 2002 Student assistant as tutor of optics course (3rd semester)
March 2002 – March 2005 PhD thesis in astronomy at Sternwarte Bonn
 Topic: *Dwarf galaxies in nearby clusters*
 Supervisor Dr. M. Hilker, Prof. Dr. K. S. de Boer
 March 2002 – Nov. 2003 Stay at the astronomical institute of the PUC
 Supervisor Prof. Dr. L. Infante.
 Nov. 2003 – April 2005 Research assistant at Sternwarte Bonn
 June 2004 Supervisor of observational practical studies
 at the Observatory Hoher List, Bonn

Awards:

Diploma thesis grant of State of Nordrhein-Westfalen
 from 09/00 to 06/01 during stay in Chile
 PhD grant of DAAD (German Academic Exchange service)
 from 03/02 to 11/03 during stay in Chile

“Die Wissenschaft besteht nur aus Irrtümern. Aber diese Irrtümer muss man begehen.
Es sind die Schritte zur Wahrheit.”

Jules Verne